Trinity College Dublin
Coláiste na Tríonóide, Baile Átha Cliath
The University of Dublin

SCHOOL OF CHEMISTRY

STRUCTURAL AND ELECTRICAL CHARACTERISATION OF TRANSITION METAL DICHALCOGENIDES

CANSU ILHAN

January 2025

Under the supervision of Prof Mick Morris

SUBMITTED IN PARTIAL FULFILMENT OF THE REQUIREMENTS FOR THE DEGREE OF DOCTOR OF PHILOSOPHY

Declaration

I hereby declare that this Thesis is entirely my own work and that it has not been submitted as an exercise for a degree at this or any other university.

I declare that this thesis has not been submitted as an exercise for a degree at this or any other university and it is entirely my own work.

I agree to deposit this thesis in the University's open-access institutional repository or allow the Library to do so on my behalf, subject to Irish Copyright Legislation and Trinity College Library conditions of use and acknowledgement.

I consent to the examiner retaining a copy of the thesis beyond the examining period, should they so wish (EU GDPR May 2018).

Signed: _____ Date: _____

_____

Cansu Ilhan

Abstract

This thesis explores modification of transition metal dichalcogenides (TMDs) through doping and synthesis techniques to tailor their electronic properties, including sensor technology. The work is divided into three main studies: Rhenium (Re) doping in Molybdenum Disulfide (MoS_2) to achieve n-type characteristics, Niobium (Nb) doping in Tungsten Disulfide (WS_2) to induce p-type behavior, and the synthesis and application of $PtSe_2$ in strain sensors.

The first study investigates Re doping in Thermally Assisted Conversion (TAC) MoS_2 films, with three compositions: pristine, 2.63 at.% Re, and 10.48 at.% Re. Based on Hall effect measurements, both 2.63 at.% and 10.48 at.% Re-doped MoS_2 showed n-type behavior with reliable signal-to-noise ratio. Optimal 2.63 at.% Re doping enhanced conductivity and reduced activation energy, as confirmed by Arrhenius plots. Hall measurements showed the highest mobility at 2.63 at.% Re doping (0.51 $cm^2/V{\cdot}s$) and a resistivity of 2.5 $\Omega{\cdot}cm$. TEM and EELS analyses indicated Re segregation and integration into the MoS_2 matrix, providing insights into polycrystalline MoS_2 film doping.

The second study addresses achieving weak p-type conductivity in TAC grown WS_2 through Nb doping, with two compositions: pristine and 1.76 at.% Nb. Introducing Nb at 1.76 at.% and converting at 900°C for 30 minutes resulted in highly textured structures in both pristine and Nb-doped WS_2 samples. Field effect measurements showed pristine WS_2 had n-type behavior with a mobility of approximately 0.1 $cm^2/V{\cdot}s$ and an on/off ratio of 8, while Nb-doped WS_2 exhibited weak p-type

conduction, attributed to incomplete conversion. This study underscores the need for further optimization of the doping process and provides a basis for improving doped WS_2 film quality.

The third study focuses on $PtSe_2$ synthesis and its application in sensors, motivated by an energy-efficient electrochemical exfoliation (EE) process, large $PtSe_2$ flakes with aspect ratios exceeding 1000 were produced and deposited using the Langmuir-Schaefer technique to achieve highly aligned networks. The semitransparent sensors, with $\approx 60\%$ transparency (light passes through) at 1000 nm, showed potential applications in textile electronics. The sensors exhibited a consistent response with 0.5% strain with a negative gauge factor of -5.45, attributed to changes in the band structure upon deformation, and remained robust for 1000 cycles.

This thesis provides insight into semiconducting material synthesis and characterization, and suggests future pathways to optimize these materials.

Acknowledgements

I would like to thank Colm McAtamney and Amanda for arranging me some funding to stay in the research.

Tian Carey, thank you for being a role model. Eoin Caffrey, thank you for being positive.

I am grateful to my dear friend Hugh Conlon for always being there. We will see good days, Hugh.

Salma and Canan, though we may not be in touch, your presence is always felt; you are always in my mind and heart. Thank you.

I appreciate Ross Smith for sharing all his subscriptions with me. Thanks for being patient with me, Ross. Wishing you more years of patience with me.

Thanks to all my wonderful friends and colleagues: Amy, Ardak, Brian, Darragh, German Chris, Gwenael, Igor, Lee, Lucy, Matteo, Shixin, Simon. You were always kind to me. Ardak, thanks a lot for being my friend.

I extend my heartfelt thanks to my parents. Though you never fully understand why I am putting myself through this, your support mean a lot to me. Thank you.

Lastly, I want to thank myself, I have never struggled in my life like I struggled in my stay in Ireland. I let life to hit me.. it is a rope-a-dope... Now I will hit it back.

Contents

List of Figures

List of Tables

Nomenclature

ADF	Annular Dark Field
CVD	Chemical Vapor Deposition
EBID	Electron Beam Induced Deposition
EDS	Energy Dispersive Spectroscopy
EE	Electrochemical Exfoliation
EELS	Electron Energy Loss Spectroscopy
FET	Field Effect Transistor
HAADF	High Angle Annular Dark Field
HREM	High-Resolution Electron Microscopy
LPE	Liquid Phase Exfoliation
LS	Langmuir-Schaefer
PA	Polyamide
PET	Polyethylene Terephthalate
SEM	Scanning Electron Microscopy
TA	Thermally Assisted
TAC	Thermal Annealing Conversion
TEM	Transmission Electron Microscopy
TM	Transition Metal
TMD	Transition Metal Dichalcogenide
UV	Ultraviolet
XRD	X-Ray Diffraction
XRR	X-Ray Reflectivity

1 Introduction

The relentless pursuit of advancements in the semiconductor industry has driven the exploration of both traditional materials, such as silicon, and emerging alternatives like transition metal dichalcogenides (TMDs). These materials exhibit tunable electronic, optical, and mechanical properties, offering significant potential for next-generation electronic devices. With their unique layered structures and exceptional versatility, TMDs have emerged as strong candidates for applications ranging from transistors and sensors to optoelectronic devices.

This thesis investigates two primary approaches for material synthesis: bottom-up techniques, such as Thermally Assisted Conversion (TAC), and top-down methods like Electrochemical Exfoliation (EE). TAC, a scalable variant of Chemical Vapor Deposition (CVD), enables controlled growth of polycrystalline films with tunable properties, making it particularly suitable for large-scale production. Conversely, EE provides a cost-effective route for high-quality low-dimensional materials by minimizing defect generation during the exfoliation process.

This chapter begins by discussing the foundational principles of semiconductors, including their electronic structure, and doping mechanisms. It then provides an overview of synthesis techniques employed for fabricating emerging semiconductor materials. The chapter concludes with a discussion of the potential applications of these materials, emphasizing their integration into electronic devices, as explored in this thesis.

1.1 Introduction to Semiconductors and Their Properties

Semiconductors, which serve as the fundamental building blocks of modern electronics, are materials whose electrical conductivity can be precisely tuned through temperature, the application of electric fields, and the deliberate introduction of impurities. They form the basis of a wide range of electronic devices, including transistors, diodes, solar cells, LEDs, and photodetectors. At the heart of these capabilities is the presence of a bandgap, an energy range in which no electronic states exist, lying between the fully occupied valence band (E_V) and the empty conduction band (E_C), as shown in Figure 1.1 (a), (b), (c). Materials can be broadly classified based on the size of their bandgap (E_g). Insulators, such as silicon dioxide (SiO_2) and diamond, possess large bandgaps ($E_g \approx 9\,\text{eV}$ for SiO_2 and $E_g \approx 5.47\,\text{eV}$ for diamond), which prevent significant electron excitation from the valence band to the conduction band, even at high temperatures, making them electrically non-conductive. In contrast, semiconductors, with moderate bandgaps ranging from $0.6\,\text{eV}$ to $1.5\,\text{eV}$, can have their conductivity significantly enhanced by thermal excitation or doping. Silicon, with a bandgap of approximately $1.12\,\text{eV}$ at room temperature, is the most widely used semiconductor due to its abundance, well-developed processing technologies, and well-established fabrication infrastructure. Other commonly employed semiconductors include germanium ($E_g \approx 0.66\,\text{eV}$) and gallium arsenide (GaAs, $E_g \approx 1.41\,\text{eV}$), with GaAs offering a direct bandgap and high electron mobility, making it suitable for high-speed and optoelectronic applications. Metals, on the other hand, exhibit no bandgap ($E_g = 0$) due to the overlap of their conduction and valence bands, which allows free electrons to move freely and results in high electrical conductivity [1, 2].

Figure 1.1 illustrates the differences in bandgap energies across insulators, semiconductors, and metals, highlighting how these properties govern electrical conduc-

tivity. The ability to tune the bandgap through material selection and doping processes is critical to advancing electronic and optoelectronic technologies. Silicon's dominance as a semiconductor is due to its moderate bandgap, allowing operation at room temperature, and its compatibility with Conventional Metal Oxide Semiconductor (CMOS) processing. Other semiconductors, such as Ge and GaAs, are used for specific applications requiring smaller bandgaps or higher mobility. Compound semiconductors like indium phosphide (InP) extend this versatility, offering properties suited for telecommunications and high-speed electronics.

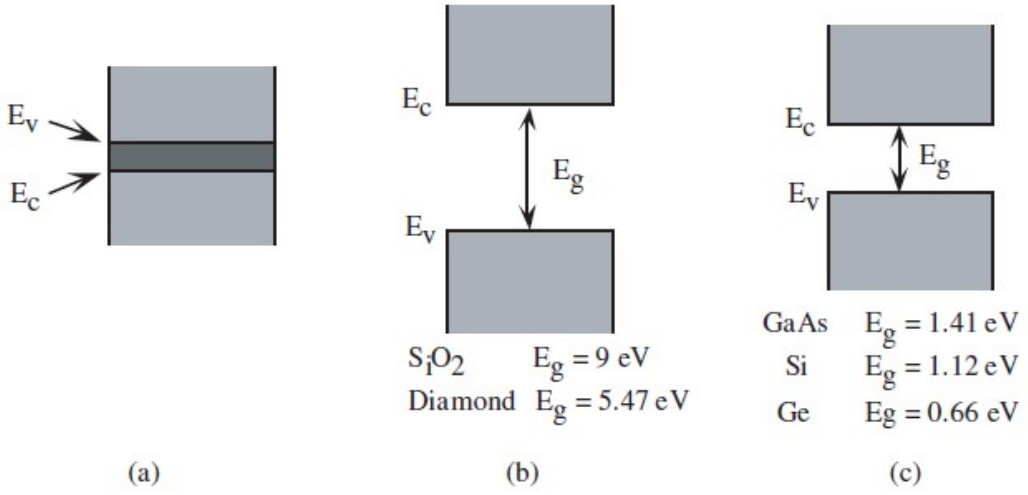

Figure 1.1: Schematic of the band gaps in different classes of materials: insulators (SiO_2 and diamond), semiconductors (GaAs, Si, Ge), and metals (no bandgap) [2].

In intrinsic semiconductors such as pure Si, each silicon atom forms covalent bonds with four neighboring atoms, as shown in Figure 1.2(a) and (b), filling its valence band with electrons that remain bound until sufficient thermal energy is provided for some of these electrons to jump into the conduction band, leaving behind positively charged vacancies called holes. At room temperature, the conductivity of intrinsic silicon is very low due to the lack of excited electrons.

By introducing controlled impurities, known as doping, one can dramatically alter the concentration of free carriers in an intrinsic semiconductor. Adding phosphorus (P), a group V element with five valence electrons, to Si creates loosely bound electrons that can be thermally excited into the conduction band with a comparatively

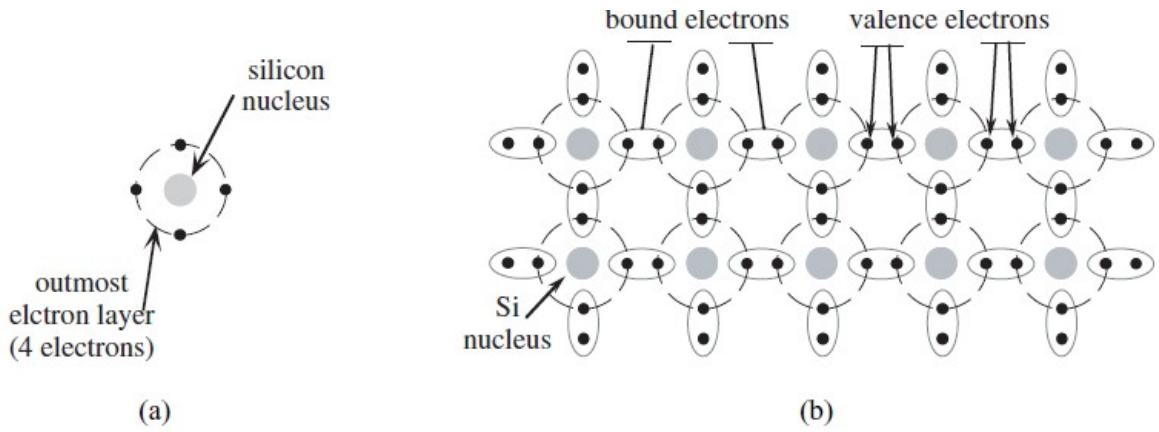

Figure 1.2: (a) Schematic of a silicon atom with four valence electrons. (b) In the crystal lattice, each Si atom shares electrons with neighbors, forming covalent bonds. Thermal or doping-induced excitation frees some electrons into the conduction band, leaving behind holes in the valence band [2].

small activation energy of about 40-50 meV, generating n-type Si, where electrons outnumber holes [3]. Conversely, adding boron (B), a group III element, introduces electron deficiencies or acceptor levels just above the valence band, allowing holes to form more easily at room temperature with a similar small activation energy, thus producing p-type Si. Intrinsic carrier concentrations in Si and GaAs are on the order of $10^{10}\,\mathrm{cm}^{-3}$ and $10^{6}\,\mathrm{cm}^{-3}$ respectively, while doping increases these carrier densities by many orders of magnitude [4]. In germanium, with its smaller bandgap, doping can be even more effective at room temperature, and in GaAs or InP, donor and acceptor activation energies may be as low as a few meV, ensuring high carrier concentrations at relatively low thermal energies. In all cases, extrinsic semiconductors (i.e., doped materials) exhibit free carrier densities approximately equal to the dopant concentration, thereby achieving conductivities orders of magnitude higher than their intrinsic counterparts [4].

For the presence of electrons to contribute to the conductivity of a semiconductor, the electrons must occupy energy states where movement is possible. As temperature increases, electrons obey Fermi-Dirac statistics, which describe the probability of occupation of electronic energy states [5]. At absolute zero, all energy states below the Fermi level E_F are completely occupied by electrons, while those above E_F are empty, meaning no thermal energy is available to excite electrons. For $T > 0$, ther-

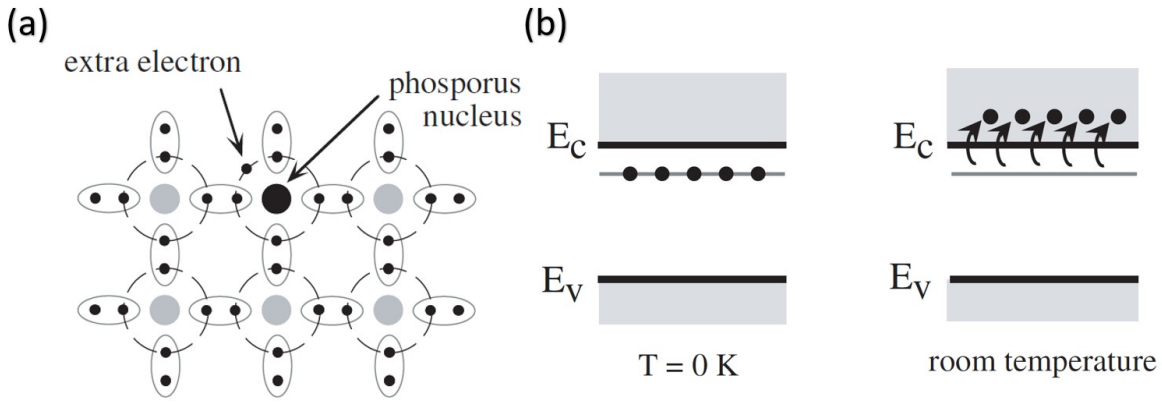

Figure 1.3: (a) Incorporating a donor atom such as phosphorus into silicon results in extra electrons that can be thermally excited into the conduction band at low activation energies. (b) The energy diagram shows the donor level just below the conduction band edge, facilitating this excitation [2].

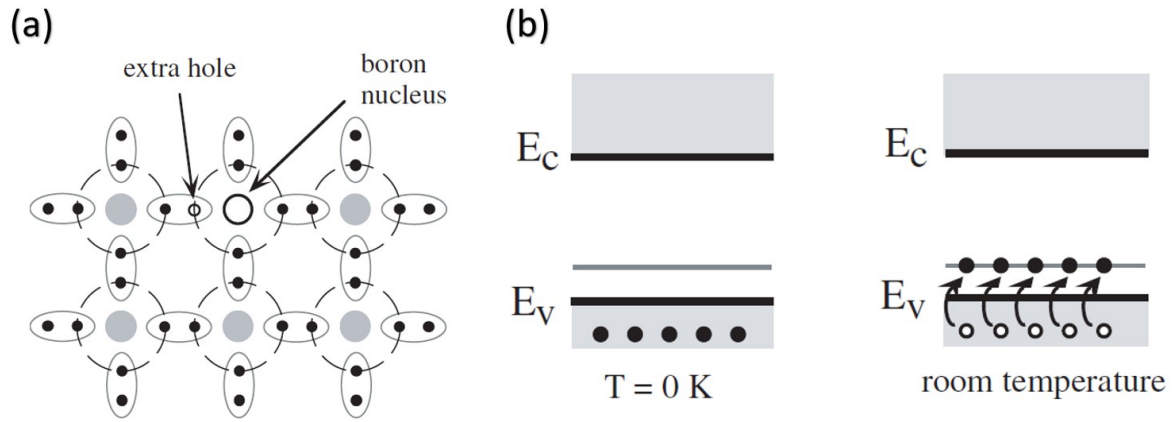

Figure 1.4: (a) Incorporating an acceptor atom such as boron into silicon introduces energy levels just above the valence band, promoting the formation of holes. (b) The energy diagram shows these acceptor levels, allowing electrons to be captured easily and thus leaving behind free holes [2].

mal excitation causes some electrons to gain enough energy to occupy states above E_F, leaving behind unoccupied states (holes) in the valence band. This distribution of electrons over available energy states is governed by the Fermi-Dirac probability function, given by:

$$f(E) = \frac{1}{1 + e^{\frac{E-E_F}{kT}}}, \tag{1}$$

where $f(E)$ is the probability of an electronic state with energy E being occupied, k is Boltzmann's constant, and T is the absolute temperature.

This equation indicates that at absolute zero ($T = 0$), $f(E)$ transitions sharply from 1 for $E < E_F$ (all states below E_F are filled) to 0 for $E > E_F$ (all states above E_F are empty). However, as $T > 0$, the transition becomes smoother, with states near E_F partially filled due to thermal excitation. This results in electrons gaining energy and moving into higher energy states, leaving behind positively charged vacancies (holes) in lower energy states. The magnitude of this thermal excitation is directly influenced by the exponential term in the equation, $\exp\left(\frac{E-E_F}{kT}\right)$, which increases with temperature. Therefore, at higher temperatures, a greater number of electrons are thermally excited, enhancing the overall carrier concentration and, consequently, the conductivity of the semiconductor [6].

For intrinsic semiconductors at room temperature, the number of thermally excited electrons and holes is small because the bandgap energy (E_g) is relatively large compared to the thermal energy (kT). In these materials, both electrons and holes are generated in equal numbers, and their concentrations are determined by the intrinsic carrier concentration. However, when dopants are introduced, impurity states are created within the bandgap, closer to the conduction band for n-type doping or closer to the valence band for p-type doping. These impurity states significantly reduce the energy required to excite carriers. For example, in n-type semiconductors, donor levels allow electrons to be thermally excited into the conduction band with a much smaller activation energy, while in p-type semiconductors, acceptor levels facilitate the creation of holes in the valence band. As a result, doping enhances the carrier concentration by several orders of magnitude, enabling semiconductors to transition from low-conductivity intrinsic materials to highly conductive extrinsic materials [5, 6].

This relationship, described by the Fermi-Dirac function, not only explains the temperature dependence of carrier concentration but also highlights the critical role of doping in modifying the electronic properties of semiconductors. For example, while intrinsic Si at around 300 K has an electron concentration on the order of $10^{10}\,\mathrm{cm}^{-3}$, doping Si with phosphorus at a level of $10^{15}\,\mathrm{cm}^{-3}$ leads to a free electron

concentration of nearly the same magnitude, substantially increasing conductivity [4].

On the other hand, temperature-dependent behavior of carrier concentration in semiconductors is characterized by three distinct regions: intrinsic, extrinsic, and ionization (freeze-out) regions. This behavior is illustrated in Figure 1.5.

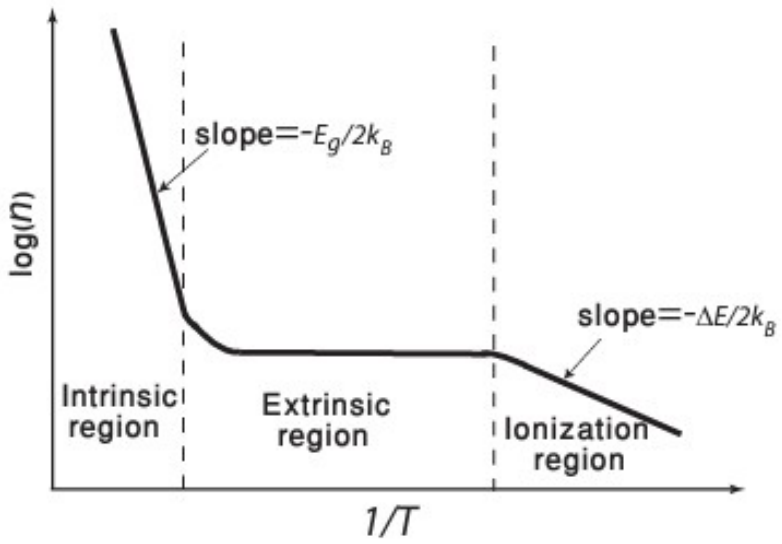

Figure 1.5: The temperature dependence of the electron concentration in an n-type semiconductor, showing the ionization, extrinsic, and intrinsic regimes. The horizontal axis is $1/T$, and the vertical axis is the carrier concentration. The slope in the intrinsic region is proportional to $-E_g/2k_B$, where E_g is the bandgap energy, while the slope in the ionization (freeze-out) region corresponds to $-\Delta E/k_B$, where ΔE is the dopant ionization energy. Adapted from Ref: [7].

In the intrinsic region, at high temperatures, the carrier concentration is dominated by thermally generated electron-hole pairs. The relationship governing this behavior is given by:

$$n = N_c N_v \exp\left(-\frac{E_g}{2k_B T}\right), \tag{2}$$

where E_g is the bandgap energy, k_B is Boltzmann's constant, T is the absolute temperature, and N_c, N_v are the effective density of states in the conduction and valence bands, respectively. In this regime, the slope of the graph is proportional to $-E_g/2k_B$, providing a method to experimentally determine the bandgap energy [7].

In the extrinsic region, which occurs at intermediate temperatures, the carrier concentration is dominated by the ionization of dopants. In this regime, all dopants are effectively ionized, leading to a nearly constant carrier concentration. For n-type semiconductors such as Si doped with phosphorus, the free electron concentration is approximately equal to the donor concentration N_D, resulting in a plateau in the carrier concentration vs. $1/T$ plot [7].

In the ionization (freeze-out) region, observed at low temperatures, thermal energy is insufficient to ionize all dopants, causing the carrier concentration to decrease exponentially. This behavior is described by:

$$n = N_D \exp\left(-\frac{\Delta E}{k_B T}\right), \tag{3}$$

where ΔE is the ionization energy of the dopants. The slope of this region is proportional to $-\Delta E/k_B$, enabling the determination of dopant activation energy from experimental data. This systematic temperature dependence of carrier concentration provides a powerful tool for understanding and characterizing doping in semiconductors, making it an essential framework for validating doping processes and calculating activation energies [7].

By introducing controlled impurities, known as doping, one can dramatically alter the concentration of free carriers, as shown in Figure 1.6.

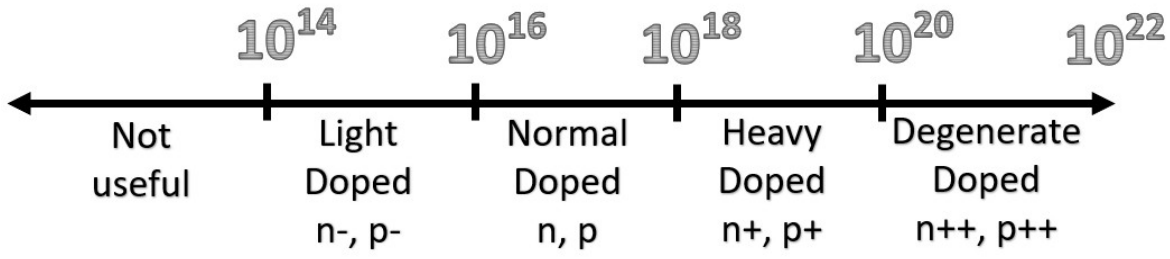

Figure 1.6: Schematic of the doping levels of semiconductors, categorized by carrier concentration (cm^3). Adapted from Ref: [8].

Figure 1.6 illustrates the varying levels of doping in semiconductors and their associated carrier concentrations. At low doping levels, below $10^{14}\,cm^{-3}$, the semi-

conductor remains close to its intrinsic state and is typically not useful for practical applications. Lightly doped silicon, with carrier concentrations between $10^{14}\,\mathrm{cm}^{-3}$ and $10^{16}\,\mathrm{cm}^{-3}$, is suitable for applications such as photodiodes. Normally doped silicon, ranging from $10^{16}\,\mathrm{cm}^{-3}$ to $10^{18}\,\mathrm{cm}^{-3}$, forms the foundation for most electronic devices, including transistors. As the doping level increases to $10^{18}\,\mathrm{cm}^{-3}$ and beyond, heavily doped silicon (n^+ or p^+) is employed to reduce resistivity, making it ideal for contact layers in transistors. At extremely high levels of doping, above $10^{20}\,\mathrm{cm}^{-3}$, silicon exhibits degenerate behavior, akin to metals, and is used in tunneling devices, thermoelectric applications, and metallic contacts [8]. This tunability in doping levels highlights the versatility of doped semiconductors for a wide range of applications. The next section will explore these applications, focusing primarily on normally doped semiconductor films. Key examples include transistors and piezoresistive sensors.

1.2 Applications of Semiconducting Materials

This section will cover common applications of semiconductors that this thesis aims to explore. Specifically, these applications include transistors and piezoresistive sensors

1.2.1 Transistors

Transistors serve as fundamental components for constructing electronic circuits. Unlike passive elements such as resistors, capacitors, inductors, and diodes, transistors exhibit current and voltage characteristics that depend on the voltage or current applied to a control terminal. There are two main types of transistors based on distinct physical principles: bipolar junction transistors (BJTs) and field-effect transistors (FETs). While BJTs operate based on current control, FETs rely on electric field control. Since BJTs are beyond the scope of this thesis, this section focuses on FETs, their working mechanisms, and figures of merit.

A field-effect transistor consists of three electrodes: source, drain, and gate, where conduction between the source and drain depends on the availability of charge carriers in a semiconducting channel [5]. FETs act as electronic switches, where the conductance of the semiconducting channel can be modulated by a gate electrode that is electrostatically coupled to the channel through a thin dielectric layer. Figure 1.7(a) illustrates a bottom-gated FET structure, where the gate electrode is positioned beneath the semiconductor and separated by a dielectric layer. Although the gate can also be placed on top of the channel, the working principles remain consistent regardless of the configuration, with the choice determined by design and fabrication considerations.

Figure 1.7 illustrates the electrical characteristics of thin-film transistors through two key graphs: transfer and output characteristics. The transfer characteristic, shown in Figure 1.7(b), depicts the logarithmic variation of the drain current (I_D) with the gate voltage (V_G) at a fixed drain voltage (V_D). In the off-state ($V_G < V_T$), the device exhibits minimal drain current due to insufficient carrier accumulation in the channel. As $V_G > V_T$, the device transitions to the on-state, where I_D increases exponentially, indicating the formation of a conductive channel. The subthreshold swing (SS), defined as the slope of the curve in the subthreshold region, is a crucial figure of merit that quantifies how efficiently the device can switch between the off and on states. A lower SS value corresponds to faster and more efficient switching.

The output characteristic, shown in Figure 1.7(c), presents the relationship between I_D and V_D for various fixed values of V_G. In the linear region, observed at small V_D, the current increases proportionally with V_D, exhibiting Ohmic behavior. As V_D increases further, the channel near the drain becomes depleted, leading to the pinch-off phenomenon and the saturation region. In this region, the drain current becomes nearly independent of V_D and is primarily determined by V_G. The linear and saturation regions are particularly important in practical applications, as they define the operational range of the device and its ability to provide stable and controlled current.

The current behavior in these regions can be described by two key equations. In the linear region, the drain current is expressed as:

$$I_D = \frac{W}{L}\mu C(V_G - V_T)V_D, \tag{4}$$

where W and L are the channel width and length, respectively, μ is the carrier mobility, C is the dielectric capacitance, and V_T is the threshold voltage. In the saturation region, the current is given by:

$$I_D = \frac{W}{2L}\mu C(V_G - V_T)^2. \tag{5}$$

Figures of merit for FETs include carrier mobility (μ), subthreshold swing (SS), transconductance (g_m), and the on/off current ratio. Carrier mobility determines the ease of charge transport in the channel, directly affecting device speed and performance. Transconductance (g_m) is defined as:

$$g_m = \frac{\partial I_D}{\partial V_G}, \tag{6}$$

and quantifies the sensitivity of the drain current (I_D) to changes in the gate voltage (V_G), making it a critical parameter for amplification applications. A higher transconductance indicates greater current control and improved switching efficiency. Subthreshold swing (SS) describes the change in gate voltage required to increase the drain current (I_D) by one decade in the subthreshold region, with lower values signifying faster switching capabilities. The on/off current ratio, on the other hand, reflects the ratio of the current in the "on" state to that in the "off" state, illustrating the device's ability to minimize leakage current and ensure efficient switching behavior. These figures of merit are fundamental for assessing FETs performance and summarized in Table 1.1 [8].

Table 1.1: Summary of Figures of Merit for FETs with desired outcome [8].

Figure of Merit	**Description and Desired Value**
Threshold Voltage (V_{th})	The minimum gate voltage required to turn the transistor on by forming a conductive channel. A moderate V_{th} is preferred to balance low-power operation and switching reliability.
Saturation Current (I_{sat})	The maximum current in the saturation region when the channel is fully inverted. High I_{sat} is desirable for better current-carrying capability and faster switching.
Subthreshold Swing (SS)	The change in gate voltage required to increase the current by one order of magnitude in the subthreshold region. A lower SS is preferred for faster and more efficient switching.
Transconductance (g_m)	The rate of change of drain current with respect to gate voltage, indicating the amplification capability of the transistor. High g_m is desirable for strong current control and high gain.
Carrier Mobility (μ)	Indicates how easily charge carriers move through the channel under an electric field. High μ is preferred for faster switching and lower power consumption.
On/Off Ratio	The ratio of the current in the on-state to the off-state. A high on/off ratio ensures efficient switching and minimizes leakage in the off-state.

1.2.2 Piezoresistance

Strain sensing is a technique used to detect and measure the deformation of materials subjected to external forces. These deformations, often resulting from mechanical stress, are converted by strain sensors into measurable electrical signals, typically reflected as changes in resistance, capacitance, or inductance [10].

The advent of strain sensors dates back to the early 1940s with the development of metal foil-based sensors [11]. These sensors have been utilized to measure strains up to 5%, including minor distortions in composites and solid objects, as depicted in Figure 1.8.

The sensitivity of a strain gauge, known as the gauge factor (GF), is given by the formula:

$$\mathrm{GF} = \frac{1}{R_0}\frac{dR}{d\varepsilon} + (1 + 2\nu) \tag{7}$$

Here, ε denotes the applied strain, R represents resistivity, R_0 is the material's resistivity without strain, and ν is the Poisson ratio [12]. The Poisson ratio, ν, is a measure of the transverse strain (ε_t) to the axial strain (ε_a) and is defined as:

$$\nu = -\frac{\varepsilon_t}{\varepsilon_a} \tag{8}$$

It quantifies how a material deforms laterally in response to an applied axial strain. A positive Poisson ratio indicates that the material contracts laterally when stretched axially and expands laterally when compressed axially. For most metals, ν ranges between 0.25 and 0.35, playing a significant role in determining the gauge factor.

Metal foil gauges, commonly composed of a nickel-copper alloy, integrate seamlessly with conventional circuitry without requiring complex additional components. These gauges can be tailored to various geometries for measuring tensile strain, shear, and pressure, as illustrated in Figure 1.8. However, they have inherent

limitations in sensitivity, which is relatively low due to geometric constraints associated with the Poisson effect, resulting in a gauge factor GF challenging-to-measure output in the low strain region, due to system noise [13]. The low sensitivity is attributed to the absence of a band gap in these metal foils, which exhibit minimal changes in resistivity under strain or compression, resulting in GF values typically ranging from 1 to 5 [14].

Piezoresistance in Semiconductors

The piezoresistive effect in semiconductors arises from strain-induced changes in their band structure, which alters the carrier density and mobility. The carrier density in intrinsic semiconductors is proportional to $e^{-E_g/2k_BT}$, where E_g is the bandgap energy, T is the temperature, and k_B is the Boltzmann constant [8]. Strain modifies the band structure, influencing carrier density and mobility, thereby enhancing the gauge factor GF of the material.

In 1954, Charles Smith observed the piezoresistive effect in semiconductors while working at Bell Labs. He reported that n-type silicon exhibited a negative gauge factor of approximately -135, while p-type silicon achieved a positive gauge factor of 175 [15]. The GF in semiconductors is significantly influenced by the doping concentration, type of dopant, and the crystallographic direction of strain. Lower doping levels generally result in higher GF values because the mobility of carriers transitioning to lower energy levels is greater than in heavily doped materials [16]. However, semiconductors are sensitive to external factors such as temperature, environmental conditions, and self-heating effects, which can influence their piezoresistive response [17].

Nonlinear behavior in piezoresistors becomes more pronounced at higher strain levels. Increased doping reduces resistance, nonlinearity, and temperature dependence but often decreases the GF [18]. Single-crystal semiconductors typically operate within low strain limits, usually up to 0.1%, and can endure an elastic strain range of up to 0.5% before failure. This brittleness limits their applications in high-strain

environments [19].

Unlike bulk semiconductors, van der Waals layered materials, such as transition metal dichalcogenides, exhibit high elasticity and Young's moduli. Young's modulus, denoted by E, is a fundamental mechanical property that measures the stiffness of a material. It is defined as the ratio of stress (force per unit area) to strain (deformation relative to the original length) within the elastic limit:

$$E = \frac{\sigma}{\varepsilon} \tag{9}$$

Here, σ is the stress, and ε is the strain. A higher Young's modulus indicates a stiffer material that resists deformation under applied stress [7].

These materials are highly sensitive to deformation and can sustain large localized strains without structural failure [20]. The bandgap energy (E_g) is the energy required to excite an electron from the valence band to the conduction band, dictating a material's electrical and optical properties. The Boltzmann constant (k_B) is a physical constant that relates temperature to energy, essential in statistical mechanics.

Such properties make van der Waals materials promising candidates for strain sensors and other piezoresistive applications, achieving high GF values while maintaining mechanical durability [21]. A figure of merit for high level gauge sensor applications is summarized in Table 1.2 using Ref: [22].

Linearity, in the table, indicates that the output signal (e.g., resistance change) is directly proportional to the applied strain over the sensor's operating range. This relationship simplifies calibration and data interpretation, making the sensor's behavior more reliable and easier to model mathematically.

1.3 Limitations of Current Semiconducting Materials

The semiconductor industry has relied on silicon as the backbone of electronic devices for decades due to its abundance, ease of fabrication, straightforward application of substitutional doping to create p- and n-type materials, and resultant electronic properties [23]. However, as silicon device dimensions approach sub-5 nm scales, silicon faces significant challenges, limiting its scalability and performance [24]. The evolution of transistor architectures, as shown in Figure 1.9, highlights the industry's response to the limitations of silicon scaling at sub-5 nm nodes. Planar FETs, the traditional design, feature a gate above a planar channel with current flowing horizontally between the source and drain. While effective for decades, this architecture struggles with short-channel effects, reduced gate control, and scaling limitations as dimensions shrink below 28 nm [25].

To address these challenges, FinFETs introduced a three-dimensional vertical fin structure with the gate wrapping around three sides of the channel. This design significantly improves gate control, reduces short-channel effects, and supports higher drive currents, making it suitable for nodes down to 7 nm. However, FinFETs encounter challenges at sub-5 nm nodes, particularly in maintaining effective gate control [28].

The GAA (Gate-All-Around) nanosheet FET is the next step in transistor evolution, where stacked nanosheets are completely surrounded by the gate. This architecture provides unparalleled gate control, minimizes leakage currents, and enables high drive currents at sub-3 nm nodes [29].

One major issue in applying miniaturization is the reduction in carrier mobility. Carrier mobility (μ) quantifies how efficiently charge carriers (electrons or holes) move in response to an electric field. At nanoscale dimensions, mobility decreases due to surface roughness scattering, phonon interactions, and Coulomb scattering in heavily doped regions [30]. For bulk silicon, electron mobility (μ_n) is approxi-

mately 1200 cm^2/Vs, and hole mobility (μ_p) is around 450 cm^2/Vs. However, for nanoscale silicon devices (e.g., 10 nm channel length), μ_n drops to 200−500 cm^2/Vs and μ_p to 100−200 cm^2/Vs. This significant reduction, by up to 85%, directly impacts device performance by lowering current drive (I_D) and speed [31]. Table 1.3 summarizes these limitations and compares them with low-dimensional TMD materials like MoS_2.

The subthreshold swing (SS) is a critical parameter in transistors, as described in Section 1.2.1, defining the voltage required to increase the current by a factor of ten in the subthreshold region. An ideal SS is around 60 mV/dec at room temperature, indicating efficient switching with minimal voltage change. However, achieving low SS values becomes challenging as silicon scales, impacting the energy efficiency of devices [8].

Drain-Induced Barrier Lowering (DIBL) occurs when a high drain voltage reduces the barrier height at the source-channel junction, leading to increased off-state leakage currents. DIBL worsens in shorter channels, with values increasing from 50 mV/V in 100 nm transistors to 200 mV/V in 10 nm transistors. This degradation causes significant power losses and limits the performance of scaled silicon devices [32].

Moderately high doping densities, necessary for maintaining threshold voltage control, introduce severe ionized impurity scattering [33]. For doping levels of $N_d = 10^{15}\,cm^{-3}$, mobility remains near 1400 cm^2/Vs, but at $N_d = 10^{19}\,cm^{-3}$, mobility drops to 100 cm^2/Vs [34].

To address these limitations, low-dimensional transition metal dichalcogenide materials emerge as promising alternatives. These materials, with atomic-scale thickness and tunable properties such as electrical and optical band gaps, offer significant advantages over silicon. Unlike silicon, low-dimensional TMD materials exhibit promising carrier mobility [35], enhanced gate control [36], and reduced short-channel effects [24]. Moreover, their mechanical flexibility enables applications in flexible displays, sensors, and wearable electronics, areas where silicon struggles

[37]. Table 1.3 compares the limitations of traditional semiconductors like silicon with low-dimensional TMD materials.

1.4 Necessities for Doping Semiconductor Films

Doping has been a cornerstone of the semiconductor industry, enabling the development of advanced electronic devices by modifying the electrical properties of materials. In traditional semiconductors like silicon, doping introduces controlled impurities to create n-type (electron-rich) and p-type (hole-rich) regions, which are essential for forming p-n junctions and transistors. Through doping, silicon properties can be tailored to meet specific application requirements, these requirements are summarized from Ref: [42]:

- **Enhancing Carrier Concentration:** Doping increases the availability of charge carriers, enabling higher electrical conductivity.
- **Creating p-n Junctions:** The formation of p-n junctions is the basis of devices like transistors, diodes, and solar cells.
- **Improving Contact Properties:** Heavily doped regions reduce resistance at metal-semiconductor interfaces, ensuring efficient current flow.

As new materials like transition metal dichalcogenides are explored as alternatives, doping remains equally critical for unlocking their full potential [43]. The next section will highlight the materials investigated in this thesis.

1.5 Properties of Transition Metal Dichalcogenides

Transition metal dichalcogenides (TMDs) are a fascinating class of materials that have attracted significant attention due to their unique layered van der Waals structures. These compounds follow the general chemical formula MX_2, where M represents a transition metal, and X denotes a chalcogen element such as sulfur (S), selenium (Se), or tellurium (Te), which belong to Group 16 of the periodic table. The

layered structure of TMDs is composed of covalently bonded *M*-*X* planes that are weakly held together by van der Waals forces. This structural anisotropy underpins their diverse range of physical and chemical properties, making them suitable for applications in electronics, optoelectronics, catalysis, and energy storage [44].

TMDs exhibit a variety of structural and electronic behaviors, which are influenced by the specific transition metal and chalcogen involved. Group 4–7 and Group 9-10 TMDs are predominantly layered, while some TMDs from Group 8 are commonly found in non-layered structures. Stronger covalent bonding between the layers of Group 8 leads to three-dimensional network structures, in contrast to the weakly van der Waals-bonded layered structures observed in the rest [45]. In particular, Molybdenum disulfide (MoS_2) is a well-studied TMD that exhibits polymorphism, meaning it can exist in multiple crystal phases. The polymorphism of molybdenum disulfide (MoS_2) is characterized by distinct atomic arrangements that significantly influence its electronic properties [46]. As illustrated in Figure 1.10 (a), MoS_2 can crystallize in several phases, notably the 1T, 2H, and 3R phases (T for trigonal, H for hexagonal, and R for rhombohedral).

The number represents the stacking sequence of layers within the unit cell. These phases correspond to distinct crystallographic configurations, each characterized by unique structural symmetries and electronic properties. The octahedral coordination in the 1T phase involves six sulfur atoms symmetrically surrounding each molybdenum atom, the top view of 1T phase can be seen in Figure 1.10 (b). This arrangement facilitates significant overlap between the *d*-orbitals of molybdenum and the *p*-orbitals of sulfur, resulting in a continuous electronic band. Consequently, the delocalization of *d*-electrons is a key factor in the metallic nature of the 1T phase, enabling efficient electrical conductivity. This delocalization arises directly from the symmetry and bonding environment inherent to the octahedral coordination [49].

Conversely, 2H and 3R phases of MoS_2 exhibit trigonal prismatic coordination of

Mo atoms, where each Mo atom is surrounded by six S atoms forming a trigonal prism, as shown in Figure 1.10(a) and top view of 2H phase is shown in Figure 1.10 (c). This arrangement results in the splitting of Mo d-orbitals into bonding and antibonding states, creating a finite bandgap and giving these phases their semiconducting properties [45]. Density functional theory calculations reveal that, in the monolayer H-phase of MoS_2, the valence band (VB) and conduction band (CB) are predominantly composed of *Mo* $d_{x^2-y^2}$, d_{z^2}, and *S* p_x, p_y orbitals. The p_x and p_y orbitals are degenerate due to the high symmetry of the H-phase crystal structure. This orbital hybridization generates a direct bandgap of approximately 1.7 eV, located at the K-point in the Brillouin zone [50].

In contrast, the 1T phase features octahedral coordination of Mo atoms, where the distortion of the lattice leads to significant hybridization between Mo d_{z^2}, d_{xy}, and S p_z orbitals. This hybridization causes overlapping of the VB and CB, eliminating the bandgap and resulting in metallic behavior. The delocalization of electrons further stabilizes the 1T phase, enhancing its conductivity. External electric fields or lattice distortions can induce structural changes that amplify electron delocalization and conductivity in the metastable 1T phase [50–52].

All three phases (2H, 1T, 3R) can be synthesized in a laboratory [53], but the 2H phase occurs naturally in molybdenite [54] and is the only thermodynamically stable phase under ambient conditions, the rest are known as metastable. These polymorphic variations underscore the versatility of MoS_2 as a material, where slight modifications in atomic coordination and stacking can lead to differences in electronic behavior, thereby enabling tailored applications in electronics and optoelectronics [55].

Furthermore, a calculated energy-momentum diagram reveals that the electronic properties of MoS_2 and WS_2 vary with changing thicknesses. These materials undergo an indirect-to-direct bandgap transition after lowering the number of layers, with a monolayer having a direct band gap of 1.8 eV, different from the bulk's in-

direct band gap of 1.2 eV, as shown in Figure 1.11. For WS_2, the band gap of the monolayer is calculated to be $\approx$ 2.1 eV with a direct transition and $\approx$ 1.3 eV indirect bandgap in the bulk form [56].

In monolayer MoS_2 and WS_2, quantum confinement refers to the restriction of electron and hole motion within the two-dimensional plane of the material. This confinement alters the electronic band structure, causing a transition from an indirect bandgap in the bulk material to a direct bandgap in the monolayer form [57]. This direct bandgap significantly enhances the efficiency of photon absorption and emission, leading to higher quantum yields compared to indirect bandgap semiconductors. This phenomenon is depicted in Figure 1.11.

The quantum yield, in this context, represents the ratio of photons emitted to the number of electron-hole pairs recombined in the material. The direct bandgap in monolayers eliminates the need for phonon assistance in electron-hole recombination, as no momentum change is required for the transition. This property makes monolayers highly suitable for optical applications, such as light-emitting diodes (LEDs) and lasers [58, 59].

Moreover, the less studied material $PtSe_2$ (Platinum Diselenide) is another TMD with an unique electronic properties. Unlike MoS_2 or WS_2, where the 2H phase is semiconducting phases can be found, $PtSe_2$ generally crystallizes in the 1T structure, which is semimetallic. $PtSe_2$ exhibits a tunable electronic bandgap that transitions from indirect in multilayers ($\sim 0.3\,eV$) to direct in monolayers ($\sim 1.2\,eV$) [60].

It must be noted that optical band gap is a critical property for optoelectronic devices as it determines the wavelength of light that a material can absorb or emit. In applications, the ability to absorb light within specific wavelength ranges, generate excitons (electron-hole pairs), and subsequently harness their recombination is essential [61]. Some materials like monolayer TMDs such as MoS_2 and WS_2 exhibit direct optical band gaps, which enhance light-matter interaction, leading to high photoluminescence quantum yields and strong excitonic effects even at room tem-

perature [62]. However, this thesis will primarily focus on electrical applications, as the result chapters include examples more relevant to electrical transport properties, such as charge carrier mobility, conductivity and etc.

1.6 Applications for TMDs and doped-TMDs

Transition Metal Dichalcogenides are being aggressively studied, with proof-of-concept research in transistor applications [63, 64]. Understanding the electrical characteristics of TMD films is fundamentally important for their integration into mass production applications, particularly for integrated circuits. Among TMDs, doping MoS_2 has been shown to significantly enhance its electrical properties and provide better control over material behavior for device applications [65].

Initially, in a study by Hallam et al., Re-doped MoS_2 films exhibited n-type behavior with electron concentrations in the mid-to-high $10^{17}\,cm^{-3}$ range, whereas undoped MoS_2 films displayed p-type behavior. Undoped MoS_2 films displayed p-type behavior with hole concentrations varying between approximately $3 \times 10^{17}\,cm^{-3}$ and $1 \times 10^{19}\,cm^{-3}$. The electron mobility in Re-doped samples ranged from 0.1 to $0.7\,cm^2/V{\cdot}s$, while hole mobility in undoped samples was between 0.1 and $0.6\,cm^2/V{\cdot}s$ [66]. Furthermore, precise control over the Re doping concentration in MoS_2 was achieved, with levels as low as 500 ppm, demonstrating the feasibility of controlled substitutional doping [67].

The transfer characteristics revealed differences between pristine MoS_2, H_2S-annealed MoS_2, and Re-doped MoS_2, as shown in Figure 1.12 (a). All show n-type characteristics as positive applied back gate give higher current. After H_2S annealing, there is a noticeable improvement in I_{DS}, which is attributed to the reduction of sulfur vacancies, partially passivating defects and improving the electronic properties. In comparison, the Re-doped MoS_2 exhibits the highest I_{DS}, showing a clear n-type enhancement. This improvement is accounted for by the effective substitutional doping of Re atoms into the MoS_2 lattice, as shown in the corresponding STEM images, as shown in Figure 1.12 (b) and (c) [67].

This improvement was directly linked to the reduction in defect density [68] and the n-type doping effect introduced by Re. These studies underscore the potential of Re

doping in enhancing carrier mobility, suppressing defects, and improving transport properties, advancing the performance of MoS_2-based electronic devices [69].

Additionally, a study by Zhang et al. achieved in-situ Re doping of monolayer MoS_2 with concentrations of approximately 1 atomic percent (at.%). This doping level resulted in nearly degenerate n-type behavior, aligning well with density functional theory calculations [70, 71]. Low-temperature photoluminescence measurements from this study revealed significant quenching of defect-bound emissions upon Re incorporation, suggesting the passivation of Mo–O bonds and sulfur vacancies [70].

Common dopants for n-type and p-type MoS_2 are summarized in Table 1.4. For this thesis, substitutional doping is chosen due to its suitability for mass production and applicability to conventional semiconducting doping systems.

Briefly these doping methods in the literature are [84]:

- **Substitutional Doping**: Replaces host atoms in the lattice with dopant atoms, providing precise doping control. Rhenium (Re) doping in MoS_2 is a scalable example suitable for large-area film production.
- **Plasma Immersion Doping**: Introduces dopants by ionizing them in plasma and embedding them into the surface using an electric field.
- **Surface Charge Transfer Doping**: Modifies surface states by charge transfer from or to dopant species.
- **Intercalation Doping**: Inserts atoms or molecules between TMD layers, altering electronic properties without disrupting the crystal structure.
- **Molecular Doping**: Utilizes chemical species like chlorine or fluorine to modulate properties.
- **Adsorption Doping**: Relies on physical adsorption of species like lithium to induce charge transfer.

As a proof of concept for p-type semiconductor applications, substitutional Nb doping of WS_2 has shown promising results in transistor applications. Modulation of carrier density in WS_2 through Nb doping has been demonstrated, highlighting a transition from native n-type to p-type conductivity [43, 85, 86].

Similar to the results presented in this thesis, Qin et al. reported that by adjusting the Nb molar ratio in the precursor, the hole carrier density in the p-type WS_2 layer increased from approximately $1.87 \times 10^7\,\mathrm{cm}^{-2}$ at 1.5 at.% Nb to $1.16 \times 10^{13}\,\mathrm{cm}^{-2}$ at 8.1 at.% Nb [87].

Three-probe measurements were employed to investigate these effects, and the details of the measurement are provided in Section 2.7.2. Output characteristics (I_{ds} vs. V_{ds}) for pristine and 10.3 at.% Nb-doped WS_2 were recorded while varying the back-gate voltage from $-80\,\mathrm{V}$ to $+80\,\mathrm{V}$, as shown in Figure 1.13 (a) and (d). For pristine WS_2, higher current was observed at positive gate voltages, as illustrated in Figure 1.13 (b), indicating n-type conductivity where electrons accumulate in the channel, enhancing device conductivity. The threshold voltage, located between $20\,\mathrm{V}$ and $40\,\mathrm{V}$, reflects the presence of majority electron carriers and is determined by the slope of the red curve in Figure 1.13 (b). The STEM image of pristine WS_2 in Figure 1.13 (c) confirms a hexagonal arrangement of tungsten atoms.

Upon Nb doping (10.3 at.%), higher current was observed at negative gate voltages, as seen in Figure 1.13 (e), indicating the accumulation of holes in the channel and p-type conductivity. The threshold voltage shifted to negative values due to the presence of majority hole carriers, which is also determined by the slope of the red curve in Figure 1.13 (e). The corresponding STEM image in Figure 1.13 (f) reveals sparsely distributed Nb atoms substituting W atoms in the lattice.

While increased Nb content effectively induced p-type behavior, it also led to a reduction in current levels, as shown in Figure 1.13 (d). This transition was confirmed through field-effect transistor devices, which exhibited an n- to p-type crossover at higher Nb concentrations. The emergence of hole conductivity and the shift in

threshold voltage verified Nb as an effective p-type dopant.

These findings demonstrate the ability to tailor the electronic properties of WS_2, positioning Nb doping as a reliable method for achieving p-type behavior in transition metal dichalcogenides [88].

Table 1.5 summarizes the dopants used for WS_2, highlighting their effect on conductivity type, the doping method employed, and corresponding references.

1.7 Synthesis of TMD materials

Numerous techniques are available for creating TMD materials, each producing materials with varying specifications of quality, which include structural integrity, phase purity, electronic performance, and thickness uniformity, among other parameters. Consequently, the method of synthesis plays a crucial role in determining the properties and potential applications of the resultant material. This section introduces the commonly employed synthesis techniques, which are categorized into two principal approaches: top-down and bottom-up.

The top-down approach involves breaking down bulk materials to produce thin layers or nanosheets. This method is well-suited for obtaining multilayer materials and includes techniques such as mechanical or electrochemical exfoliation. These processes often require minimal thermal input, making them advantageous for applications where high-temperature processes are not feasible.

In contrast, the bottom-up approach constructs materials by assembling atomically defined components. This technique is widely used for synthesizing monolayer or multilayer structures with precise control over thickness and composition. High-temperature conversion processes, such as chemical vapor deposition (CVD), Thermally Assisted Conversion, are examples of bottom-up approaches, offering scalability and uniformity.

This thesis focuses on both approaches. Initial chapters present results obtained using bottom-up techniques, specifically high-temperature conversion processes. The final chapter explores top-down methods, with an emphasis on electrochemical exfoliation, where thermal input is not required. The following sections will provide detailed insights into these synthesis approaches, highlighting their respective advantages and limitations.

1.7.1 Mechanical Exfoliation

The method of mechanical exfoliation, also known as the Scotch tape method, is one of the most recognized techniques for producing two-dimensional (2D) materials, achieving the highest quality of low-dimensional materials to date. Originally developed by Novoselov and Geim for the isolation of graphene monolayers [95], this method has also proven effective for separating monolayer TMDs [96]. By utilizing adhesive tape, this procedure systematically separates TMD layers, which are initially held together by relatively weak Van der Waals forces. The mechanical force exerted by the tape disrupts these forces, gradually reducing the number of layers until ultimately isolating a monolayer through repeated application [97].

The bulk TMD crystals subjected to mechanical exfoliation are typically synthesized using the Chemical Vapor Transport (CVT) technique [98]. Significantly, CVT employs transport agents such as chlorine, bromine, and iodine to facilitate the growth of bulk crystals by transporting these agents through the gas phase, enabling the formation of high-purity crystalline structures [99]. This method is widely used to grow high-quality crystals for subsequent exfoliation.

Dong et al. reported that approximately 40 different and thermodynamically stable TMD materials can be formed from various combinations of transition metals and chalcogen elements [100]. Computational studies, however, predict the existence of over 1000 potential low-dimensional materials [101]. While not all these materials are experimentally verified or thermodynamically stable under ambient conditions, theoretical calculations provide a roadmap for discovering new low-dimensional materials with tailored properties.

A major drawback of the mechanical exfoliation method lies in the limited size of the resultant flakes, which typically range from 1 to 50 μm on SiO_2/Si substrates [53]. Although larger flakes can be obtained on metal substrates, many applications require insulating substrates, limiting the utility of mechanically exfoliated flakes for certain device applications. Moreover, this method lacks precise control

over the size and placement of flakes on a substrate, posing challenges for scalable electronic device manufacturing. Additionally, the method necessitates a polymer-based transfer process and electron-beam lithography for device measurements, which further complicates integration [102].

Despite these limitations, mechanically exfoliated materials have enabled the exploration of unique physical phenomena. For example, Moiré patterns can be created by overlaying two similar or distinct TMD flakes at a specific twist angle. This allows the observation of novel physical behaviors such as superconductivity, ferroelectricity, and correlated insulating states [103]. Other applications include the study of quantum confinement [104], and valleytronics [105], which require high-quality monolayers obtained via mechanical exfoliation.

1.7.2 Liquid Phase Exfoliation

Liquid-phase exfoliation (LPE) was developed as an alternative to mechanical exfoliation for separating layered crystals [106]. Similar to mechanical exfoliation, LPE operates on the principle of breaking the van der Waals forces that hold interlayers together. The same bulk crystals used in mechanical exfoliation can also be employed in this method. However, LPE disrupts these interlayer forces using either ultrasonic waves or shear forces within a controlled and stabilizing environment [107].

The process begins with the sonication of bulk crystals or powders in a solvent, producing a dispersion. This dispersion is stabilized through interactions between the solvent molecules and the exfoliated TMD layers. Alternatively, surfactants may be added to the dispersion. Surfactants prevent the reaggregation of exfoliated layers by providing steric or electrostatic stabilization, especially when the solvent's surface energy does not closely match that of the TMD layers. By preventing recombination, surfactants enable the exfoliated nanosheets to remain dispersed. The resulting LPE-processed TMD dispersions can then be used to create functional ma-

terials such as inks [108] and composites [109].

One challenge of LPE is the high degree of polydispersity[1], which results in a wide range of sheet dimensions. This variability can significantly affect the electronic properties of the materials, particularly the bandgap, which depends on the number of layers [110]. This issue can be addressed using centrifugal processing, which separates nanosheets by size and mass, enabling the selection of materials with specific dimensions [111].

In LPE, overcoming van der Waals interactions alone is insufficient for successfully exfoliating layered crystals. Without proper stabilization, the exfoliated nanosheets are prone to reaggregation. A suitable solvent must stabilize the exfoliated nanosheets through appropriate solvent-nanosheet interactions so reduce the energy barrier required for exfoliation [112]. To achieve more precise control over the structural properties of TMD films—such as thickness, conformability, and defect density—and to reduce reliance on intense mechanical forces, the electrochemical exfoliation process presents an advantageous alternative synthesis technique.

1.7.3 Electrochemical Exfoliation

Electrochemical exfoliation (EE) has become a leading method for producing large-sized, solution-processed low-dimensional materials with just a few layers. Initially, it was successful in creating graphene [113], but it has since proven effective for synthesizing other TMDs as well [114]. The process works by using an electric field to drive ions into the crystal structure of TMDs, causing them to intercalate and expand, eventually leading to exfoliation [115]. This method can be finely adjusted by changing the applied voltage, electrolyte composition, and electrode type. Figure 1.14) shows a schematic of this technique.

For this technique, the counter electrode (CE) should be made from stable materials like platinum (Pt) foil/wire or glassy carbon electrodes, while the working elec-

[1]Polydispersity refers to the variation in the size and thickness of the exfoliated nanosheets.

trode (WE) is composed of bulk layered material, shaped as rods, foils, flakes, or plates. The WE can function as either an anode or a cathode, depending on whether the intercalant is an anion or a cation, classifying EE as either anionic or cationic [116]. Anodic exfoliation, typically conducted in aqueous electrolytes, always uses a positive potential to drive anions from the electrolyte into the anodic working electrode, effectively intercalating anions such as (SO_4^{2-}) into the bulk TMD materials [117]. The reduction of intercalated sulfate ions and the self-oxidation of water produce gaseous species like SO_2, O_2, and H_2, which cause the delamination of TMD nanosheets [118]. While the anodic exfoliation process allows for efficient production with high yields, such as generating gram-scale quantities within minutes to hours in the lab, it also leads to oxidation of the exfoliated materials due to radical formation in aqueous media [116]. This oxidation can be a significant disadvantage for certain applications, particularly in electronics where high-quality TMD materials are essential.

Cathodic exfoliation, on the other hand, is conducted in non-aqueous electrolytes containing organic solvents like N-methyl-2-pyrrolidone (NMP), propylene carbonate (PC), dimethyl carbonate (DMC), and dimethylformamide (DMF). Organic solvents here limit the oxidation of the nanosheets, making this method more favorable. It uses a negative potential to drive cations into the cathodic working electrode [119]. The size of intercalating ions, their concentration in the electrolyte, the applied potential, and the interlayer spacing of the bulk crystals are key parameters influencing the thickness and lateral dimensions of the exfoliated nanosheets. Generally, large, single-crystalline bulk material yields thin and large low-dimensionalnanosheets [120]. The next section discusses the deposition techniques suitable for electrochemical exfoliation, which is essential because, after preparing the ink of low-dimensional materials, it must be ready to interact with any substrate to form a network for the potential devices.

Network Deposition Techniques

The primary objective of depositing TMD nanosheet networks is to regulate their electrical conductivity. While conductivity is often considered an intrinsic property of a material, in thin, disordered, nanostructured films, it is highly dependent on the film's thickness and connectivity [121]. For relatively thick films (up to 5 layers for MoS_2), conductivity follows the bulk-like behavior of the material [122]. However, as thickness decreases below a critical threshold, the conductivity declines significantly due to the disordered nature of these films. In thinner films, the number of conductive pathways reduces, impairing current transport [123]. When the thickness reaches a critical minimum, the film achieves only a single conductive pathway, known as the percolation threshold [124]. Figure 1.15 illustrates this behavior.

Figure 1.15 depicts the stepwise evolution of conductivity in TMD nanosheet networks:

- Panel (i): Nanosheets are sparsely distributed, with no conductive pathways across the network, resulting in an insulating state.
- Panel (ii): Increased deposition leads to higher density, with some conductive paths forming; however, the network remains below the percolation threshold.
- Panel (iii): A continuous conductive path forms between the electrodes, achieving the percolation threshold. The network becomes conductive, though resistance remains high due to limited connectivity.
- Panel (iv): A densely packed network with overlapping nanosheets is formed, reducing resistance and resulting in bulk-like conductivity.

This percolation behavior is observed in various systems, including nanostructured networks of nanotubes, nanowires, and nanosheets, as well as evaporated thin metal films [126]. Deposition techniques must carefully modulate film thickness to control the percolation characteristics of TMD networks. Common methods include spray coating [127] and spin coating [128]. Among these, the Langmuir-Schaefer

(LS) deposition technique is particularly effective in creating uniform and functional films.

The LS method relies on natural interfacial energy minimization, avoiding the need for additional energy inputs. As illustrated in Figure **??**, flakes are dispersed in isopropyl alcohol (IPA) and introduced at the water-hexane interface. The surface tension gradient drives the flakes to assemble into a compact low-dimensionalfilm at the interface. The substrate is then lifted horizontally through the monolayer, transferring the film and ensuring dense and uniform nanosheet packing [129]. This process creates a highly connected nanosheet network suitable for applications requiring controlled electrical properties.

1.7.4 Chemical Vapor Deposition

Chemical Vapor Deposition (CVD) is a widely used technique to create thin layers of solid material on a substrate through chemical reactions between gaseous precursors within a reaction chamber [130]. This process involves both vapor-phase and surface reactions. The method begins with the introduction of various gases into the chamber simultaneously. The CVD process includes several key steps: gas molecules are transported to the substrate surface, where they adsorb, diffuse, react, and eventually integrate into the solid film, with by-products being removed, as illustrated in Figure 1.16.

The outcomes of the CVD process are highly dependent on the selection of precursors and reaction conditions. By fine-tuning these parameters, the synthesis process can be tailored to meet specific requirements [132]. While CVD is suitable for industrial applications, its reliance on high temperatures presents challenges for integration with silicon-based technologies, such as CMOS (Complementary Metal-Oxide-Semiconductor), which generally require process temperatures below 450°C [133]. This temperature limitation is an essential requirement for compatibility with silicon-based platforms.

Recent advancements in CVD technology, including improved temperature control, optimized precursor selection, enhanced chamber designs, and the incorporation of additional energy sources like plasma, have expanded its applicability. For example, the choice of precursor can significantly influence the required reaction temperature. Using precursors with low decomposition temperatures, such as molybdenum hexa-carbonyl ($Mo(CO)_6$), enables the synthesis of MoS_2 at temperatures as low as 200°C, addressing the temperature limitations of traditional CVD methods [134].

Alternatively, plasma-assisted CVD can enhance the reactivity of precursor gases, increasing the growth rate of materials like MoS_2 [135]. This not only reduces the required processing time but also enables film growth at lower temperatures by facilitating precursor decomposition [136]. Such advancements make CVD a more versatile and efficient technique for modern manufacturing.

The next section explores an alternative deposition method, Thermally Assisted Conversion, which directly utilizes metal films as a source material instead of relying on gaseous precursors.

1.7.5 Thermally Assisted Conversion

In the exploration of scalable and controlled growth methods for two dimensional TMD materials, Thermally Assisted Conversion (TAC) has emerged as a promising technique. Addressing limitations such as scalability, quality, and precise growth control associated with previous methods, TAC can be accepted as a variant of CVD. This method is initiated by depositing a metal layer, typically transition metal or transition metal oxide, onto a substrate, followed by exposure to chalcogen vapor at elevated temperatures. The synthesis of sulfur-based TMDs has a common reaction under sulfur environment as seen in (Equation: 10):

$$M_s + 2S_g \rightarrow MoS_2(s) \tag{10}$$

This reaction can happen at 550°C and has been shown to result in large-area MoS_2 [137, 138]. Instead of using the metal, metal oxide can also serve as a precursor such as MoO_3 [139]. When using metal oxide, the reaction mechanism is different from sulfurizing the metal film; the sulfur vapor first reacts with the oxide to form a sulfoxide and a metal sub-oxide, as shown in (Equation: 11): The sub-oxide then reacts with sulfur to form the TMD film, as depicted in (Equation: 12):

$$MoO_3 + S_g \rightarrow MoO_{3-x}(s) + SO_x(g) \tag{11}$$

$$MoO_{3-x} + 3S_g \rightarrow MoS_2(s) + SO_{3-x}(g) \tag{12}$$

The same mechanisms apply to other sulfide such as WS_2 [140] and even selenide-based TMD materials such as $PtSe_2$ [141]. It has been initially found that thicker initial metal layers (greater than 10 nm) tend to develop vertically standing TMD layers under high-temperature and low-pressure conditions [142]. Observations indicate that higher pressures and/or lower temperatures lead to the formation of TMD films oriented perpendicular to the substrate [143]. The studies, later, have demonstrated vertical growth of MoS_2 and $MoSe_2$ at 550°C and pressures above 100 mTorr, particularly when the initial metal layer thickness exceeds 3 nm [144].

Recent research has investigated the influence of growth parameters. At lower growth pressures (5-10 mTorr), WS_2 films exhibit a two-dimensional layer-by-layer growth. As the pressure increases (15-25 mTorr), the films form three-dimensional vertical nanowalls due to the Stranski-Krastanov growth mode, where initial layers grow in 2D, followed by 3D growth due to strain and surface energy considerations [145] as depicted in Figure 1.17 (c).

This phenomenon not only observed in MoS_2 as seen in Figure 1.17(a), (b), WS_2 as seen in Figure 1.17(d), (e), (f) but also applied to Platinum-based TAC films, Pt is converted to $PtSe_2$, as seen in Figure 1.17(g), (h), (i), (l), and (k) [146]. It has

been noted that thin, discontinuous layers prefer horizontal growth, whereas thicker layers that are firmly attached to substrates face challenges in horizontal expansion [147, 148]. Researchers have found that this orientation difference in thicker and thinner samples is due to the substantial volume increase when Mo is converted to MoS_2 [149] or in WS_2 as shown in Figure 1.17 (d),(e),(f).

Horizontally aligned (HA) films found optimal for optoelectronic applications, while vertically aligned films are more suited for hydrogen evolution reactions and solar cells due to their chemically reactive edges [151, 152]. The performance of vertically aligned TMDs, such as MoS_2, in HER is measured by their exchange current density and overpotential. The exchange current density, a key parameter in electrochemistry, represents the reaction rate at equilibrium (zero overpotential). Overpotential refers to the additional voltage required to drive the reaction beyond the equilibrium potential. Vertically aligned MoS_2 nanosheets exhibit an exchange current density approximately 70 times higher than bulk MoS_2, indicating superior intrinsic catalytic activity [143]. This enhancement is attributed to the abundance of exposed edges in VA films, which act as active sites for catalytic reactions [153]. It is important to note that the orientation of TMD films significantly influences their applications.

Other Synthesis Techniques

The most frequently mentioned synthesis techniques have been discussed in earlier sections. However, the methods are not limited to just five different approaches, which range from the use of a simple blender for Liquid Phase Exfoliation (LPE) to very high-temperature furnaces, such as those used in Chemical Vapor Transport (CVT), Chemical Vapor Deposition (CVD), and Thermally Assisted Conversion. Beyond these, additional techniques like Atomic Layer Deposition (ALD) have also been utilized in specific sections of this thesis to provide a broader context for comparing results and understanding the limitations of different method [154].

ALD is particularly notable for its compatibility with CMOS technology, as it op-

erates at relatively lower temperatures compared to other high-temperature techniques. This makes ALD a favorable choice for integrating low-dimensionalmaterial growth into existing silicon-based technologies. However, the method also comes with its challenges. Achieving a self-limiting deposition process in ALD often requires careful optimization of a wide range of parameters. Without proper control, the resulting films may exhibit surface roughness or small grain sizes, which can limit their applicability [155, 156].

1.8 Aim of this Thesis

The rapid growth of the electronics industry has introduced applications where high-cost, high-performance fabrication processes are unnecessary [105]. In this context, the simplicity of manufacturing and deposition processes has made Transition Metal Dichalcogenides (TMDs), such as MoS_2, WS_2, and $PtSe_2$, particularly appealing for integration into electronic devices, including flexible and portable applications [157, 158].

While extensive research has focused on monolayer TMDs, the doping of bulk TMDs remains underexplored. Bulk materials offer valuable insights into the behavior of intermediate thicknesses, bridging the gap between the unique properties of monolayers and the established behaviors of conventional semiconductors. Investigating TMDs in the bulk regime provides an opportunity for foundational research and potential applications in electronics.

The aim of this thesis is to structurally and electrically investigate pristine MoS_2 and WS_2 films, followed by introducing dopants into these films using the same deposition technique under consistent conditions, including identical furnace setups, temperatures, and thicknesses in the same TMD groups. The doping concentration will range from 1.63 at.% to a maximum of 10.48 at.%, introduced into the films with controlled nominal thicknesses. The goal is to observe how the vibrational modes, diffraction patterns, and electrical behavior of these TMD films are influenced by dopants while maintaining consistent deposition and characterization methodologies.

The aim is to investigate the structural and electronic properties of pristine and rhenium (Re)-doped MoS_2 films. These films will be synthesized using the Thermal Assisted Conversion method, where molybdenum and sulfur precursors are annealed in a controlled atmosphere with a rhenium dopant source. This involves examining the impact of Re doping on vibrational modes using Raman spectroscopy and

crystallographic orientations through X-ray diffraction. Additionally, changes in electrical behavior, such as carrier type and resistivity, will be analyzed using Hall effect measurements and four-point probe techniques to understand the effects of varying doping concentrations. Microstructural changes will be studied through transmission electron microscopy to correlate dopant distributions with electrical performance. Ultimately, the goal is to develop Re-doped MoS_2 as an n-type semiconducting channel material for electronic applications.

The aim of WS_2 films focuses on their synthesis and niobium (Nb) doping using the Thermal Assisted Conversion method. This study aims to evaluate the effect of Nb doping on vibrational properties and crystallinity, as well as to characterize electrical behavior, confirming the formation of a p-type semiconducting channel. Structural changes induced by Nb doping will also be examined through TEM, linking dopant incorporation to the observed device performance.

For $PtSe_2$ films, the objective is to study a novel, low-temperature, solution-based method for synthesizing $PtSe_2$ networks and to evaluate their potential for piezoresistive sensor applications. Additionally, this chapter aims to elucidate the strain transfer mechanisms in these networks and their effects on resistivity, using a model developed by Prof. Jonathan Coleman. This involves examining the structural properties of electrochemically exfoliated $PtSe_2$ films, including flake alignment and crystallinity. The electromechanical response under tensile strain will also be tested, with a particular focus on the negative gauge factor and mechanical stability. This study aims to address the growing need for flexible, wearable, and transparent materials in the Internet of Things (IoT) by exploring $PtSe_2$ as a promising material for piezoresistive sensors.

By addressing these aims, this thesis seeks to contribute to the understanding of doped bulk TMDs and their potential for use in electronic and sensing applications.

1.9 Thesis Outline

This thesis provides an analysis of the development and characterization of TMDs produced through Thermally Assisted Conversion and Electrochemical Exfoliation, which generate thin films of polycrystalline TMDs and networks of TMDs, respectively. Accordingly, the following chapters include information that is highly relevant to studies on doped TAC TMD films and electrochemically exfoliated piezoresistive sensors based on TMD films.

Chapter 2: Methodology

This chapter 2 delves into the various techniques utilized throughout the thesis, explaining their underlying principles and mechanisms. These techniques include magnetron deposition, X-ray reflectivity, high-temperature conversion under relatively low vacuum, Raman spectroscopy, X-ray diffraction, UV-Vis spectroscopy, UV-lithography, and scanning electron microscopy. The transmission electron microscopy (TEM) analysis data, which I did not personally handle, was provided by CNR/Catalonia. However, I have full responsibility for completing the rest on my own.

Chapter 3: Modulating MoS_2 Properties through Introduction of Rhenium Impurities

This chapter 3 aims to create complementary metal oxide semiconductor counterparts using TMD-based van der Waals layered materials. The initial focus is on obtaining an n-type material with MoS_2, known for being a stubborn n-type semiconductor that can become a poorly functioning p-type semiconductor due to oxidation. This chapter explores the introduction of Rhenium (Re) impurities into MoS_2 at concentrations of 2.63 at.% and 10.48 at.%. After fundamental characterizations such as Raman, XRD, and low-temperature resistance measurements, Hall effect measurements are conducted to observe carrier concentration, resistivity, and mobility via

doping. The key question addressed is how Re doping atoms are accommodated within MoS_2 lattices, affecting the electrical properties of the material.

Chapter 4: Modulating WS_2 Properties through Introduction of Niobium Impurities

This chapter 4 tackles the challenge of limited p-type charge carriers in van der Waals layered semiconductor materials by attempting to produce p-type WS_2 through Niobium (Nb) doping. Nb is introduced at 1.76 at.% in a 0.2 nm layer within a nominal 10 nm stack, followed by a conversion process at 900°C for 30 minutes. Initial characterizations using Raman spectroscopy and XRD are performed to observe phonon and electron interactions and plane orientation in the WS_2 lattice, respectively. Field-effect transistor measurements and cross-sectional TEM images provide insights into orientation, composition, and Nb distribution.

Chapter 5: Solution-Processed Negative Gauge Factor $PtSe_2$ Strain Sensors

This chapter 5 focuses on the use of an energy-efficient process of ~ 0.05 Wh mg^{-1}, through which electrochemical exfoliation of a novel low-dimensionalsemiconductor, $PtSe_2$, was achieved. Large flakes with average aspect ratios exceeding 10,300 were produced. These flakes were deposited using Langmuir-Schaefer (LS) techniques to form highly aligned flake networks, which were utilized as semi transparent (60% at 1 μm wavelength) strain sensors. Strain of up to 0.5% was applied, resulting in a linear response corresponding to a negative gauge factor of -5.45, which is attributed to changes in the semiconductor band structure upon deformation. The response was shown to be cyclic for over 1000 cycles, enabling the sensors to be implemented in flexible optoelectronics.

References

(1) W. Heywang and K. Zaininger, *Silicon: evolution and future of a technology*, 2004, 25–42.

(2) J. Segura and C. F. Hawkins, *CMOS Electronics: How It Works, How It Fails*, John Wiley & Sons, Hoboken, NJ, 1st, 2004.

(3) H. Wu, K. Li, X. Gao and Y. Dan, *Aip Advances*, 2017, **7**.

(4) E. E. Education, *Intrinsic carrier concentrations in Silicon and Gallium Arsenide*, Accessed: November 7, 2024, n.d.

(5) C. Kittel, *Introduction to solid state physics*, John Wiley & sons, inc, 2005.

(6) DoITPoMS, *The Microstructure of Semiconductors*, Accessed: 07 November 2024, n.d.

(7) W. D. Callister and D. G. Rethwisch, *Materials Science and Engineering: An Introduction*, John Wiley Sons, Hoboken, NJ, USA, 9th, 2014, ch. 19.6-19.12.

(8) S. M. Sze, Y. Li and K. K. Ng, *Physics of semiconductor devices*, John wiley & sons, 2021.

(9) S. R. Thomas, P. Pattanasattayavong and T. D. Anthopoulos, *Chemical Society Reviews*, 2013, **42**, 6910–6923.

(10) L. Duan, D. R. D'hooge and L. Cardon, *Progress in Materials Science*, 2020, **114**, 100617.

(11) W. D. Van Dyke and P. A. Dennis, *Metal foil type strain gauge and method of making same*, US Patent 2,457,616, 1948.

(12) S. Biccai, C. S. Boland, D. P. O'Driscoll, A. Harvey, C. Gabbett, D. R. O'Suilleabhain, A. J. Griffin, Z. Li, R. J. Young and J. N. Coleman, *Acs Nano*, 2019, **13**, 6845–6855.

(13) Kulite, *Selecting Strain Gages: Silicon vs. Metal Foil*, Online, Accessed: 2024-05-01, 2024.

(14) W. Wu, L. Wang, Y. Li, F. Zhang, L. Lin, S. Niu, D. Chenet, X. Zhang, Y. Hao, T. F. Heinz et al., *Nature*, 2014, **514**, 470–474.

(15) C. S. Smith, *Physical Review*, 1954, **94**, 42–49.

(16) A. Fiorillo, C. Critello and S. Pullano, *Sensors and Actuators A: Physical*, 2018, **281**, 156–175.

(17) W. Dang, V. Vinciguerra, L. Lorenzelli and R. Dahiya, *Flexible and Printed Electronics*, 2017, **2**, 013003.

(18) W. P. Mason, *Crystal Physics of Interaction Processes*, Academic Press, New York, NY, 1966.

(19) C. Si, Z. Sun and F. Liu, *Nanoscale*, 2016, **8**, 3207–3217.

(20) C. Wang, S.-X. Yang, H.-R. Zhang, L.-N. Du, L. Wang, F.-Y. Yang, X.-Z. Zhang and Q. Liu, *Frontiers of Physics*, 2016, **11**, 1–5.

(21) S. Lee, J. Kim, I. Yun, G. Y. Bae, D. Kim, S. Park, I.-M. Yi, W. Moon, Y. Chung and K. Cho, *Nature communications*, 2019, **10**, 2468.

(22) A. not specified, *Journal of Materials Science: Materials in Electronics*, 2024, **35**, This review discusses figures of merit for strain sensors, including gauge factor, strain limits, and environmental stability, with a focus on polymer-based and TMD materials., 12923–12945.

(23) I. Aberg, O. Olubuyide, C. N. Chléirigh, I. Lauer, D. Antoniadis, J. Li, R. Hull and J. Hoyt, Digest of Technical Papers. 2004 Symposium on VLSI Technology, 2004. 2004, pp. 52–53.

(24) K. S. Kim, J. Kwon, H. Ryu, C. Kim, H. Kim, E.-K. Lee, D. Lee, S. Seo, N. M. Han, J. M. Suh et al., *Nature Nanotechnology*, 2024, **19**, 895–906.

(25) S. Datta, *The Electrochemical Society Interface*, 2013, **22**, 41.

(26) S.-K. Su, C.-P. Chuu, M.-Y. Li, C.-C. Cheng, H.-S. P. Wong and L.-J. Li, *Small Structures*, 2021, **2**, 2000103.

(27) G. Moore, *Electronics Magazine*, 1965, **38**, 114.

(28) K. Karimi, A. Fardoost and M. Javanmard, *Micromachines*, 2024, **15**, 1187.

(29) S. Srivastava and A. Acharya, in *Device Circuit Co-Design Issues in FETs*, CRC Press, 2024, pp. 231–258.

(30) I.-T. Lu, J.-J. Zhou, J. Park and M. Bernardi, *Physical Review Materials*, 2022, **6**, DOI: 10.1103/PhysRevMaterials.6.L010801.

(31) D. B. M. Klaassen, *Solid-State Electronics*, 1992, **35**, 961–967.

(32) Y. Liu, X. Duan, H.-J. Shin, S. Park, Y. Huang and X. Duan, *Nature*, 2021, **591**, 43–53.

(33) R. Clerc et al., *Microelectronics Reliability*, 2008, **48**, 1500–1504.

(34) I. Institute, *Silicon: Electrical Properties*, https://www.ioffe.ru/SVA/NSM/Semicond/Si/electric.html, Accessed: 2024-09-04.

(35) C. A. Bhuyan, K. K. Madapu, K. Prabakar, K. Ganesan, A. Pandian and S. Dhara, *arXiv preprint arXiv:2402.13564*, 2024.

(36) H. Li, Q. Li, Y. Li, Z. Yang, R. Quhe, X. Sun, Y. Wang, L. Xu, L.-m. Peng, H. Tian et al., *Advanced Functional Materials*, 2024, 2402474.

(37) Z. Yao, J. Deng and L. Li, *Matter*, 2024.

(38) T.-E. Lee, Y.-C. Su, B.-J. Lin, Y.-X. Chen, W.-S. Yun, P.-H. Ho, J.-F. Wang, S.-K. Su, C.-F. Hsu, P.-S. Mao et al., 2022 International Electron Devices Meeting (IEDM), 2022, pp. 7–4.

(39) W. Wu, D. De, S.-C. Chang, Y. Wang, H. Peng, J. Bao and S.-S. Pei, *Applied Physics Letters*, 2013, **102**, 142106.

(40) A. Chaves, J. G. Azadani, H. Alsalman, D. Da Costa, R. Frisenda, A. Chaves, S. H. Song, Y. D. Kim, D. He, J. Zhou et al., *npj 2D Materials and Applications*, 2020, **4**, 29.

(41) J. Ke, B. Wang, Z. Yao and J. Zhang, *Surface and Coatings Technology*, 2024, **493**, 131299.

(42) R. F. Pierret, *Semiconductor Device Fundamentals*, Addison-Wesley, Reading, MA, USA, 1996.

(43) L. Loh, Z. Zhang, M. Bosman and G. Eda, *Nano Research*, 2021, **14**, 1668–1681.

(44) N. S. Arul and V. D. Nithya, *Two Dimensional Transition Metal Dichalcogenides*, Springer, 2019.

(45) J. Strachan, A. F. Masters and T. Maschmeyer, *ACS Applied Energy Materials*, 2021, **4**, 7405–7418.

(46) Q. H. Wang, K. Kalantar-Zadeh, A. Kis, J. N. Coleman and M. S. Strano, *Nature nanotechnology*, 2012, **7**, 699–712.

(47) A. Kuc, *Journal of Materials Chemistry C*, 2014, **2**, 12292–12301.

(48) M. Chhowalla, H. S. Shin, G. Eda, L.-J. Li, K. P. Loh and H. Zhang, *Nature chemistry*, 2013, **5**, 263–275.

(49) Y. Zhang, J. Li, X. Li, L. Shan, W. Zhao, J. Wang, Q. Gao, Z. Cai, C. Zhou, B. Han et al., *Nano Letters*, 2024, **24**, 3331–3338.

(50) A. V. Kolobov and J. Tominaga, *Two-dimensional transition-metal dichalcogenides*, Springer, 2016, vol. 239.

(51) S. Tongay, H. Sahin, C. Ko, A. Luce, W. Fan, K. Liu, J. Zhou, Y.-S. Huang, C.-H. Ho, J. Yan et al., *Nature communications*, 2014, **5**, 3252.

(52) M. H. Guimaraes, H. Gao, Y. Han, K. Kang, S. Xie, C.-J. Kim, D. A. Muller, D. C. Ralph and J. Park, *ACS nano*, 2016, **10**, 6392–6399.

(53) K. S. Novoselov, D. Jiang, F. Schedin, T. Booth, V. Khotkevich, S. Morozov and A. K. Geim, *Proceedings of the National Academy of Sciences*, 2005, **102**, 10451–10453.

(54) I. F. Barton, C. A. Rathkopf and M. D. Barton, *Mining, Metallurgy & Exploration*, 2020, **37**, 21–37.

(55) W. Zhang, Q. Wang, Y. Chen, Z. Wang and A. T. Wee, *2D Materials*, 2016, **3**, 022001.

(56) A. Kuc, N. Zibouche and T. Heine, *Physical Review B—Condensed Matter and Materials Physics*, 2011, **83**, 245213.

(57) E. Blundo, M. Felici, T. Yildirim, G. Pettinari, D. Tedeschi, A. Miriametro, B. Liu, W. Ma, Y. Lu and A. Polimeni, *Physical Review Research*, 2020, **2**, 012024.

(58) S. Hwangbo, L. Hu, A. T. Hoang, J. Y. Choi and J.-H. Ahn, *Nature Nanotechnology*, 2022, **17**, 500–506.

(59) E. Elahi, M. Ahmad, A. Dahshan, M. Rabeel, S. Saleem, H. Hegazy, S. Aftab et al., *Nanoscale*, 2024, **16**, 14–43.

(60) A. Kandemir, B. Akbali, Z. Kahraman, S. Badalov, M. Ozcan, F. İyikanat and H. Sahin, *Semiconductor Science and Technology*, 2018, **33**, 085002.

(61) M. Turunen, *Aalto University Research Papers*, 2024, Preprint or unpublished if applicable, DOI: `10.xxxx/aalto.2024.optics`.

(62) K. Zhang, A. Jain, W. Wu, J. Ranasinghe, Z. Wang and S. Huang, in *Novel Optical Materials*, World Scientific, 2024, pp. 1–30.

(63) Y. Zhang, H. L. Zhao, S. Huang, M. A. Hossain and A. M. van der Zande, *ACS nano*, 2024, **18**, 12377–12385.

(64) H. Yu, L. Huang, L. Zhou, Y. Peng, X. Li, P. Yin, J. Zhao, M. Zhu, S. Wang, J. Liu et al., *Advanced Materials*, 2024, **36**, 2402855.

(65) H. Liu, Z. Huang, H. Qiao and X. Qi, *Physical Chemistry Chemical Physics*, 2024.

(66) T. Hallam, S. Monaghan, F. Gity, L. Ansari, M. Schmidt, C. Downing, C. P. Cullen, V. Nicolosi, P. K. Hurley and G. S. Duesberg, *Applied Physics Letters*, 2017, **111**.

(67) R. Torsi, K. T. Munson, R. Pendurthi, E. Marques, B. Van Troeye, L. Huberich, B. Schuler, M. Feidler, K. Wang, G. Pourtois et al., *ACS nano*, 2023, **17**, 15629–15640.

(68) K. T. Munson, R. Torsi, F. Habis, L. Huberich, Y.-C. Lin, Y. Yuan, K. Wang, B. Schuler, Y. Wang, J. B. Asbury et al., *Advanced Electronic Materials*, 2024, 2400403.

(69) S. Li, J. Hong, B. Gao, Y.-C. Lin, H. E. Lim, X. Lu, J. Wu, S. Liu, Y. Tateyama, Y. Sakuma, K. Tsukagoshi, K. Suenaga and T. Taniguchi, *Advanced Science*, 2021, **8**, 2004438.

(70) K. Zhang, B. M. Bersch, J. Joshi, R. Addou, C. R. Cormier, C. Zhang, K. Xu, N. C. Briggs, K. Wang, S. Subramanian et al., *Advanced Functional Materials*, 2018, **28**, 1706950.

(71) H. Gao, J. Suh, M. C. Cao, A. Y. Joe, F. Mujid, K.-H. Lee, S. Xie, P. Poddar, J.-U. Lee, K. Kang et al., *Nano Letters*, 2020, **20**, 4095–4101.

(72) Y. Zhang, W. Chen, H. Li, J. Smith and L. Kim, *Nano Research*, 2023, **16**, 543–551.

(73) X. Tang, Z. Liu, M. Zhou and Y. Wang, *AIP Applied Materials*, 2023, **9**, 121115.

(74) M. R. Laskar, D. N. Nath, L. Ma, E. W. Lee, C. H. Lee, T. Kent, Z. Yang, R. Mishra, M. A. Roldan, J.-C. Idrobo et al., *Applied Physics Letters*, 2014, **104**.

(75) A. Smith, L. Kim and Y. Zhao, *Journal of Materials Chemistry C*, 2022, **10**, 3520–3530.

(76) W. Chen, M. Zhang and H. Li, *Journal of Electronic Materials*, 2023, **52**, 1460–1471.

(77) L. Wang, X. Liu and M. Zhao, *IEEE Transactions on Electron Devices*, 2017, **64**, 2171–2177.

(78) C. Taylor, A. Patel and R. Smith, *Journal of Materials Chemistry C*, 2023, **11**, 4000–4010.

(79) X. Wang, X. Shen, Z. Wang, R. Yu and L. Chen, *ACS nano*, 2014, **8**, 11394–11400.

(80) L. Yang, K. Majumdar, H. Liu, Y. Du, H. Wu, M. Hatzistergos, P. Hung, R. Tieckelmann, W. Tsai, C. Hobbs et al., *Nano Letters*, 2014, **14**, 6275–6280.

(81) J. H. Kang, W. A. Goddard and Y. Wang, *Journal of Physical Chemistry C*, 2013, **117**, 25643–25649.

(82) J. Ma, Y. Wang and X. Zhang, *Physical Review B*, 2013, **88**, 075420.

(83) R. Sharma, P. Singh and M. Gupta, *RSC Advances*, 2021, **11**, 3520–3530.

(84) H. Yoo, K. Heo, M. H. R. Ansari and S. Cho, *Nanomaterials*, 2021, **11**, 832.

(85) Y. Tong, M. Bouaziz, H. Oughaddou, H. Enriquez, K. Chaouchi, F. Nicolas, S. Kubsky, V. Esaulov and A. Bendounan, *RSC advances*, 2020, **10**, 30934–30943.

(86) C. Wang, Z. Liu and G. Xiong, *Scientific Reports*, 2024, **14**, 23388.

(87) Z. Qin, L. Loh, J. Wang, X. Xu, Q. Zhang, B. Haas, C. Alvarez, H. Okuno, J. Z. Yong, T. Schultz et al., *Advanced Electronic Materials*, 2023, **9**, 2400403.

(88) X. Guan, H. Zhao, L. Wang et al., *Nature Microsystems Nanoengineering*, 2024.

(89) M. E. Pam, J. Hu, Y. S. Ang, S. Huang, D. Kong, Y. Shi, X. Zhao, D. Geng, S. J. Pennycook, L. K. Ang and H. Y. Yang, *ACS Applied Materials & Interfaces*, 2019, **11**, 34862–34868.

(90) L. Tang, R. Xu, J. Tan, Y. Luo, J. Zou, Z. Zhang, R. Zhang, Y. Zhao, J. Lin, X. Zou, B. Liu and H.-M. Cheng, *arXiv preprint arXiv:2012.02984*, 2020.

(91) S. Zhang, H.-J. Chuang, S. T. Le, C. A. Richter, K. M. McCreary, B. T. Jonker, A. R. Hight Walker and C. A. Hacker, *AIP Advances*, 2022, **12**, 085222.

(92) M. W. Iqbal, M. Z. Iqbal, M. F. Khan, M. A. Shehzad, Y. Seo and J. Eom, *Nanoscale*, 2015, **7**, 747–757.

(93) M. Han, Y. Mu, Y. Cai, L. Wei, L. Zeng and T. Zhao, *Journal of Materials Chemistry A*, 2022, **10**, 20138–20148.

(94) M. W. Iqbal, M. Z. Iqbal, M. F. Khan, M. A. Kamran, A. Majid, T. Alharbi and J. Eom, *RSC Advances*, 2016, **6**, 24365–24371.

(95) K. S. Novoselov, A. K. Geim, S. V. Morozov, D.-e. Jiang, Y. Zhang, S. V. Dubonos, I. V. Grigorieva and A. A. Firsov, *science*, 2004, **306**, 666–669.

(96) Y. Huang, E. Sutter, N. N. Shi, J. Zheng, T. Yang, D. Englund, H.-J. Gao and P. Sutter, *ACS nano*, 2015, **9**, 10612–10620.

(97) F. Liu, *Progress in Surface Science*, 2021, **96**, 100626.

(98) D. Hu, G. Xu, L. Xing, X. Yan, J. Wang, J. Zheng, Z. Lu, P. Wang, X. Pan and L. Jiao, *Angewandte Chemie International Edition*, 2017, **56**, 3611–3615.

(99) W. Zhu, P. Wu, L. Song et al., *Nature Materials*, 2017, **16**, 814–821.

(100) R. Dong and I. Kuljanishvili, *Journal of Vacuum Science & Technology B*, 2017, **35**.

(101) G. Cheon, K.-A. N. Duerloo, A. D. Sendek, C. Porter, Y. Chen and E. J. Reed, *Nano letters*, 2017, **17**, 1915–1923.

(102) N. J. Clark, *Fabrication and Applications of Suspended Grapheme Membranes*, The University of Manchester (United Kingdom), 2016.

(103) A. Weston, E. G. Castanon, V. Enaldiev, F. Ferreira, S. Bhattacharjee, S. Xu, H. Corte-León, Z. Wu, N. Clark, A. Summerfield et al., *Nature nanotechnology*, 2022, **17**, 390–395.

(104) Q. Li, K. Wu, H. Zhu, Y. Yang, S. He and T. Lian, *Chemical Reviews*, 2024, **124**, 5695–5763.

(105) C. E. Shuck, X. Xiao and Z. Wang, *Challenges and Opportunities in 2D Materials*, 2024.

(106) Y. Hernandez, V. Nicolosi, M. Lotya, F. M. Blighe, Z. Sun, S. De, I. T. McGovern, B. Holland, M. Byrne, Y. K. Gun'Ko et al., *Nature nanotechnology*, 2008, **3**, 563–568.

(107) K. R. Paton, E. Varrla, C. Backes, R. J. Smith, U. Khan, A. O'Neill, C. Boland, M. Lotya, O. M. Istrate, P. King et al., *Nature materials*, 2014, **13**, 624–630.

(108) D. McManus, S. Vranic, F. Withers, V. Sanchez-Romaguera, M. Macucci, H. Yang, R. Sorrentino, K. Parvez, S.-K. Son, G. Iannaccone et al., *Nature nanotechnology*, 2017, **12**, 343–350.

(109) E. B. Secor, S. Lim, H. Zhang, C. D. Frisbie, L. F. Francis and M. C. Hersam, *Advanced Materials (Deerfield Beach, Fla.)*, 2014, **26**, 4533–4538.

(110) M.-W. Lin, I. I. Kravchenko, J. Fowlkes, X. Li, A. A. Puretzky, C. M. Rouleau, D. B. Geohegan and K. Xiao, *Nanotechnology*, 2016, **27**, 165203.

(111) A. G. Kelly, T. Hallam, C. Backes, A. Harvey, A. S. Esmaeily, I. Godwin, J. Coelho, V. Nicolosi, J. Lauth, A. Kulkarni et al., *Science*, 2017, **356**, 69–73.

(112) P. Sahoo, R. C. Sahoo and H. R. Matte, *ACS Applied Nano Materials*, 2023, **6**, 21957–21966.

(113) X. You, J.-H. Chang, B. K. Ju and J. J. Pak, *Journal of nanoscience and nanotechnology*, 2011, **11**, 5965–5968.

(114) S. Yang, P. Zhang, A. S. Nia and X. Feng, *Advanced Materials*, 2020, **32**, 1907857.

(115) S. Wang, J. Xue, D. Xu, J. He, Y. Dai, T. Xia, Y. Huang, Q. He, X. Duan and Z. Lin, *Nature Protocols*, 2023, **18**, 2814–2837.

(116) M. Zhao, C. Casiraghi and K. Parvez, *Chemical Society Reviews*, 2024.

(117) Y. Yang, H. Hou, G. Zou, W. Shi, H. Shuai, J. Li and X. Ji, *Nanoscale*, 2019, **11**, 16–33.

(118) K. Parvez, Z.-S. Wu, R. Li, X. Liu, R. Graf, X. Feng and K. Müllen, *Journal of the American Chemical society*, 2014, **136**, 6083–6091.

(119) Y. L. Zhong and T. M. Swager, *Journal of the American Chemical Society*, 2012, **134**, 17896–17899.

(120) Z. Zeng, Z. Yin, X. Huang and H. Li, *Angew. Chem. Int. Edit*, 2011, **50**, 11093.

(121) G. Cunningham, M. Lotya, N. McEvoy, G. S. Duesberg, P. van der Schoot and J. N. Coleman, *Nanoscale*, 2012, **4**, 6260–6264.

(122) Y. Yu, Y. Yu, Y. Cai, W. Li, A. Gurarslan, H. Peelaers, D. E. Aspnes, C. G. Van de Walle, N. V. Nguyen, Y.-W. Zhang et al., *Scientific reports*, 2015, **5**, 16996.

(123) S. De and J. N. Coleman, *Mrs Bulletin*, 2011, **36**, 774–781.

(124) D. Stauffer and A. Aharony, *Introduction to percolation theory*, Taylor & Francis, 2018.

(125) A. G. Kelly, Ph.D. Thesis, Trinity College Dublin, 2018.

(126) V. Roldughin and V. Vysotskii, *Progress in organic coatings*, 2000, **39**, 81–100.

(127) X. Zhao, A. A. Koos, B. T. Chu, C. Johnston, N. Grobert and P. S. Grant, *Carbon*, 2009, **47**, 561–569.

(128) R. H. Schmidt, I. A. Kinloch, A. N. Burgess and A. H. Windle, *Langmuir*, 2007, **23**, 5707–5712.

(129) J. Neilson, *Liquid-liquid assembled 2D materials for large-area electronics*, The University of Manchester (United Kingdom), 2021.

(130) S. Najmaei, Z. Liu, W. Zhou, X. Zou, G. Shi, S. Lei, B. I. Yakobson, J.-C. Idrobo, P. M. Ajayan and J. Lou, *Nature materials*, 2013, **12**, 754–759.

(131) L. Sun, G. Yuan, L. Gao, J. Yang, M. Chhowalla, M. H. Gharahcheshmeh, K. K. Gleason, Y. S. Choi, B. H. Hong and Z. Liu, *Nature Reviews Methods Primers*, 2021, **1**, 5.

(132) H. O. Pierson, *Handbook of chemical vapor deposition: principles, technology and applications*, William Andrew, 1999.

(133) X.-T. Yan and Y. Xu, *Chemical vapour deposition: an integrated engineering design for advanced materials*, Springer Science & Business Media, 2010.

(134) S.-W. Chung, S. Ganorkar and S.-I. Kim, *Journal of the Korean Physical Society*, 2023, **82**, 1211–1215.

(135) T. Yamada, J. Kim, M. Ishihara and M. Hasegawa, *Journal of Physics D: Applied Physics*, 2013, **46**, 063001.

(136) A. T. Hoang, L. Hu, B. J. Kim, T. T. N. Van, K. D. Park, Y. Jeong, K. Lee, S. Ji, J. Hong, A. K. Katiyar et al., *Nature Nanotechnology*, 2023, **18**, 1439–1447.

(137) D. Chiappe, I. Asselberghs, S. Sutar, S. Iacovo, V. Afanas' ev, A. Stesmans, Y. Balaji, L. Peters, M. Heyne, M. Mannarino et al., *Advanced Materials Interfaces*, 2016, **3**, 1500635.

(138) Y. Zhan, Z. Liu, S. Najmaei, P. M. Ajayan and J. Lou, *arXiv preprint arXiv:1111.5072*, 2011.

(139) Y.-H. Lee, X.-Q. Zhang, W. Zhang, M.-T. Chang, C.-T. Lin, K.-D. Chang, Y.-C. Yu, J. T.-W. Wang, C.-S. Chang, L.-J. Li et al., *arXiv preprint arXiv:1202.5458*, 2012.

(140) V. Marinova, K. Buchkov, V. Videva, I. Dionisiev, N. Minev, V. Strijkova, D. Dimov, H. Dikov, I. Avramova, P. Rafailov et al., *Evolution of WSe2 Flakes Synthesized by Thermally Assisted Conversion Method. Coatings 2022, 12, 353*, 2022.

(141) G. Wang, Z. Wang, N. McEvoy, P. Fan and W. J. Blau, *Advanced Materials*, 2021, **33**, 2004070.

(142) H. Liu, K. A. Antwi, J. Ying, S. Chua and D. Chi, *Nanotechnology*, 2014, **25**, 405702.

(143) H. Li, H. Wu, S. Yuan and H. Qian, *Scientific reports*, 2016, **6**, 21171.

(144) S.-L. Shang, G. Lindwall, Y. Wang, J. M. Redwing, T. Anderson and Z.-K. Liu, *Nano letters*, 2016, **16**, 5742–5750.

(145) Y. Kocak and E. Gur, *ACS applied materials & interfaces*, 2020, **12**, 15785–15792.

(146) S. S. Han, J. H. Kim, C. Noh, J. H. Kim, E. Ji, J. Kwon, S. M. Yu, T.-J. Ko, E. Okogbue, K. H. Oh et al., *ACS applied materials & interfaces*, 2019, **11**, 13598–13607.

(147) M. Sojková, K. Vegso, N. Mrkyvkova, J. Hagara, P. Hutár, A. Rosová, M. Čaplovičová, U. Ludacka, V. Skákalová, E. Majková et al., *RSC advances*, 2019, **9**, 29645–29651.

(148) A. Shaji, K. Vegso, M. Sojkova, M. Hulman, P. Nadazdy, P. Hutar, L. Pribusova Slusna, J. Hrda, M. Bodik, M. Hodas et al., *The Journal of Physical Chemistry C*, 2021, **125**, 9461–9468.

(149) D. Kong, H. Wang, J. J. Cha, M. Pasta, K. J. Koski, J. Yao and Y. Cui, *Nano letters*, 2013, **13**, 1341–1347.

(150) S. Balasubramanyam, M. A. Bloodgood, M. van Ommeren, T. Faraz, V. Vandalon, W. M. Kessels, M. A. Verheijen and A. A. Bol, *ACS applied materials & interfaces*, 2019, **12**, 3873–3885.

(151) Y. Yan, B. Xia, N. Li, Z. Xu, A. Fisher and X. Wang, *Journal of Materials Chemistry A*, 2015, **3**, 131–135.

(152) C. Liu, L. Wang, Y. Tang, S. Luo, Y. Liu, S. Zhang, Y. Zeng and Y. Xu, *Applied Catalysis B: Environmental*, 2015, **164**, 1–9.

(153) S. Wang, X. Zhang, C. Li, Y. Tian and P. Yang, *International Journal of Hydrogen Energy*, 2024, **90**, 853–864.

(154) N. Aspiotis, K. Morgan, B. März, K. Müller-Caspary, M. Ebert, E. Weatherby, M. E. Light, C.-C. Huang, D. W. Hewak, S. Majumdar et al., *npj 2D Materials and Applications*, 2023, **7**, 18.

(155) R. Huang and A. H. Kitai, *Journal of electronic materials*, 1993, **22**, 215–220.

(156) J. Aarik, A. Aidla, A.-A. Kiisler, T. Uustare and V. Sammelselg, *Thin Solid Films*, 1999, **340**, 110–116.

(157) S. J. Yun, H. Ko, S. Park, B. H. Lee, N. Kim, H. P. Duong, Y. Lee, S. M. Kim and K. K. Kim, *Advanced Functional Materials*, 2024, **3**, 240.

(158) J. Chen, M.-Y. Sun, Z.-H. Wang, Z. Zhang, K. Zhang, S. Wang, Y. Zhang, X. Wu, T.-L. Ren, H. Liu et al., *Nano-Micro Letters*, 2024, **16**, 264.

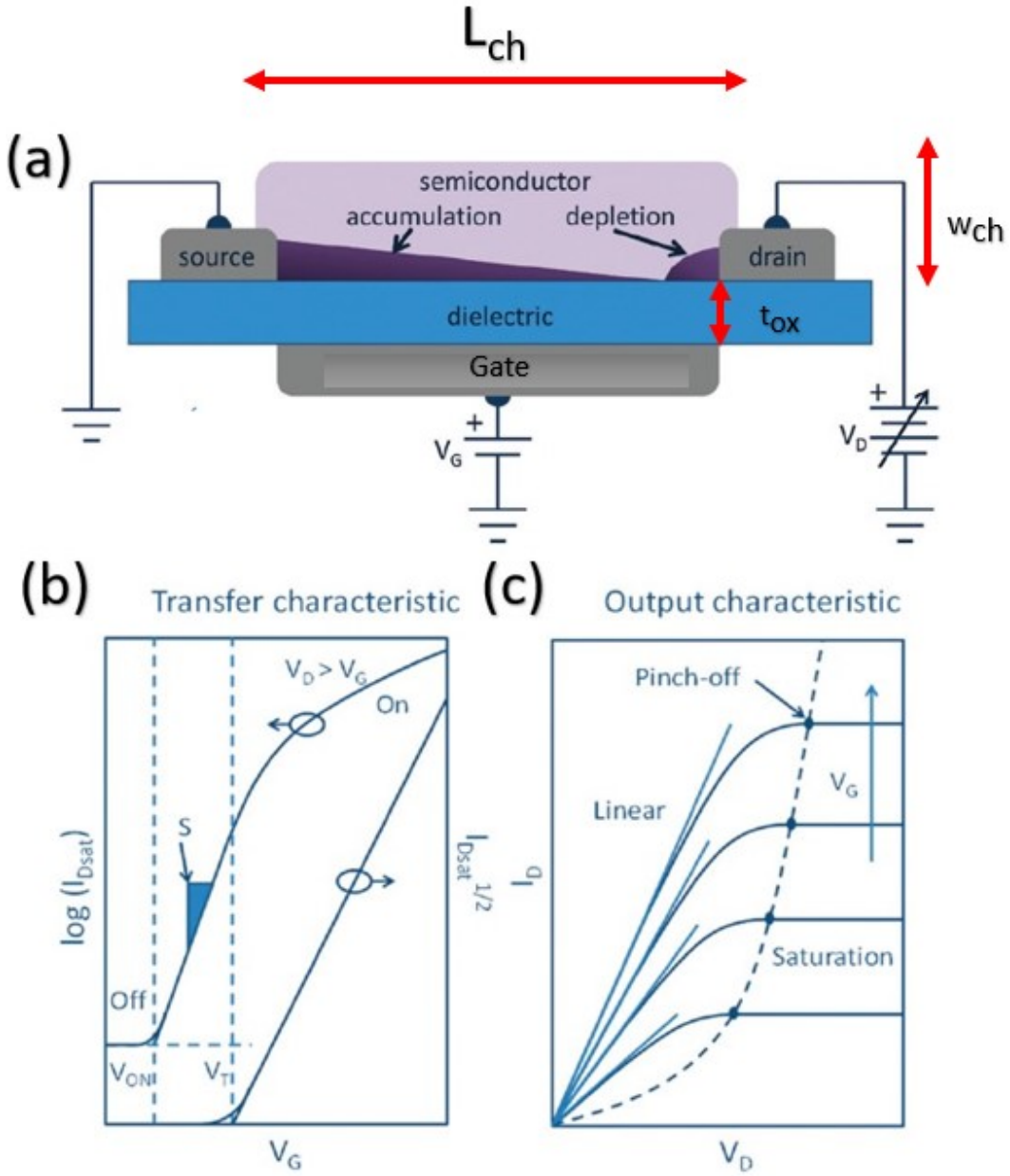

Figure 1.7: (a) Schematic of a transistor illustrating the source, drain, and gate contacts, along with the dielectric layer and a semiconductor. The diagram depicts charge accumulation and depletion regions, which are controlled by the gate voltage (V_G). The channel length (L_{ch}) is defined as the distance between the source and drain contacts, while the channel width (W_{ch}) refers to the dimension of the channel perpendicular to the direction of current flow. The oxide thickness (t_{ox}) represents the thickness of the dielectric layer separating the gate electrode from the semiconductor. (b) Transfer characteristic showing the drain current (I_D) on a logarithmic scale as a function of gate voltage (V_G) on the primary y-axis, while the square root of the drain current ($\sqrt{I_D}$) is plotted on the secondary y-axis. The relationship between $\sqrt{I_D}$ and V_G is linear in the saturation region, facilitating the determination of the threshold voltage (V_T) by extrapolating the straight-line portion to the x-axis where $\sqrt{I_D} = 0$. (c) Output characteristic showing the relationship between the drain current (I_D) and the drain voltage (V_D) for various gate voltages (V_G), highlighting the linear and saturation regions of operation. The image is adapted from Ref: [9].

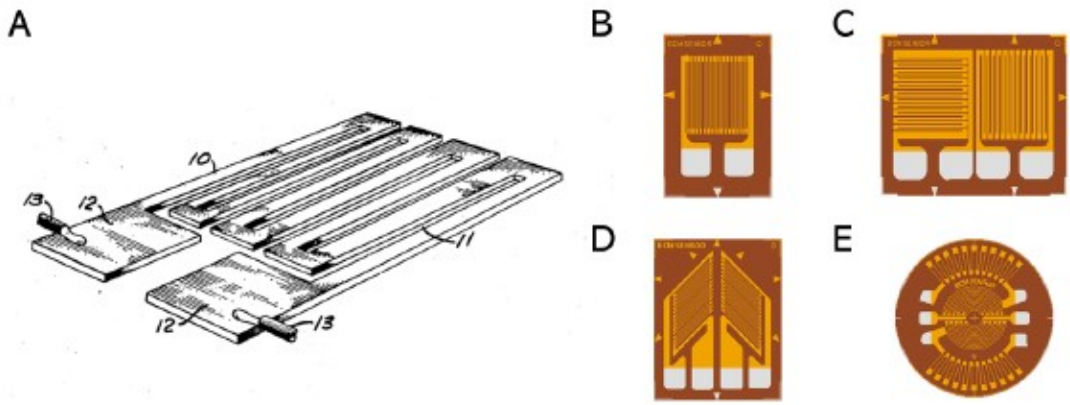

Figure 1.8: Metal foil strain gauges: A) Image from the first commercial metal foil gauge patent [11]. Modern commercial metal foil strain gauges for measuring tensile strain, with patterned foils for measuring B) Tensile strain, C) Perpendicular tensile strains, D) Shear, and E) Pressure tensile strain.

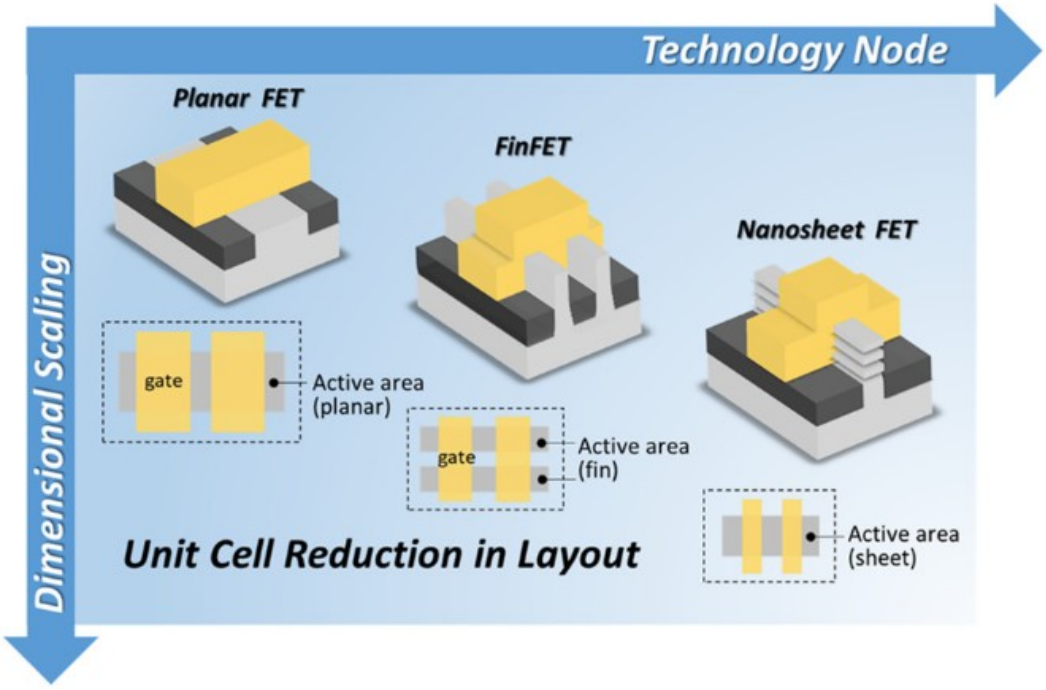

Figure 1.9: Schematic of scaling limits in silicon-based technologies [26]. This progression from planar FET to FinFET to Nanosheet FET reflects the semiconductor industry's efforts to overcome physical and performance limits while achieving smaller technology nodes (e.g., 7 nm, 5 nm, and beyond). Technology nodes represent the advancement in semiconductor manufacturing, allowing for higher transistor densities and improved performance at reduced power consumption. The concept of unit cell reduction in layout is also illustrated, highlighting how the active area of a transistor becomes more compact with each architectural improvement, enabling increased integration density. Each step ensures continued advancements in microelectronics, in line with Moore's law [27].

Table 1.2: Figures of Merit for Gauge Sensors and Desired Properties.

Figure of Merit	**Desired Properties**
Gauge Factor (GF)	High GF for greater sensitivity to small strains. Desirable, GF $>$ 100 for semiconductors and advanced materials.
Strain Limit	Wide strain range to accommodate large deformations. Desired strain limits: up to 5% for metals and >2% for flexible materials.
Linearity	High linearity ensures accurate and predictable response under varying strain. Nonlinear effects should be minimized.
Temperature Sensitivity	Low temperature dependence for stable operation in fluctuating environments. Desired: minimal drift with temperature variations.
Elastic Modulus	Moderate elastic modulus to maintain high mechanical flexibility and durability, especially for flexible or wearable applications.
Durability and Fatigue Resistance	High durability to withstand repeated strain cycles without degradation. Materials should endure >10^6 cycles for long-term applications.
Power Consumption	Low power consumption to support energy-efficient operation, especially for portable and wearable devices.
Environmental Stability	Robust performance under varying environmental conditions such as humidity, temperature, and mechanical vibrations.

Table 1.3: Comparison of bulk silicon and low-dimensional TMD Materials (e.g., monolayer MoS_2), channel length is 10 nm for both materials.

Figure of Merit	**Silicon (Traditional)**	**Low-dimensional materials (e.g., MoS_2)**
Carrier Mobility (max) (μ)	$1400\,cm^2/Vs$ [31]	$2400\,cm^2/Vs$ [35]
Subthreshold Swing (SS)	$\sim 60\,mV/dec$ [8]	$60-70\,mV/dec$ [38]
On/Off Ratio	$\sim 10^4-10^6$ [8]	10^8-10^{10} [39]
Bandgap	1.12 eV (indirect) [8]	1.8 eV (direct) [40]
Short-Channel Effects [32]	Severe at sub-10 nm: Increased drain-induced barrier lowering (DIBL) and high leakage currents.	Minimal due to atomic thickness and superior gate control.
Flexibility	Rigid [8]	Flexible [41]

Table 1.4: Summary of dopants for MoS_2, their semiconductor type, doping method, and references.

Dopant	**Type of Semiconductor**	**Doping Method**	**Reference**
Rhenium (Re)	n-type	Substitutional	[66, 67, 72]
Niobium (Nb)	p-type	Substitutional	[73, 74]
Tantalum (Ta)	p-type	Substitutional	[75]
Nitrogen (N)	p-type	Plasma immersion	[76]
Aluminum Oxide (AlO_x)	n-type	Surface charge transfer	[77]
Sodium (Na)	p-type	Intercalation	[78, 79]
Chlorine (Cl)	n-type	Molecular doping	[80]
Phosphorus (P)	p-type	Substitutional	[81]
Lithium (Li)	n-type	Adsorption doping	[82]
Fluorine (F)	p-type	Molecular doping	[83]

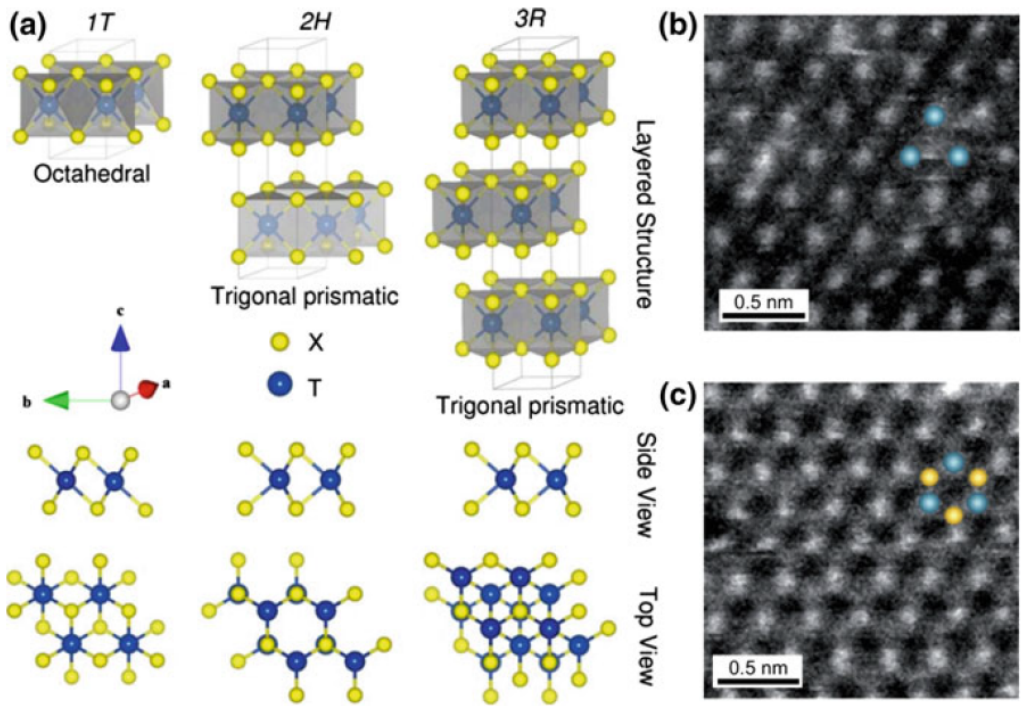

Figure 1.10: (a) Structural models of the 1T, 2H, and 3R phases, illustrating the octahedral and trigonal prismatic coordination of molybdenum (Mo) atoms by sulfur (S) atoms [47]. The 1T phase exhibits octahedral coordination and metallic behavior, whereas the 2H and 3R phases feature trigonal prismatic coordination, resulting in semiconducting properties. (b) High-resolution electron microscopy (HREM) image showing the layered structure of MoS_2 or WS_2 in the 1T phase. (c) HREM images depicting top view of MoS_2 or WS_2 in the 2H phase, highlighting the precise positioning of Mo or W and S atoms. [48].

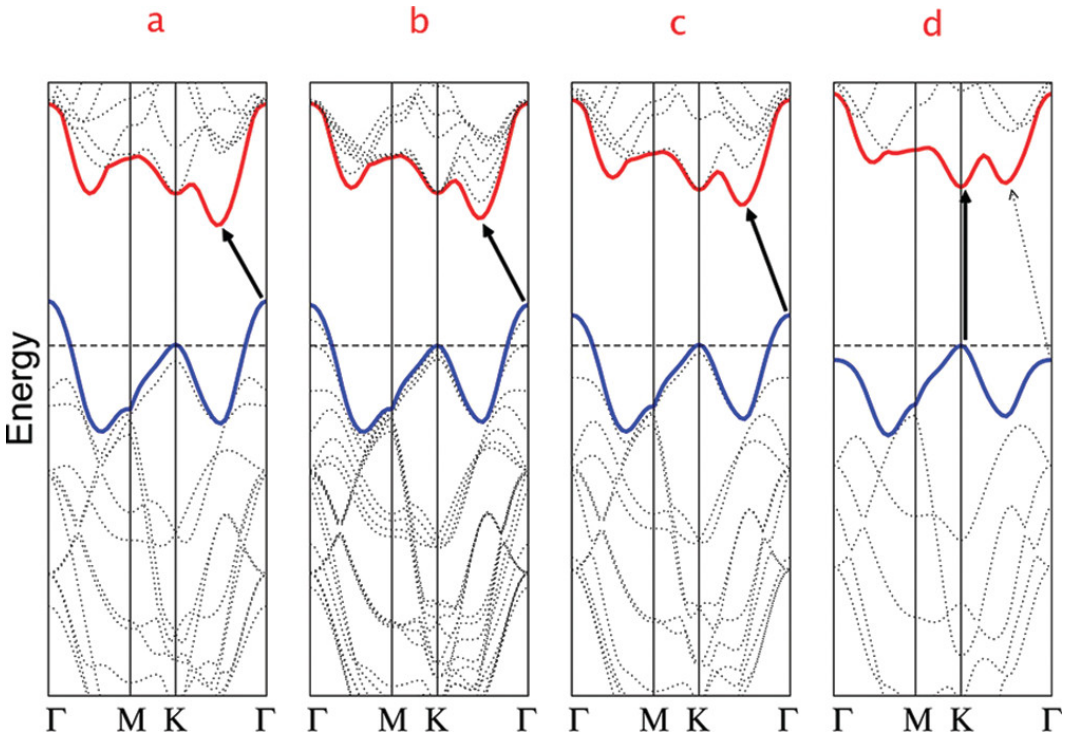

Figure 1.11: Band structure evolution of 2H phase of MoS_2 or WS_2 with thickness. The bandgap transitions from indirect in bulk (left) to direct in a monolayer (right). The conduction band minimum and valence band maximum positions shift, resulting in an increased bandgap energy in thinner layers [48].

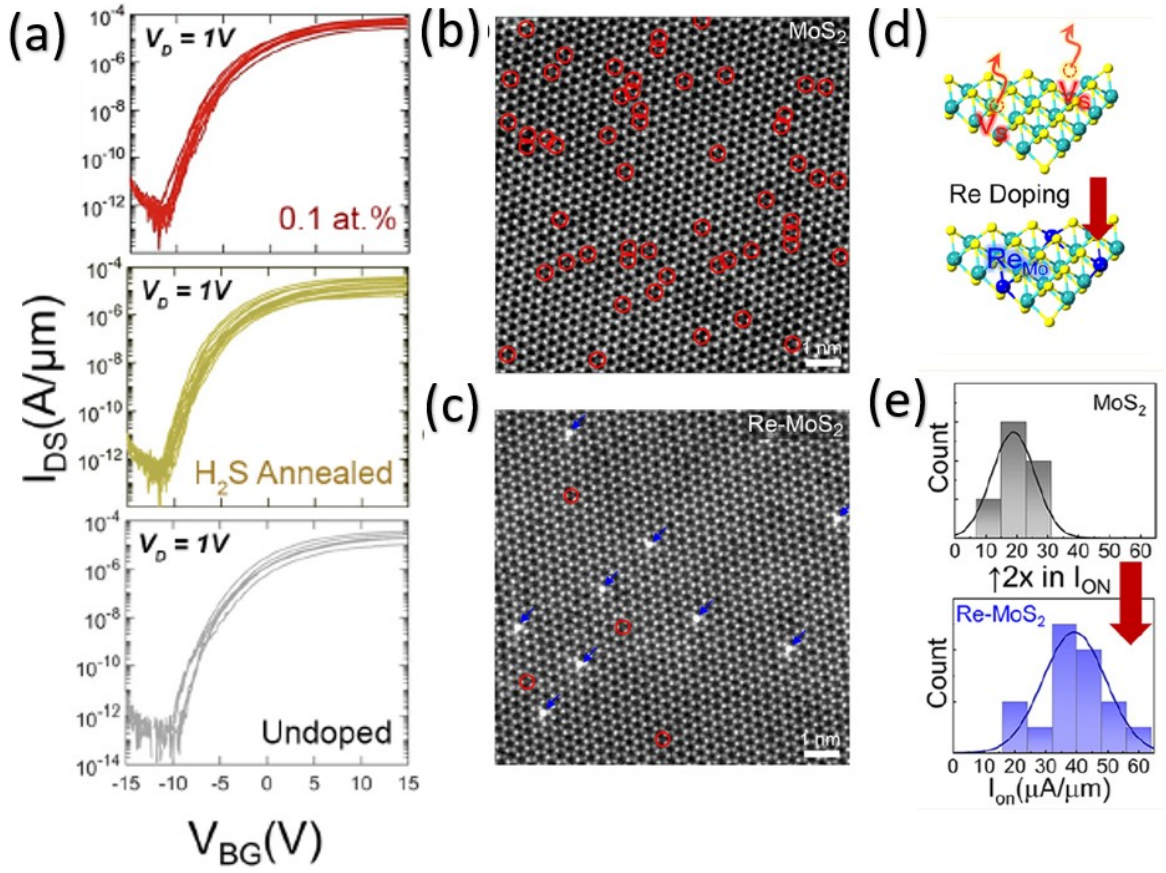

Figure 1.12: Impact of Rhenium Doping on MoS_2 Properties. (a) Transfer characteristics of undoped MoS_2, H_2S-annealed MoS_2, and 0.1 at.% Re-doped MoS_2 back-gated field-effect transistors showing improved drain current (I_{DS}) with Re doping. (b, c) High-resolution STEM images of sulfur site defects (marked in red circles) in undoped MoS_2 (b) and significant reduction of defect density in Re-doped MoS_2 (c) (marked in blue). (d) Schematic illustrating the suppression of sulfur vacancies (V_S) at MoS_2 edges due to Re substitution at Mo sites (Re_{Mo}). (e) Statistical analysis of on-state current (I_{ON}) highlighting a 2× improvement in Re-doped MoS_2 compared to undoped samples. Adapted from [67].

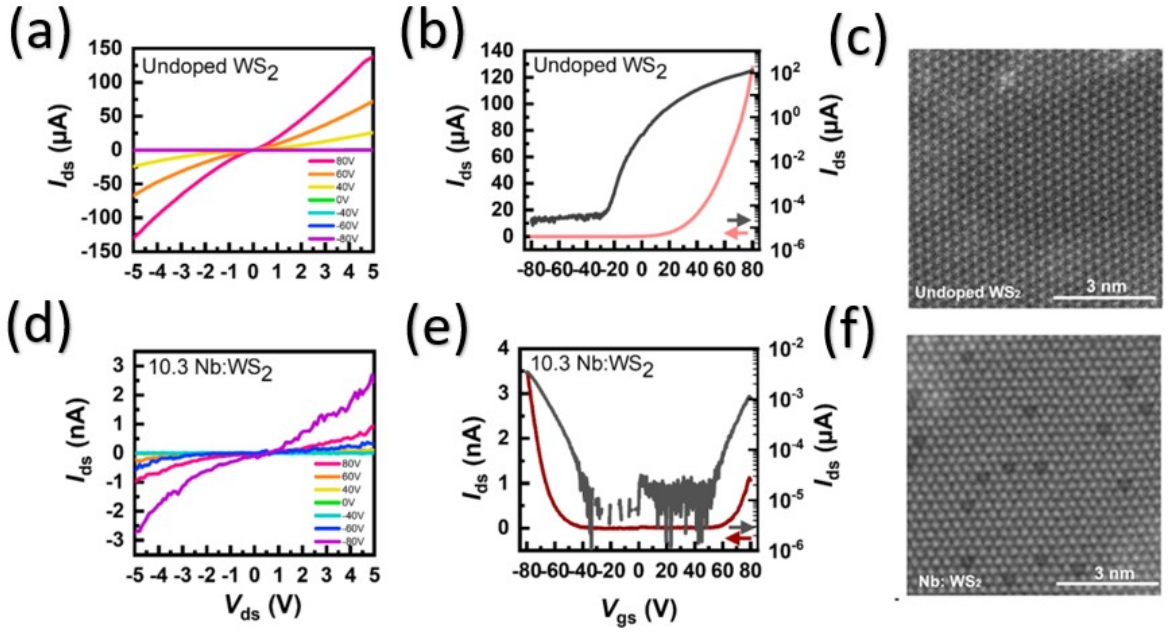

Figure 1.13: Impact of Niobium Doping on WS_2 Properties. (a) Output characteristics (I_{ds} vs V_{ds}) of an undoped WS_2 FET device showing strong n-type behavior. (b) Transfer characteristics (I_{ds} vs V_{gs}) of the same undoped device on linear and logarithmic scales. (c) High-resolution STEM image of undoped WS_2 showing hexagonally arranged tungsten atoms. (d) Output characteristics (I_{ds} vs V_{ds}) of a 10.3 at.% Nb-doped WS_2 FET device indicating the emergence of hole conductivity. (e) Transfer characteristics (I_{ds} vs V_{gs}) of the 10.3 at.% Nb-doped device, highlighting the n- to p-type crossover. (f) High-resolution STEM image of Nb-doped WS_2 showing sparsely distributed Nb atoms as substitutional dopants. Adapted from [87].

Figure 1.14: Schematic of Electrochemical Exfoliation. The setup includes two electrodes, an electrolyte, and a voltage source. TMD crystals are used as the working electrode, and depending on the chosen electrolyte, ions are forced to intercalate between the van der Waals layers of the crystal, causing expansion and leading to easy exfoliation [116].

Table 1.5: Summary of dopants for WS_2, their semiconductor type, doping method, and references.

Dopant	Type of Semiconductor	Doping Method	Reference
Niobium (Nb)	p-type	Substitutional	[89, 90]
Rhenium (Re)	n-type	Substitutional	[91]
Phosphorus (P)	n-type	Plasma immersion	[92]
Lithium (Li)	p-type	Intercalation	[93]
Fluorine (F)	n-type	Molecular doping	[80]
Chlorine (Cl)	n-type	Molecular doping	[80]
Sodium (Na)	p-type	Intercalation	[93]
Tungsten (W)	n-type	Substitutional	[91]
Aluminum Oxide (AlO_x)	n-type	Surface charge transfer doping	[94]
Nitrogen (N)	p-type	Plasma immersion	[92]

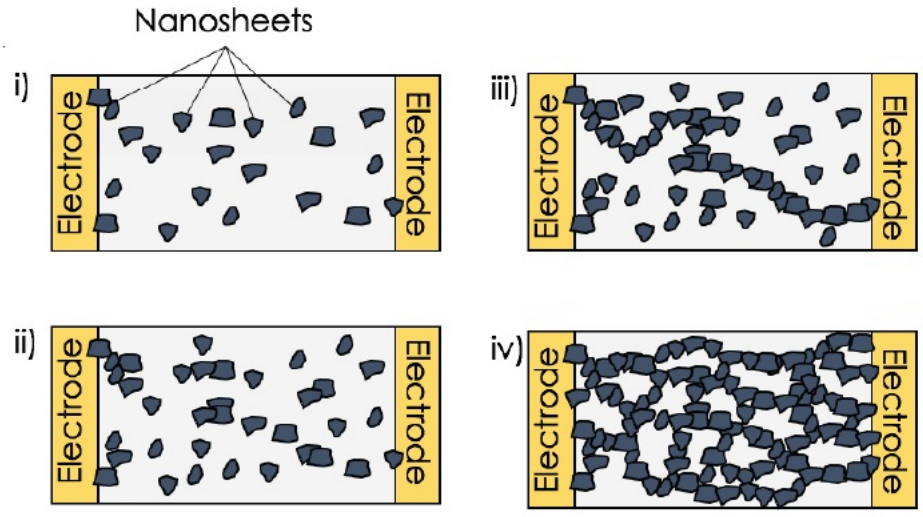

Figure 1.15: Schematic of percolation behavior in a TMD nanosheet network as additional layers are deposited: (i) Sparse nanosheet distribution with no conductive path; (ii) increased density with partial connections, still below the percolation threshold; (iii) formation of a continuous conductive pathway, marking the percolation threshold; (iv) densely packed network with overlapping nanosheets, exhibiting bulk-like conductivity. Adapted from [125].

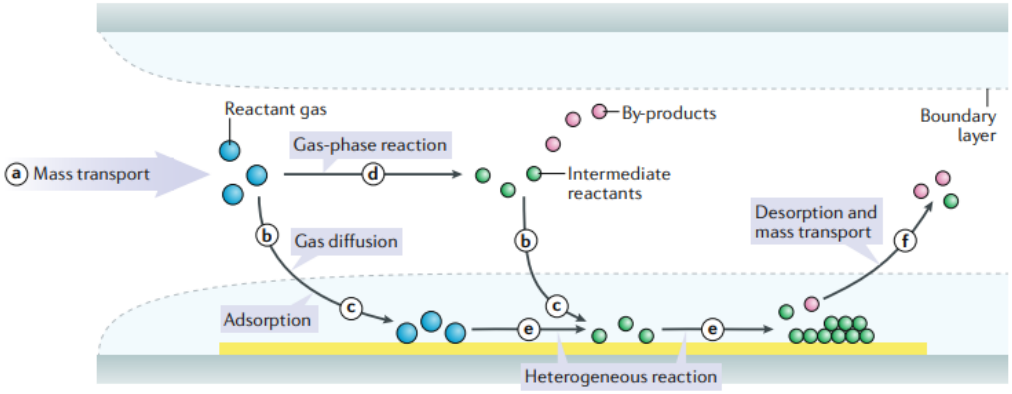

Figure 1.16: Schematic of a typical CVD process. Reactant gases (blue circles) are introduced into the reactor (step a). These gases either diffuse directly through the boundary layer (step b) to adsorb on the substrate (step c) or undergo gas-phase reactions, forming intermediates (green circles) and by-products (red circles) (step d). Intermediates diffuse to the substrate (step b), where surface diffusion and heterogeneous reactions occur (step e), forming thin films or coatings. By-products and unreacted gases are desorbed and expelled as exhaust (step f) [131].

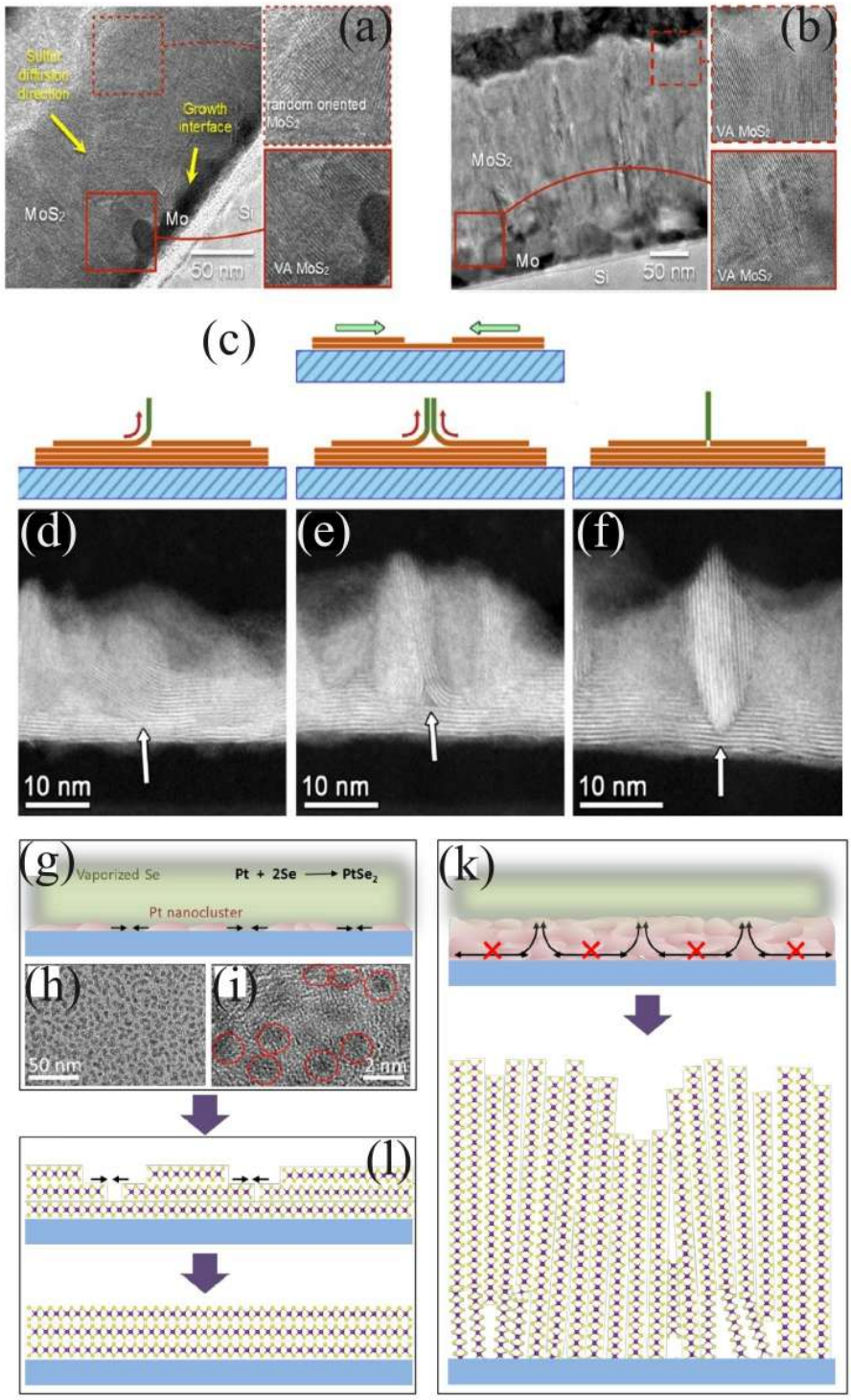

Figure 1.17: Structural and growth mechanisms of vertically aligned (VA) TMD films. (a), (b) TEM images of MoS_2 layers grown using the TAC method, showing the transition from random orientation to vertical alignment at the Mo substrate interface [143]. (c) Schematic representation of growth conditions influencing vertical alignment. (d), (e), (f) Cross-sectional TEM images showing the evolution of WS_2 growth from horizontal layers to vertically aligned nanowalls with increasing thickness and strain [150]. (g), (h), (i) $PtSe_2$ synthesis via TAC, demonstrating the conversion of Pt nanoclusters into vertically aligned $PtSe_2$ structures. (k), (l) Schematic of horizontal versus vertical growth modes, highlighting the role of strain and surface interactions in determining the orientation of low-dimensional TMD films [146].

2 | Experimental Methods

Introduction

In this section, the applied methods will be mentioned with the fundamental mechanisms of the techniques used.

2.1 Depositions

The Thermally Assisted Conversion (TAC) technique is pivotal in the transformation of transition metals into sulphide-based semiconductors. The process begins with the deposition of metal films, which serve as the precursor layers for subsequent conversion. In this thesis, several deposition techniques are explored, notably electron beam deposition and magnetron sputtering deposition. These methods are instrumental in laying down thin films of metal, referred to as the target material.

For the purposes of this study, a variety of transition metals including molybdenum (Mo), tungsten (W), titanium (Ti), rhenium (Re), niobium (Nb), and gold (Au) are utilized as targets. The deposition process is carried out under high vacuum conditions to ensure the purity and quality of the metal films. It is important to note that while Ti and Au are deposited as part of the metal films, their role is primarily to serve as contacts for device measurement. These metals are not converted into sulphide-based thin films but are essential for the functional integration of the devices.

The focus of the conversion process is on metals such as Mo, W, Re, and Nb. The prepared layered W-Nb and co-sputtered Mo-Re stacks are specifically used to convert to sulphide-based semiconducting films. These films are characterized by their van der Waals layered structure, classifying them under Transition Metal Dichalcogenides (TMDs). The deposition and conversion techniques described herein are critical to the successful synthesis of TMDs. The quality of the metal films directly impacts the structural and electronic properties of the final semiconducting layers, underscoring the importance of the initial metal deposition phase in the TAC technique.

2.1.1 Magnetron deposition

In magnetron sputtering, a magnetic field is applied to enhance the efficiency and control of the deposition process. The basic mechanism exploits the charge nature of ions, their behavior and velocity that can be controlled using a magnetic field [1]. The sputtering process requires a plasma in a high vacuum and a negative electronic bias on the target material to force positive ions into itself. Hence, the ions bombard the target material, freeing the atoms from the surface to the substrate. Meanwhile, the plasma is restrained by an array of magnets behind the target. To disintegrate these gas molecules into ions and electrons either radio-frequency (RF) or direct current (DC) power sources are employed. Both power sources exist in the Shamrock Sputtering System. Shamrock sputtering system consists of the cassette module (CM), transfer module (TM), and process modules known as Chamber B and Chamber A that are designed for depositing metal, thin, films. The compartments and what they include are shown in Figure 2.1.

Cassette Module (CM): This compartment contains a high vacuum loading rack that can hold 16 wafers.

Transfer Module (TM): The transfer module includes a robotic arm that allows transferring wafers from CM to Chamber A and Chamber B.

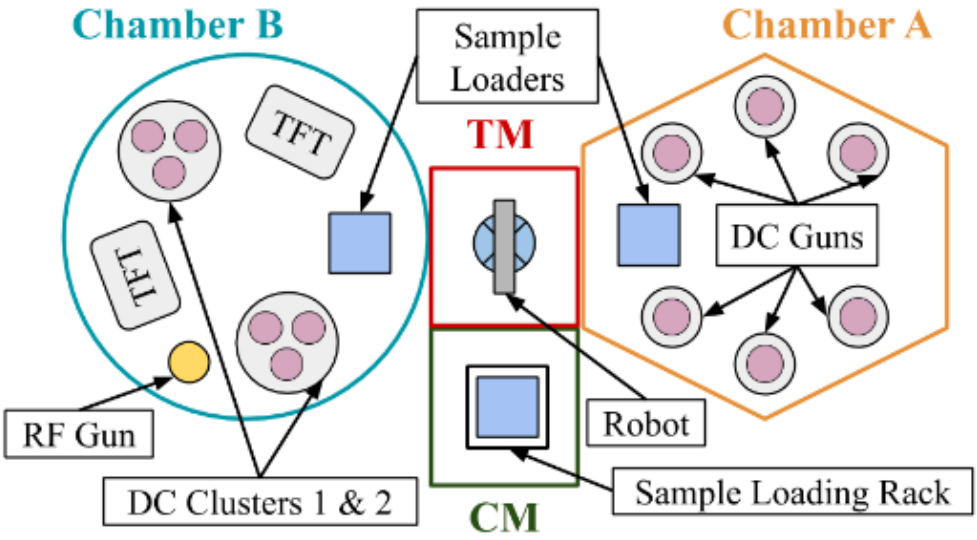

Figure 2.1: Schematic depicts the Shamrock Magnetron Sputtering System, which consists of two chambers (Chambers A and B), a Transfer Module (TM), and a Cassette Module (CM). The Cassette Module (CM) serves as the load-lock unit, where wafers or substrates are initially loaded. This ensures that substrates enter the vacuum environment without compromising the pressure in the deposition chambers. The Transfer Module (TM) is used to transfer wafers from the Cassette Module to the chambers, maintaining distinct pressure conditions between the loading area and the processing chambers. Within the chambers, both RF and DC guns are utilized. RF guns, operating at high frequencies (e.g., 13.56 MHz), are designed for sputtering insulating or dielectric materials by preventing charge buildup on the target. In contrast, DC guns are optimized for sputtering conductive materials by applying a constant direct current to the target, causing ionized gas particles to eject material for deposition. Additionally, the system features a TFT (Target Face to Target) configuration, where targets are positioned face-to-face, ensuring uniform material deposition and minimizing cross-contamination. Together, these components enable precise and controlled thin-film deposition for a variety of materials and applications [2].

Chamber A: It has a base pressure of 3x 10^{-7} Torr with a total of 6 DC magnetron guns. In the DC source chamber, the static electric field is applied between the target (cathode-negative charged) and the substrate (anode-positive charge) and then an inert gas is introduced into the chamber, high pressure is temporarily obtained to provide a reliable plasma over the target until the plasma is sustained. The positively charged ions in the plasma are directed toward the negatively charged target due to the applied static electric field. The positive ions bombard the target with a force to cause the ejection of atoms from the surface. The freed atoms are later, deposited on a substrate located above the target. One of the drawbacks of the DC

source is that it requires the target to be conductive; otherwise, charge builds up on the target. For this reason, the RF gun is preferred to deposit insulating films.

Chamber B: It has a base pressure of 1 x 10^{-8} Torr and contains 3 DC sputter guns and 2 RF sputter guns.

2.1.2 Electron Beam Evaporation

Thermal evaporation is a recognized technique for depositing a thin film wherein the source material is heated to evaporation in a vacuum. This process allows vapor particles to travel and directly adhere to a substrate, where they revert to a solid state [3]. The vacuum condition can be around 10^{-6} Torr to allow evaporation flow to coat the substrate and also supports evaporation of the metal target. This pressure range can be achievable with a combination of rough and cryo-pumps. As shown in Figure 2.2, the samples are placed onto a rotating stage above the crucible. The distance is arranged considering the mean free path of ejected material under a high vacuum.

The mechanism of the system boils down to taking advantage of thermionic emission. Thermionic emission refers to phenomena in which electrons are ejected from a heated metal when it is heated under vacuum by heating a filament to create electrons and then accelerating them until they obtain sufficient energy for evaporation of any materials. The evaporated material flow is directed to the substrate on the rotating stage [5]. The fundamental source of the electron beams (e-beams) in the system is pulled around to the target metal surface by a magnetic field. The magnetic field is shown pointing inward in the schematic in the Figure 2.2. Hence the Lorentz law is active to direct e-beams.

2.2 High Temperature Conversion/Furnace Process

Transition Metal Dichalcogenides (TMDs) such as MoS_2 were synthesized using a technique referred to as TAC, which involves exposure to chalcogen vapors under

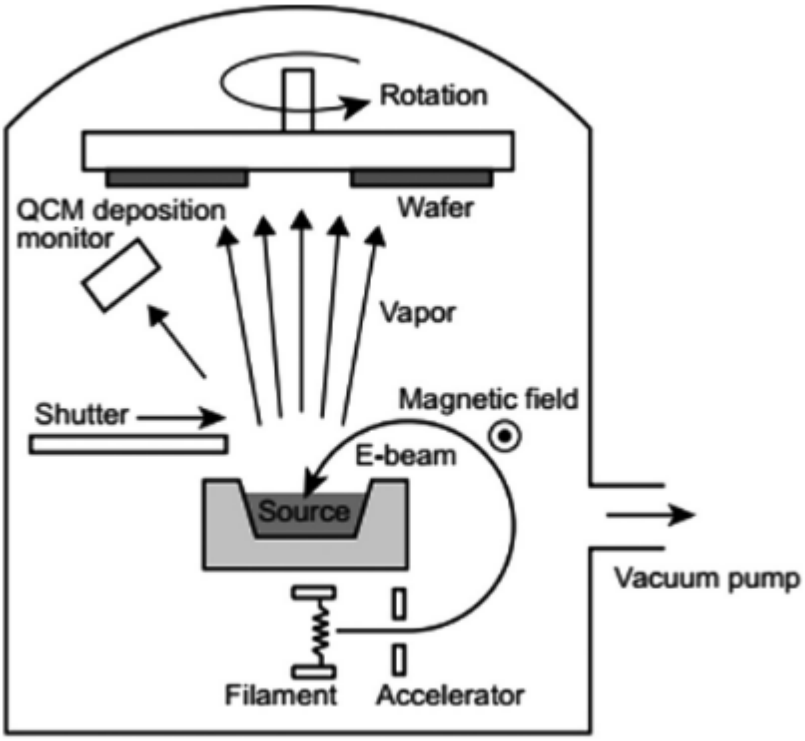

Figure 2.2: Schematic of a Temascal system. The distance between the substrate and the target metal is arranged considering the mean free path of ejected material under a high vacuum [4].

specific conditions. The method, detailed by Gatensby et al. [6], was adapted in our experiments as described below.

2.2.1 Preparation for Furnace Process

The substrates were positioned in the ceramic boat. The dimensions of the chips can be up to 2 cm in length, Figure 2.3 (a) The boat containing the chips was placed in the hot zone at the center of the quartz tube furnace, Figure: 2.3 (b) which was then heated to high temperature 900°C. Another ceramic boat filled with sulfur powder (MaTecK, 99%), Figure: 2.3 (c) was placed in a separately heated zone upstream from the sample boat, Figure 2.3 (d) shows the detailed diagram of the sulfur conversion furnace setup. The labeled sections include the sample loading port, Baratron pressure transducer, sliding track, cold trap, furnace, rough pressure gauge, halogen light assembly, gas inlet line, temperature controller, pressure controller, and mass flow controller (MFC).

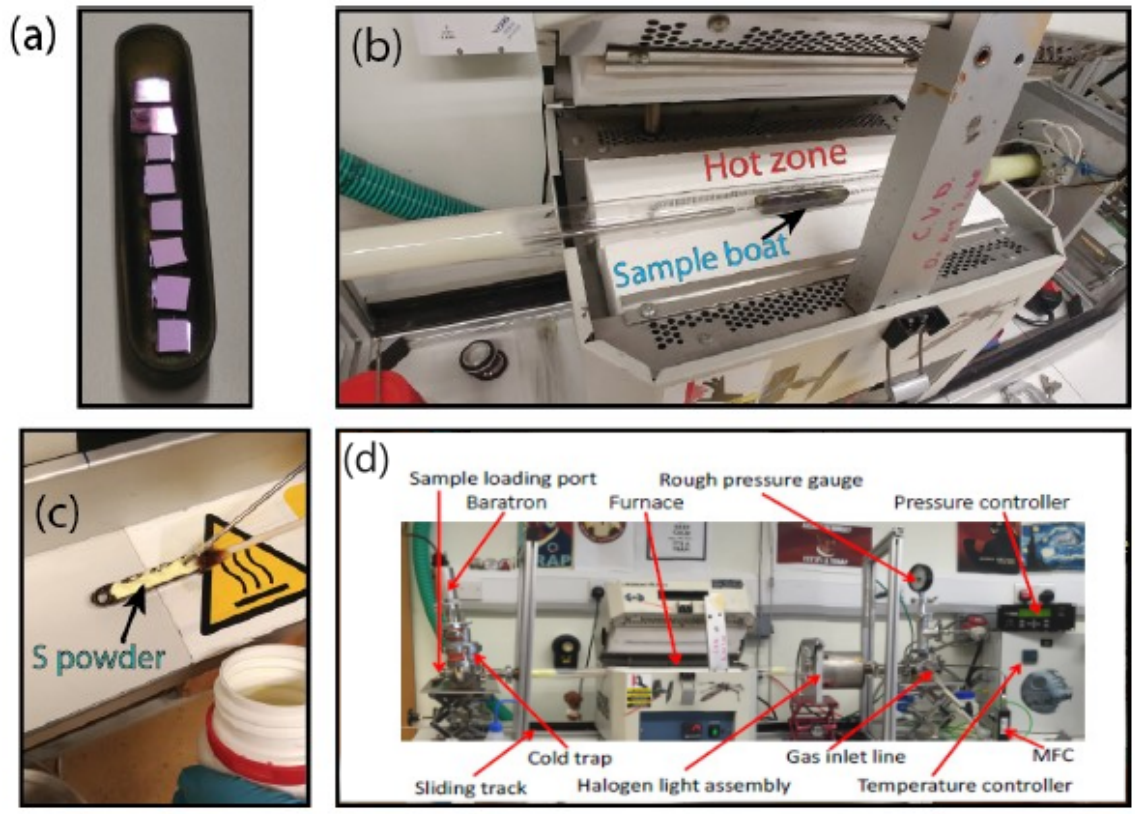

Figure 2.3: The image of the sulfur furnace used in this thesis with detailed sections of it [6].(a) A photograph of the SiO_2 substrates placed inside the ceramic boat before being inserted into the growth furnace. (b) A zoomed-in image of the growth furnace, showing the substrate in the ceramic boat positioned at the center of the furnace. (c) A photograph of a sulfur ceramic boat. The sulfur ceramic boat is placed inside the halogen light assembly to melt the sulfur powder, which is then transported by carrier gases to the growth furnace. (d) A detailed diagram of the sulfur conversion furnace setup. The MFC measures the gas flow rate, while the growth furnace pressure is monitored by a Baratron pressure transducer. The rough pressure gauge indicates a pressure range of 1–800 Torr. The rough pressure gauge is primarily monitored at two key stages. First, after placing the substrates into the furnace, before the conversion process begins, while lowering the pressure in the furnace. Second, after the conversion, just before removing the substrates, once the furnace has cooled down to room temperature. To safely remove the substrates, the pressure inside the furnace must be equalized with atmospheric pressure (760 Torr).

2.2.2 Conversion Process

The setup consists of a custom-built, one-zone quartz tube furnace. Once the growth region where thin films are located, reach the target temperature, the secondary heating zone was activated to melt sulfur powder, which was maintained at 135°C. The resultant sulfur vapor was directed towards the heated Mo films. The films

were exposed to the sulfur vapor for 30 minutes. Following this, the chalcogen heating was discontinued, maintaining the same pressure and flow rate, The substrate was then annealed at the growth temperature (900°C) for an additional 30 minutes. The boat is then cooled to room temperature by opening the furnace. A liquid nitrogen sheath is used to condense and collect excess sulfur vapor from the powder-heating zone, preventing over-saturation of the quartz tube with gaseous sulfur.

2.3 Raman Spectroscopy

This section introduces Raman spectroscopy and briefly discusses the underlying theory, adapted from Ferraro, Nakamoto, and Brown [7]. Raman spectroscopy is a powerful technique for exploring the vibrational states of compounds. It operates by measuring the inelastic scattering of light, which occurs when photons interact with phonons in the material. The technique involves shining a laser light at a specific wavelength onto a sample. The light scattered by the sample is then measured as Raman shifts, which indicate the difference in energy between the incident laser photons and the scattered photons. Raman spectra display peaks corresponding to the characteristic vibrational modes of phonons or molecular vibrations in the compound, plotted with intensity on the Y-axis and Raman shift/wavenumber (cm^{-1}) on the X-axis. Wavenumber is inversely related to wavelength and directly proportional to energy [8].

When a monochromatic laser beam interacts with a crystalline sample, most photons scatter elastically, retaining their original energy, in a process known as Rayleigh scattering. However, a small fraction of photons undergo inelastic scattering, exchanging energy with the vibrational or phonon modes of the material. This interaction results in a shift in the energy of the scattered photons, known as the Raman effect, which corresponds to either a gain (anti-Stokes) or loss (Stokes) of energy, as shown in Figure 2.4. Unlike fluorescence or phosphorescence, Raman scattering

does not involve the absorption of light or excitation of the sample to an electronic excited state. The Raman shift provides detailed insights into the vibrational modes and structural characteristics of the sample.

For Raman-active compounds, the incoming photon interacts with the sample's electronic cloud, causing a temporary distortion in the polarizability of the molecule or lattice. This interaction leads to inelastic scattering, where the scattered light has a frequency different from the incident light due to vibrational energy exchanges. This energy shift can be represented mathematically [9]:

$$\Delta\tilde{\nu} = \frac{1}{\lambda_0} - \frac{1}{\lambda_1} \tag{1}$$

For instance, considering a 532 nm laser, the energy of the incident photons is calculated using the relationship

$$E = \frac{hc}{\lambda}.$$

Given the wavelength $\lambda = 532 \times 10^{-9}\,\mathrm{m}$, and substituting the values for Planck's constant ($h = 6.626 \times 10^{-34}\,\mathrm{J{\cdot}s}$) and the speed of light ($c = 3 \times 10^{8}\,\mathrm{m/s}$), the photon energy is:

$$E = \frac{(6.626 \times 10^{-34}\,\mathrm{J{\cdot}s}) \cdot (3 \times 10^{8}\,\mathrm{m/s})}{532 \times 10^{-9}\,\mathrm{m}} = 2.33\,\mathrm{eV}. \tag{2}$$

This corresponds to approximately $3.73 \times 10^{-19}\,\mathrm{J}$, converted to 2.33 eV using the conversion factor $1\,\mathrm{eV} = 1.602 \times 10^{-19}\,\mathrm{J}$. While this energy represents the full energy of the incident photons, the Raman effect involves only small energy shifts relative to this value. For example, a Raman shift of 408 cm^{-1} corresponds to approximately 50 meV ($\sim 0.05\,\mathrm{eV}$), which is much smaller than the laser energy. These shifts, caused by interactions with vibrational or phonon modes in the material, provide critical insights into properties such as crystallinity, impurity levels, and structural effects like thickness dependencies [10]. The rest of the energy remains with

the scattered photon. Hence, it is not released or converted to another form.

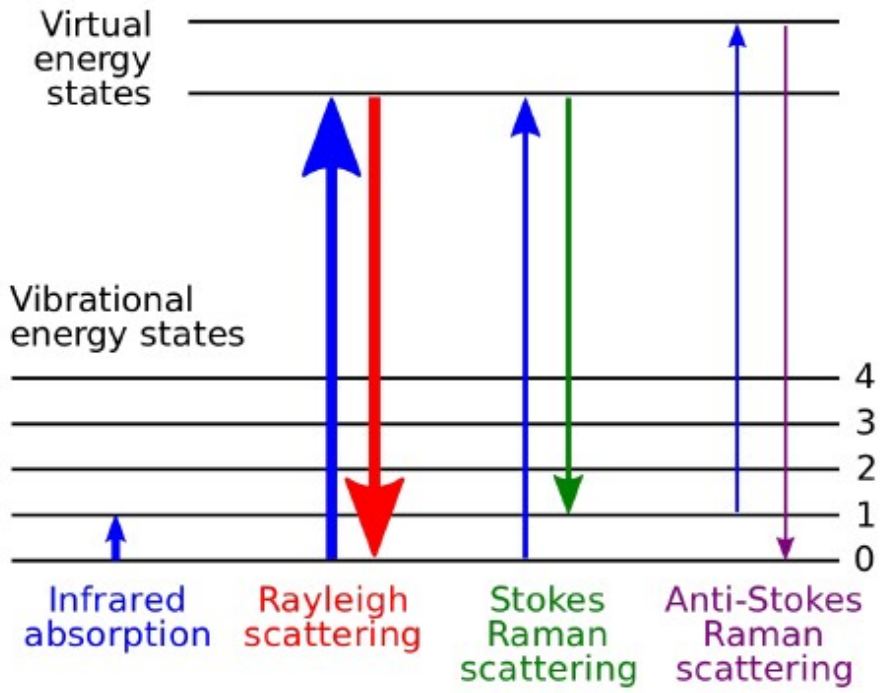

Figure 2.4: Schematic of a Jablonski diagram illustrating the Raman scattering process [11].

The Raman selection rule dictates that for a vibration mode to be Raman active, the derivative of the polarizability with respect to the normal coordinate of the vibration must be non-zero [12]. This is what distinguishes Raman spectroscopy from other optical techniques like Infrared (IR) spectroscopy, which measures absorption due to changes in the molecular dipole moment. Raman spectroscopy, instead, is sensitive to changes in polarizability, making it particularly useful for analyzing non-polar molecules.

The procedure for analyzing Raman spectroscopy results used in this thesis is as follows:

1. Baseline correction is applied to eliminate background noise.
2. Peaks are normalized to substrate peaks to facilitate comparison between different data sets.
3. Lorentzian fitting is generally not used when dealing with bulk-type TMD

films, as the focus is on distinguishing up to four layers. Beyond that, the sample is considered bulk, and additional fitting does not provide further useful information.

2.4 Uv-Vis Spectroscopy

UV-Vis Spectroscopy is a technique that serve to measure the absorption and scattering effects of the matter. Absorption here refers to absorbing light energy. Scattering, on the other hand, refers to deflection of light in various direction due to interaction with the matter. Absorption is critical when the matter experience electronic transitions excluding the cases where absorption takes place without electronic excitation of the matter. So, only energies of the light equal and higher than the band gap of the matter get absorbed. Consequently, the method provides information about the electronic structure such as optical band gap of the compounds.

In the spectrophotometer, the light is separated into discrete wavelengths using a monochromator consists of a series of slits, mirrors and diffraction gratings as pictured in Figure 2.5.

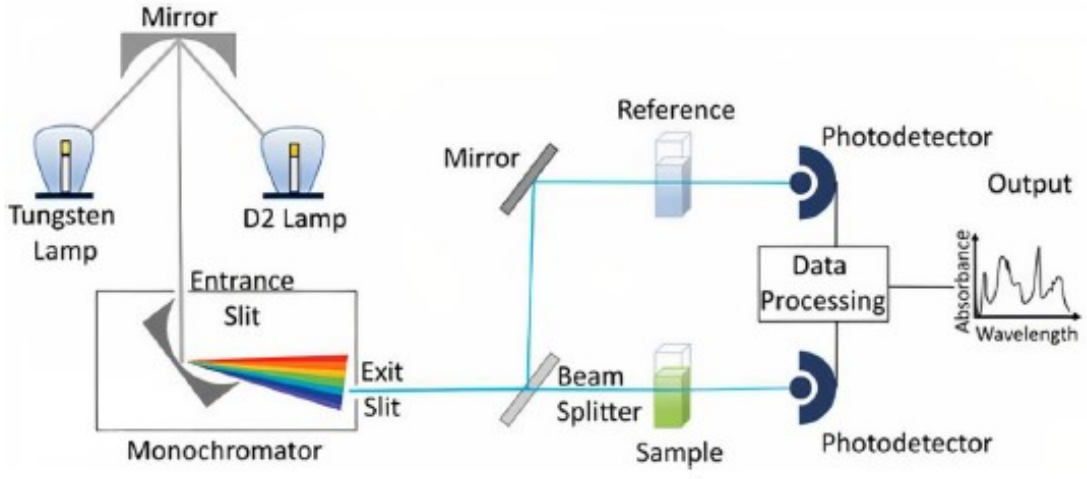

Figure 2.5: A schematic of dual-beam UV-Vis spectrophotometer [13].

These wavelengths involves the range of Ultraviolet (UV) region wavelengths from 10 nm to 400 nm, Visible (Vis) region wavelengths from 400 nm to 700 nm. In the

system, the beam is split, permitting both the sample and a reference to be analysed concurrently, allowing for accurate measurements through the removal of scattering and absorption in both the sample and the reference. The reference, here, can be a cuvette for liquid samples such as electrochemically exfoliated TMD films.

The difference between the incident radiation and the transmitted radiation represents the amount of light absorbed by the material. The concept of transmittance quantifies the fraction of incident light that successfully passes through the sample. The mathematical expressions for transmittance are given by:

$$T = \frac{I}{I_0} \tag{3}$$

and as a percentage,

$$\%T = \left(\frac{I}{I_0}\right) \times 100 \tag{4}$$

Absorbance, on the other hand, is a measure of the light absorption and is calculated using the logarithm of the inverse of transmittance:

$$A = -\log(T) \tag{5}$$

Briefly, absorbance and transmittance measurements are crucial for determining the concentration of substances and understanding their properties by quantitatively analyzing how much light a sample absorbs or transmits.

2.5 X-Ray Diffraction

X-Ray diffraction (XRD) is an analytical technique used to characterise crystalline materials. When X-rays interact with a crystalline sample, they undergo reflection, diffraction, scattering, and transmission. In XRD, the fundamental interactions between electromagnetic waves and matter are governed mainly by two mechanisms: Thomson scattering and wavelength matching. Thomson scattering provides the

basic scattering mechanism that involves the specular reflection of photons off the atomic planes within the crystal. The photons do not lose energy during the interaction as the process is elastic. It allows X-rays to be diffracted by the electron clouds of the atoms in the crystal. Without this scattering process, the X-rays would pass through the crystal without interacting with atoms.

Wavelength matching, the wavelength of X-rays are on the same order of magnitude as the interatomic distance within crystals (0.15 - 0.5 nm). This similarity facilitates diffraction as the X-rays interact constructively or destructively with the electron clouds of atoms, influenced by their characteristic crystal plane spacing. The interaction of X-rays with the electrons in a crystalline structure results in scattering, which redirects the X-rays in various directions. Specific scattering events that follow the conditions for constructive interference obey Bragg's law 6:

$$n\lambda = 2d_{hkl} \sin\theta \tag{6}$$

Bragg's law simply implies that the distance between the scattered X-rays is equal to the integer then diffraction occurs constructively. This constructive interference results in peaks in the diffraction spectra. These peaks provide a fingerprint of the crystal structure. Further, analyzing these peaks' positions and intensities reveals details such as atomic arrangement and crystallinity of the materials [14].

The critical point to know about diffraction methods is that there are two types: in-plane and out-of-plane. The common method, used in this thesis, is out-of-plane diffraction, as shown in Figure 2.6. This method only probes the diffraction planes whose normal are perpendicular to the sample surface due to $2\theta/\omega$ configuration.

XRD relies on periodicity, one can wonder how to analyse amorphous films with XRD. An amorphous film generally fails to meet the periodicity condition; however, it might possess short-range order of periodicity, resulting in large and low inten-

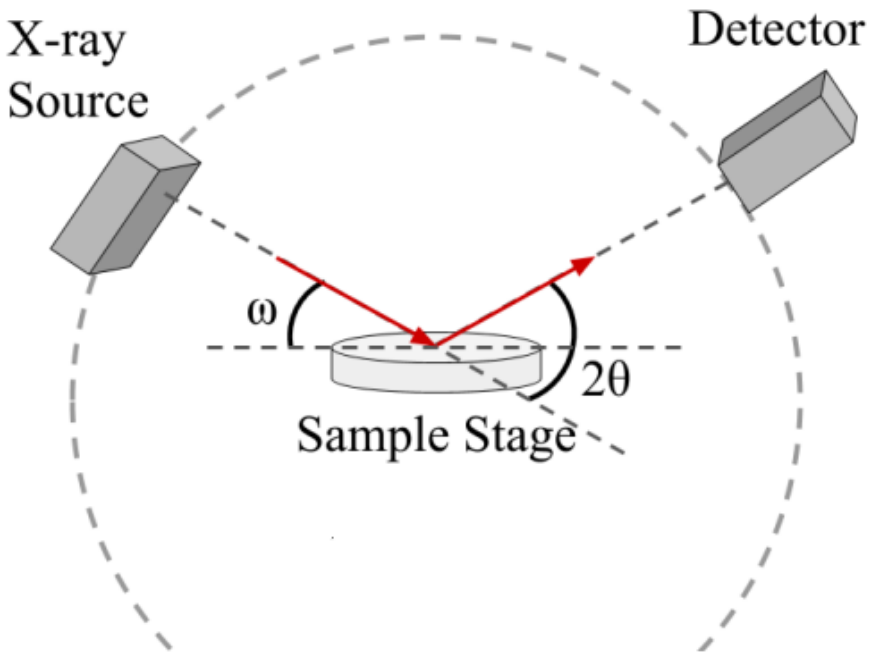

Figure 2.6: Schematic of Bragg Brentano configuration of X-Ray Diffractometry. In this traditional configuration, the detector moves to record the diffracted X-rays at an 2θ angle from the incident beam. The image is adapted from the Ref: [2].

sity peak or peaks. Regardless, amorphous materials can be considered as hard to analyse.

2.6 X-Ray Reflectivity

X-ray reflectivity (XRR) is a method used to study films' properties such as thickness, interface roughness, surface roughness, and density. These films can be amorphous or crystalline and may have single or multiple layers. XRR works by examining how X-rays interact with matter, a process described by Snell's Law. Snell's Law explains how electromagnetic waves change direction when transitioning between two media with different refractive indices [15].

In the context of XRR, n_a and n_b represent the refractive indices of the first and second media, respectively. These media could include the ambient environment (e.g., air, where $n_a \approx 1$) and the thin film material ($n_b < 1$ for X-ray wavelengths). The angles θ_a and θ_b correspond to the angles of incidence and refraction, respectively,

measured relative to the surface normal. Snell's Law relates these parameters as follows:

$$n_a \sin\theta_a = n_b \sin\theta_b \tag{7}$$

When X-rays hit an interface between two media with different refractive indices, they are partly reflected and partly refracted. At a specific angle, known as the critical angle (θ_{critical}), the refracted ray travels parallel to the interface ($\theta_b = 90^\circ$). This angle is determined by the density (ρ) of the material and provides essential information about the film's composition. Beyond the critical angle, X-rays penetrate the material and reflect off multiple internal interfaces, generating interference patterns.

These reflections create periodic oscillations in the reflectivity as a function of the incidence angle (2θ), as shown in Figure 2.7. These oscillations result from constructive and destructive interference and fade at higher angles due to X-ray absorption and roughness effects.

Key features of XRR measurements are:

- **Critical angle (θ_c)**: The reflectivity drop near the critical angle depends on the material's density (ρ).
- **Oscillation period ($\Delta\theta$)**: The spacing between oscillation peaks reveals the film thickness (d), with regular peaks indicating multiple layers.
- **Oscillation decay rate**: The rate at which oscillations diminish at higher angles corresponds to surface or interface roughness (σ).
- **Amplitude of oscillations**: The amplitude reflects the density contrast between adjacent layers.
- **Intensity decay at higher angles**: Surface roughness further contributes to the intensity decay of reflected X-rays.

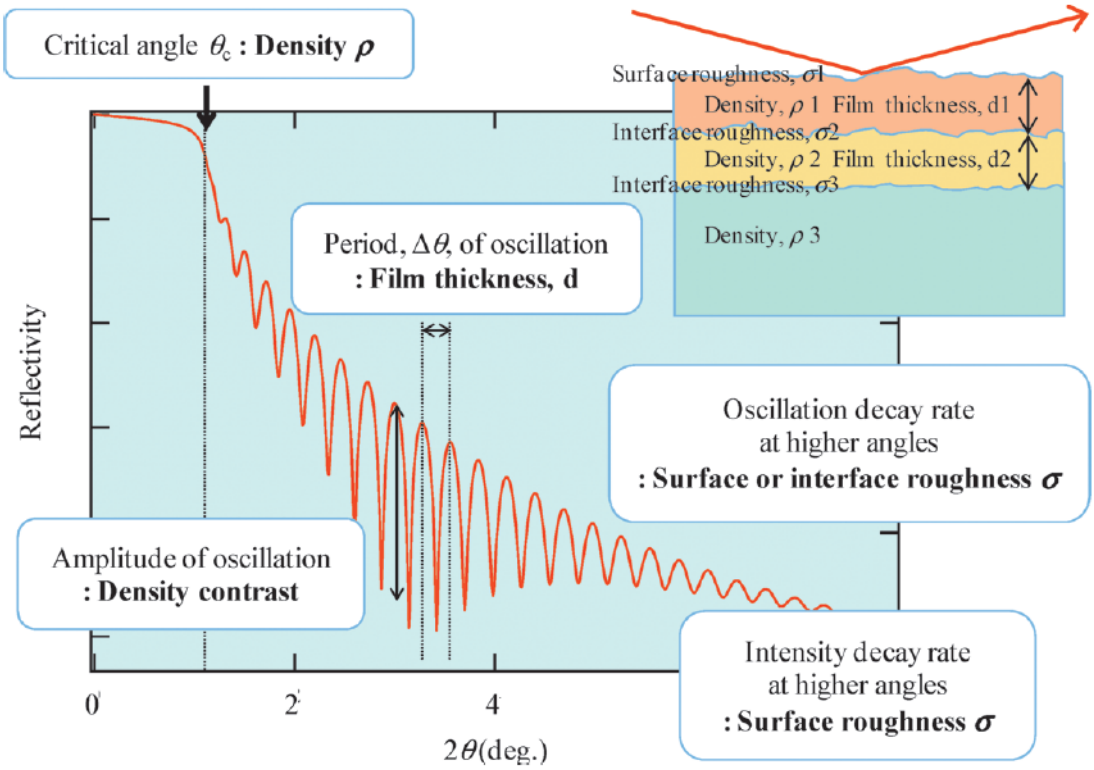

Figure 2.7: The XRR reflectivity curve shows key features used to analyze thin films. The critical angle (θ_c) corresponds to the material density (ρ), the oscillation period ($\Delta\theta$) reflects film thickness (d), and the oscillation decay rate indicates surface or interface roughness (σ) [16].

By analyzing these features, XRR enables precise determination of film properties such as density, thickness, and roughness, providing insights into the structural characteristics of thin films. Briefly, from a XRR scan, fundamental information can be obtained:

- Electron density: The critical angle relates to the material's electron density. If two adjacent layers have similar density values, like W and Mo, distinguishing signals and fitting the pattern is challenging. Thus, for thickness calibration to verify sputtering rates, using a substrate with a different density than the material of interest is helpful.

- Thickness: The thickness is inversely proportional to the oscillation frequency.

- Surface and interface roughness: The intensity of reflected X-rays and the oscillation decay rate at higher angles correlate to the layers' surface and inter-

face roughness. Rougher surfaces and interfaces scatter X-rays more, causing a steeper intensity drop at higher angles. Therefore, rougher films cannot be analyzed with this technique due to the absence of oscillations.

It is important to understand that the penetration depth of X-rays varies with the incident angle, which significantly influences X-ray Reflectivity (XRR) spectra. At lower 2θ angles, where the incident angle ω is smaller, the X-rays have a shallower penetration depth, affecting a larger surface area of the sample. Conversely, at higher 2θ angles, the incident angle increases, allowing the X-rays to penetrate deeper into the sample, although covering a smaller surface area [17]. This variation in penetration depth based on the incident angle is crucial for analyzing surface parameters such as roughness and density, which are prominently observed in XRR spectra at lower angles. For instance, the significance of surface roughness is demonstrated in Figure 2.8.

Figure 2.8(a) shows the XRR spectrum for pristine MoS_2, where the fitting becomes challenging due to the high surface roughness. In contrast, Figures 2.8(b) and 2.8(c) illustrate the XRR spectra of a deposited Mo layer with a significantly lower roughness of 0.65 nm, where a clear fit was achieved in graph (c). These results underscore the importance of minimizing surface roughness to enable reliable XRR fitting and accurate determination of film parameters.

In this thesis, the XRR analysis was performed by fitting the experimental reflectivity curve, as seen in Figure2.8 (c), to a theoretical model using the GenX software [18]. The thickness, roughness, and density of each layer were determined by optimizing the model parameters to minimize the difference between the simulated and experimental data. The thickness was extracted from the oscillation period, roughness from the oscillation decay, and density from the critical angle and oscillation amplitude.

In order to fit the reflectivity curve, important step is to know the GENX density. The following explanation is given with Molybdenum example which is the host

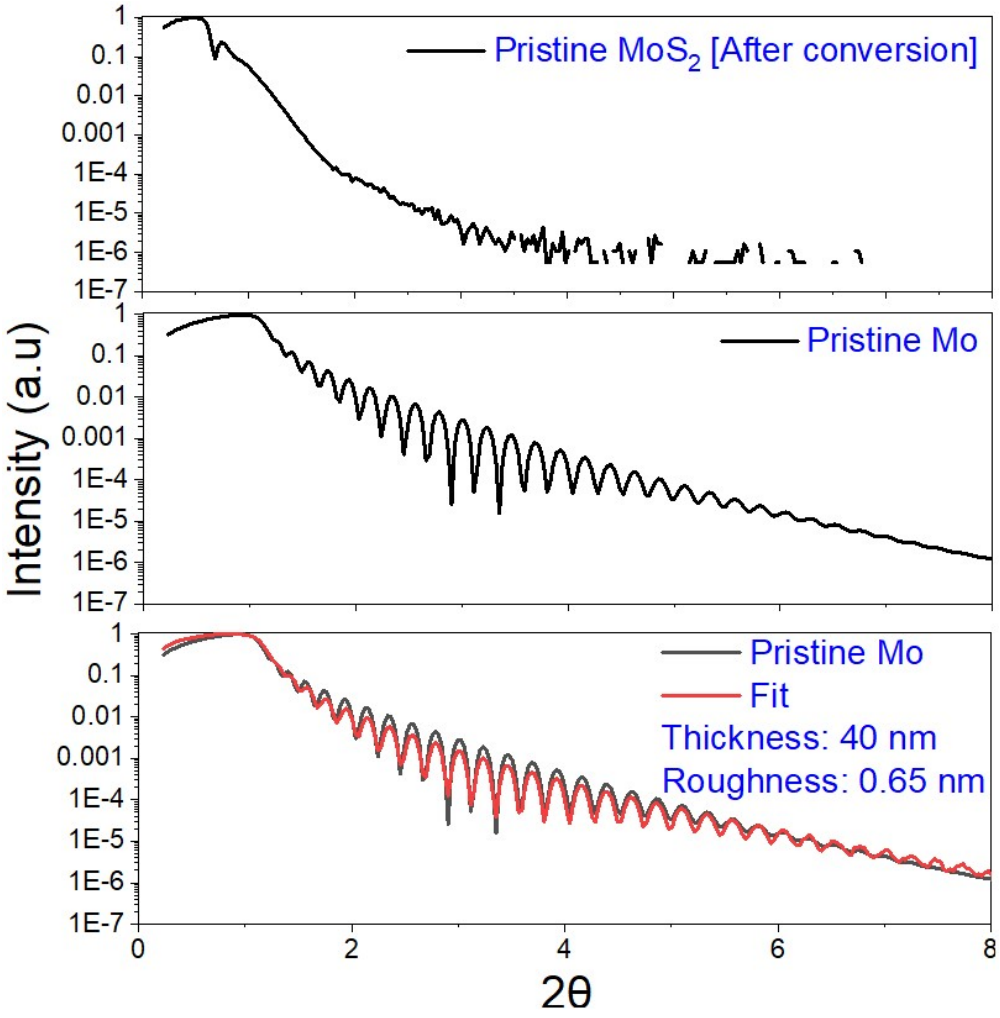

Figure 2.8: Three examples of XRR results illustrating the impact of film roughness on fitting accuracy. Panel (a) shows the XRR data for pristine MoS_2 after conversion, where fitting becomes challenging due to the lack of diffusely scattered X-rays from a rough film. As the coherence of reflected X-rays is disrupted, and the signal-to-noise ratio decreases. (a) The thickness of MoS_2 was determined to be 40 nm based on AFM characterization, with the roughness discussed in Appendix A1.8. (b) and (c) show the XRR results for the deposited Mo layer, with a roughness of 0.65 nm as determined by fitting.

element of the next chapter. It can be calculated as follow:

Step 1: Start with Real Density (ρ)

Real density in $\mathrm{g/cm^3}$ (e.g., $\rho = 10.28\,\mathrm{g/cm^3}$).

Step 2: Convert to $\mathrm{kg/m^3}$

$$\rho_{\mathrm{kg/m^3}} = \rho \times 1000 \tag{8}$$

Step 3: Identify Atomic Mass (u_{scatt})

Use atomic/molecular weight in g/mol (e.g., $u_{\text{Mo}} = 95.95\,\text{g/mol}$).

Step 4: Apply GenX Formula

$$\text{GenX Density} = \frac{\rho_{\text{kg/m}^3}}{1.66054 \times 10^3 \times u_{\text{scatt}}} \tag{9}$$

Step 5: Example (Molybdenum)

$$\rho_{\text{real}} = 10.28\,\text{g/cm}^3 \quad \rightarrow \quad \rho_{\text{kg/m}^3} = 10280 \tag{10}$$

$$\text{GenX Density} = \frac{10280}{1.66054 \times 10^3 \times 95.95} \approx 0.0645 \tag{11}$$

The constant 1.66054×10^3 ensures that the atomic weight (u) in g/mol is properly scaled to work with the mass density (ρ) in kg/m^3, allowing for the calculation of the number density in scatterers per unit volume. Scatterers refer to atomic or molecular units within the material. For a pure element like molybdenum, a scatterer corresponds to a single atom, whereas for a compound like MoS_2, a scatterer represents a formula unit (e.g., one Mo atom and two S atoms). The number of scatterers per unit volume ($n_{\text{scatterers}}$) is calculated using the relationship $n_{\text{scatterers}} = \frac{\rho \cdot N_A}{u}$, where N_A is Avogadro's number (6.022×10^{23} atoms/mol). This links the macroscopic density of a material to its atomic-scale composition, providing the number of atomic or molecular units per unit volume, which is essential for X-ray reflectivity fitting [18, 19].

2.7 Electrical Characterization

Understanding the electrical properties of TMD films can be challenging due to the impact of contact resistance. This resistance can mask the true behavior of the TMD films, making it difficult to assess their intrinsic properties accurately during device measurements.

In practice, it is standard to check if the contacts exhibit ohmic behavior, which is defined by a linear relationship between current and voltage, or Schottky behavior, where this relationship is nonlinear. Ohmic contacts are ideal as they follow Ohm's law, $V = IR$, where V is voltage, I is current, and R is resistance. This linearity ensures efficient energy transfer and minimal loss in electronic devices. In contrast, Schottky contacts, which create a potential barrier at the metal-semiconductor junction, do not have a linear I-V relationship and are useful in devices like diodes where rectifying behavior is needed [20]. The sections that follow will delve into 2-Point Probe (2PP), 3-Point Probe (3PP), and 4-Point Probe measurements with Van der Pauw (VdP) configuration techniques.

2.7.1 2-Point Probe (2PP) Measurement

The 2PP by using two pairs of probes: one pair to source or measure the current and another to sense the voltage difference. The current is injected through the outer probes, and voltage is measured across the inner probes, ensuring that the voltage measurement is not influenced by the contact resistance, as shown in Figure 2.9.

In the 2PP configuration, a single source-measure unit (SMU1) is used to apply a drain-source voltage (V_{ds}) across the channel and measure the resulting current (I_{ds}). The positive terminal of SMU1 is connected to the drain, while the negative terminal is connected to the source, which is grounded. The gate electrode is left floating, meaning no gate voltage (V_{gs}) is applied to the device. This configuration measures the total resistance of the device, which includes contributions from both the channel and the contact resistances. The current through the channel, assuming linear Ohmic behavior, can be expressed as:

$$I_{ds} = \frac{V_{ds}}{R_{ch}}, \tag{12}$$

where R_{ch} is the total resistance of the device, given by:

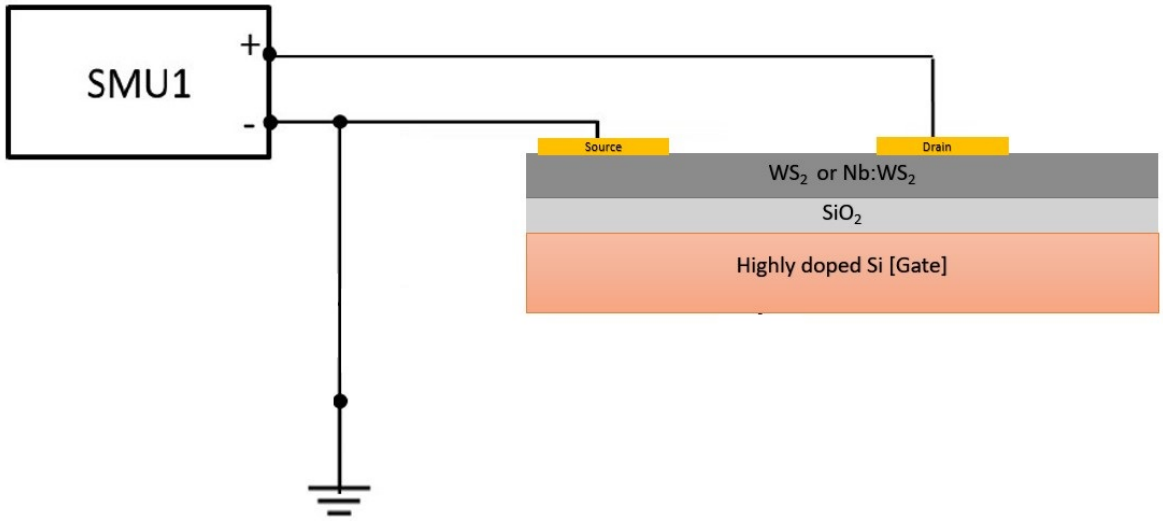

Figure 2.9: Schematic of 2-point probe (2PP) configuration: SMU1 applies a voltage (V_{ds}) between the drain (positive terminal) and source (negative terminal, grounded) while measuring the current (I_{ds}). This setup captures the total resistance of the device, including channel and contact resistances, with the gate left floating. The grounding of the negative terminal is primarily to establish a reference point, and it could also be the positive terminal depending on the configuration.

$$R_{ch} = R_{contact} + R_{channel}. \tag{13}$$

Here:

- $R_{contact}$ represents the resistance at the metal-semiconductor interfaces.
- $R_{channel}$ is the intrinsic channel resistance, which depends on the material properties of WS_2 or Nb:WS_2.

Without a gate voltage, the channel resistance is governed primarily by the intrinsic carrier concentration in the semiconductor, which depends on the material's doping level and temperature. This method is straightforward for characterizing the baseline conductivity of the material but does not allow control over the carrier concentration.

2.7.2 3-Point Probe (3PP) Measurement

The 3PP (three-point probe) measurement utilizes two Source Measure Units (SMUs) for electrical characterization, as shown in Figure 2.10:

- **SMU1** applies a voltage (V_{ds}) between the source and drain terminals and measures the resulting current (I_{ds}).
- **SMU2** applies a gate voltage (V_{gs}) to the gate terminal, with its negative terminal grounded to the source.

The gate voltage induces an electric field across the SiO_2 dielectric, modulating the carrier density in the semiconducting channel (e.g., WS_2 or Nb:WS_2) via the field effect. This setup enables the study of the transistor-like behavior of the device by controlling the carrier concentration in the channel.

From the measured data, the field-effect mobility (μ) of the channel can be extracted using the following equation:

$$\mu = \frac{L}{WC_{ox}V_{ds}} \frac{\partial I_{ds}}{\partial V_{gs}},$$

where:

- L is the length of the channel, which is the distance between the source and drain terminals.
- W is the width of the channel, representing the active area where current flows.
- C_{ox} is the gate capacitance per unit area, which depends on the dielectric properties and thickness of the SiO_2 layer. It is calculated as:

$$C_{ox} = \frac{\epsilon_{ox}}{t_{ox}},$$

  where ϵ_{ox} is the permittivity of the SiO_2 layer, and t_{ox} is its thickness.

- V_{ds} is the drain-source voltage applied across the channel to drive the current.

- $\frac{\partial I_{ds}}{\partial V_{gs}}$ is the slope of the transfer curve in the linear region, which reflects the sensitivity of the drain current (I_{ds}) to changes in the gate voltage (V_{gs}).

This configuration provides a robust method to extract key electronic parameters, such as mobility (μ), which characterizes the ability of charge carriers to move through the semiconducting channel under the influence of an electric field.

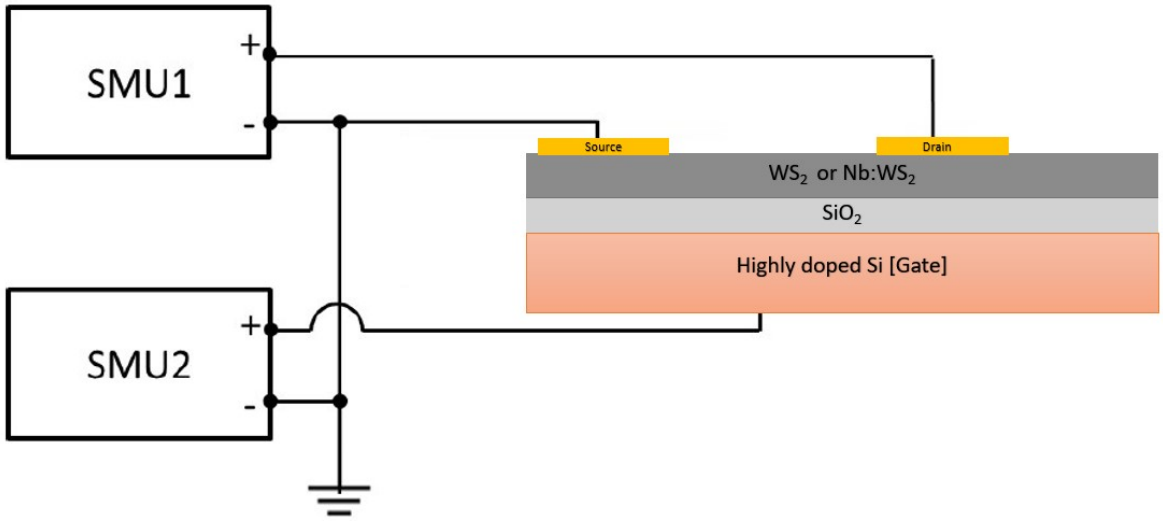

Figure 2.10: 3-point probe (3PP) configuration: SMU1 applies a voltage (V_{ds}) between the drain (positive terminal) and source (negative terminal, grounded), while SMU2 applies a gate voltage (V_{gs}) to modulate the carrier concentration in the channel. The gate (highly doped Si) is connected to the positive terminal of SMU2, with its negative terminal grounded. Grounding the source serves as a common reference point for both V_{ds} and V_{gs}, enabling independent control of the drain current (I_{ds}) and gate field. This setup allows for the extraction of key parameters such as mobility and threshold voltage.

Following sections will further explore 4PP techniques, such as using the Van der Pauw configuration, which simplifies the measurement process by not requiring patterning or lithography techniques, as the contacts are placed on the edges of the film on the substrate, allowing for easy extraction of material properties such as resistivity and sheet resistivity [21].

2.7.3 4-point probe measurements with VdP

The Van der Pauw (VdP) method is a simple method of measuring the resistivity of thin films. This is a another where the contacts are around the perimeter of the sample [22]. Most films used in this configuration, are either square or rectangular in shape so the contacts are always placed in the corner of the sample as the schematic in Figure 2.11. The advantages of van der Pauw configuration include:

- Four contacts are necessary.
- There is no need to measure sample widths or length between contacts.
- Simple geometries can be used.

For the measurements, the most common approach involves applying a current through two leads and measuring the voltage drop between the other two leads. Since the samples typically have multiple contacts as is depicted in Figure 2.11, and the current source and voltmeter can be connected in various combinations. If a current is passed from contact 1 to contact 2 (I_{12}), and a voltage drop is concurrently measured between contact 4 and contact 3 (V_{43}) as the schematic is presented in the left image of Figure 2.11, a resistance can be calculated using Ohm's Law:

$$R_{12;43} = \frac{V_{43}}{I_{12}} \tag{14}$$

This is the one resistance along the horizontal direction. To increase the accuracy, the same measurement is performed with the same current of reversed polarity (I_{21}) and also along the opposite edge, meaning current directions is reversed, so the voltage drop will be measured from (V_{34}).

This repetition minimizes errors due to resistance of the contacts and the inhomogenities in the grown TMD films to provide a more accurate representation of the material's true resistivity or conductivity. Then all of the resistances are averaged over. What it is meant by horizontal and vertical resistances:

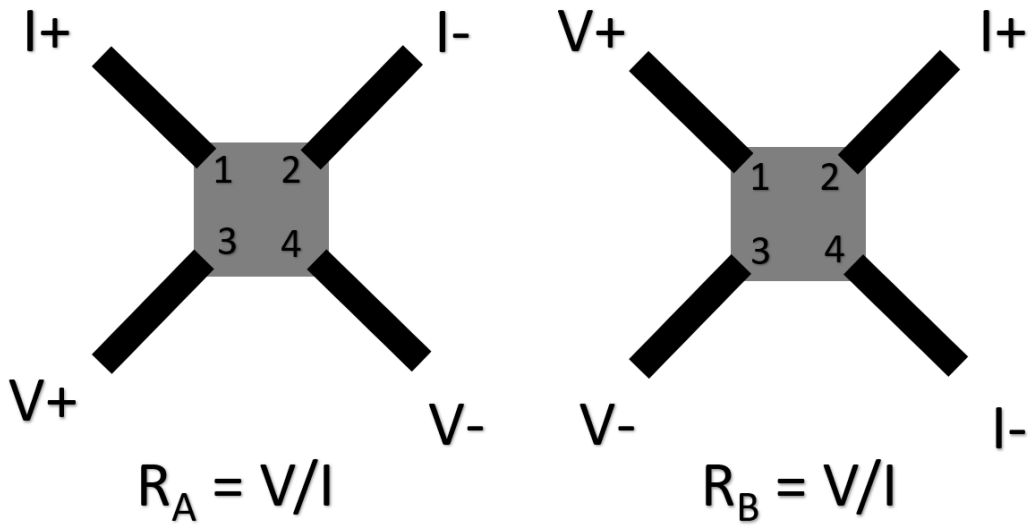

Figure 2.11: The VdP method for measuring sheet resistance involves taking two measurements with opposite polarities for each column. I+ and I- contacts where the current is applied, while V+ and V- contacts indicate where the voltage is measured in both images left and right. The left image represents the horizontal measurement and the right image represents the vertical measurements.

Set A (horizontal) resistances:

$$R_{12,34} = \frac{V_{34}}{I_{12}}, \quad R_{21,43} = \frac{V_{43}}{I_{21}} \tag{15}$$

$$R_{34,12} = \frac{V_{12}}{I_{34}}, \quad R_{43,21} = \frac{V_{21}}{I_{43}} \tag{16}$$

Set B (vertical) resistances:

$$R_{13,24} = \frac{V_{24}}{I_{13}}, \quad R_{31,42} = \frac{V_{42}}{I_{31}} \tag{17}$$

$$R_{24,13} = \frac{V_{13}}{I_{24}}, \quad R_{42,31} = \frac{V_{31}}{I_{42}} \tag{18}$$

Repeating these measurements for all four sides of a sample provides eight values of resistance. We average them to obtain R_A and R_B

$$R_A = \frac{R_{12,34} + R_{21,43} + R_{34,12} + R_{43,21}}{4} \tag{19}$$

$$R_B = \frac{R_{13,24} + R_{31,42} + R_{24,13} + R_{42,31}}{4} \tag{20}$$

Sheet resistance and conductivity then can be calculated numerically using the following VdP equation:

$$\exp\left(-\frac{\pi R_A}{R_{SH}}\right) + \exp\left(-\frac{\pi R_B}{R_{SH}}\right) = 1 \tag{21}$$

It can be simplified as:

$$\sigma = \frac{1}{R_{SH} \cdot t_{CH}} \tag{22}$$

where t_{CH} is the thickness of the film and R_{SH} is sheet resistance of the film that have a unit of ($\Omega/\square$) and σ is conductivity of the film with the unit of (S/m). Sheet resistance is converted into resistivity by multiplying by the thickness of the film. Once the resistivity reciprocal of conductivity of the TMD film is determined, the Hall voltage is measured. So the following section will cover the Hall Effect Measurements using VdP method.

2.7.4 Low temperature resistivity measurements

The useful part of using temperature dependent resistance measurements is initially to observe whether the material is semiconducting, semi-metallic, or metallic, and secondly, if the material is semiconducting to determine the activation energy of the charge carriers.

Electrons in the valence band are in a low-energy state, bound to the atoms of the material. To become mobile charge carriers, they need to overcome the Band Gap.

This requires energy equal to or greater than the band gap (Eg) to transition from the valence band to the conduction band.This energy known as activation energy. Experimentally, measuring the resistivity at different temperatures and fitting the data to the Arrhenius equation provides insights into the energy barrier that charge carriers must overcome to contribute to electrical conduction [23]. The Arrhenius equation is, here, a mathematical expression for the dopants to overcome in electronic devices and is often used to explore how resistance/resistivity changes with temperature [6]. The equation can be written as:

$$\ln(R) = \ln(R_0) + \frac{E_a}{k} \cdot \frac{1}{T} \tag{23}$$

where R_0 is a constant related to the pre-exponential factor, setting the scale for the resistance at a given reference point. E_a is the activation energy. k is the Boltzmann constant (8.617×10^{-5} eV/K). T is the absolute temperature in Kelvin.

Lower activation energy means a shallower slope in the plot, which is desirable if higher conductivity is needed [24]. With this purpose, the van der Pauw configuration was utilized, and sheet resistance for the samples at room temperature was calculated.

2.7.5 Hall Effect Measurement with VdP

Hall measurement systems utilize a material's Hall voltage to determine its Hall mobility. Hall measurement is used to ascertain properties of the thin films such as carrier concentration, mobility, resistivity, and carrier type. The fundamental principle of the Hall effect relies on the Lorentz force. Electrons flow along a channel in the presence of an electric field (E_x), with drift velocity (v_d). When a perpendicular magnetic field (B_z) is applied, the electrons experience the Lorentz force, which alters their path, Figure 2.12. Unlike the electric field force applied to stationary charges, the magnetic field force affects only moving charges influenced by current flow [15]. The cross product of the drift velocity and the magnetic field is shown in

Equation 24.

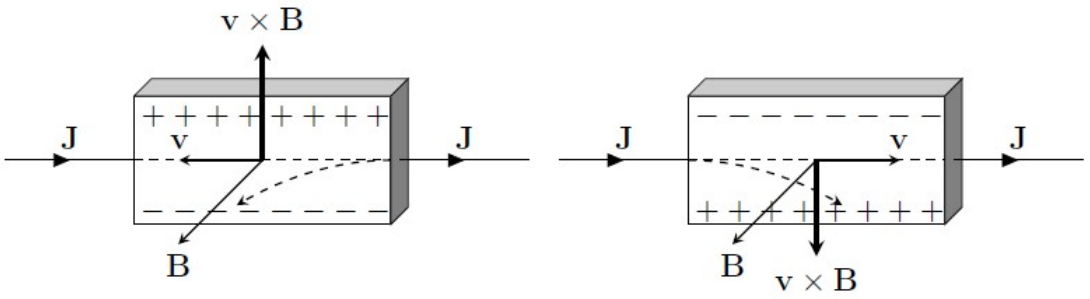

(a) Electrons (b) Holes

Figure 2.12: The Lorentz force impacts charge carriers within a material, with the Hall field direction differing depending on whether the charge carriers are (a) electrons or (b) holes. The dashed arrow illustrates the exaggerated deflection that the specified charge carrier experiences while moving through the material. The image adapted from ref: [25].

$$F = |q| v_d \times B \tag{24}$$

The magnetic field (B) is perpendicular ($\sin\phi = 1$) to the drift velocity (v_d) of the charged particles. The resulting Lorentz force causes charges to accumulate on one side of the material, creating a transverse electric field (E_H) on the other side. The electric field ($E_H = \frac{F}{q}$) reaches a steady state, canceling the Lorentz force. This is represented by:

$$qE_H + qv_d \times B = 0 \quad \Rightarrow \quad qE_H = -qv_d \times B \quad \Rightarrow \quad E_H = v_d \times B \tag{25}$$

Drift velocity (v_d) is related to the current density (J) by $J = qnv_d$, where n is the carrier concentration. Rearranging gives $v_d = \frac{J}{qn}$. Substituting v_d into E_H, we have:

$$E_H = \frac{J}{qn} \cdot B \tag{26}$$

Using $J = \frac{I}{wt}$ (current density in terms of current I, width w, and thickness t):

$$E_H = \frac{I}{qnwt} \cdot B \tag{27}$$

Substituting E_H into $V_H = E_H \cdot w$:

$$V_H = \frac{IB}{qnt} \tag{28}$$

Introducing the Hall coefficient ($R_H = \frac{1}{qn}$):

$$V_H = \frac{R_H IB}{t} \tag{29}$$

The Hall voltage is a critical parameter and is required to calculate the Hall coefficient. The sign of V_H determines the type of majority carriers in the material. A positive V_H indicates a p-type material (holes are the majority carriers), while a negative V_H corresponds to an n-type material (electrons are the majority carriers). The magnitude of V_H depends on the carrier density, applied current, and magnetic field.

Unlike electric forces acting on electric charges, magnetic forces act on any moving charges with the condition that the movement of the charges is not parallel to the magnetic field. The Hall voltage, generated perpendicular to both current and magnetic field directions, is measured to determine the carrier concentration and mobility of charge carriers in a material. The Hall coefficient is related to the carrier concentration (n) by:

$$R_H = \frac{\pm r}{qn} \tag{30}$$

where q is the charge and n is the carrier density. Note that the Hall scattering factor (r) depends on the scattering mechanism of the charge carriers, typically assumed to be $r = 1$ when the scattering mechanism is unknown. This factor is accepted as 1

in this thesis.

Additionally, the mobility of charge carriers (μ) can also be determined using Hall measurements. Mobility quantifies how effectively carriers move through a material under an electric field. It is calculated as:

$$\mu = \frac{\sigma}{qn} \quad \text{or equivalently,} \quad \mu = \frac{R_H \sigma}{t}, \tag{31}$$

where σ is the electrical conductivity. High mobility signifies that carriers experience less scattering and travel more freely, which is critical for electronic applications.

Hall effect measurements in this thesis were conducted under an alternating current (AC) field to mitigate setup imperfections such as uneven electrical contacts and temperature gradients across the sample. These imperfections can generate additional voltages that may lead to inaccurate results [26]. AC Hall measurements are particularly common for low-mobility or highly resistive films [26]. Unlike the DC method, which uses a linear current, the AC approach employs a sinusoidal current generated by a lock-in amplifier. This technique offers superior noise reduction, making it well-suited for low-mobility films where Hall voltage signals are often weak and susceptible to noise interference [27].

2.8 Tensile Testing

Tensile testing is widely used to measure key material properties, such as the applied stress (σ) and the fractional length change (strain, ϵ). These parameters are crucial for understanding material behavior under mechanical loads [28]. In this applied tensile testing for this thesis, the stress-strain relationship is analyzed. The Young's modulus is determined as the slope of the linear region of the stress-strain curve, which is illustrated in Figure 2.13.

The tensile tester setup measures both the displacement between the clamps and

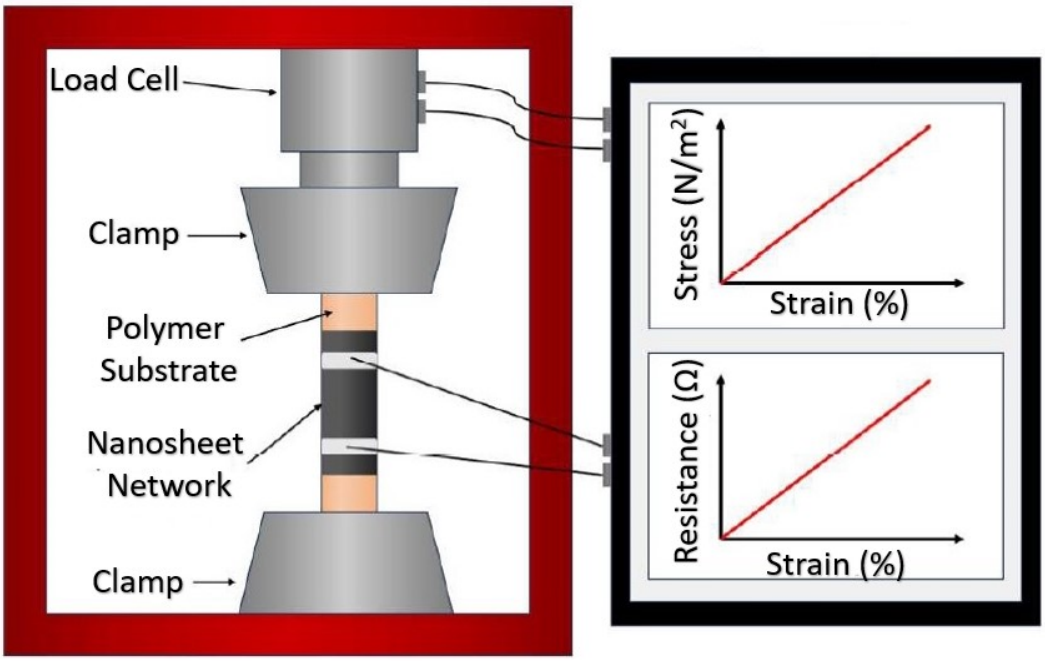

Figure 2.13: A schematic representation of a Tensile testing setup (left), The simultaneous output of electromechanical testing: Stress (N/m^2) versus Strain (%) and Resistance Ω versus Strain (%).

the force applied, which is recorded through a load cell. This allows precise control over applied stress. For simultaneous electrical testing, the system uses strain gauges connected through a Wheatstone bridge circuit [29]. These gauges output a signal proportional to the material deformation. The displacement of the clamps is controlled to vary the crosshead position. This is achieved using a proportional-integral-derivative (PID) system, ensuring stable force application during the experiment [30]. In this setup, all applied loads were controlled to maintain accuracy. This combined setup provides a detailed understanding of the mechanical and electrical performance of the material as it undergoes stress. Modeling studies were completed by Proffesor Jonatthan Coleman.

2.9 Atomic Force Microscopy

Atomic force microscopy (AFM) is a widely used scanning probe technique for measuring the topography of surfaces at the nanoscale. The AFM operates by scanning a sharp tip across the sample surface, where interactions between the tip and the

surface provide information about the surface features. The vertical movement of the tip, controlled by a piezoelectric scanner, is measured to generate a topographical map of the surface [31]. The schematic of an AFM setup can be seen in Figure 2.14.

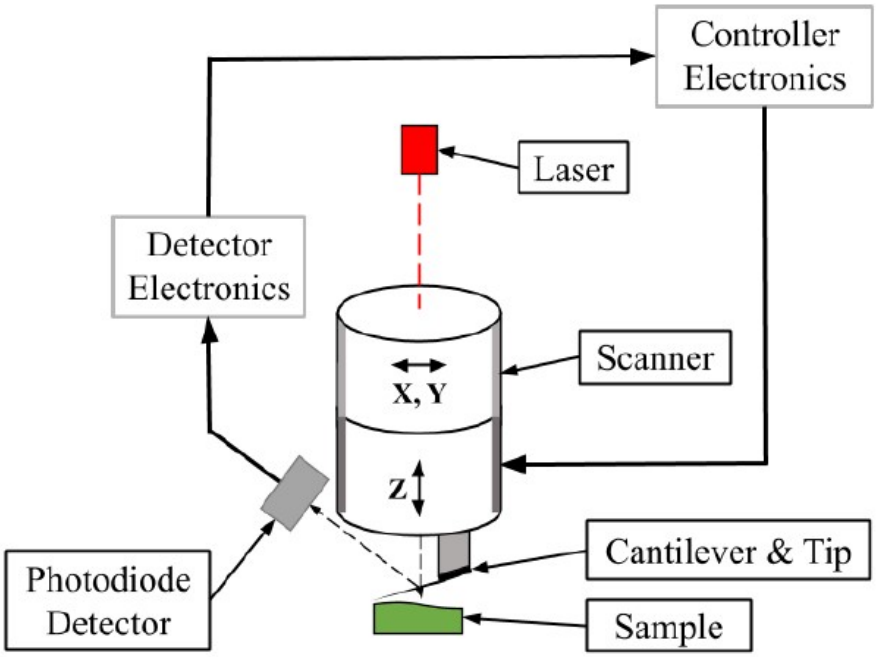

Figure 2.14: Schematic of an atomic force microscopy apparatus [2].

The AFM setup includes a laser beam that reflects off the cantilever onto a position-sensitive photodetector, which records deflections as the cantilever interacts with the surface. These deflections are converted into a detailed three-dimensional topographical map. AFM provides high-resolution imaging with precise control over force, making it a powerful tool for surface analysis in various scientific and engineering fields. AFM imaging typically operates in one of three modes: contact, non-contact, or tapping mode. In tapping mode, the cantilever oscillates near its resonance frequency, intermittently contacting the surface, which minimizes lateral forces and potential damage to the sample or the tip. This makes tapping mode particularly effective for soft or delicate surfaces [32].

Gwyddion is an open-source software designed for the visualization and analysis of atomic force microscopy (AFM). It supports a wide range of file formats and provides tools for surface topography analysis, height profile extraction, roughness

calculation. In this thesis, Gwyddion [33] was used to extract the height profiles from the AFM micrograph and to analyze the surface topography of the 2.63 at.% Re-doped MoS_2 film A1.6 and $PtSe_2$ network 5.2.4.

2.10 Scanning Electron Microscopy

Scanning Electron Microscopy (SEM) is a technique used in materials science to examine samples. SEM works by using an electron beam to interact with the sample and gather information about it. The electrons come from an electron gun, which can be a heated tungsten filament or a sharp LaB_6 tip [34]. Figure 2.15(a) shows the SEM setup. To keep the electron gun stable, it operates in a very high vacuum environment of about 10^{-9} mbar and is rarely exposed to air. The chamber where the sample is tested is kept in a high vacuum of about 10^{-4} to 10^{-7} mbar.

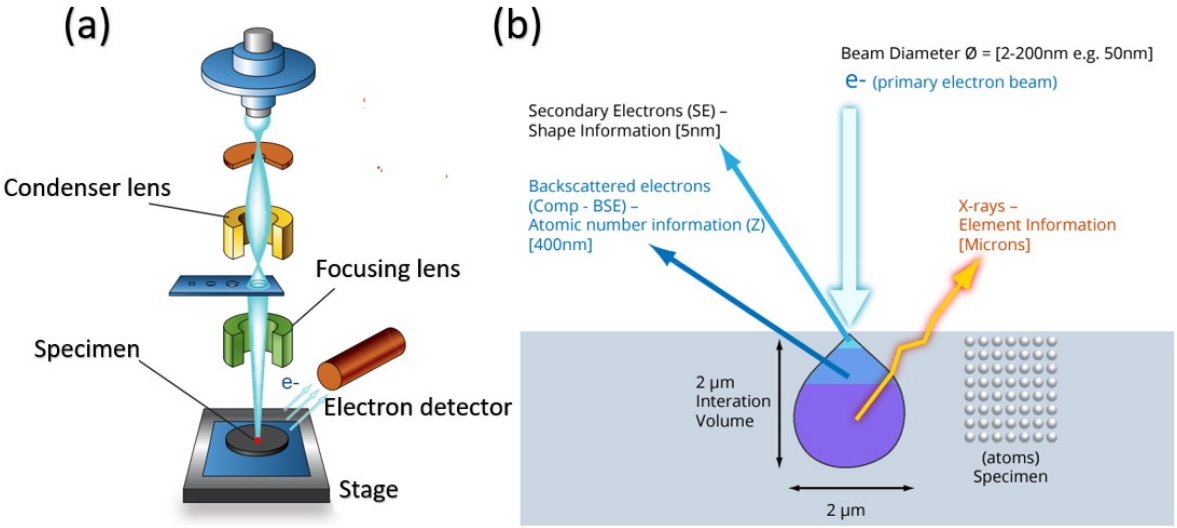

Figure 2.15: (a) Diagram of the SEM column, showing electron lenses, sample stage, and detector positions. (b) How the electron beam interacts with a sample inside the SEM The images were adapted from the ref: [35].

During scanning, electrons are accelerated (usually 0.5 - 20 kV) and focused into a beam that enters the specimen chamber. As shown in Figure 2.15(b), when the electron beam hits the sample, it produces various signals that can be detected and analyzed. These signals include, as shown in Figure 2.15 (b):

Secondary Electrons: Provide detailed images of the surface [34].

Back-Scattered Electrons: Show differences in composition based on atomic number [36].

Characteristic X-rays: Give information about the elements present in the sample through energy-dispersive X-ray spectroscopy (EDS) [34].

Secondary electrons, with their low energy, provide high-resolution images of the sample's surface. Back-scattered electrons, which have higher energy, give compositional information with with less detail. SEM uses different types of electron interactions to provide detailed images and compositional information about a sample, making it a reliable tool in materials science [37].

2.11 Photolithography

Photolithography, also known as optical lithography, is a process used to create integrated circuits by transferring patterns from a mask to a light-sensitive material (photo-resist) on a substrate [38]. This technique involves using light to etch patterns onto a substrate, Figure 2.16.

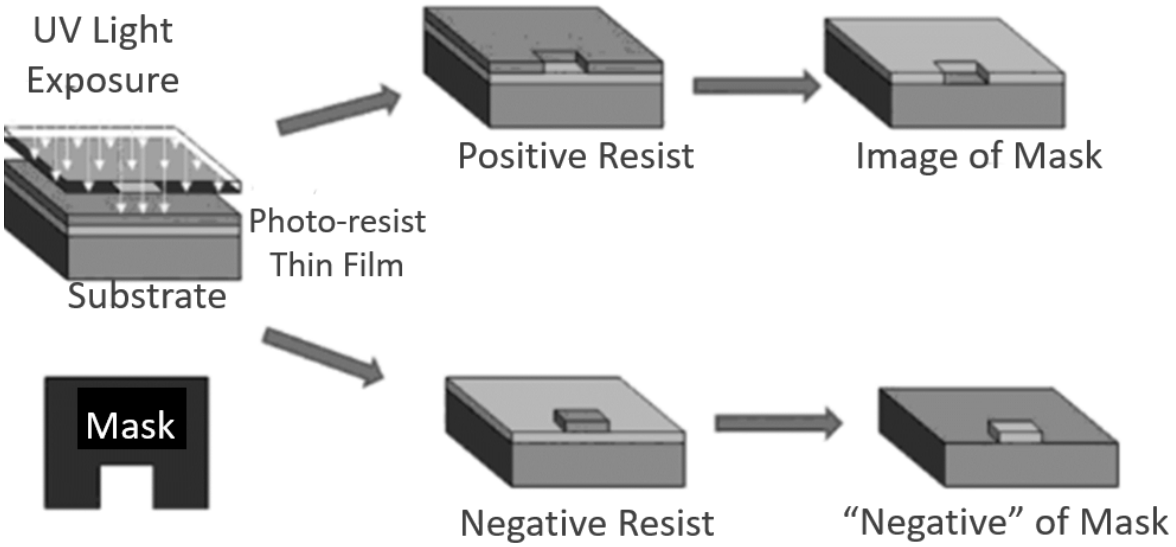

Figure 2.16: A schematic representation of photolithography process. Image is modified from Ref: [39]

When exposed to light, the photoresist undergoes chemical changes, enabling the pattern transfer. There are two main types of photo-resists: positive and negative.

In positive photoresists, the exposed areas become soluble and are removed during development, leaving the unexposed areas intact. This type is commonly used in semiconductor fabrication [40]. Conversely, in negative photo-resists, the exposed areas become insoluble and remain after development, while the unexposed areas are removed.

The choice between positive and negative photo-resists depends on specific application requirements, such as resolution and the nature of the substrate. Figure 2.16 depicts two scenarios: Positive resist where the exposed areas become soluble and are removed, resulting in the mask pattern on the substrate. And, negative resist where the exposed areas become insoluble, and the unexposed areas are removed, resulting in the negative of the mask pattern on the substrate. The resolution of photolithography is crucial for achieving smaller feature sizes and higher device density, but it is limited by the wavelength of the light used and the capability of the lens system to capture enough diffraction orders from the illuminated masks. The Rayleigh equation describes this diffraction limit [41]:

$$R = \frac{k_1 \lambda}{NA} \tag{32}$$

where R is the minimum resolvable feature size, λ is the exposure wavelength, NA is the numerical aperture of the optical system, and k_1 is a constant related to the photo-resist.

2.12 Transmission Electron Microscopy

Transmission Electron Microscopy (TEM) uses high-energy electrons to penetrate deeply into a sample, often several microns, or pass completely through nanomaterials, as schematic of it in Figure 2.17. As these electrons travel through the sample, they interact with it, either elastically or inelastically, and the resulting attenuated signal forms the basis of TEM images.

The TEM consists of three main components: the illumination system, the specimen stage, and the imaging system. Illumination System, it includes the electron source, which is chosen based on the desired resolution. For normal resolution, thermionic LaB_6 or tungsten filaments are used. For high resolution, Schottky field emission or cold field-emission guns are preferred. The electron gun is paired with condenser lenses that focus the electrons onto the sample, controlling the beam's diameter and intensity [36]. Specimen Stage, it holds the sample and allows it to be inserted and removed from the microscope. For clear images, the stage must remain completely stationary.

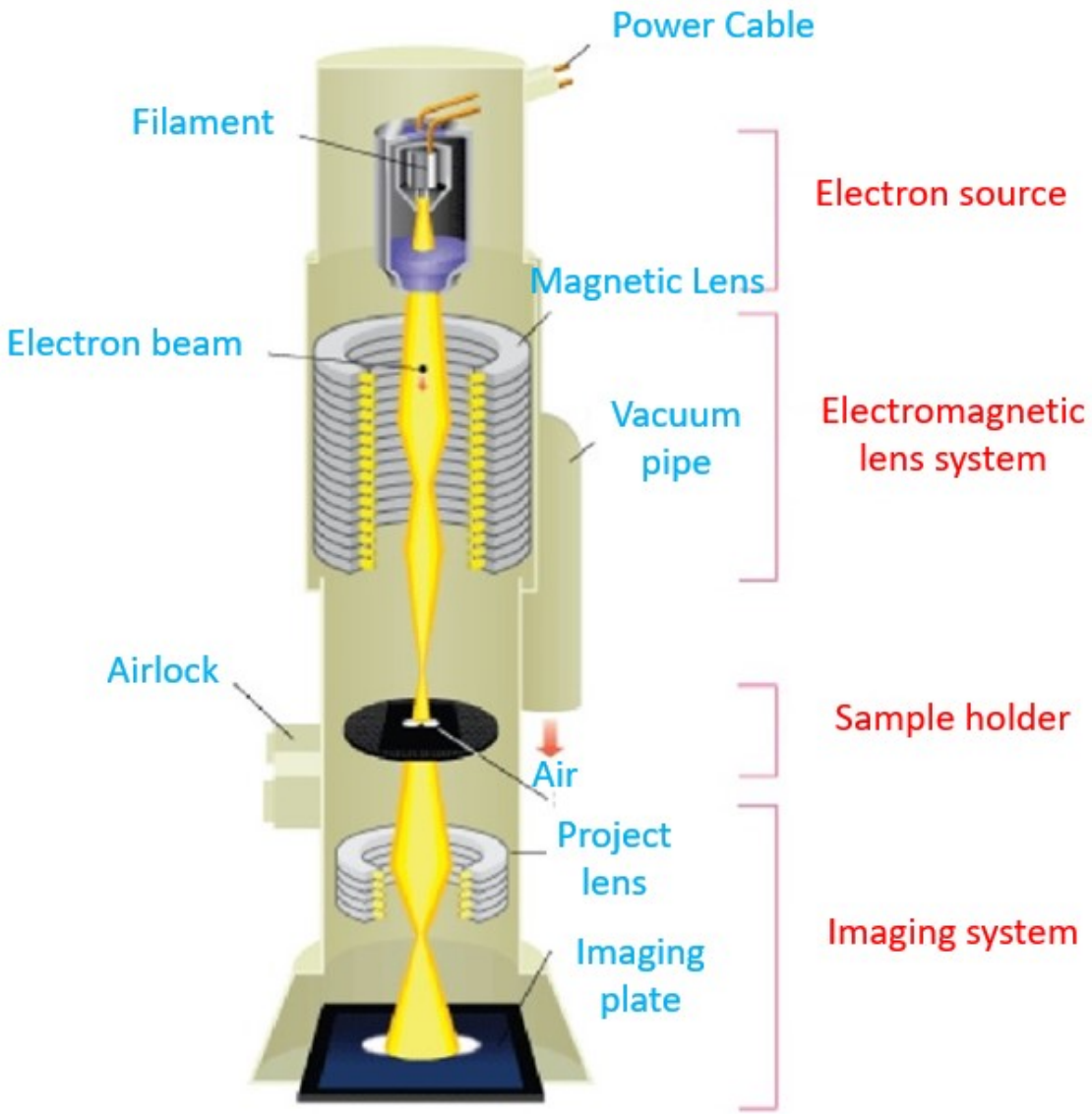

Figure 2.17: A schematic representation of a TEM column. Image is modified from Ref: [42].

Imaging System, as electron beam passes through the specimen, some electrons go straight through, while others scatter in various directions. The imaging system captures and magnifies the image using a series of lenses, projecting it onto a cooled CCD for recording. The magnification and resolution are determined by the design of these lenses. Despite the picometer wavelengths of the electrons, typical resolutions are around 0.5 nm due to various aberrations. Spherical aberrations arise from imperfections in the focusing system, chromatic aberrations from electrons with different energies, and astigmatisms from asymmetric magnetic fields along the pole piece [43].

TEM offers two characteristic modes for detailed imaging: Annular Dark Field (ADF) and Bright Field (BF) modes.

Bright Field Mode

This mode creates an image using electrons that pass through the sample without scattering, providing contrast based on variations in the sample's thickness and density. It uses a central aperture to collect these unscattered electrons [44].

Annular Dark Field Mode

This mode collects scattered electrons using an annular detector placed around the optic axis. The detector captures electrons scattered to high angles by interactions with the atomic nuclei, providing compositional and structural information with atomic number contrast (Z-contrast). The main instrumental difference between these modes is the type and positioning of detectors: BF mode uses a central aperture for unscattered electrons, while ADF mode uses an annular detector for scattered electrons, enhancing contrast based on atomic number differences [44].

Additionally, Energy Dispersive X-ray Spectroscopy (EDS) and Electron Energy Loss Spectroscopy (EELS) are techniques often attached to TEM to enhance its capabilities. EDS identifies the elemental composition of the sample by detecting characteristic X-rays emitted when the sample is bombarded with an electron beam [44].

EELS analyzes the energy distribution of electrons that have passed through the sample, providing detailed information about the electronic structure and elemental composition [45].

TEM analysis's, in this thesis, were performed by Gianfranco Sfuncia from the Institute for Microelectronics and Microsystems (IMM) group at CNR in Catania

References

(1) F. Penning, *US Patent*, 1939, **2**.

(2) K. E. Siewierska, Accessed: 2024-05-02, PhD Thesis, Trinity College Dublin, 2020.

(3) T. Nimalan and M. Begam, *Int. J. Thin. Fil. Sci. Tec*, 2024, **13**, 59–66.

(4) J. X. Zhang and K. Hoshino, *Molecular Sensors and Nanodevices*, 2019, 43–111.

(5) A. Bashir, T. I. Awan, A. Tehseen, M. B. Tahir and M. Ijaz, *Chemistry of Nanomaterials*, 2020, **51**, 87.

(6) R. J. Gatensby, PhD Thesis, Trinity College Dublin. School of Chemistry. Discipline of Chemistry, Dublin, Ireland, 2018.

(7) J. R. Ferraro, *Introductory raman spectroscopy*, Elsevier, 2003.

(8) DoITPoMS, *Raman Spectroscopy*, `https://www.doitpoms.ac.uk/tlplib/raman/index.php`, Accessed: 2024-05-10, 2024.

(9) E. D. Hudspeth, D. Cleveland, K. L. Batchler, P. A. Nguyen, T. L. Feaser, L. E. Quattrochi, J. Morenz, S. A. Balram, R. G. Michel, J. X. Zhou et al., *Spectroscopy letters*, 2006, **39**, 99–115.

(10) H. Li, Q. Zhang, C. C. R. Yap, B. K. Tay, T. H. T. Edwin, A. Olivier and D. Baillargeat, *Advanced Functional Materials*, 2012, **22**, 1385–1390.

(11) University of Cambridge, *DoITPoMS - TLP Library Raman Spectroscopy*, Accessed: 2024-06-02, 2024.

(12) G. Giridhar, R. Manepalli and G. Apparao, in *Spectroscopic methods for nanomaterials characterization*, Elsevier, 2017, pp. 141–161.

(13) F. S. Rocha, A. J. Gomes, C. N. Lunardi, S. Kaliaguine and G. S. Patience, *The Canadian Journal of Chemical Engineering*, 2018, **96**, 2512–2517.

(14) G. F. Harrington and J. Santiso, *Journal of Electroceramics*, 2021, **47**, 141–163.

(15) H. D. Young, R. A. Freedman, T. Sandin and A. L. Ford, *University physics*, Addison-Wesley Reading, MA, 1996, vol. 9.

(16) M. Yasaka et al., *The Rigaku Journal*, 2010, **26**, 1–9.

(17) M. R. Sardela Jr, in *Practical materials characterization*, Springer, 2014, pp. 1–41.

(18) M. Björck and G. Andersson, *Journal of Applied Crystallography*, 2007, **40**, 1174–1178.

(19) A. Glavic and M. Björck, *Journal of applied crystallography*, 2022, **55**, 1063–1071.

(20) S. Mitta et al., *Electrical characterisation of 2D materials-based field-effect transistors. 2D Mater. 8 (2021)*.

(21) C. Melios, N. Huang, L. Callegaro, A. Centeno, A. Cultrera, A. Cordon, V. Panchal, I. Arnedo, A. Redo-Sanchez, D. Etayo et al., *Scientific Reports*, 2020, **10**, 3223.

(22) L. J. van der Pauw, *Philips technical review*, 1958, **20**, 220–224.

(23) H. Xu, H. Zhang, Y. Liu, S. Zhang, Y. Sun, Z. Guo, Y. Sheng, X. Wang, C. Luo, X. Wu et al., *Advanced Functional Materials*, 2019, **29**, 1805614.

(24) K. Lethy, D. Beena, R. Vinod Kumar, V. Mahadevan Pillai, V. Ganesan, V. Sathe and D. Phase, *Applied Physics A*, 2008, **91**, 637–649.

(25) D. Mullarkey, Ph.D. Thesis, Trinity College Dublin, 2018.

(26) F. Werner, *Journal of Applied Physics*, 2017, **122**.

(27) J. Lindemuth and S.-I. Mizuta, Thin Film Solar Technology III, 2011, vol. 8110, pp. 65–71.

(28) W. D. Callister Jr, *WILEY 2011-Lecture Notes*, Elsevier, 2014.

(29) A. L. Window and G. S. Holister, *Strain Gauge Technology*, Elsevier Applied Science, London, UK, 1982.

(30) J. R. Davis, *Tensile Testing*, ASM International, 2004.

(31) P. Eaton and P. West, *Atomic Force Microscopy*, Oxford University Press, Oxford, UK, 2010.

(32) Y. Seo and W. Jhe, *Reports on Progress in Physics*, 2007, **71**, 016101.

(33) D. Nečas and P. Klapetek, *Gwyddion*, `http://gwyddion.net`, Version 2.36, `http://gwyddion.net`, 2012.

(34) W. Zhou and Z. L. Wang, *Scanning microscopy for nanotechnology: techniques and applications*, Springer science & business media, 2007.

(35) MyScope, *Structure of an SEM*, Accessed: 2024-11-27, 2024.

(36) R. F. Egerton et al., *Physical principles of electron microscopy*, Springer, 2005, vol. 56.

(37) Wikipedia, *Electron microscope*, `https://en.wikipedia.org/wiki/Electron_microscope`, Accessed: 2019-05-16, 2019.

(38) L. F. Thompson, in *Introduction to Microlithography*, ed. L. F. Thompson, C. G. Willson and M. J. Bowden, ACS Publications, 1983, pp. 3–30.

(39) X.-M. Zhao, Y. Xia and G. M. Whitesides, *Journal of Materials Chemistry*, 1997, **7**, 1069–1074.

(40) J. R. Groves, *Iowa Geological and Water Survey Guidebook*, 2008, 53–56.

(41) H. J. Levinson, *Principles of lithography*, SPIE press, 2005, vol. 146.

(42) tem, *Image of a TEM Column*, Accessed: 2024-01-30, 2024.

(43) L. Reimer, *Transmission electron microscopy: physics of image formation and microanalysis*, Springer, 2013, vol. 36.

(44) MyScope Training, *TEM Image Formation Basics*, `https://myscope.training/TEM_Image_formation_basics`, Accessed: 2024-05-24, 2024.

(45) R. Egerton and M. Malac, *Journal of Electron Spectroscopy and Related Phenomena*, 2005, **143**, 43–50.

3 Modulating MoS_2 Properties through Introducing of Rhenium Content

3.1 Background and Motivation

For emerging electronic applications of Transition Metal Dichalcogenides (TMDs), particularly in developing complementary metal-oxide-semiconductor (CMOS) devices, modulating free carrier concentrations is essential for creating p-n junctions [1]. Molybdenum Disulfide (MoS_2), an n-type semiconductor with thickness-dependent adjustable bandgap characteristics, is a competitive candidate for electrical applications [2]. However, optimizing MoS_2-based devices for CMOS analogs requires addressing two key challenges: contact resistance and defects [3, 4]. Defects, particularly sulfur vacancies, are a primary cause of Fermi-level pinning and impaired charge injection and collection, which affect electrical, optical, and energy device performance [5–8].

Defect densities in MoS_2 vary significantly with synthesis methods. Physical vapor deposition (PVD) introduces Mo interstitial defects and sulfur vacancies, leading to higher resistivity and lower mobility compared to mechanical exfoliation and chemical vapor deposition (CVD) [9, 10]. Polycrystalline growth techniques, such as the thermal-assisted conversion (TAC) process, also produce structural defects, including grain boundaries, further impairing electrical performance [11, 12].

Doping has been proposed to mitigate contact resistance and defect concentration.

Substitutional doping, where metal atoms replace Mo in the lattice, provides stable and consistent electronic properties compared to transient physisorption-based doping methods [13].

Doping shifts the Fermi level toward the conduction or valence band depending on the dopant type, while preserving the stability of the 2H phase unless high dopant concentrations induce a phase transition to the 1T phase [14, 15].

Density Functional Theory (DFT) calculations reveal that transition metal dopants with higher d-electron counts than Mo introduce donor states near the conduction band minimum (CBM), enhancing conductivity and reducing the Schottky barrier in MoS_2 transistors [16, 17]. Rhenium, with low activation energy, is particularly effective as an n-type dopant [18, 19]. Recent studies have explored Re-doping effects on MoS_2, but gaps remain in understanding dopant positions and their influence on structural and electrical properties of TAC-grown bulk MoS_2 films [20]. This chapter investigates these effects for Re-doped MoS_2 films with a nominal thickness of 45 $\pm$ 4 nm, aiming to address these questions.

3.2 Methodology

Substrate Preparation

Depositions were performed on hexagonal R-cut sapphire (Al_2O_3) substrates with orientation 01-12 and 02-24, each measuring 1 cm x 1 cm and C-cut sapphire with (0006) orientation. The orientation $01\bar{1}2$ (commonly written as $01-12$) represents a specific crystallographic plane in the sapphire lattice. Similarly, $02\bar{2}4$ (or $02-24$) corresponds to another plane. Besides C-cut sapphire (0006) exposes a basal plane. These orientations define the atomic arrangement and spacing of the sapphire surface, which directly impacts the growth, alignment, and properties of the deposited thin films. The substrates underwent pre-cleaning in an ultrasonic bath with acetone, isopropyl alcohol (IPA), and deionized water for 5 minutes each, followed by

drying with nitrogen (N_2) gas.

Transition Metal Deposition

Thin-film samples were deposited using Molybdenum (Mo) as the host metal and Rhenium (Re) as the impurity metal. The deposition was done using a co-sputering method of a DC and RF magnetron sputterings under high vacuum conditions, as shown in Figure 3.1. The sputtering targets, 3-inch diameter Mo (99.99%) and Re (99.99%), were sourced from Kurt J. Lesker. The substrate temperature was maintained at room temperature, with a target-to-substrate distance of 15 cm and a substrate holder rotation of 30 rpm.

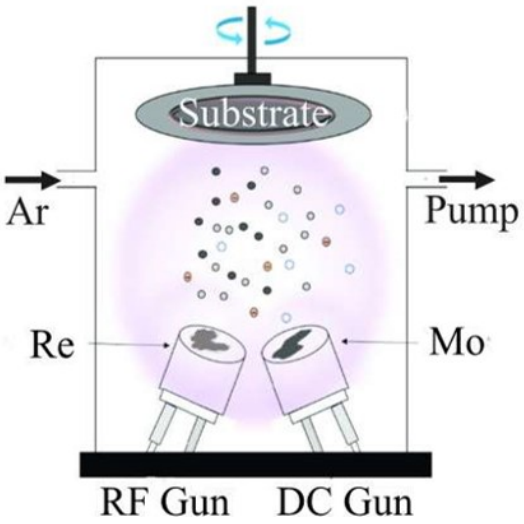

Figure 3.1: A schematic of the target metals and the deposition chamber.

X-Ray Reflectivity

X-Ray Reflectivity (XRR) was employed to calibrate the deposition rate and confirm film thickness post-deposition. Measurements were performed using a Phillips Panalytical X'Pert Pro diffractometer. The open-source program GENX was used for reflectivity analysis [21]. Pristine, 2.63 at.% Re-doped, and 10.48 at.% Re-doped Mo films were prepared for this study.

Conversion Process

Post-deposition, the films were placed in the growth furnace, and 5 g of sulfur powder (Sigma-Aldrich 99.998%) was placed into a quartz crucible inside the sulfur furnace, as shown in the furnace schematic in Figure 3.2(a). The sulfur was heated to 135 °C, while the films were heated to 900 °C. The furnace, connected to an Argon (Ar) supply, was heated at 19 °C/min to the process temperature. Sulfurization was maintained for 30 minutes, followed by 30 minutes of annealing and subsequent cooling to room temperature. The carrier Ar gas carries the evaporated sulfur towards the growth furnace. The sulfur powder completely evaporated after 30 minutes of growth. Throughout the conversion and annealing process, the Ar flow was maintained at 100 sccm. Figure 3.2(b) shows the furnace setup with the temperature-time profile.

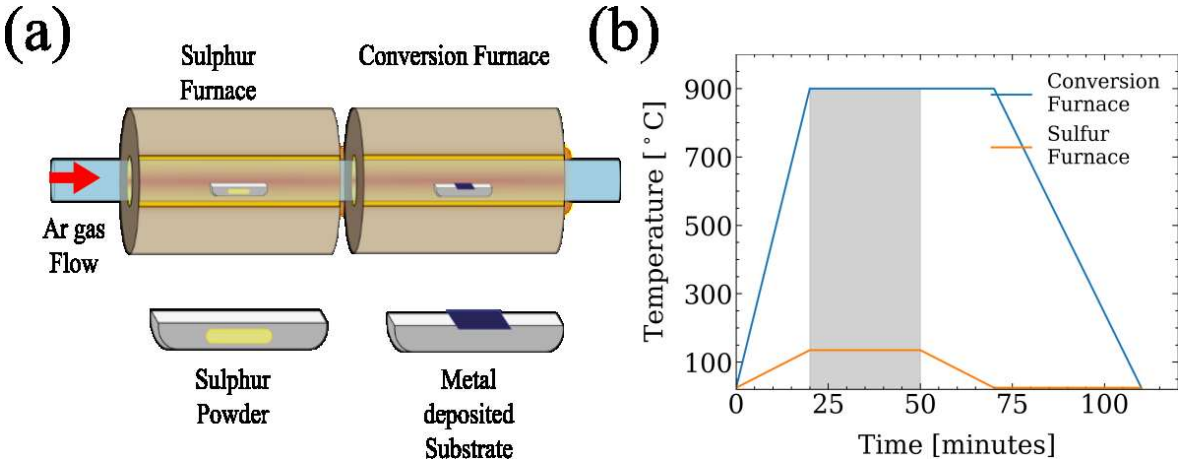

Figure 3.2: (a) Schematic of the furnace. (b) Diagram of the furnace setup with temperature-time profile information used during the sulfurization process for MoS_2 film growth, involving a 30-minute growth phase followed by 30 minutes of annealing under Ar gas. The cooling rate cannot be controlled; 25 minutes is the standard time, which is repeatable, for the furnace to reach room temperature from 135 °C.

Typically, the entire growth process lasts about 110 minutes, consisting of the sulfurization phase (conversion of transition metal to sulfide-based TMD) and the annealing phase (re-crystallization). It should be noted that there is no control over the heating and cooling

Raman Spectroscopy

The Raman spectroscopy was performed using the Witec Alpha 300R spectrometer with an excitation wavelength of 532 nm. A spectral grating with 1800 lines/mm and a 100× microscope objective (0.95 N.A) with a spot size of approximately 0.3 nm were utilized for the Raman spectra. To prevent laser damage to the surface, the laser power was maintained below 100 μW. Measurements were conducted in air at 25 °C and atmospheric pressure. A grating with 1800 grooves per mm was used for spectral dispersion, providing a system-wide spectral resolution of approximately 0.75 cm^{-1}. All Raman spectra were recorded under ambient conditions.

X-Ray Diffraction

X-ray diffraction (XRD) was used to elucidate the crystallographic features of the films post-conversion and Raman characterization. Measurements were performed with a Panalytical X'Pert Pro diffractometer using 2θ-ω scans, Cu Kα radiation (1.5406 Å) in Bragg-Brentano geometry, with a step size of 0.02 degrees/step and a step time of 0.5 s/step. Crystallographic phases were identified using reference patterns from the International Centre for Diffraction Data (ICDD), and the Crystallography Open Database (COD)

Low temperature Electrical Characterisation

Low-temperature resistivity measurements were completed using the Keithley 2636B semiconductor characterization system in a homemade low-vacuum station, with measurements carried out in high vacuum 10^{-5}mbar with a ranging temperature between 300 K to 100 K. A Van der Pauw configuration was employed, where four electrical contacts were placed at the corners of the sample without the use of lithography. Instead, contacts were made using indium wires.

Transmission Electron Microscopy

For the structural characterization of TMD films, a JEOL ARM200F Transmission Electron Microscope (TEM) operating at 200 kV was used, equipped with advanced detectors for Energy Dispersive X-ray Spectroscopy (EDS) and Electron Energy Loss Spectroscopy (EELS). These capabilities allowed for detailed elemental and chemical analysis of the sample, providing insights into its composition. EELS was used to determine the composition, and EDS was used to detect Re impurities in the MoS_2 matrix.

Hall Effect Measurements

Hall effect measurements were performed at room temperature using a van der Pauw configuration with a LakeShore Model 8404 AC Hall-effect measurement system. In this configuration, four electrical contacts were placed near the edges of the sample, forming the same geometry as used in the Arrhenius measurement setup. The AC magnetic field was fixed at 1.2 T RMS at a frequency of 0.1 Hz. The van der Pauw configuration was used without the need for lithography. Figure 3.3 shows how the sample is located in the holder and positioned between the magnets.

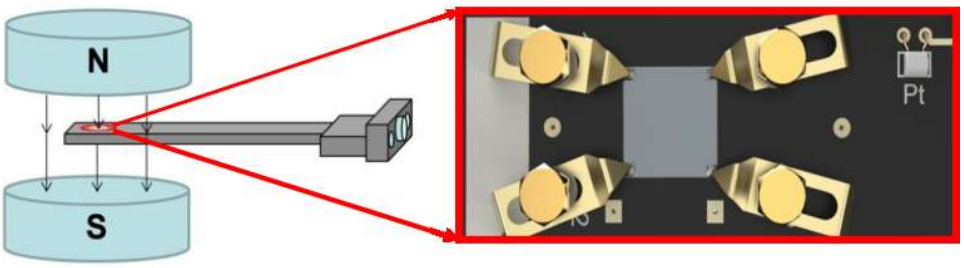

Figure 3.3: Holder for Hall measurement. The special holder with gold clamps is designed to lower the contact resistance, which influences the resistance measurement.

For materials with low mobility and/or high resistance, like polycrystalline TMD films, achieving proper contact is crucial and extremely challenging. This significantly impacts the Hall voltage, even more than it affects resistivity measurements.

To minimize contact resistance, Indium (In) solder contacts are placed in the corners of the film. The fully filled $4d^{10}$ orbital contributes to the stability and lower reactivity of indium compared to transition metals with partially filled d-orbitals. This results in a bonding behavior that is beneficial for forming stable and reliable contacts because the lack of d-orbitals makes indium less reactive [22].

3.3 Experimental Results

In this chapter, the co-sputtering method was employed to achieve the incorporation of host and impurity atoms. The goal was to ensure the uniform distribution of impurities of rhenium (Re) throughout the matrix of molybdenum (Mo). The depositions were carried out using direct current (DC) and radio frequency (RF) magnetron sputtering, both of which are physical vapor deposition (PVD) techniques performed under high vacuum conditions, as detailed in Section 2.1.1.

The doping levels of rhenium were set to achieve pristine Mo, 2.63 at.% Re, and 10.48 at.% Re in a nominal 20 nm thick Mo-Re film before the conversion process. These atomic percentage values were determined based on deposition parameters and verified through calculations shown in Appendix A1.1 after X-Ray Reflectivity characterization. The objective was to study how varying impurity concentrations influence the electrical behavior of the thin films after the conversion process.

The deposition parameters used to fabricate the films are summarized in Table 3.1. The table shows the applied current for the DC and RF guns, as well as the sputtering duration for each film. The co-sputtering method was employed, where both the DC and RF guns operated simultaneously. The current applied to each gun was calibrated to achieve the desired doping levels, as determined by the operator's guidance during the calibration process. Notably, the pristine Mo film was deposited using only the DC gun, while the Re-doped films required the additional RF gun to sputter Re targets. The deposition times were optimized to ensure a total thickness of around 20 nm for each sample.

The relationship between the guns and deposition rates is defined by constants in nm/min·mA: For Molybdenum (Mo): The deposition rate is 3.27×10^{-5} nm/min · mA, meaning that at 1 mA of current, 3.27×10^{-5} nm of Mo is deposited per minute. For Rhenium (Re): The deposition rate is 1.9×10^{-5} nm/min · mA, meaning that at 1 mA of current, 1.9×10^{-5} nm of Re is deposited per minute.

For the deposition, selected compositions were Pristine, 2.63 at.% Re, and 10.48 at.% Re for a nominal total thickness of 20 nm.

Material	**DC Gun (mA)**	**RF Gun (mA)**	**Time (sec)**
Pristine Mo	400	–	100
2.63 at.% Re	400	21	92
10.48 at.% Re	400	64	90

Table 3.1: Deposition parameters for pristine Mo and Re-doped Mo thin films using a magnetron sputtering system. The co-sputtering method involved simultaneous operation of the DC and RF guns. The applied current values were determined during the calibration process to achieve the desired doping levels.

3.3.1 X-Ray Reflectivity (XRR)

The impurity concentrations correspond to 2.63 at.% Re, which is 0.5 nm of Re, and 10.48 at.% Re, which is 2 nm of Re, in a nominal of 20 nm stack. The thicknesses of the transition metal deposited films were measured based on the XRR simulation results, shown in Appendix A1.1. The values are as follows: 18.7 nm for the Pristine Mo film, 19.6 nm for the 2.63 at.% Re-doped Mo film, and 19.9 nm for the 10.48 at.% Re-doped Mo film. Table 3.2 presents the information obtained from the GENX fit, shown in Figure A1.1. The corresponding GENX density and real density shown in the Table 3.2. Besides, the section 2.6 covers the information about the conversion densities.

X-ray reflectivity is suitable before the conversion process to primarily determine the thickness and densities of the films, ensuring that the desired compositions are achieved. However, after the conversion to sulfide-based semiconducting materials, the films exhibit significantly higher roughness (more than 10 times compared to be-

Concentration (at. %)	Pristine	2.63 at.% Re	10.48 at.% Re
Thickness (nm)	18.1	19.6	19.9
GenX Density (scatterers/unit volume)	0.0645	0.0651	0.0660
Real Density (g/cm^3)	10.28	10.35	10.50

Table 3.2: The thicknesses, GenX densities, and real densities for different doping levels of Re impurities (at.%).

fore conversion). This increased roughness renders XRR measurements unfeasible post-conversion. Therefore, XRR is reliable only prior to the conversion process, as demonstrated in Figure 2.8 in the Section 2.6.

This inherent roughness makes XRR fitting impractical after the conversion, as discussed and shown in Chapter 2. The thickness and morphology of the converted Mo films to MoS_2 are illustrated in Appendix A1.8.

3.3.2 Conversion Process

The sulfur was maintained at a temperature of 135 °C, while the films were heated to 900 °C. The furnace, equipped with an Argon (Ar) gas supply, was ramped to the target temperature at a rate of 19 °C/min. A sulfurization duration of 30 minutes was chosen due to practical limitations associated with the sulfur supply within the furnace. The quantity of sulfur powder determines the amount of sulfur vapor available during the process. Once the sulfur is fully evaporated and depleted, further conversion of Mo to MoS_2 halts, and the process transitions into an annealing phase. Consequently, the growth duration is intrinsically constrained by the availability of sulfur. The tube pressure was maintained at 0.6 Torr during both the conversion (100 sccm Ar flow) and annealing stages.

The thicknesses of the films after conversion are summarized in Table A1.1.1 in the Appendix. Supporting evidence is provided in Appendix A1.5, A1.6, and A1.7, respectively.

3.3.3 Raman Spectroscopy

Raman spectroscopy is the primary characterization tool used post-growth to analyze the characteristic peaks of pristine and doped MoS_2 films grown on both R-cut substrates. It has been utilized to study different crystalline structures of MoS_2 [23–26]. In this chapter, a 532 nm laser (2.33 eV) is used to observe off-resonance Raman peaks of MoS_2 films.

Although there are four Raman active characteristic peaks used to evaluate MoS_2 structure, the A_{1g} and E_{2g} modes are primarily analyzed and compared in the literature due to their sharp and intense peak structure, sensitivity to the number of layers (thickness) [27], and ability to reflect changes in the structure such as poor crystallinity (evidenced by peak broadening) and defects (evidenced by changes in peak intensity or peak location shift) [28]. Among these two peaks, the E_{2g} mode involves the opposing vibration of two sulfur atoms relative to the molybdenum atom, while the A_{1g} mode is associated with the out-of-plane vibration of sulfur atoms in opposite directions. Below, the Raman spectra of pristine MoS_2 and Re-doped MoS_2 films using a 532 nm laser is shown on C-cut Al_2O_3 substrates in Figure 3.4 and on R-cut Al_2O_3 substrates in Figure 3.5.

The table 3.3 shows a summary of the results. There is no significant shift in the E_{2g} and A_{1g} peaks positions with increasing Re doping concentration on both substrates. This suggests that the in-plane vibrations or out-of-plane vibrations in the lattice are not significantly affected by Re doping, similar to some studies in the literature [29–34].

In the literature, the A_{1g} mode is particularly sensitive to doping in MoS_2 films; electron doping (n-type) results in a decrease in phonon frequency, also known as a red shift, due to the softening of the out-of-plane vibrations caused by the increased electron density screening. In contrast, the E^1_{2g} mode is less affected. For instance, Krishna et al. observed A_{1g} shifts of 4.5 cm^{-1} in monolayer MoS_2 after n-type chemical doping with benzyl viologen (BV). This shift reduced to 2.6 cm^{-1} in

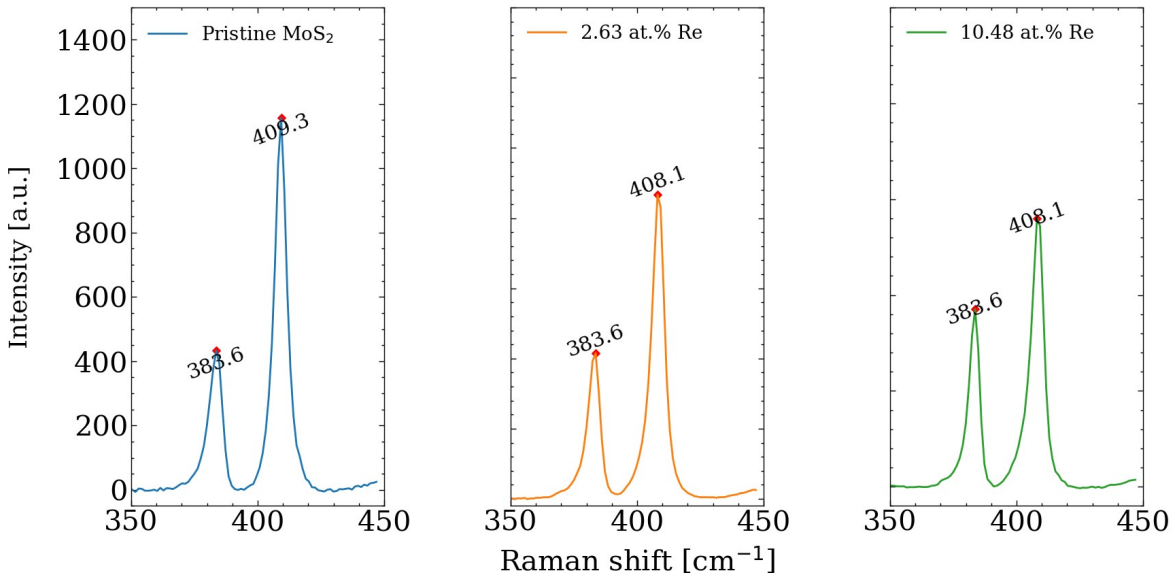

Figure 3.4: Raman spectroscopy results of pristine and Re-doped MoS_2 thin films on C-cut Al_2O_3 substrates with 532 nm (2.33 eV) laser line. The Raman spectra scan conditions and the laser power were kept constant for the samples, and the result was averaged over 20 scan points from different locations across the samples.

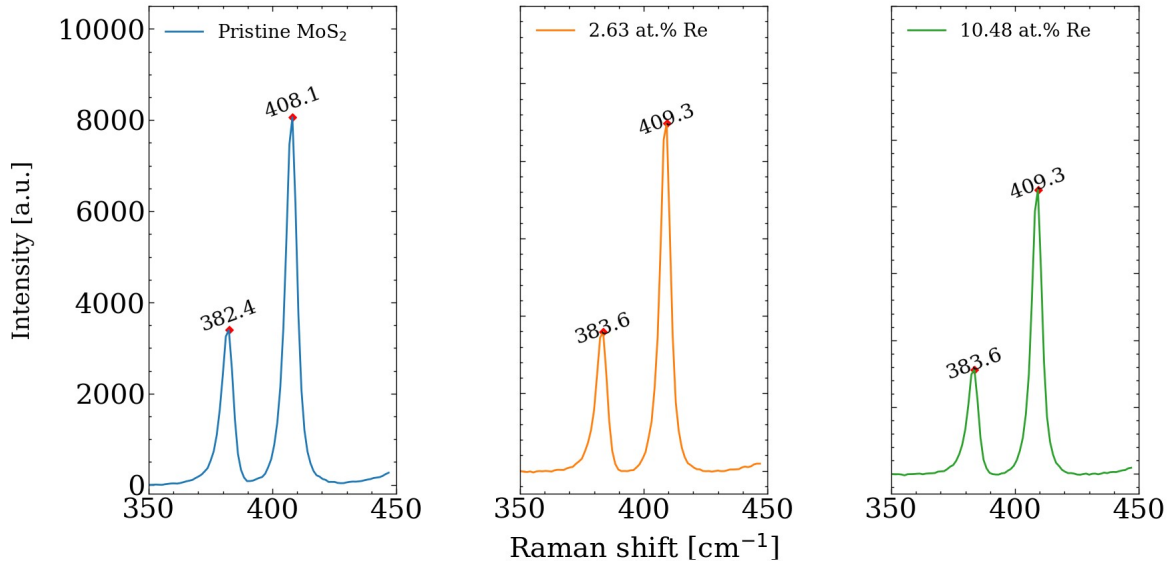

Figure 3.5: Raman spectroscopy results of pristine and Re-doped MoS_2 thin films on R-cut Al_2O_3 substrates with 532 nm (2.33 eV) laser line. The Raman spectra scan conditions and the laser power were kept constant for the samples, and the result was averaged over 20 scan points from different locations across the samples.

bilayer MoS_2 and disappeared in bulk MoS_2 when using the same amount of a 10 μL droplet of BV [35] in all thicknesses. Chee et al. [36] and Chakraborty et al. [37] also reported A_{1g} shifts to lower phonon frequencies upon n-type chemical doping. However, the observed peak shifts in these studies were less than 1 cm^{-1}. Consid-

Substrate	Doping Concentration	Mode	Raman Shift (cm^{-1})
R-cut	Pristine	E_{2g}	382.4
	2.63 at.% Re	E_{2g}	383.6
	10.48 at.% Re	E_{2g}	383.6
	Pristine	A_{1g}	408.2
	2.63 at.% Re	A_{1g}	409.3
	10.48 at.% Re	A_{1g}	409.3
C-cut	Pristine	E_{2g}	383.6
	2.63 at.% Re	E_{2g}	383.6
	10.48 at.% Re	E_{2g}	383.6
	Pristine	A_{1g}	409.3
	2.63 at.% Re	A_{1g}	408.1
	10.48 at.% Re	A_{1g}	408.1

Table 3.3: Raman shifts for E_{2g} and A_{1g} modes at different Re doping concentrations and Pristine MoS_2 films on R-cut and C-cut Al_2O_3 substrates.

ering the sensitivity of Raman spectra, which is approximately 0.75 cm^{-1} [38]. This value represents the smallest energy difference that can be reliably distinguished by the Raman spectrometer. Therefore, concluding the significant influence of n-type dopants on phonon modes becomes challenging.

3.3.4 X-Ray Diffraction

MoS_2 has a 2H crystal structure with a hexagonal crystal structure of the space group $P6_3/mmc$. The space group $P6_3/mmc$ can be described as follows: P indicates that it is a primitive lattice, meaning atoms are located only at the corners of the unit cell. 6_3 refers to a six-fold screw axis of rotation, which combines a rotation with a translation along the axis. And, mmc describes the presence of mirror planes and a center of symmetry in the crystal structure. Rhenium, on the other hand, has a space group $P6_3/mmc$, representing a hexagonal close-packed (hcp) crystal structure. This structure is characterized by two lattice parameters, $a \approx 2.76$ Å and $c \approx 4.46$ Å, indicating the hexagonal symmetry and the c/a ratio typical of hcp systems [39].

To obtain additional information on the crystallinity of the pristine and doped MoS_2, XRD was carried out on C-cut (0006) grown sapphire samples. The results are shown in Figure 3.6.

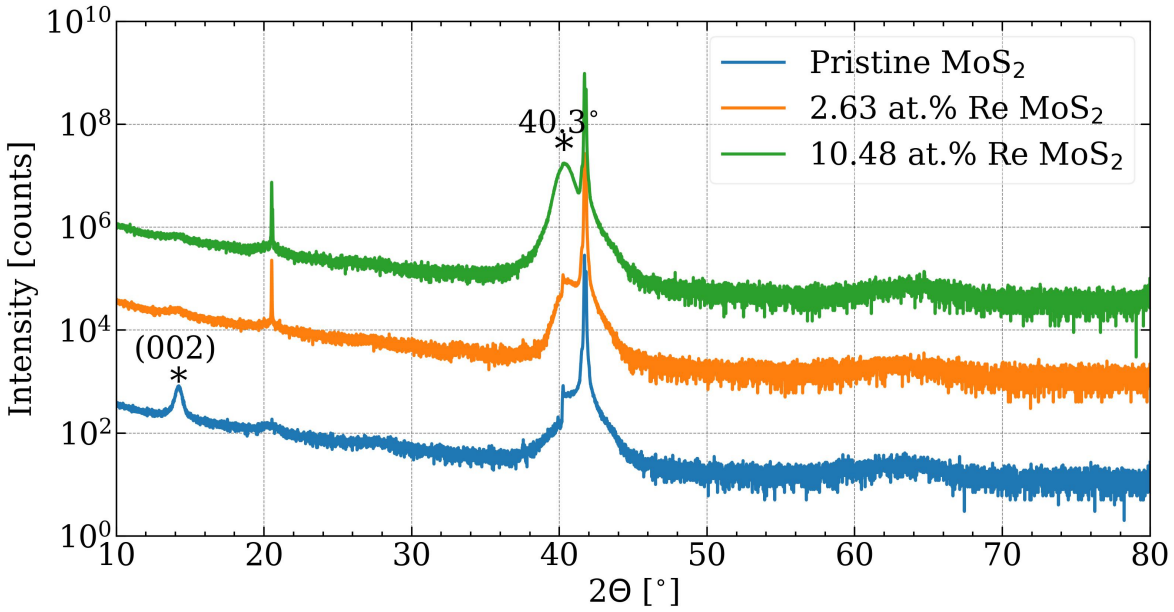

Figure 3.6: X-Ray Diffraction spectra. The graph shows the XRD scans of pristine, 2.63 at.% Re, and 10.48 at.% Re-doped MoS_2 films grown on C-cut Al_2O_3 with (0006) orientation. The asterisks represent the MoS_2 (103) orientation at 40.3° diffraction. The experimental diffraction patterns were compared with the reference diffraction data provided by the International Centre for Diffraction Data (ICDD) PDF card no. 00-037-1492, corresponding to hexagonal MoS_2 with a space group of $P6_3/mmc$.

For MoS_2 films, the (002) diffraction peak at 14.2° 2θ is a characteristic feature of the

2H phase of MoS_2 [40, 41], corresponding to the basal planes of the layered structure being oriented parallel to the substrate. This peak is typically the strongest in XRD patterns of MoS_2 films that grow with a horizontal alignment, where the c-axis is perpendicular to the substrate [42]. Pristine MoS_2 shows the (002) peak at 14.2° 2θ. However, for films with 2.63 at.% and 10.48 at.% Re doping, the (002) peak is very weak or almost invisible. This suggests that Re doping alters the growth mechanism, resulting in either vertical or polycrystalline growth. A TEM study, discussed in Section 3.3.5, provides further insights.

The absence of the (002) peak in the XRD pattern, while the presence of MoS_2 is confirmed by other characterization techniques (e.g., Raman spectroscopy, as shown in Section 3.3.3), indicates a different film orientation. In such cases, the MoS_2 layers may be aligned vertically, with their basal planes standing perpendicular to the substrate [43, 44]. This vertical growth changes the diffraction conditions, causing the (002) peak to disappear or become negligible in intensity, as the structure no longer satisfies the Bragg condition for that reflection [45].

Examples in the literature show the disappearance of the strongest characteristic (002) peak with doping. For instance, Laskar et al. demonstrated this effect with Nb doping in MoS_2 [46], while Wang et al. observed a similar trend with Mn doping, where varying levels of carrier doping were introduced [47].

Additionally, for the 10.48 at.% Re-doped MoS_2 film, a (103)-oriented MoS_2 peak is observed at 40.3° 2θ. This suggests that the diffraction plane is not parallel to the basal plane of the surface, and this doping level of the film exhibits vertical growth due to the absence of (00n) diffraction peaks in the spectra [48].

3.3.5 Transmission Electron Microscopy

The primary aim of utilizing Transmission Electron Microscopy (TEM) is, here, to investigate some aspects of the films, such as the presence and distribution of impurity atoms, and whether specific regions of the MoS_2 film show accumulation of Re atoms, as questioned in Section 3.1. Additionally, TEM is used to determine the orientation of the films (vertical or horizontal) and to examine the expansion coefficient of the films after conversion. Cross-sectional TEM serves as a reliable technique for measuring the final thickness of the films, alongside Atomic Force Microscopy, which is preferred when the films are rough, as XRR becomes less effective under such conditions. Roughness at the interface causes a loss in specular reflection because some X-rays are scattered diffusely instead of being reflected coherently. That is why XRR is not feasible with rougher films as fit is not possible, as shown in Figure 2.8.

For pristine MoS_2, 2.63 at.% Re-doped MoS_2, and 10.48 at.% Re-doped MoS_2 films, only one sample for each was prepared on an R-cut Al_2O_3 substrate. These same samples were used for low-temperature resistivity and Hall effect measurements before structural characterizations. The images presented in this section correspond to pristine and 10.48 at.% Re-doped MoS_2 films. For thickness analysis, MoS_2 films doped with 2.63 at.% Re were examined using AFM to determine the resultant thickness, as shown in Appendix A1.6. The shown images, here, with different scale bars represent different areas of each respective sample.

The High-Angle Annular Dark Field (HAADF-TEM) mode was utilized for pristine and 10.48 at.% Re-doped MoS_2 films grown on R-cut substrates. In HAADF-TEM, the intensity of the collected electrons is proportional to the atomic number of the elements in the sample, resulting in heavier elements appearing brighter in the images. This property makes HAADF-TEM particularly useful for detecting elements like Re, Mo and W. Figure 3.7 presents cross-sectional HAADF-TEM images of pristine MoS_2. These images reveal the growth orientation of MoS_2 layers on an R-cut

Al_2O_3 substrate and confirms the polycrystalline nature of it.

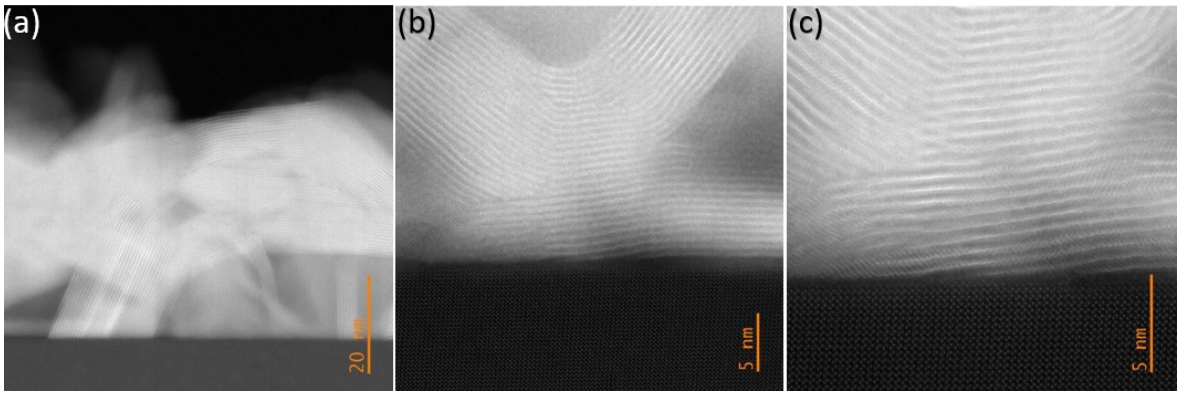

Figure 3.7: HAADF-TEM cross-sectional images of the pristine MoS_2 film. The thickness of the converted MoS_2 was found to be 49 nm, for intensity profile Appendix A1.5. Scale bars are on the images. Films shows relatively mix orientation and proves polycrystalline nature of it. For the analysis of pristine MoS_2 film, the film was prepared on an R-cut Al_2O_3 substrate and the same sample was used for low-temperature resistivity and Hall effect measurements. The presented images correspond to different areas of this single sample.

The lower magnification of (a) show the overall distribution and random orientation of the MoS_2 layers. It must be noted that MoS_2 layers can be easily bent and redirected during their growth while maintaining the interlayer van der Waals bond owing to high mechanical flexibility [49]. Therefore, the images show a random stacking with layers randomly rotated relative to each other. This random stacking suggests a lack of long-range order in the arrangement of the MoS_2 layers. The overall thickness of the pristine MoS_2 film was found to be 49 nm, intensity profile can be seen in Appendix A1.5. This detailed structural analysis shows that the expansion coefficient from Mo to MoS_2 is around 2.45 [50], indicating the change as Mo transitions to MoS_2. This ratio is found by comparing the initial XRR thickness before conversion and TEM intensity profile after conversion, shown in a Appendix A1.1.1. The literature maintains the film expansion coefficient in a relatively large range from 2.5 [51] to 4 [52]. However, the presented studies utilized atomic force microscopy, where dirt attached to the tip and moisture influence the interaction between the tip and the surface, leading to an extra thickness of a few nanometers [53]. The higher magnification images (b) and (c) provide detailed insights into the crystalline nature of the MoS_2 layers, showing well-defined and uniformly spaced

layers.

For the analysis of 10.48 at.% Re-doped MoS_2 films, similar to pristine MoS2, HAADF-TEM is employed as shown in Figure 3.8. The TEM image of the 10.48 at.% Re-doped MoS_2 film reveals the presence of Re atoms. It is observed that the Re atoms tend to cluster in regions of the film that are close to the substrate.

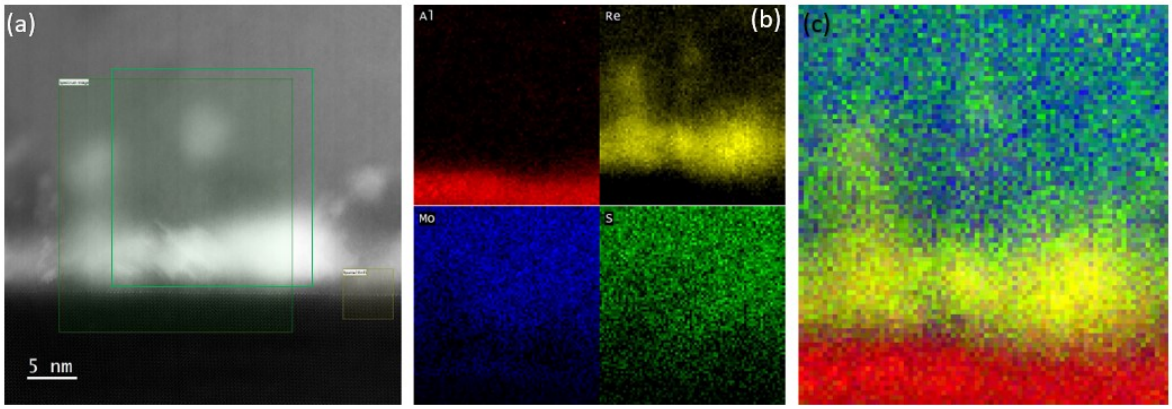

Figure 3.8: Compositional Analysis of 10.48 at.% Re-doped MoS_2 film. (a) shows the HAADF-TEM image revealing substitutional Re atoms as brighter spots in MoS_2 matrix, clustering near the substrate. (b) provides elemental mapping for Re, Mo, and S in the green highlighted region of (a).(c) is a composite map showing the spatial distribution of these elements. Scale bars are on the images. For the analysis of 10.48 at.% Re doped MoS_2 film, the film was prepared on an R-cut Al_2O_3 substrate and the same sample was used for low-temperature resistivity and Hall effect measurements. The presented images correspond to different areas of this single sample.

The Figure 3.8 (a) shows the segregated Re atoms, due to their higher atomic number, appear brighter than the surrounding MoS_2 matrix [54]. The brighter spots confirm the Re atoms. The Figure 3.8 (b) shows the elemental mapping of the chosen region, inside the green square in Figure 3.8 (a), with separate images for Re, Mo, S and Al indicating where these elements are localized within the sample. Figure 3.8 (c) is a composite image of the elemental maps, showing the spatial distribution of Re, Mo, Al, and S together.

Furthermore, to learn the concentration of Re atoms in the MoS_2 film, Figure 3.9 is presented. Note that EELS presents atomic percentages based on the signal of the elements counted in the chosen region. For EELS analysis, the detection of specific electron shells (K, L, M) for different elements is influenced by their atomic structure and the binding energies of their electrons [55].

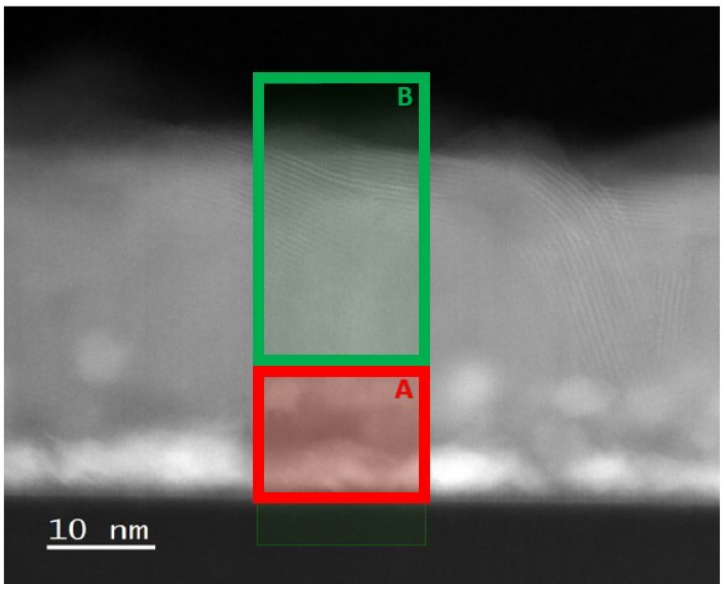

A

Element	Shell	Comp. (at.%)
Re	M	8.0 ± 1.5
S	K	63 ± 2
Mo	L	29 ± 2

Table A: Composition Results for Region A

B

Element	Shell	Comp. (at.%)
Re	M	1.1 ± 0.2
S	K	69 ± 2
Mo	L	30 ± 2

Table B: Composition Results for Region B

Figure 3.9: A TEM image of the 10.48 at.% Re-doped MoS_2 film highlights the region where EELS analysis was conducted. The thickness of the 10.48 at.% Re-doped MoS_2 is found to be 41 nm, as shown in the intensity profile in Appendix A1.7, and also in the scale bar here. The dopant Re (Z = 75) appears in brighter contrast in the HAADF-TEM images due to the significant difference in atomic number between Mo (Z = 42) and S (Z = 16), as shown on the left. The table on the right illustrates the distribution of Re, Mo, and S elements in the selected areas, with two different colorings indicating the distinct regions. The red area, labeled as A, shows the region closer to the substrate, while the green area, labeled as B, represents the area farther from the substrate. In comparison, the Rhenium content, in terms of at.%, increases, whereas the ratios of the other elements remain relatively constant.

For Re, the M-shell peaks are particularly accessible and prominent due to their lower energy losses. In contrast, for S, the K-shell peak is significant owing to its fewer electrons and overall lower binding energies, making the K-shell feature more pronounced. For Mo, the L-shell peaks are important because they are more easily ionized compared to K-shell electrons and fall within the detectable energy range for EELS [55]. The red area in Figure 3.9 (A), at the interface with the substrate, is where the Re atoms have accumulated. The EELS data for this region indicates a high concentration of Re atoms, with the composition results showing approximately 8.0 at.% Re. This accumulation of Re atoms at the interface suggests that Re tends to segregate to the bottom regions of the film. Similar results were published by Yadgarov et al., who observed that Re atoms self-assemble into an ordered monolayer on the substrate and substitute for molybdenum atoms within the monolayer

MoS_2 lattice [56] during growth at 810°. Additionally, Dulaimi et al. observed Re clustering in MoS_2 films, causing a change in morphology from lamellar to clustered structures with increased concentration at 6 mol% during growth at 475° [57, 58].

Figure 3.9 (B) represents the top region of the MoS_2 film. The EELS analysis for this region reveals a lower concentration of Re atoms (around 1.1 at.%), whereas the Mo and S contributions are similar to those in Panel (A). This analysis provides information about the distribution and accumulation of Re atoms in the MoS_2 film for the chosen regions. The preferential orientation of the films is observed, showing the polycrystalline nature of the MoS_2 films [43, 44, 50]. With 10.48 at.% Re-doped MoS_2, the orientation appears to be more vertical. Based on the presented results, this observation might suggest an influence of Re doping on the crystallographic orientation of the MoS_2 layers. However, TEM focuses on a very small area, approximately 2400 nm^2 at maximum. Hence, drawing a solid conclusion is not realistic. This will be further discussed in the Discussion section 3.4.

Unlike pristine MoS_2, the thickness of the 10.48 at.% Re-doped MoS_2 is found to be 41 nm, as shown in the intensity profile in Appendix A1.7. This can be explained by Re atoms accumulating instead of joining the MoS_2 lattice. Similar behavior is observed in other studies, where Mo is not fully converted in pristine MoS_2 [59] during TAC growth.

3.3.6 Low temperature resistivity measurements

Low-temperature resistivity measurements are used to understand the conduction mechanisms in semiconducting materials. By analyzing how resistivity or resistance varies with temperature, insights can be gained about carrier activation, defect states, and material quality. An Arrhenius plot, which represents $\ln(R)$ versus $\frac{1}{T}$, is commonly used to evaluate thermally activated conduction, more details provided in Section 2.7.4. In this plot, a linear relationship indicates that resistance follows an exponential temperature dependence, and the slope of the line provides the activation energy (E_a), a critical parameter reflecting the energy barrier for charge carrier excitation [1]. Figure 3.10 shows temperature dependent resistance and $\ln(R)$ analysis of MoS_2 films with varying Rhenium concentrations, grown on R-cut Al_2O_3 substrates.

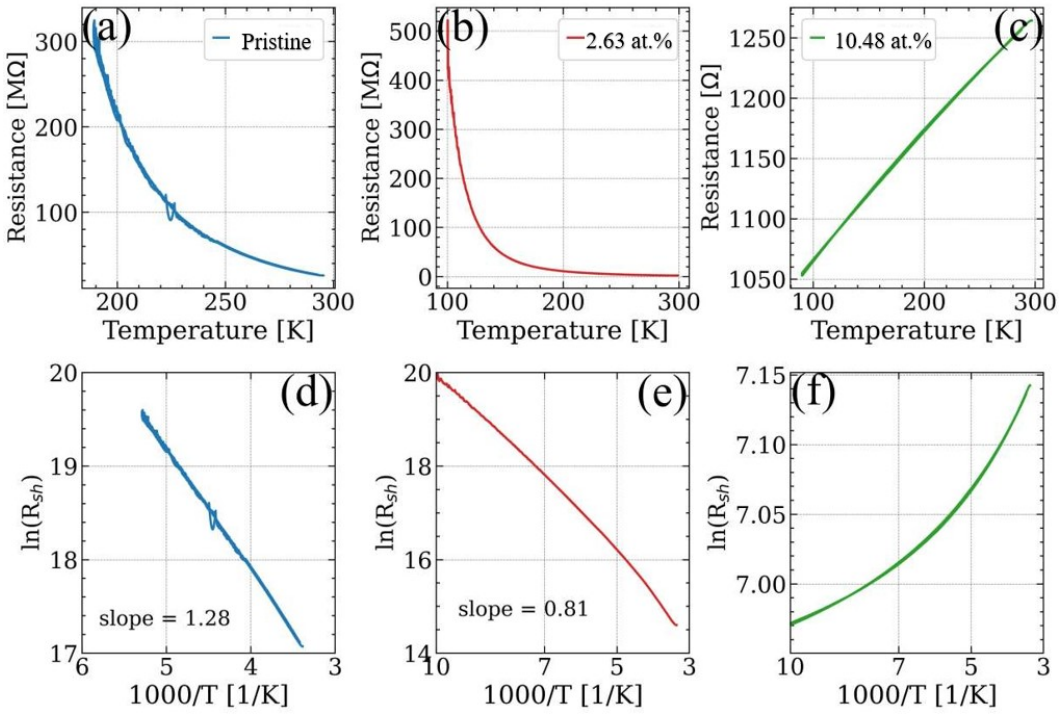

Figure 3.10: Temperature dependent resistance and $\ln(R)$ analysis of MoS_2 films with varying Rhenium concentrations that grown on R-cut. (a), (b), and (c) show the resistance as a function of temperature for pristine, 2.63 at.%, and 10.48 at.% Rhenium-doped MoS_2, respectively. (d), (e), and (f) represent $\ln(R)$ vs. $1/T$ plots for the same samples. The slope values (1.28 for pristine, 0.81 for 2.63 at.%, and nonlinear behavior for 10.48 at.%) indicate Arrhenius-type conduction for pristine and 2.63 at.% films, while the 10.48 at.% film deviates, showing metallic behavior.

The initial resistance values for the MoS_2 samples are approximately 100 MΩ for the pristine sample, 5 MΩ for the 2.63 at.% Rhenium-doped sample, and 1.2 kΩ for the 10.48 at.% Rhenium-doped sample. This indicates a significant decrease in resistance with increasing Rhenium doping. It can be seen from Figure 3.10 (a),(d) that pristine MoS_2 exhibits semiconductor behavior. The linearity of panel (d) indicates that the resistivity follows an Arrhenius-type behavior so excitation conduction, where the conductivity increases exponentially with temperature. The slope, which is 1.28, corresponds to an activation energy of approximately 110.2 meV for charge carriers to conduct, calculations can be found in the Appendix A1.4.

Introducing 2.63 at.% Rhenium into MoS_2 reduces the activation energy for conduction to approximately 69.8 meV, Figure 3.10 (b),(e). Rhenium atoms likely introduce donor levels close to the conduction band, facilitating easier excitation of electrons into the conduction band [19, 39]. The lower slope (e), 0.81, signifies that charge carriers require less thermal energy to move, leading to increased conductivity. The material still shows semiconductor behavior but with improved conductive properties.

For a 10.48 at.% Rhenium concentration, Figure 3.10 (c) and (f), the behavior deviates from the typical Arrhenius-type and exhibits metallic behavior, as resistance increases with temperature—characteristic of metallic films [1].

In literature, lower activation energies, such as 0.18 eV and 0.19 eV, have been reported for TAC-grown pristine MoS_2 films with lower thicknesses (around 10 nm) [59]. These lower values are attributed to shallow dopant levels, which lie close to the conduction (n-type) or valence (p-type) band and require minimal thermal energy (around 0.1 eV) to ionize [60]. Another study shows that lithium intercalation into the van der Waals gaps of MoS_2 induces structural distortions and disorder, forming localized states within the bandgap. These states reduce the activation energy for charge carriers to transition from the valence to the conduction band, enhancing electrical conductivity [12].

3.3.7 Hall Effect Measurement

The Hall effect measurement is utilized to determine electrical properties of materials, such as carrier concentration, carrier type, and mobility, the detail information is provided in Section 2.7.5. The Hall measurement was conducted using a system provided by Lakeshore, which is designed to streamline the process. After providing the film thickness as an input parameter and connecting the MoS_2 film edges to the probes of the Hall setup, the system automatically calculates and outputs the necessary electrical properties [61]. The thicknesses of the films, after conversion, shown in Appendix A1.5, A1.6, and A1.7.

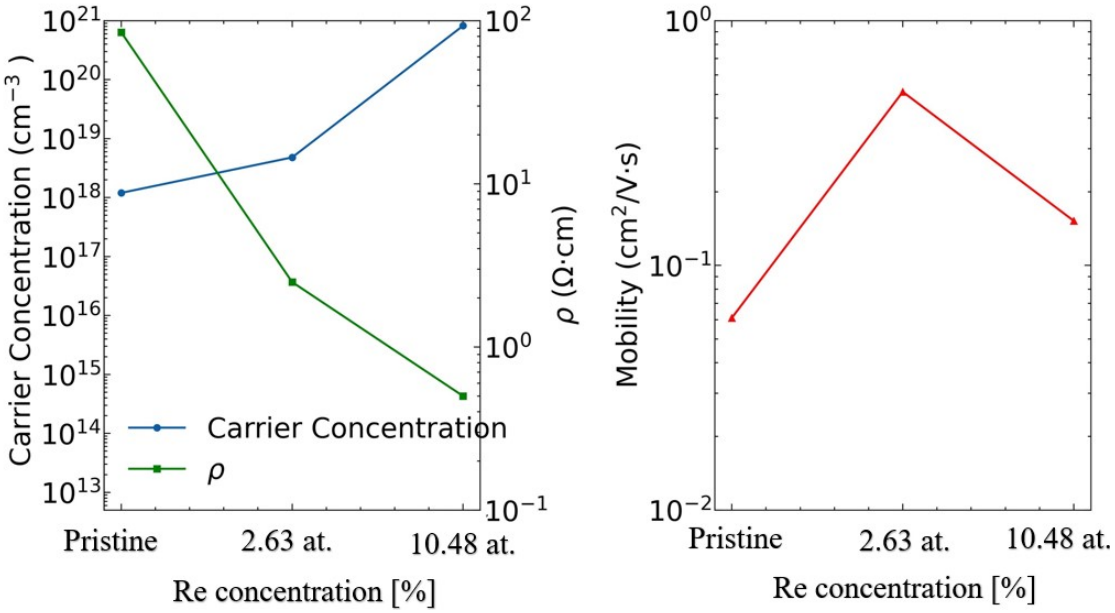

Figure 3.11: The left graph reveals that both the carrier concentration and sheet carrier concentration change along with increased Re impurities. The right graph shows the change in mobility versus Re concentration.

One of the most important parameters in Hall effect measurements is the Hall coefficient (R_H). The sign of R_H indicates the type of charge carriers in the material: a positive ($+R_H$) value signifies that the dominant carriers are holes (p-type conductivity), whereas a negative ($-R_H$) value indicates that the dominant carriers are electrons (n-type conductivity). This allows the identification of the material's doping type, such as n-type or p-type semiconductors. Furthermore, R_H enables the calculation of carrier concentration n, where a positive R_H represents hole concen-

tration and a negative R_H represents electron concentration. Additionally, the Hall coefficient is crucial for determining the mobility (μ) of charge carriers when combined with resistivity (ρ). For thin films, R_H is also used to calculate the sheet carrier concentration (n_s) by relating the Hall coefficient per square to the charge carrier density, shown in Section 2.7.5. These calculations underscore the significance of R_H in understanding material properties, as reflected in the values presented in Table 3.4. Besides, the figure of merit for electrical characterization is presented in Figure 3.11. The graphs illustrate the relationship between Rhenium concentration and the electrical properties of MoS_2 films.

Parameter	**Pristine**	**2.63 at.% Re**	**10.48 at.% Re**
Resistivity (ρ) [$\Omega \cdot$ cm]	85	2.5	0.05
Carrier Concentration (n) [cm^{-3}]	1.20×10^{18}	4.8×10^{18}	8.22×10^{20}
Hall Coefficient (R_H) [cm^3/C]	5.2	-1.28	-0.0076
Carrier Type	p	n	n
Thickness (t) [nm]	49	50	41
Sheet Resistivity (R_s) [Ω/sq]	1.73×10^7	5.0×10^5	1.22×10^4
Sheet Hall Coefficient (R_{Hsheet}) [cm^2/C]	2.55×10^{-5}	6.4×10^{-6}	3.12×10^{-8}
Sheet Carrier Concentration (n_s) [cm^{-2}]	5.89×10^{12}	2.44×10^{13}	3.37×10^{15}
Mobility (μ) [$cm^2/V{\cdot}s$]	0.061	0.5125	0.152

Table 3.4: Experimental results from 4-point measurements using Van der Pauw configuration, as well as AC Hall-effect measurements of pristine and Re-doped MoS_2 films, were conducted on films grown on R-cut Al_2O_3 substrates. The Hall factor was assumed to be unity. The necessary thicknesses of the samples provided in Appendix for Pristine MoS_2:A1.5, for 2.63 at.% Re: A1.6, for 10.48 at.% Re: A1.7.

Pristine MoS_2 showed p-type characteristic whereas other concentration showed n-type characteristics, as can be seen from Hall coefficient polarity. Potential reason of p-type of pristine MoS_2 can be accounted for the oxygen content in the MoS_2 matrix [62, 63]. Neal et. al, showed that oxygen incorporation alters the local charge distribution within MoS_2. Due to oxygen's higher electronegativity compared to sulfur, oxygen atoms pull electrons from nearby molybdenum atoms, creating an

imbalance that promotes hole conduction. This charge redistribution supports the formation of acceptor levels and enhances the material's ability to transport holes [62].

In figure 3.11, the first graph (left) reveals that the carrier concentration increases and resistivity decreases with higher Re doping. Specifically, the bulk carrier concentration rises from $1.20 \times 10^{18} cm^{-3}$ at Pristine to $4.8 \times 10^{18} cm^{-3}$ at 2.63 at.% Re and $8.22 \times 10^{20} cm^{-3}$ at 10.48 at.% Re, while the resistivity decreases from 85 ohm.cm to 2.5 ohm.cm and then 0.5 ohm.cm over the same doping range. It can be surmised that pristine and 2.63 at.% Re-doped MoS_2 films exhibit heavily doped p-type and n-type behavior consecutively, as shown in Figure 1.6. These heavily doped films demonstrate low resistivity and can be utilized in areas where heavily doped source and drain regions are required to create conductive pathways for charge carriers in a transistor [1].

The results indicates that Re doping enhances the number of charge carriers, reducing resistivity, thereby improving the material's conductivity. Similar work by Romanov et al. on monolayer MoS_2 shows the same behavior. However, with stabilized 1T-MoS_2 phase formation by Re doping, the resistivity of the films was found to be reduced by 130 times compared to the pristine sample in their work [64].

The second graph (right) in Figure 3.11 shows that mobility exhibits a non-linear relationship with Re concentration. Mobility peaks at 2.63 at.% Re, reaching 0.5125 $cm^2/V{\cdot}s$, but decreases at both lower and higher concentrations, with a notable drop to 0.061 $cm^2/V{\cdot}s$ at Pristine and 0.1705 $cm^2/V{\cdot}s$ at 10.48 at.% Re. This suggests that there is an optimal Re doping level around 2.63 at.% that maximizes mobility, while higher doping levels may introduce scattering mechanisms that reduce mobility [65]. The expectation from electrical characterization is to achieve the highest possible mobility to enable the use of the films in integrated circuits for high-speed electronic applications. However, the results show very low mobilities, similar to those observed in TAC TMD films [66].

The dopant concentrations for pristine and 2.63 at. % Re films are located in the normal dope regime as shown in Figure 1.6

3.4 Discussion

Transmission electron microscopy (TEM) and electron energy loss spectroscopy (EELS) analyses reveal that Re atoms tend to segregate towards the bottom of the substrate, forming Re-rich regions that locally enhance conductivity near the substrate interface. Since the deposition occurs via co-sputtering at room temperature with no thermal input before sulfurization, it is unlikely that Re atoms segregate prior to the conversion process. A very recent paper showed at high dopant concentrations (> 1 atom%), significant Re clustering throughout the Re-MoS_2 lattice are revealed by TEM measurements [19]. There was no Re clustering prior to temperature input.

The presence of Re in the MoS_2 matrix after conversion is critical for understanding the doping effects. Raman spectroscopy only showed the characteristic of MoS_2 peaks independent from the substrate and independent from the introduce dopant contents. However, XRD did not confirm this presence due to atomic displacement caused by Re doping, which disrupts the crystal structure sufficiently to disturb periodicity along certain crystallographic planes, leading to the disappearance of specific XRD peaks [67]. It is necessary to quantify the amount of Rhenium after the conversion. The current TEM-EDS results reveal the atomic percentages however they only focuses on a small areas ($\approx 2400\,\mathrm{nm}^2$). More statistical results are necessary for imaging, it will be discuss in the Future work.

The rapid sulfur diffusion along the van der Waals layers, influenced by the sulfur partial vapor pressure, the details are shared in the Section 3.3.2, contributes to this orientation diversity. This variation might also explain the absence of XRD peaks in Re-doped MoS_2 samples, except for the undoped ones, as the XRD configuration aligns the basal planes parallel to the substrate surface and may fail to detect

vertically aligned planes [68].

Theoretical calculations suggest that higher concentrations of Re impurities localize in the MoS_2 lattice, forming a mini-band below the conduction band [56]. This aligns with our findings, where lowered activation energy in Re-doped MoS_2 allows charge carriers easier access to the conduction band, utilizing additional energy levels provided by Re impurities [15, 69].

At high doping levels (10.48 at.% Re), Re diffuses along and against the growth direction, accumulating at the substrate interface in a metallic form. These Re clusters locally alter conductivity at the film's bottom. The Hall effect measurement, encompassing the entire conductive path, could be influenced by these clusters. This behavior was also observed by Li et al., who noted challenges in achieving a homogeneous matrix after substantial Re incorporation in single-layer MoS_2 [70]. However, the reliability of TEM images may be limited due to their small sampled areas.

The Hall coefficient of a 10.48 at.% Re-doped MoS_2 sample showed negative polarity, which is a signature of n-type behavior in MoS_2. However, as explained by Munson et al. [19], at higher doping concentrations (3.6 at.% and above), clustering of Re atoms reduces the efficiency of n-type doping due to increased ionization energy. When Re atoms are isolated, their ionization energy is relatively low, facilitating electron donation. In clustered Re atoms, their electronic states overlap, and interactions between the dopants increase the ionization energy, making it more difficult for these Re atoms to donate electrons to the MoS_2 lattice. It is important to note that Munson et al. conducted their experiments using monolayer MoS_2 [19].

Lastly, it might be considered necessary for the dopants in the MoS_2 matrix to be measured after the conversion. This will be addressed in the future work.

3.5 Conclusion

This study investigates the impact of rhenium doping on the structural and electrical properties of MoS_2 films. Re impurities were introduced into Mo stacks using a co-sputtering magnetron system, and the effects of doping were analyzed through characterization techniques. The films were successfully grown, as confirmed by Raman spectroscopy, with characteristic peaks serving as proof of the material's identity. However, the substrate type and rhenium content did not influence the Raman spectroscopy results, indicating that the vibrational modes of MoS_2 remain unaffected by these factors.

X-ray diffraction analysis revealed significant structural changes with increased Re content. A more vertical growth pattern was observed in the 10.48 at.% Re sample compared to the undoped film, along with peak deterioration. The (103) orientation of MoS_2 appeared exclusively in the highest doped sample, highlighting the influence of Re doping on crystallographic texture.

Thermal activation behavior, examined using Arrhenius plots, demonstrated improved conductivity and reduced activation energy at optimal doping levels around 2.63 at.% Re. However, deviations from simple thermal activation behavior at 10.48 at.% Re suggest a shift in conduction mechanisms, indicating an interplay between Re concentration and carrier dynamics.

Hall measurements confirmed substantial changes in carrier concentration and mobility due to Re doping. The carrier concentration increased from 10^{18} cm^{-3} for pristine MoS_2 to 10^{20} cm^{-3} for the 10.48 at.% Re-doped sample. The highest mobility, 0.51125 $cm^2/V{\cdot}s$, was observed at 2.63 at.% Re, while lower mobilities were recorded for pristine MoS_2 (0.152 $cm^2/V{\cdot}s$) and 10.48 at.% Re (0.061 $cm^2/V{\cdot}s$). These results confirm the n-type influence of Re impurities and their role in enhancing electrical properties up to an optimal doping level.

Transmission electron microscopy provided insights into the elemental distribution

within the films. Re segregation was observed near the bottom regions of the substrate, while Re incorporation into the MoS_2 matrix was also confirmed. These findings suggest preferential accumulation of Re during high-temperature conversion at 900 °C. Furthermore, the presence of Re in the film influenced the orientation of MoS_2, with the (103) orientation appearing at 40.3° in the 10.48 at.% Re-doped sample, showing a tendency toward vertical alignment.

3.5.1 Number of Devices and repeatability

The table 3.5 summarizes the substrates used to characterize pristine and Re-doped MoS_2 films. The films grown on R-cut Al_2O_3 for TEM analysis were subsequently used for low-temperature resistivity and Hall effect measurements, as well as Raman spectroscopy and XRR.

Table 3.5: Number of devices for pristine and Re-doped MoS_2 samples. The numbers in parentheses next to the substrate in the table indicate the total number of devices.

Sample	**XRR**	**XRD**	**Raman**	**TEM**	**Hall Effect**
Pristine MoS_2	Rcut(1)	Ccut(1)	R+Ccuts(6)	Rcut(1)	Rcut(1)
2.63 at.% Re-MoS_2	Rcut(1)	Ccut(1)	R+Ccuts(6)	Rcut(1)	Rcut(1)
10.48 at.% Re-MoS_2	Rcut(1)	Ccut(1)	R+Ccuts(6)	Rcut(1)	Rcut(1)

The reproducibility of the films, considering the same characterization techniques will be applied with the same compositions, is very high when the same samples are used consistently for characterization.

3.6 Future Work

The findings of this study necessitates several areas for further investigation to understand the rhenium doping effects in MoS_2 films and to optimize their structural and electrical properties for practical applications.

Firstly, it is imperative to quantitatively measure the Re dopant concentration within the MoS_2 matrix after the conversion process. Advanced characterization tech-

niques such as atom probe tomography (APT), secondary ion mass spectrometry (SIMS) with higher spatial resolution could provide precise dopant distribution profiles. These measurements would validate the extent of Re incorporation and help correlate dopant concentration with the observed electrical and structural properties.

Secondly, the apparent discrepancy between Raman spectroscopy and X-ray diffraction results necessitates a more detailed analysis. While Raman spectroscopy showed the characteristic MoS_2 peaks regardless of substrate type or Re content, XRD did not confirm the presence of Re within the lattice. Employing synchrotron XRD could enhance detection sensitivity to subtle structural changes induced by Re doping. Additionally, transmission electron microscopy studies with multiple sampled areas could provide more reliable insights into the microstructural changes and Re distribution.

Thirdly, to address the influence of sulfur flow rate on the orientation diversity of MoS_2 films, systematic experiments varying the sulfur partial pressure and flow rate are necessary. Understanding the relationship between sulfurization parameters and film orientation could lead to controlled synthesis of films with desired crystallographic textures, potentially improving their electronic properties.

Additionally, expanding the sample set by fabricating and testing more Re-doped MoS_2 films with varying doping levels and substrate types will enhance the statistical significance of the results. This would also allow for optimization of the doping concentration to achieve the best trade-off between conductivity enhancement and structural integrity.

Finally, exploring the electrical properties of the films at different temperatures and under varying environmental conditions could provide insights into the stability and performance of Re-doped MoS_2 in real-world applications. Long-term stability tests and device fabrication experiments would be valuable for assessing the practical potential of these materials.

In summary, future work should focus on:

- Quantitative measurement of Re dopant concentration and distribution post-conversion.
- Systematic study of sulfurization parameters to control film orientation.
- Fabrication and testing of additional samples to optimize doping levels and validate findings.
- Evaluation of electrical properties under varying conditions for application assessment.
- Measurement of dopants in the MoS_2 matrix after conversion to validate Re incorporation.

These efforts will contribute to the understanding of Re-doped MoS_2 films.

References

(1) S. M. Sze, Y. Li and K. K. Ng, *Physics of semiconductor devices*, John wiley & sons, 2021.

(2) D. Lembke, S. Bertolazzi and A. Kis, *Accounts of chemical research*, 2015, **48**, 100–110.

(3) M. Houssa, K. Iordanidou, A. Dabral, A. Lu, G. Pourtois, V. Afanasiev and A. Stesmans, *ACS Applied Nano Materials*, 2019, **2**, 760–766.

(4) S. McDonnell, R. Addou, C. Buie, R. M. Wallace and C. L. Hinkle, *ACS nano*, 2014, **8**, 2880–2888.

(5) V. K. Sangwan and M. C. Hersam, *Annual review of physical chemistry*, 2018, **69**, 299–325.

(6) P. Bampoulis, R. van Bremen, Q. Yao, B. Poelsema, H. J. Zandvliet and K. Sotthewes, *ACS applied materials & interfaces*, 2017, **9**, 19278–19286.

(7) Y. Guo, D. Liu and J. Robertson, *Applied Physics Letters*, 2015, **106**.

(8) H. Jin, E. Debroye, M. Keshavarz, I. G. Scheblykin, M. B. Roeffaers, J. Hofkens and J. A. Steele, *Materials Horizons*, 2020, **7**, 397–410.

(9) J. Hong, Z. Hu, M. Probert, K. Li, D. Lv, X. Yang, L. Gu, N. Mao, Q. Feng, L. Xie et al., *Nature communications*, 2015, **6**, 6293.

(10) Y. Zhu, J. Lim, Z. Zhang, Y. Wang, S. Sarkar, H. Ramsden, Y. Li, H. Yan, D. Phuyal, N. Gauriot et al., *ACS nano*, 2023, **17**, 13545–13553.

(11) S. Chen, J. Gao, B. M. Srinivasan, G. Zhang, M. Yang, J. Chai, S. Wang, D. Chi and Y.-W. Zhang, *ACS applied materials & interfaces*, 2019, **11**, 46090–46100.

(12) J. Hrdá, M. Moško, I. Píš, T. Vojteková, L. Pribusová Slušná, P. Hutár, M. Precner, E. Dobročka, M. Španková, M. Hulman et al., *Applied Physics Letters*, 2024, **124**.

(13) K. Zhang, B. M. Bersch, J. Joshi, R. Addou, C. R. Cormier, C. Zhang, K. Xu, N. C. Briggs, K. Wang, S. Subramanian et al., *Advanced Functional Materials*, 2018, **28**, 1706950.

(14) J. Suh, T. L. Tan, W. Zhao, J. Park, D.-Y. Lin, T.-E. Park, J. Kim, C. Jin, N. Saigal, S. Ghosh et al., *Nature communications*, 2018, **9**, 199.

(15) B. Xia, P. Liu, Y. Liu, D. Gao, D. Xue and J. Ding, *Applied Physics Letters*, 2018, **113**.

(16) S. H. Woo, L. Yadgarov, R. Rosentsveig, Y. Park, D. Song, R. Tenne and S. Y. Hong, *Israel Journal of Chemistry*, 2015, **55**, 599–603.

(17) Z. Cai, T. Shen, Q. Zhu, S. Feng, Q. Yu, J. Liu, L. Tang, Y. Zhao, J. Wang, B. Liu et al., *Small*, 2020, **16**, 1903181.

(18) T. Hallam, S. Monaghan, F. Gity, L. Ansari, M. Schmidt, C. Downing, C. P. Cullen, V. Nicolosi, P. K. Hurley and G. S. Duesberg, *Applied Physics Letters*, 2017, **111**.

(19) K. T. Munson, R. Torsi, F. Habis, L. Huberich, Y.-C. Lin, Y. Yuan, K. Wang, B. Schuler, Y. Wang, J. B. Asbury et al., *Advanced Electronic Materials*, 2024, 2400403.

(20) P. Hays, M. Sayyad, C.-L. Wu, S. Tongay and S. Susarla, *Understanding the Distribution of Rhenium Dopants in Monolayer Molybdenum Disulfide*, 2023.

(21) A. Glavic and M. Björck, *Journal of applied crystallography*, 2022, **55**, 1063–1071.

(22) J. Kwon, J.-Y. Lee, Y.-J. Yu, C.-H. Lee, X. Cui, J. Hone and G.-H. Lee, *Nanoscale*, 2017, **9**, 6151–6157.

(23) X. Ling, L. Liang, S. Huang, A. A. Puretzky, D. B. Geohegan, B. G. Sumpter, J. Kong, V. Meunier and M. S. Dresselhaus, *Nano letters*, 2015, **15**, 4080–4088.

(24) A. Molina-Sanchez and L. Wirtz, *Physical Review B*, 2011, **84**, 155413.

(25) C. Lee, H. Yan, L. E. Brus, T. F. Heinz, J. Hone and S. Ryu, *ACS nano*, 2010, **4**, 2695–2700.

(26) S. J. Sandoval, D. Yang, R. Frindt and J. Irwin, *Physical Review B*, 1991, **44**, 3955.

(27) B. Chakraborty, H. R. Matte, A. Sood and C. Rao, *Journal of Raman Spectroscopy*, 2013, **44**, 92–96.

(28) H. Li, Q. Zhang, C. C. R. Yap, B. K. Tay, T. H. T. Edwin, A. Olivier and D. Baillargeat, *Advanced Functional Materials*, 2012, **22**, 1385–1390.

(29) A. Michail, N. Delikoukos, J. Parthenios, C. Galiotis and K. Papagelis, *Applied Physics Letters*, 2016, **108**.

(30) R. Rao, A. E. Islam, S. Singh, R. Berry, R. K. Kawakami, B. Maruyama and J. Katoch, *Physical Review B*, 2019, **99**, 195401.

(31) Y. Jin, Z. Zeng, Z. Xu, Y.-C. Lin, K. Bi, G. Shao, T. S. Hu, S. Wang, S. Li, K. Suenaga et al., *Chemistry of Materials*, 2019, **31**, 3534–3541.

(32) M. W. Iqbal, K. Shahzad, R. Akbar and G. Hussain, *Microelectronic Engineering*, 2020, **219**, 111152.

(33) J. S. Lee, C.-S. Park, T. Y. Kim, Y. S. Kim and E. K. Kim, *Nanomaterials*, 2019, **9**, 1278.

(34) J.-K. Qin, W.-Z. Shao, C.-Y. Xu, Y. Li, D.-D. Ren, X.-G. Song and L. Zhen, *ACS Applied Materials & Interfaces*, 2017, **9**, 15583–15591.

(35) K. P. Dhakal, D. L. Duong, J. Lee, H. Nam, M. Kim, M. Kan, Y. H. Lee and J. Kim, *Nanoscale*, 2014, **6**, 13028–13035.

(36) S.-S. Chee, C. Oh, M. Son, G.-C. Son, H. Jang, T. J. Yoo, S. Lee, W. Lee, J. Y. Hwang, H. Choi et al., *Nanoscale*, 2017, **9**, 9333–9339.

(37) B. Chakraborty, A. Bera, D. Muthu, S. Bhowmick, U. V. Waghmare and A. Sood, *Physical Review B*, 2012, **85**, 161403.

(38) M. Sojková, E. Dobročka, P. Hutár, V. Tašková, L. P. Slušná, R. Stoklas, I. Píš, F. Bondino, F. Munnik and M. Hulman, *Applied Surface Science*, 2021, **538**, 147936.

(39) R. Torsi, K. T. Munson, R. Pendurthi, E. Marques, B. Van Troeye, L. Huberich, B. Schuler, M. Feidler, K. Wang, G. Pourtois et al., *ACS nano*, 2023, **17**, 15629–15640.

(40) A. Pandey, S. Dutta, A. Kumar, R. Raman, A. K. Kapoor and R. Muralidhran, *Adv. Mater. Lett*, 2016, **7**, 777–782.

(41) S. H. Aleithan, K. Al-Amer, Z. Alhashem, N. A. Alati, Z. H. Alabbad and K. Alam, *AIP Advances*, 2022, **12**.

(42) R. G. Dickinson and L. Pauling, *Journal of the American Chemical Society*, 1923, **45**, 1466–1471.

(43) M. Sojková, K. Vegso, N. Mrkyvkova, J. Hagara, P. Hutár, A. Rosová, M. Čaplovičová, U. Ludacka, V. Skákalová, E. Majková et al., *RSC advances*, 2019, **9**, 29645–29651.

(44) N. Abdelazim, Y. J. Noori, S. Thomas, V. K. Greenacre, Y. Han, D. E. Smith, G. Piana, N. Zhelev, A. L. Hector, R. Beanland et al., *arXiv preprint arXiv:2104.00364*, 2021.

(45) K. Inaba, *The Rigaku Journal*, 2008, **24**, 10–15.

(46) M. R. Laskar, D. N. Nath, L. Ma, E. W. Lee, C. H. Lee, T. Kent, Z. Yang, R. Mishra, M. A. Roldan, J.-C. Idrobo et al., *Applied Physics Letters*, 2014, **104**.

(47) J. Wang, F. Sun, S. Yang, Y. Li, C. Zhao, M. Xu, Y. Zhang and H. Zeng, *Applied Physics Letters*, 2016, **109**.

(48) H. Wei, A. Tan, W. Liu, J. Piao, K. Wan, Z. Liang, Z. Xiang and Z. Fu, *Catalysts*, 2022, **12**, 947.

(49) N. Choudhary, H.-S. Chung, J. H. Kim, C. Noh, M. A. Islam, K. H. Oh, K. Coffey, Y. Jung and Y. Jung, *Advanced Materials Interfaces*, 2018, **5**, 1800382.

(50) Y. Jung, J. Shen, Y. Liu, J. M. Woods, Y. Sun and J. J. Cha, *Nano letters*, 2014, **14**, 6842–6849.

(51) M. Belete, S. Kataria, A. Turfanda, S. Vaziri, T. Wahlbrink, O. Engström and M. C. Lemme, *Advanced Electronic Materials*, 2020, **6**, 1900892.

(52) D. Zhao, S. Xie, Y. Wang, H. Zhu, L. Chen, Q. Sun and D. W. Zhang, *AIP Advances*, 2019, **9**.

(53) J. Park, N. Choudhary, J. Smith, G. Lee, M. Kim and W. Choi, *Applied Physics Letters*, 2015, **106**.

(54) J. M. LeBeau, S. D. Findlay, X. Wang, A. J. Jacobson, L. J. Allen and S. Stemmer, *Physical Review B—Condensed Matter and Materials Physics*, 2009, **79**, 214110.

(55) R. Egerton and M. Malac, *Journal of Electron Spectroscopy and Related Phenomena*, 2005, **143**, 43–50.

(56) L. Yadgarov, D. G. Stroppa, R. Rosentsveig, R. Ron, A. N. Enyashin, L. Houben and R. Tenne, *Zeitschrift für anorganische und allgemeine Chemie*, 2012, **638**, 2610–2616.

(57) N. Al-Dulaimi, D. J. Lewis, X. L. Zhong, M. A. Malik and P. O'Brien, *Journal of Materials Chemistry C*, 2016, **4**, 2312–2318.

(58) N. Al-Dulaimi, E. A. Lewis, N. Savjani, P. D. McNaughter, S. J. Haigh, M. A. Malik, D. J. Lewis and P. O'Brien, *Journal of Materials Chemistry C*, 2017, **5**, 9044–9052.

(59) R. Duffy, P. Foley, B. Filippone, G. Mirabelli, D. O'Connell, B. Sheehan, P. Carolan, M. Schmidt, K. Cherkaoui, R. Gatensby et al., *ECS Journal of Solid State Science and Technology*, 2016, **5**, Q3016.

(60) A. Carvalho and A. C. Neto, *Physical Review B*, 2014, **89**, 081406.

(61) J. R. Lindemuth, *Lake Shore Cryotronics, Inc.*, 2001, **575**.

(62) A. T. Neal, R. Pachter and S. Mou, *Applied Physics Letters*, 2017, **110**.

(63) H. Nan, Z. Wang, W. Wang, Z. Liang, Y. Lu, Q. Chen, D. He, P. Tan, F. Miao, X. Wang et al., *ACS nano*, 2014, **8**, 5738–5745.

(64) R. I. Romanov, I. V. Zabrosaev, M. G. Kozodaev, D. I. Yakubovsky, M. K. Tatmyshevskiy, A. A. Timofeev, N. V. Doroshina, S. M. Novikov, V. S. Volkov and A. M. Markeev, *ACS omega*, 2023, **8**, 16579–16586.

(65) K. Pi, K. McCreary, W. Bao, W. Han, Y. Chiang, Y. Li, S.-W. Tsai, C. Lau and R. Kawakami, *Physical Review B—Condensed Matter and Materials Physics*, 2009, **80**, 075406.

(66) R. J. Gatensby, PhD Thesis, Trinity College Dublin. School of Chemistry. Discipline of Chemistry, Dublin, Ireland, 2018.

(67) A. Heredia, M. Q. García, J. P. Mazariego and R. Escamilla, *Journal of Alloys and Compounds*, 2010, **504**, 446–451.

(68) T. Mitsunaga, *Rigaku J*, 2009, **25**, 7–12.

(69) A. Pandey, S. Dalal, S. Dutta and A. Dixit, *Journal of Materials Science: Materials in Electronics*, 2021, **32**, 1341–1368.

(70) Y.-C. Lin, D. O. Dumcenco, H.-P. Komsa, Y. Niimi, A. V. Krasheninnikov, Y.-S. Huang and K. Suenaga, *arXiv preprint arXiv:1310.2366*, 2013.

4 | Modulating WS_2 Properties through Introducing of Niobium Content

4.1 Background and Motivation

Complementary transistors and van der Waals junctions are crucial for developing Transition Metal Dichalcogenide (TMD)-based integrated circuits (ICs) for future electronics. Research has predominantly focused on n-type TMD semiconductors, such as MoS_2, WS_2, WSe_2, and $MoSe_2$, due to the prevalent electron doping from interfacial charge impurities [1]. Moreover, developing effective n-type 2D FETs is easier due to Fermi-level pinning near the conduction band. In contrast, p-type FETs face more challenges [2, 3]. One reason for Fermi-level pinning is the work function of the contact metals in TMD devices. Aligning the Fermi level near the valence band requires metals with higher work functions, which are less commonly used or are more chemically reactive [4]. This disparity in performance between TMD n-channel and p-channel field-effect transistors hinders effective integrated circuit applications [5]. Thus, developing effective p-type TMD semiconductors with controllable synthesis and mobility is essential.

It is known that niobium (Nb) has five valence electrons ($4d^4 5s^1$), compared to W's six ($5d^4 6s^2$). When Nb substitutes W in WS_2, there is one less electron per substitution, introducing a deficit of electrons that creates "holes" (positively charged carriers) in the system, effectively making the material p-type [6]. The presence of

Nb's 4d orbitals near the valence band maximum enhances the density of states (DOS), which facilitates hole conduction. DOS, here, represents the number of electronic states available per unit energy range that electrons or holes can occupy. A higher DOS near the valence band maximum means more states are accessible for holes, improving the likelihood of hole conduction and enhancing p-type behavior [7]. Moreover, both WS_2 and NbS_2 have the 2H-phase crystal structure with similar lattice constants (WS_2 [a, b, c] = [3.16, 3.16, 12.47] Å, NbS_2 [a, b, c] = [3.32, 3.32, 11.94] Å), and the covalent radii of W (137 pm) and Nb (134 pm) are very close. These features suggest the possible substitutional doping of Nb into WS_2 with few defects [8].

In addition, density-functional theory (DFT) calculations suggest Nb as an effective acceptor with favorable formation energies for substitutional doping [9]. Similar experimental studies to those discussed in this chapter have shown Nb doping enhances charge carrier transfer and conductivity in TMD films like MoS_2 [10, 11] and tungsten diselenide (WSe_2) [12]. Bulk-grown MoS_2 doped with Nb has demonstrated carrier concentrations of $1 - 1.5 \times 10^{21}$ cm^{-3} and mobilities of $0.2 - 0.8$ $cm^2/V{\cdot}s$ [13]. Mechanically exfoliated bulk MoS_2 with Nb doping showed carrier concentrations of 3.0×10^{19} cm^{-3}, presenting a degenerate p-type doping [14]. Degenerate doping here refers to a doping level so high that the dopant atoms introduce a carrier concentration comparable to or exceeding the density of states in the conduction or valence band. This results in the material behaving more like a metal than a traditional semiconductor [7].

This chapter explores the structural and electronic changes induced by Nb doping in bulk WS_2 films (approximately 30 nm thick). Using a one-step WS_2 growth process, Nb impurities are incorporated during the deposition of W. Four experimental techniques were employed to investigate the effects of Nb doping on WS_2 thin-film properties. X-ray diffraction was used to analyze diffraction patterns, Raman spectroscopy to study vibrational modes, three-probe gating measurements to calculate field-effect mobility, and transmission electron microscopy to examine the

structural behavior of the thin films, including the interlayer spacing between WS_2 layers.

4.2 Methodology

Substrate Preparation

Depositions were performed on hexagonal R-cut sapphire (Al_2O_3) substrates with orientations (10-02) and (20-04), each measuring 1 cm x 1 cm. The substrates underwent pre-cleaning in an ultrasonic bath with acetone, isopropyl alcohol (IPA), and deionized water for 5 minutes each, followed by drying with N_2 gas.

Film Deposition

Thin-film samples were prepared using DC magnetron sputtering in a high-vacuum environment. The process involved depositing a 2 nm layer of Tungsten (W), a 0.2 nm layer of Niobium (Nb), and a final 7.8 nm layer of W to encapsulate the Nb. Unlike previous co-sputtering techniques, this method employed sequential deposition. The sputtering targets, 3-inch diameter W (99.99%) and Nb (99.99%), were sourced from Kurt J. Lesker company. The deposition parameters are detailed in Table 4.1. The substrate temperature was maintained at room temperature, with a target-to-substrate distance of 15 cm and a substrate holder rotation of 30 rpm.

Parameters	Condition/Value
Target	Nb and W
Substrate	R-cut Al_2O_3
Working Pressure	10^{-6} Torr
DC Power (Nb)	50 W
DC Power (W)	100 W
Gas Flow Rate	30 sccm (Argon)

Table 4.1: Sputtering parameters for pristine WS_2 and Nb-doped W stacks before conversion The details regarding the parameters are explained in Section: 2.1.1.

The working pressure was maintained at 10^{-6} Torr, characteristic of high-vacuum sputtering. This low-pressure environment minimizes collisions between sputtered

species and residual gas molecules, ensuring high kinetic energy and enabling the deposition of high-purity, dense, and uniform thin films. DC power settings were adjusted to 50 W for Nb and 100 W for W. The lower power for Nb allowed for controlled deposition given its higher sputtering threshold, while the higher power for W enabled a faster deposition rate. The argon gas flow rate was set to 30 sccm, a standard value for inert sputtering conditions. This ensured stable plasma generation and consistent ion bombardment, avoiding excessive scattering and maintaining deposition stability.

X-Ray Reflectivity

X-Ray Reflectivity (XRR) was employed to calibrate the deposition rate and confirm film thickness post-deposition. Measurements were performed using a Phillips Panalytical X'Pert Pro diffractometer. The open-source program GENX was used for reflectivity analysis [15, 16]. Both pristine WS_2 and 1.76 at.% Nb-doped W films were prepared for this study. The atomic percentage calculation for 1.76 at.% Nb-doped film is shown in Appendix A2. The magnetron sputtering depositions were carried out by Dr. Gwenael Atcheson.

Conversion Process

Post-deposition, the films were placed with 5 g of sulfur powder (Sigma-Aldrich 99.9%) into a quartz crucible and inserted into a tube furnace. The sulfur was heated to 135 °C, while the films were heated to 900 °C. The furnace, connected to an Argon (Ar) supply, was heated at 19 °C/min to the process temperature. The 30-minute sulfurization duration was selected based on practical constraints related to the sulfur supply in the furnace. The amount of sulfur powder determines the available sulfur vapor during the process. Once the sulfur evaporates and is consumed, further conversion of transition metal to sulfide-based semiconductor stops, and the process transitions to annealing. Thus, the growth time is inherently limited by the sulfur availability. The tube pressure was kept at 0.6 Torr throughout the conversion

(30 sccm Ar flow) and annealing process.

Raman Spectroscopy

The Raman spectroscopy was performed using the Witec Alpha 300R spectrometer with an excitation wavelength of 532 nm. A spectral grating with 1800 lines/mm and a 100× microscope objective (0.95 N.A) with a spot size of approximately 0.3 nm were utilized for the Raman spectra. To prevent laser damage to the surface, the laser power was maintained below 50 μW. Measurements were conducted in air at 25 °C and atmospheric pressure.

Raman spectroscopy measurement was performed using a confocal Raman microscope (Alpha 300R, WiTec, Germany). A 532 nm excitation laser operating at a low power of 50 μm was utilized to prevent beam-induced damage. The scattered Raman signal was captured through a 100× microscope objective with a numerical aperture (NA) of 0.8 and detected by a Peltier-cooled camera. A grating with 1800 grooves per mm was used for spectral dispersion, providing a system-wide spectral resolution of approximately 0.75 cm^{-1}. All Raman spectra were recorded under ambient conditions.

X-Ray Diffraction

X-ray diffraction was used to elucidate the crystallographic orientation of the planes in the lattice of WS_2 post-conversion. Measurements were performed with a Panalytical X'Pert Pro diffractometer using Cu Kα radiation (1.5406 Å) in Bragg-Brentano geometry, with a step size of 0.02 degrees/step and a step time of 0.5 s/step. Crystallographic phases were identified using reference patterns from the International Centre for Diffraction Data (ICDD).

Device Preparation

Back-gated transistor applications are demonstrated for pristine WS_2 and Nb-doped WS_2 films. Gating studies can be achieved using either top-gating or bottom-gating configurations. Top-gating requires a pinhole-free, defect-free, high-*k* dielectric material such as Al_2O_3, SiO_2, or HfO_2 [17], deposited at ultra-high vacuum conditions on top of the WS_2 film. Alternatively, a Si/SiO_2 substrate can be utilized to deposit and thermally convert the transition metal to WS_2, with SiO_2 serving as the insulating layer.

The SiO_2 layer on the conductive Si substrate insulates the gate (p++ Si substrate) from the channel, which in this case is composed of WS_2 films. This configuration forms a capacitor-like structure where the gate voltage influences the charge distribution within the WS_2 channel. Further details regarding the device preparation process are illustrated in Figure 4.1.

Contacts were deposited on the WS_2 films using UV lithography, and the contact design is presented in Figure 4.2. The UV lithography process involved several precise steps to ensure accurate patterning during device preparation. First, S1813 photoresist was spin-coated onto the substrate at 5000 RPM for 45 seconds, with a ramp-up of 500 RPM for 5 seconds. The substrate was then exposed to UV light with a wavelength of 365 nm for 5.5 seconds. The exposed photoresist was developed in MF319 developer for 45 seconds, followed by rinsing in deionized water to stop the development process.

Finally, the contacts were fabricated using a Temescal e-beam deposition system, where a 1 nm titanium (Ti) adhesion layer was deposited, followed by a 50 nm gold (Au) layer. This process ensured robust electrical contacts between the source/drain electrodes and the WS_2 channel.

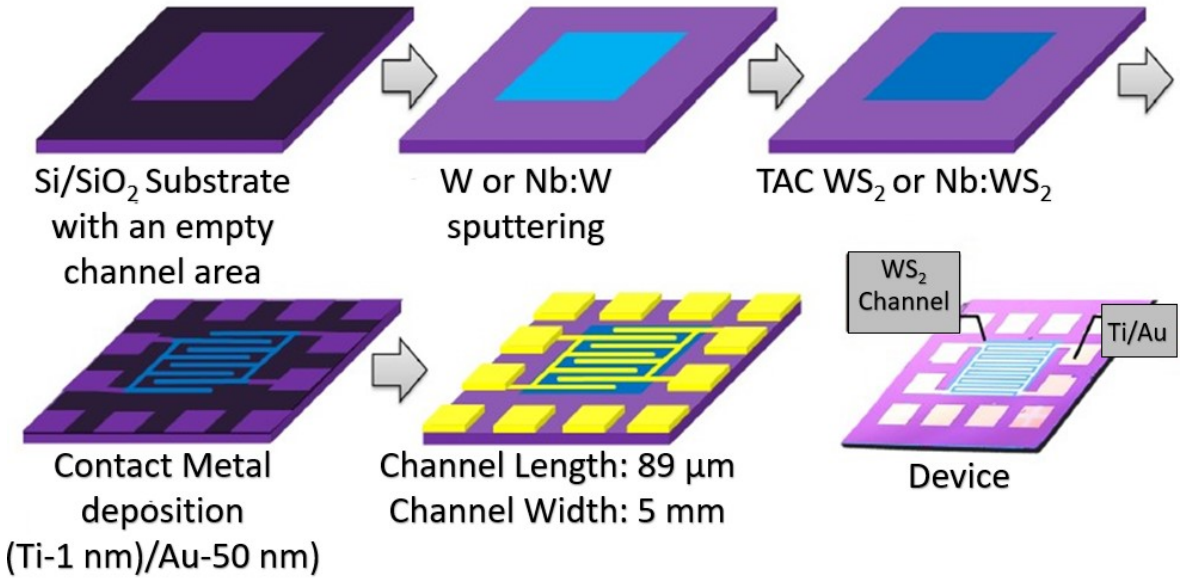

Figure 4.1: Fabrication process for pristine and Nb-doped WS_2 devices. The process begins with the preparation of a Si/SiO_2 substrate containing an empty channel area, which serves as the foundation of the device. Following substrate preparation, W or Nb:W is deposited onto the substrate using a sputtering process. The deposited W or Nb:W layers are then converted into pristine WS_2 or Nb-doped WS_2 via thermal-assisted conversion in a sulfur-rich environment. To enable electrical contact with the WS_2 films, UV lithography is employed. The lithography process defines the device geometry, resulting in a channel length of 89 μm and a width of 5 mm. For the source and drain electrodes, a thin layer of titanium (Ti, 1 nm) is deposited as an adhesion layer, followed by a thicker gold (Au, 50 nm) layer using a Temescal e-beam evaporation system. The final structure consists of a well-defined WS_2 channel, with yellow regions representing the Ti/Au metal electrodes and the blue region indicating the WS_2 channel.

Field Effect Measurements

The electrical characterization of pristine and 1.76 at.% Nb-doped WS_2 was performed using a Karl Suss probe station connected to a Keithley 2612A source meter. For the two-probe configuration, two channels of the Source Measurement Units (SMU) were used for the source and drain. Voltage was applied to one probe contacting Ti and Au electrodes deposited on the TMD films, shown in Figure 4.2.

A three-probe configuration, as shown in Figure 4.2, was also used. The silicon chip was adhered to Ti/Au coated with silver paint, and the oxides at the back of the silicon were either scratched off or dipped in HF (hydrofluoric acid). The aim was to enable back-gating contacts. Two channels of the Source Measurement Units

(SMU) were used for the source and drain, while the third channel was dedicated to the gate probe. A constant source voltage of +1V was applied while the gate voltage was varied from -30V to +30V, and the channel current was collected as a function of the applied gate voltage. The measured current was automatically plotted using LabVIEW software to generate I-V curves.

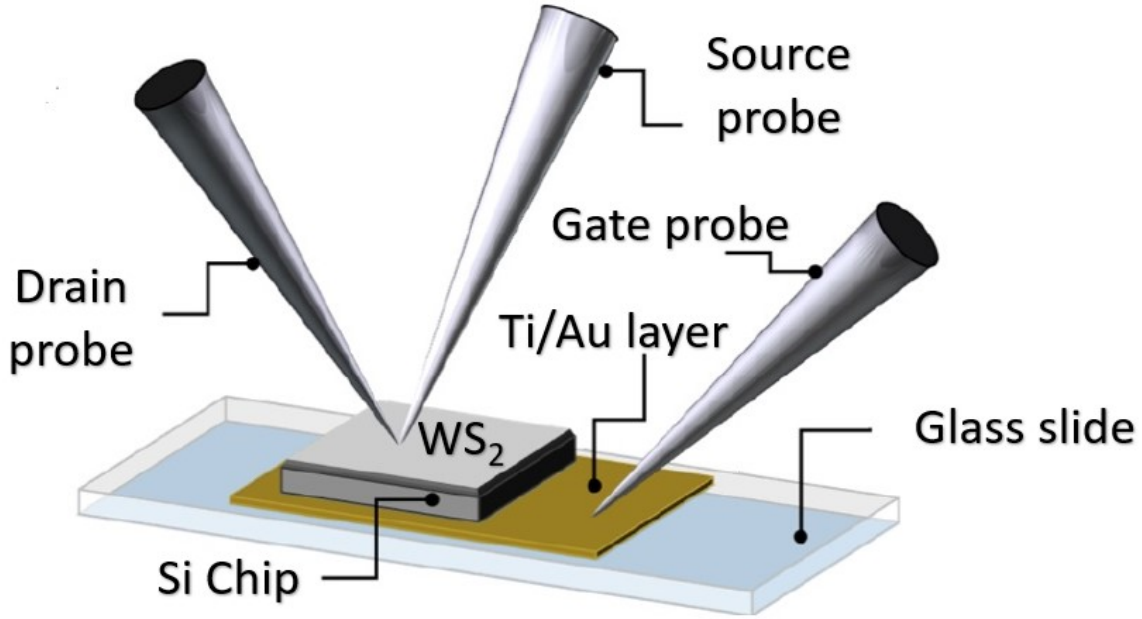

Figure 4.2: A three-probe configuration for performing electrical characterization of a WS_2 FET device on a Si/SiO_2 substrate with a back-gated setup. The image is adapted from a PhD thesis [18]. The schematic illustrates the three-probe gating setup. The two probes on top of the WS_2 film represent the source and drain electrodes. The source electrode applies voltage stress to the system, while the drain electrode measures the output current. For channel parameters: The channel length is 89 μm and the width is 5 mm are used. As the setup is designed for a bottom-gate configuration, the third probe, which controls the channel conductivity, is applied from the back of the silicon. For this purpose, the silicon substrate is adhered to the Ti/Au-coated glass. Silver paste was used to ensure adhesion and establish an electrical connection between the Ti/Au layer and the WS_2 film.

Transmission Electron Microscopy

For imaging purposes, a JEOL ARM200F Transition Electron Microscope was used at 200 kV, equipped with advanced detectors for Energy Dispersive X-ray Spectroscopy (EDS) and Electron Energy Loss Spectroscopy (EELS).

4.3 Experimental Results

The decision to focus on low concentrations of Nb impurities was influenced by several factors. It was observed in previous experiments that doping MoS_2 with Rhenium to create n-type material led to impurity atom clustering in Chapter **??**. This finding urged us to use lower impurity levels to avoid similar clustering. Additionally, theoretical studies by Dolui et al. supported this approach, as their DFT studies indicated a low pairing energy for two Nb atoms (-157 meV) [9], suggesting that maintaining a minimal impurity concentration is beneficial. Finally, the limitations of the deposition system played a role. In sputtering systems, sustaining a plasma requires a minimum current, which in turn determines the power applied to the gun. This technical constraint means there is a lower limit to the impurity concentration, as reducing it too much could disrupt the plasma, leading to no deposition. These considerations led us to focus on maintaining the lowest possible levels of Nb impurities that could sustain plasma and prevent clustering, thereby ensuring stable deposition. The final Nb level was determined with the support and expertise of Dr. Gwenael Atcheson.

4.3.1 X-Ray Reflectivity

X-Ray Reflectivity (XRR) analysis was conducted to determine only the film thickness, as observing density difference between pristine WS_2 and 1.76 at.% Nb would not be realistic. Figure 4.3 shows the typical oscillations due to X-ray interference from different interfaces within the material for both pristine WS_2 and 1.76 at.% Nb before conversion. The same figure also includes schematics representing the thick-

ness corresponding to the XRR results. The first schematic shows a pristine WS_2 W film aimed to be 10 nm thick, while the second schematic shows a 1.76 at.% Nb W film with 0.2 nm Nb and 9.8 nm W. The atomic percentage calculation of the Nb-doped WS_2 films is shown in Appendix A2.1.

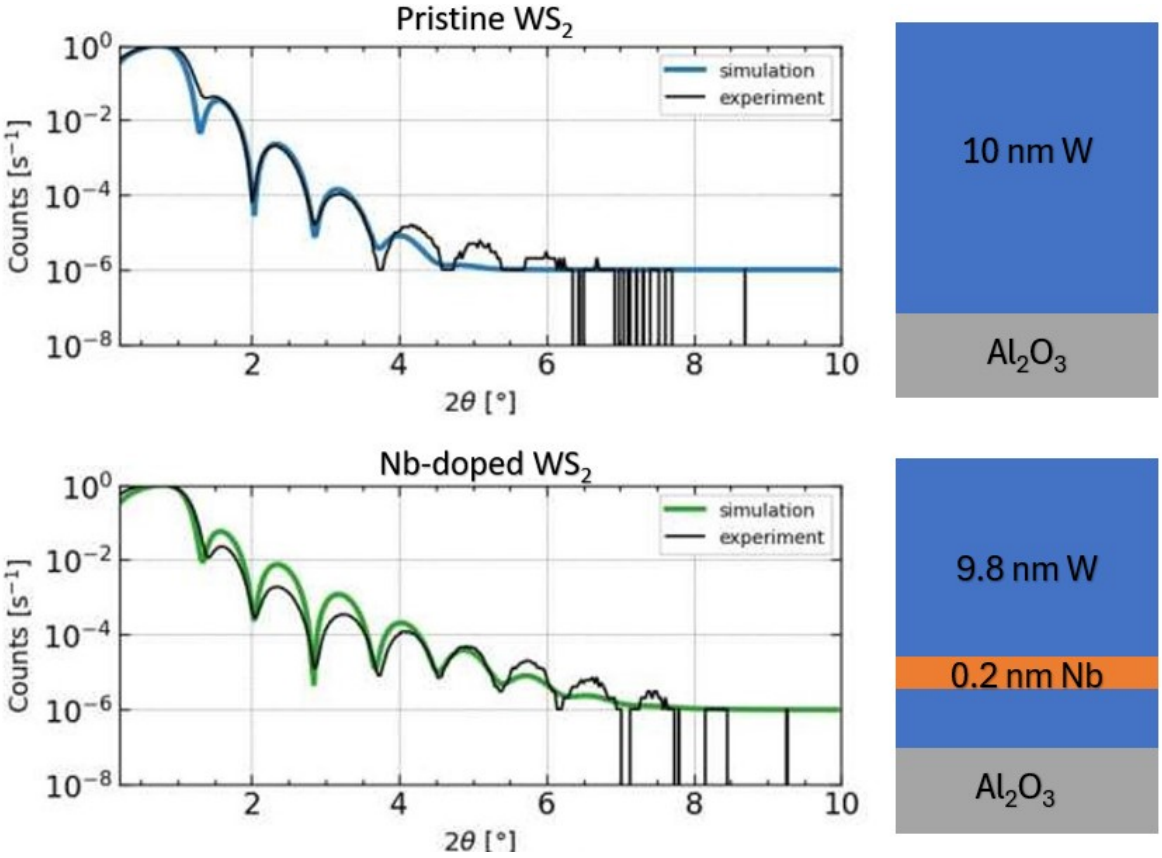

Figure 4.3: XRR results of pristine WS_2 and 1.76 at.% Nb doped W films on the left. The plots show the oscillations due to X-ray wave interference. The right side shows the layer deposition schematics on Al_2O_3 substrates. The bottom schematic indicates Nb content, which is not thick enough to form a distinct layer. Referring to Nb content as "dusted" might be more accurate.

As seen in Figure 4.3, the placement of Nb closer to the substrate, rather than the top of the film, is a preemptive measure to prevent the oxidation of Nb atoms. Additionally, depositing Nb closer to the substrate blocks chemical interactions between the Al_2O_3 substrate and Nb atoms. It must be noted that 0.2 nm Nb in the 1.76 at.% Nb doped W stack is below the lattice parameter of Nb (0.33 nm) [19]. Consequently, detecting Nb using X-ray reflectivity is unfeasible, as there would be no reflective response. Despite this limitation, the aim was to achieve the same thickness for comparison. The parameters after the fit and before the conversion process are detailed

in Table 4.2.

Host Metal	Dopant (at.%)	Thickness [nm]
W	Pristine W	9.9
W	1.76 at.% Nb	10

Table 4.2: Thickness obtained after depositions. XRR technique utilized to observe the initial transition metal thickness, before the conversion process.

It is important to note that all films were approximately 10 nm thick prior to the conversion process based on XRR results. After the conversion to sulfide-based semiconducting materials, the films exhibit roughness was higher so that applying XRR was not feasible, as shown in Section 2.8. This inherent roughness makes XRR fitting unfeasible post-conversion, as discussed and demonstrated in Chapter 2.

To determine the thickness of the converted WS_2 films, atomic force microscopy (AFM) can be utilized to measure the expansion coefficient. Literature values may also be consulted, as the resulting thickness of converted films is well-documented for TMD materials [20, 21]. Typically, the final thickness of WS_2 films is approximately quadruple the initial metal thickness following conversion to the sulfide-based semiconducting form [22]. Alternatively, cross-sectional transmission electron microscopy can be employed to determine the resultant thickness of the converted films. In this work, cross-sectional TEM is used for this purpose. Appendix A2.2 shows the thickness intensity profile of Pristine WS_2 film and Appendix A2.3 shows the zoomed in TEM image of the 1.76 at.% Nb doped WS_2 where we can see the resultant thickness.

4.3.2 Conversion Process

The sulfur was maintained at a temperature of 135 °C, while the films were heated to 900 °C. The furnace, equipped with an Argon (Ar) gas supply, was ramped to the target temperature at a rate of 19 °C/min. A sulfurization duration of 30 minutes was chosen due to practical limitations associated with the sulfur supply within the furnace. The quantity of sulfur powder determines the amount of sulfur va-

por available during the process. Once the sulfur is fully evaporated and depleted, further conversion of the transition metal to sulfide-based TMD film stops, and the process transitions into an annealing phase. Consequently, the growth duration is intrinsically constrained by the availability of sulfur. The tube pressure was maintained at 0.6 Torr during both the conversion (30 sccm Ar flow) and annealing stages.

4.3.3 Raman Spectroscopy

Raman spectroscopy was used to characterize the samples after the conversion process. Figure 4.4 shows the Raman spectra of pristine WS_2 and 1.76 at.% Nb-doped WS_2 films on R-cut Al_2O_3 and Figure 4.5 shows the same composition on Glass (Amorph SiO_2) substrates.

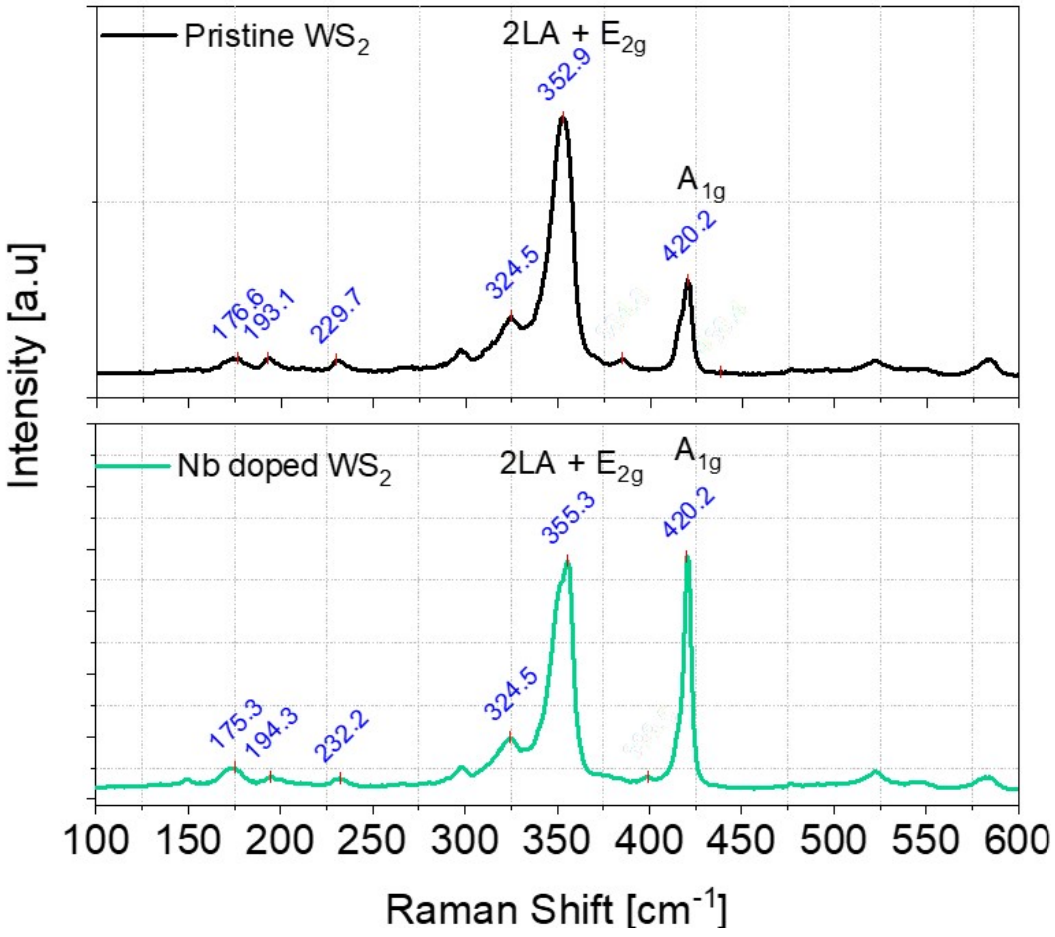

Figure 4.4: Raman spectra of pristine WS_2 and 1.76 at.% Nb-doped WS_2 films grown on R-cut Al_2O_3 substrates using a 532 nm laser.

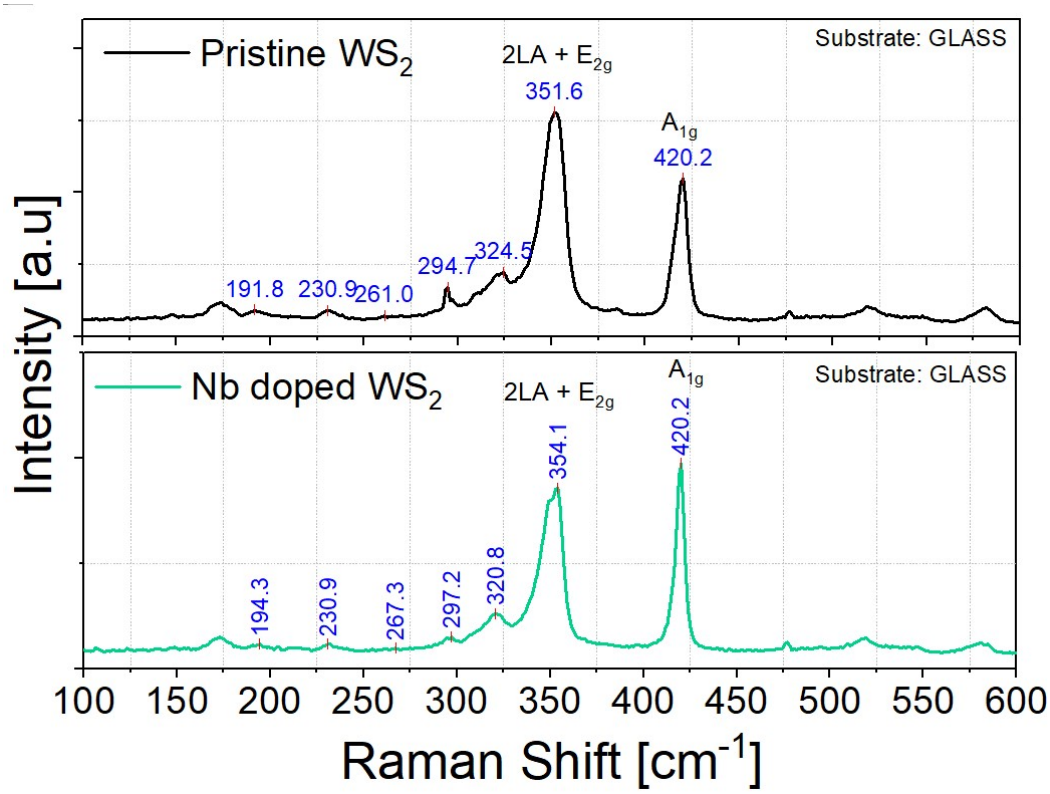

Figure 4.5: Raman spectra of pristine WS_2 and 1.76 at.% Nb-doped WS_2 films grown on Glass substrates using a 532 nm laser.

The Raman spectra reveal the vibrational properties of the pristine and Nb-doped WS_2 films. The spectra show an average of 10 different points across the samples of pristine and doped WS_2 films.

The table 4.3, shows the prominent peaks in WS_2 films corresponding to the 2LA + E_{2g} mode (in-plane vibrations) and the A_{1g} mode (out-of-plane vibrations), commonly used for spectral comparison. For pristine WS_2, the 2LA + E_{2g} peak appears at 352.9 cm^{-1} on R-cut substrates and at 351.6 cm^{-1} on glass, while the A_{1g} peak remains consistent at 420.2 cm^{-1} across both substrates. In 1.76 at.% Nb-doped WS_2, the 2LA + E_{2g} peak shifts to 355.3 cm^{-1} on R-cut substrates and to 354.1 cm^{-1} on glass, indicating subtle modifications in in-plane vibrations due to doping, while the A_{1g} peak remains unchanged at 420.2 cm^{-1}.

These results highlight the consistent influence of doping and substrate choice on the vibrational properties of WS_2. Raman spectra of the pristine and doped WS_2 films showed similar features to those reported in the literature, in terms of the

Table 4.3: Raman Peak Positions for Pristine and Nb-doped WS_2

Sample	2LA+E_{2g} Peak Position (cm^{-1})	A_{1g} Peak Position (cm^{-1})
Pristine WS_2 (RCUT)	352.9	420.2
Nb-doped WS_2 (RCUT)	355.3	420.2
Pristine WS_2 (Glass)	351.6	420.2
Nb-doped WS_2 (Glass)	354.1	420.2

characteristic peaks for WS_2 films [23–27].

4.3.4 Crystallography

The crystallinity of a semiconductor refers to the regular and repeating arrangement of its atoms. A highly crystalline structure is desirable because it reduces scattering and allows charge carriers to move more freely [28]. To determine the orientation of the diffraction planes in the pristine WS_2 and 1.76 at.% Nb-doped WS_2 films, X-ray diffraction was used. Figure 4.6 shows the diffraction patterns of the films on R-cut Al_2O_3 substrates.

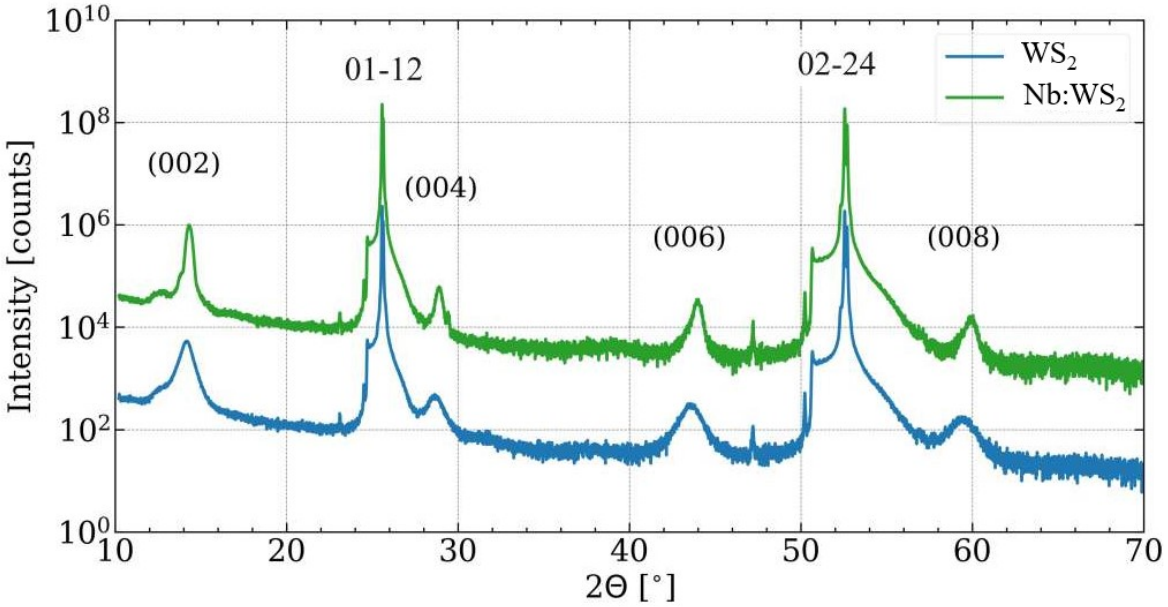

Figure 4.6: $\theta - 2\theta$ diffraction patterns of pristine WS_2 (blue) and 1.76 at.% Nb (green) -doped WS_2 films on R-cut sapphire substrates. JCPDS card no. 38-1388, is used to label the orientation. This JCPDS card provides reference data for the crystal structure of WS_2.

WS_2 typically forms a hexagonal structure belonging to the space group $P6_3/mmc$.

The XRD patterns for the pristine WS_2 and 1.76 at.% Nb-doped WS_2 films show characteristic peaks corresponding to the crystal planes. Both samples exhibit distinct diffraction peaks for the (002), (004), (006), and (008) planes.

Typical XRD peaks for hexagonal WS_2 appear at approximately 14.3° for the (002) plane, 43.87° for the (004) plane, 57° for the (006) plane, and 59.8° for the (008) plane. The crystallographic orientation for WS_2 used in this chapter is based on the standard JCPDS card no. 38-1388, which provides reference data for the crystal structure of WS_2. Moreover, these results are consistent with highly ordered WS_2 films reported in the literature [29, 30]. The prepared samples show a clear (00n) preferential orientation, similar to other studies [31–36].

4.3.5 Transmission Electron Microscopy

High-Angle Annular Dark-Field Transmission Electron Microscopy (HAADF-TEM) is applied to be able to see the contrast difference of the elements in the chosen area. The bright regions in HAADF images correspond to heavy atoms, highlighting the presence of heavy metal within the analyzed area. Figure 4.7 presents the HAADF-TEM images of WS_2 thin films with different scale bars.

The cross-sectional HAADF-TEM images of WS_2 thin films show the characteristic layered structure of the material. Images (a), (b), and (c) reveal the layers of WS_2, indicative of layer stacking. The resultant thickness after conversion can be measured to be approximately 30 nm, with the expansion coefficient being three times the initial metal thickness. Images (b), (c) show the bending of the layers creating voids between them. This structure can be explained as attempted vertical alignments. For MoS_2, Li et al. previously demonstrated that compression and extrusion during growth result in the formation of MoS_2 islands [37]. It is proposed that when two MoS_2 islands push against and collide with each other, the resulting compression forces may cause significant distortion, leading to the formation of an arch-like structure to relieve the pressure[37] .Image (f) highlights a specific area, marked in

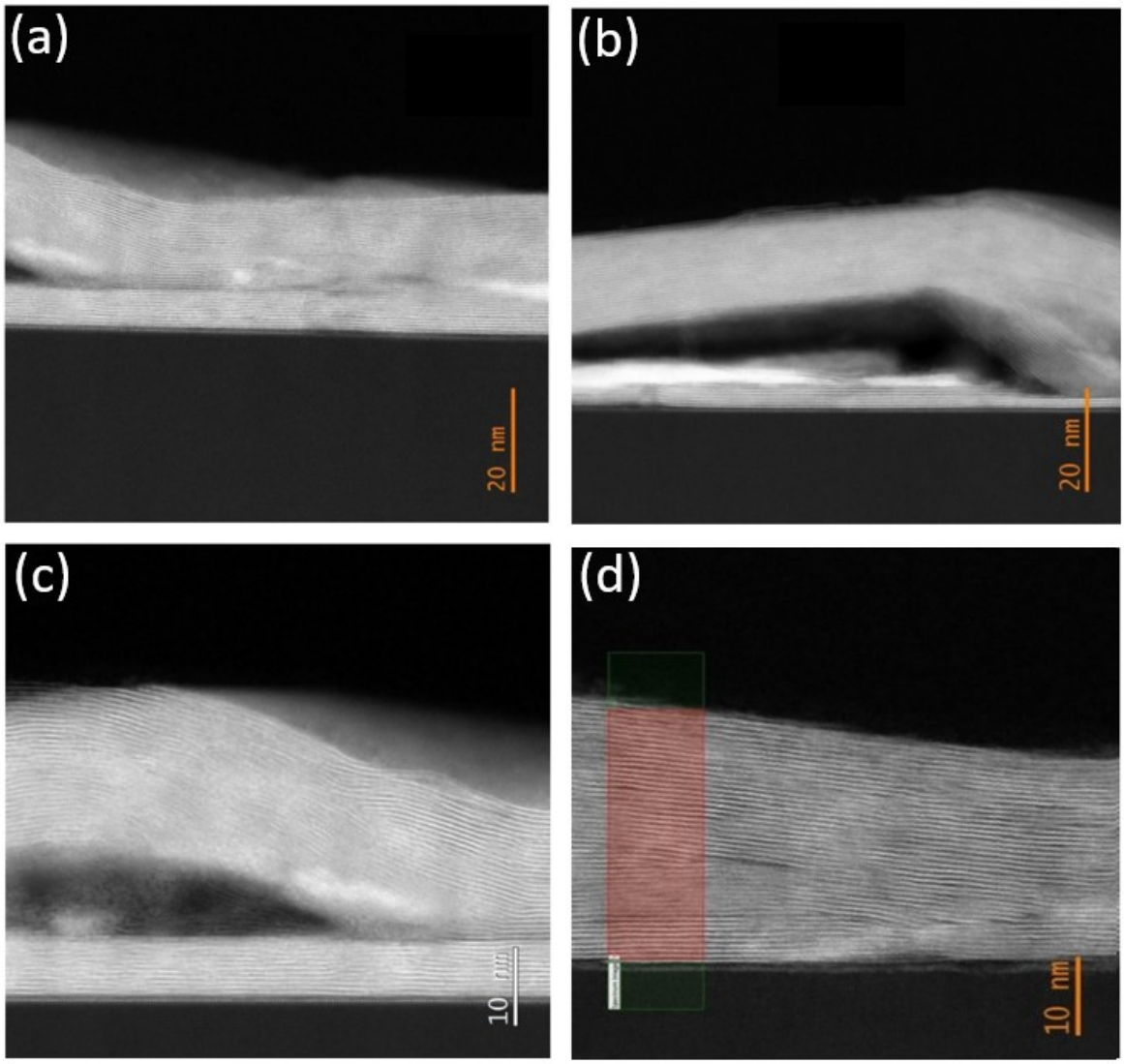

Figure 4.7: HAADF-TEM images of WS_2 thin films on R-cut Al_2O_3. Images (a), (b), and (c) show the layers of WS_2. Based on the contract, white areas represents the unconverted W residues due to higher dentist of it. Image (c) presents the void that occurred during conversion. Image (d) highlights a specific area, marked in red, where EELS (Electron Energy Loss Spectroscopy) analysis was conducted to determine the stoichiometry.

red, where EELS analysis was conducted.

EELS is a technique that analyzes the energy distribution of electrons that have inelastically scattered after interacting with a material. The EELS data of the area shown in Figure 4.7(f), presented in Table 4.4, confirms the formation of WS_2 thin film with the expected stoichiometry of 1:2 for tungsten to sulfur.

As for TEM analysis of 1.76 at.% Nb-doped film, compiled in Figure 4.8, the analysis

Table 4.4: Composition Results of EELS High Loss Spectrum of pristine WS_2 film grown on R-cut Al_2O_3 substrate

Element	Shell	Composition (at%)
W	M	32 ± 5
S	K	68 ± 5

had to be done on a film grown on Glass (amorphous SiO_2) using the same recipe as for the rest, Raman spectroscopy of this sample is shown in Figure 4.5. Overall, 1.76 at.% Nb-doped WS_2 shows failed full conversion with W clusters. Gultom et al. observed a similar result in WS_2 where full conversion from W layer to WS_2 failed, and they informed that the resulted layer was WO_3 but not W after the conversion process [38]. In this case, the utilized HAADF technique is density-sensitive, so the observed white clusters represent W clusters, as the density of WO_3 (7.16 g/cm^3) is close to the density of WS_2 (7.5 g/cm^3).

The provided EELS data confirms the formation of WS_2 thin film for 1.76 at.%Nb doped converted region. The calculated stoichiometry of almost 1:2 for tungsten to sulfur, with the results presented in Table 4.5.

Table 4.5: EELS 1.76 at.% Nb-doped WS_2 film grown on amorphous SiO_2 substrate

Element	Shell	Composition (at%)
W	M	34 ± 5
S	K	66 ± 5
Nb	K	No quantitative result

Figure 4.8 (d) shows the TEM-EDS analysis. The image displays a TEM image of the sample with regions marked for EDS analysis, where the red and green boxes indicate the areas where EDS mapping was performed. The expected EDS Nb signal in WS_2 film should be observed at Kα:16.6 keV [39]. However, the characteristic peak of Nb remained within the noise level and could not be quantified in either the W zone (red color) selected in image (d). The presence of Nb couldn't be quantified in the bulk WS_2 layer.

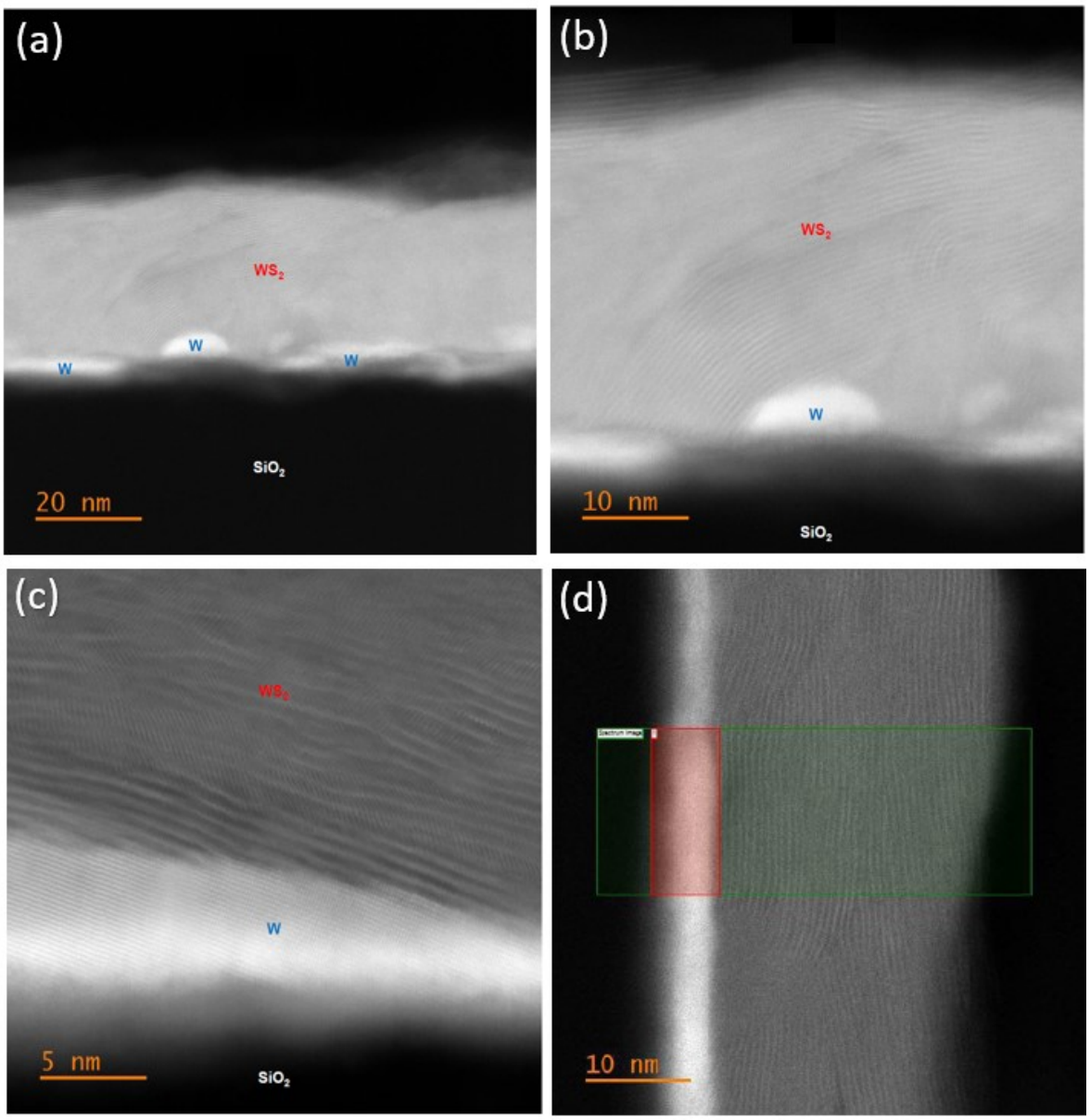

Figure 4.8: HAADF-TEM images of 1.76 at.% Nb-doped WS_2 thin films on a SiO_2 substrate. Images (a), (b), and (c) show the overall layered structure with distinct tungsten and Glass (Amorph SiO_2) regions. Images (d) highlights the areas selected for EELS analysis, marked in red and green boxes, to confirm the stoichiometry and unconverted bulk of W layer in the WS_2 matrix. Again, image (d) shows the TEM-EDS (Transmission Electron Microscopy - Energy Dispersive X-ray Spectroscopy) analysis to detect 0.2 nm of Nb content in the WS_2 matrix.

4.3.6 Field Effect Gating Studies

To investigate the electrical performance of the synthesized pristine WS_2 and 1.76 at.% Nb-doped WS_2 films, back-gated Field Effect Transistor devices were created on SiO_2/Si substrates. The theory and figure of merit of the three-probe measure-

ment and two-probe measurements are discussed in Section 2.7.2. A back-gating configuration was chosen because it avoids the need for depositing high-*k* dielectric materials on the thin film of WS_2 [40] to top gate it, meaning apply to gate voltage from the top of the device. This is why Si/SiO_2 substrates were preferred over Al_2O_3 substrates, which were used for the rest of characterizations. However, the same recipe is applied. The electrical measurements described in this section were performed at room temperature under ambient conditions. Initially, two probe measurement is applied as shown in Figure 4.9(a). For this, current-voltage ($I - V$) data were recorded. The three pristine WS_2 devices exhibit nonlinear behavior. The asymmetry in the I-V curves suggests variations in contact resistance. These differences, despite identical growth conditions, can be attributed to variations in sulfur partial pressure and temperature gradients within the growth furnace during the conversion process. These reasons might lead to variation in the resistivity, as shown in Table 4.6.

Table 4.6: Resistivity of three different pristine WS_2 devices, calculated using the two-probe measurements shown in Figure 4.9(a).

Device Number	**Device Name**	**Resistivity ($\Omega \cdot$ cm)**
1	D1	160
2	D2	84
3	D3	42

Subsequently, a third probe was attached to the bottom of the substrate to gate the oxide layer underneath the pristine WS_2 channel, the detail schematic and the information is shown in Figure 4.2. The three-probe measurement was carried out to investigate the current behavior of the pristine WS_2 films under varying gate voltage (V_{gs}) between -30 V to + 30 V, while maintaining a constant drain-source voltage (V_{ds}), which is +1V, as shown in Figure 4.9(b). The red area in graph (b) indicates the linear region of the $I_d - V_{gs}$ curve, where the transconductance (g_m) is calculated by determining the slope [7].

During gating, as shown in Figure 4.9(b), an applied positive back gate voltage attracts electrons to the interface between the n-type semiconductor and the SiO_2

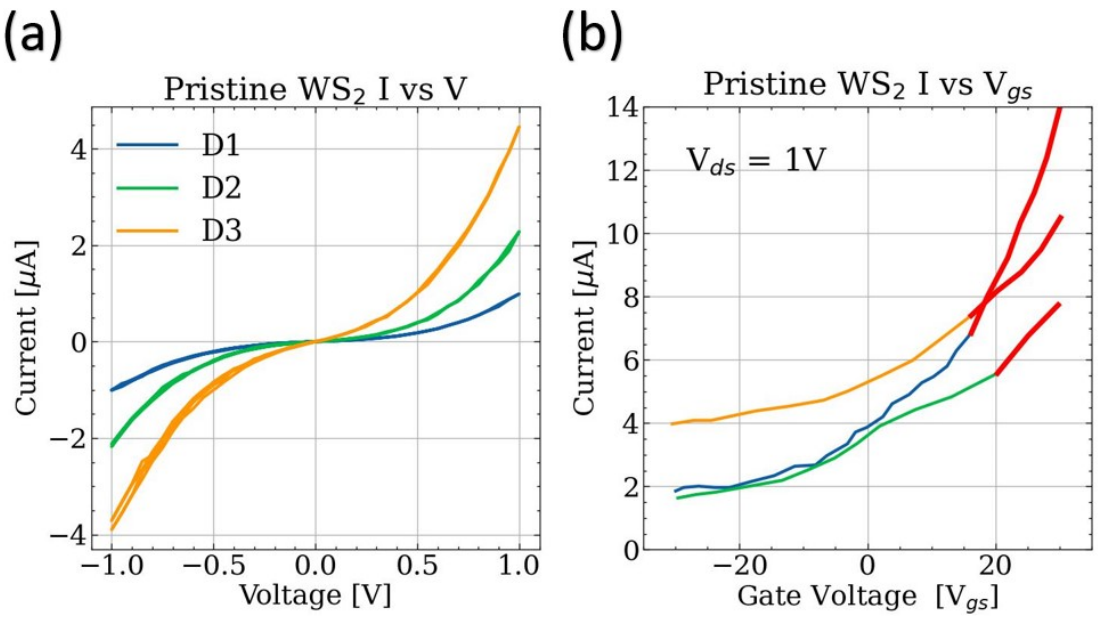

Figure 4.9: (a) Two-probe I-V characteristics of three different pristine WS_2 films. D1,D2,D3 are represented by there different pristine WS_2 devices. The colors in image (a) represents the same device in the image (b). Initially, the two-probe method is utilized to record the current and resistivity of the devices. The nonlinear behavior of the I-V curves in (a) highlights asymmetry, which suggests differences in resistivity. (b) Three-probe gating study with $V_{ds} = 1\,\text{V}$ for the same pristine WS_2 films. The three-probe method is utilized to observe the current behavior of the films over a range of gate voltages (V_{gs}) between $-30\,\text{V}$ and $+30\,\text{V}$, while maintaining a constant and small drain-source voltage (V_{ds}) of 1 V. The red-colored line in (b) represents the linear section of the $I_d - V_{gs}$ curve, where the slope is calculated to determine the transconductance (g_m).Transconductance is critical because it directly relates to carrier mobility (μ), a measure of how easily carriers (electrons or holes) move in the channel under an electric field.

layer, increasing electron concentration and enhancing conductivity. Conversely, a negative back gate voltage repels electrons, reducing electron concentration and conductivity. At zero gate voltage ($V_{gs} = 0$ V), electron density in the channel is determined by the intrinsic properties of the n-type semiconductor. Maximum electron concentration occurs at $V_{gs} = +30$ V, as seen in Figure 4.9(b), (especially for D1, above 14 μA for +30 V) leading to high conductivity, while minimum electron concentration occurs at $V_{gs} = -30$ V, leading to low conductivity. Therefore, the pristine WS_2 films showed n-type carrier transport characteristics, with source-drain current (I_{ds}) increasing with positive gate voltage (V_{gs}). To calculate the mobility (μ) of these devices:

$$\mu = \left(\frac{L_c}{W}\right)\left(\frac{1}{C_{SiO_2}}\right)\left(\frac{g_m}{V_{ds}}\right) \tag{1}$$

where μ is the mobility, L_c is the channel length is 89 μm, W is the channel width is 5 mm, C_{device} is the oxide capacitance, which is an established parameter, g_m is the transconductance, and V_{ds} is the drain-source voltage. Transconductance ($g_m = \frac{\partial I_d}{\partial V_{gs}}$) is measured from linear region of the $I_d - V_{gs}$ plot. This region, which colored as red in Figure 4.9 (b), is selected for its consistent slope, essential for accurate transconductance measurement. The table 4.7 shows the slope of the devices, considering the linear region. The oxide capacitance (C_{SiO_2}) is 1.3 F/m^2 [41]. Thus, the highest mobility (μ) is approximately 0.09 cm^2/V $\cdot$ s for the pristine D3 WS_2 device. The figures of merit for prisitine WS_2 transistor applications, such as mobility and on/off ratio, are summarized in Figure 4.10 (a) and (b).

Device	**Transconductance** g_m (μA/V)	**Mobility** μ (cm^2/V $\cdot$ s)	**Carrier Type**
D1	0.66	0.0905	n-type
D2	0.32	0.0439	n-type
D3	0.26	0.0357	n-type

Table 4.7: Transconductance, mobility, and carrier type for Devices 1, 2, and 3 of pristine WS_2 films. Transconductance is calculated from the slope of the linear regions of the Current-Gate Voltage curves in Figure 4.9(b).

Mobility directly affects the on current (I_{on}) of a transistor. The on current (I_{on}) is the maximum current flowing through the transistor when it is in its conducting state, typically achieved when a sufficiently high gate voltage (V_{gs}) is applied, driving the device into strong inversion or accumulation. Higher mobility enhances the ability of carriers (electrons or holes) to flow through the channel, resulting in a higher I_{on}. The off current (I_{off}), on the other hand, is the minimum current flowing through the transistor when it is in its non-conducting state, usually measured at a low or negative gate voltage. Ideally, I_{off} should be as small as possible to ensure minimal power consumption and leakage in the off state. The on/off ratio is defined as the ratio of the on current (I_{on}) to the off current (I_{off})

A high on/off ratio indicates a significant difference between the conducting and

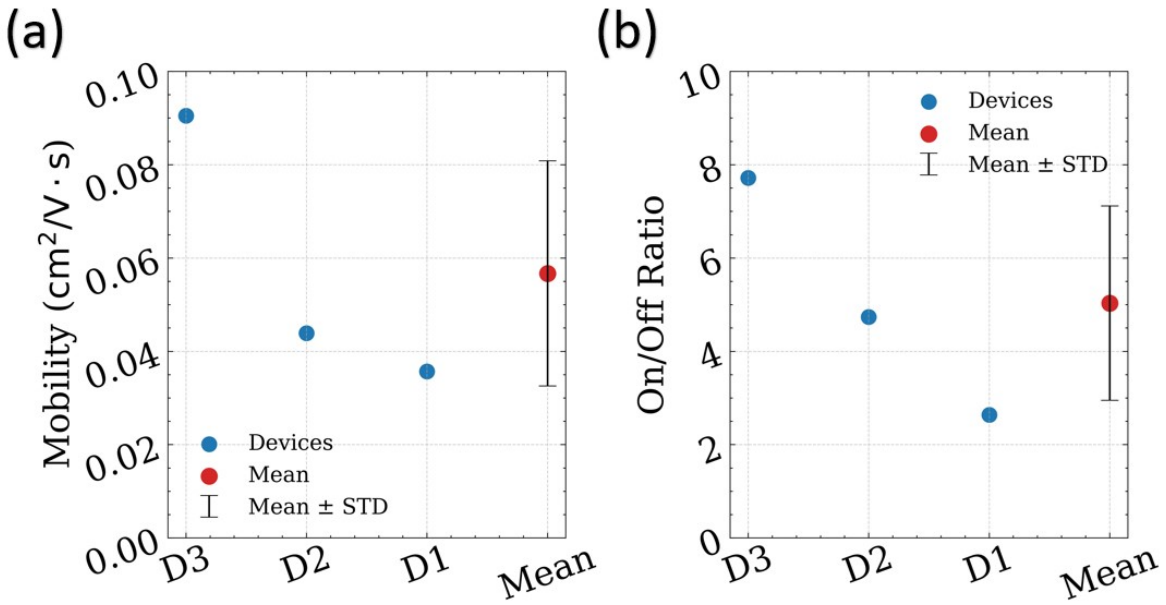

Figure 4.10: Summary of field-effect gating studies of pristine WS_2 films. The scatter plots summarize the mobility (μ) in graph(a) and on/off ratio (I_{on}/I_{off}) for devices D1, D2, and D3 in graph (b). Blue dots represent individual devices, and red dots show the mean values with standard deviation as error bars.

non-conducting states, which is critical for effective transistor switching. Conversely, an on/off ratio closer to 1 implies that the on and off states are not well differentiated, as the drain current does not vary significantly between the two states. This can result from factors such as poor gate control, high leakage currents (I_{off}), or insufficient carrier mobility [7].

Among pristine WS_2 devices, the highest mobility is about 1.54 times higher than the lowest mobility. The highest on/off ratio is about 2.92 times higher than the lowest on/off ratio, as shown in in Figure 4.10 (a) and (b).

It must be noted that for switching applications, without a clear threshold voltage, the device cannot operate as an effective switch, as it cannot distinguish between the "on" and "off" states, as shown in Figure 1.7 (c). The lack of saturation and threshold voltage suggest the device is not operating as a proper field effect transistor. Likely cause includes poor gate modulation, excessive doping [42]. Further studies are needed to identify the exact cause, including measuring gate leakage, analysing material quality, all will be discussed in the Section 4.4.

As apposed to pristine WS_2 devices, 1.76 at.% Nb-doped WS_2 devices exhibit ohmic behavior. 1.76 at.% Nb doped WS_2 devices have lower resistivity, as seen by the higher currents in both I-V and I-V_{gs} measurements, as shown in Figure 4.11 (a) and (b). The variations in resistivity among the 1.76 at.% Nb-doped WS_2 devices are not as large as those among the pristine WS_2 devices, as shown in Figure 4.8.

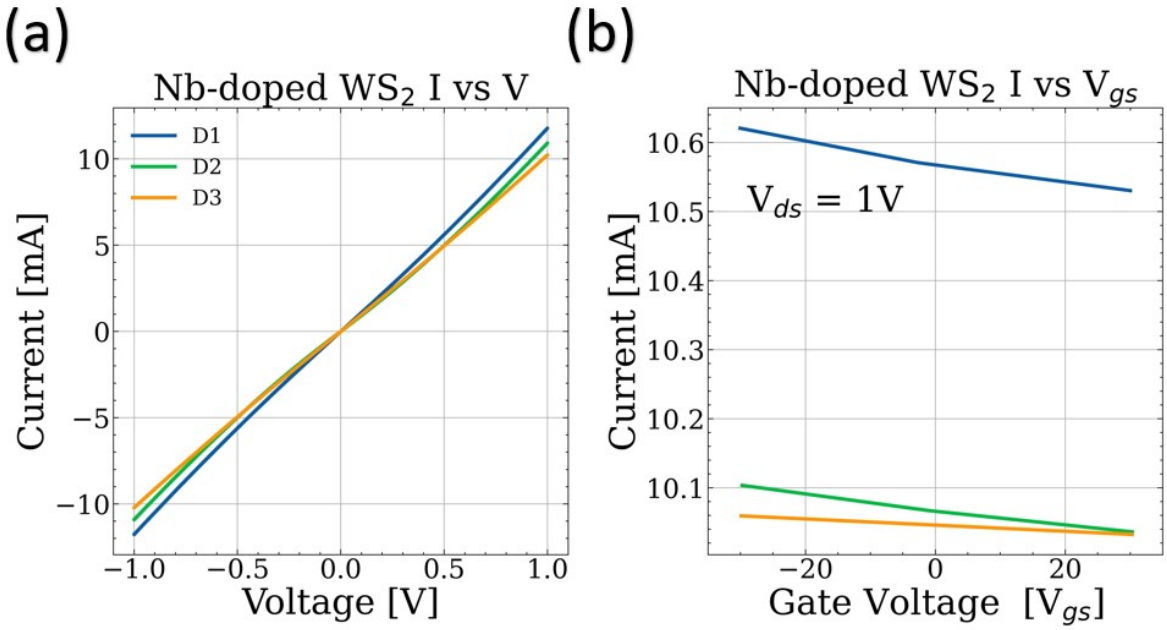

Figure 4.11: (a) Two-probe I-V characteristics of 1.76 at.% Nb-doped WS_2 films. (b) Three-probe gating study with $V_{ds} = 1V$ of 1.76 at.% Nb-doped WS_2 film.

Table 4.8: Resistivity and carrier type of three different 1.76 at% Nb-doped WS_2 devices, resistivity values calculated using the two-probe measurements in Figure 4.11(a).

Device Number	**Device Name**	**Resistivity ($\Omega \cdot$ cm)**
1	D1_doped	0.01186
2	D2_doped	0.01296
3	D3_doped	0.01400

1.76 at.% Nb doping, I_{ds} slightly decreases with the negative polarity V_{gs}, indicating that films have a very subtle tendency to be weak p-type. The gate voltage has less influence on the current in 1.76 at.% Nb-doped devices in comparison to pristine WS_2 films, suggesting a move towards metallic behavior. This behavior can be attributed to unconverted W metal residues that interfere with current modulation as observed from TEM study.

In the literature, low current modulation and resulting low on/off ratios in semiconducting devices are often attributed to presence of unconverted metal blocks or residues in the film or high gate leakage [43, 44]. If a metal layer is present in the matrix due to clustering or incomplete conversion, metals do not support carrier depletion or accumulation zones due to their continuous energy bands, leading to ineffective current switching. Additionally, strong electrostatic screening in metals neutralizes the gate's electric field [45], reducing current modulation effectiveness. Imperfections in WS_2 devices can also cause increased leakage currents, further lowering on/off ratios. The measurements in this chapter have not accounted for leakage current.

4.4 Discussion

This study highlights the challenges in synthesizing pristine and Nb-doped WS_2 films using the TAC method. Raman spectroscopy revealed that pristine and Nb-doped WS_2 films were successfully grown on different substrates, including glass and R-cut Al_2O_3. The influence of the substrate was found to be negligible, as the Raman shift (<1 cm^{-1}) of pristine and doped WS_2 films remained within the system's margin of error. However, the influence of Nb doping was not observed in the Raman characterization. This is not unusual, as Raman spectroscopy may fail to reveal such influences in bulk TMD films [46].

Crystallographic analysis revealed that both pristine and Nb-doped WS_2 films predominantly exhibited lateral (00n) growth. The films showed a preferential orientation on R-cut Al_2O_3 substrates. Sojkova et al. demonstrated experimentally that maintaining a constant TMD film thickness while varying only the carrier gas flow rate (and hence the evaporated sulfur source), the details are given in Section 4.2 led to orientations parallel to the basal plane [47].

TEM studies revealed mainly two important observations: firstly, both films were found to be polycrystalline in nature; secondly Nb-doped WS_2 films showed some

unconverted W blocks and in pristine WS_2, W residues were located in the middle of the film, as revealed by HAADF TEM, a density-sensitive technique. Interestingly, the presence of W blocks in the middle of the WS_2 layers suggests that the conversion process is not solely initiated from the top surface, where evaporated sulfur reacts with the deposited transition metal, as typically expected [48]. This finding implies that sulfur vapor interacts with the film in a more complex manner during the conversion process. The lack of sulfur partial pressure might lead to unconverted residues of W among WS_2 layers.

This unconverted W was found excessive in the Nb-doped WS_2 sample, simply incomplete conversion was observed, with W blocks located closer to the substrate. The presence of Nb could not be confirmed by EDS, which may indicate that Nb remained within the unconverted W, potentially making the alloy thermodynamically harder to convert to the sulfide based film. In the end Nb is used enhancing the refractory properties, strength, and toughness of alloys, as utilized in steel and alloying industries [49].

Electrical measurements revealed that pristine WS_2 films exhibited n-type behavior, with mobility and on/off ratios consistent with TAC-grown films. However, due to limitations in the growth process, variations in the resultant WS_2 films were observed, reaching up to 60%. Moreover, Nb-doped films demonstrated weak p-type conduction but exhibited poor gate control and higher conductivity, suggesting metallic behavior. This behavior is likely attributed to incomplete conversion and potential Nb clustering or layered formation within the films.

4.5 Conclusion

WS_2 naturally exhibits n-type behavior due to intrinsic defects, unintentional doping, and Fermi level pinning near the conduction band. This study investigates the potential of introducing niobium as a dopant to modulate the electronic properties of WS_2 and achieve p-type conductivity.

The synthesis process involved the Thermal Assisted Conversion method, where 1.76 at.% Nb was introduced into a nominal 10 nm tungsten stack prior to conversion. The conversion was performed at 900°C for 30 minutes in a sulfur-rich environment. Both pristine and Nb-doped WS_2 samples were characterized using Raman spectroscopy, X-ray diffraction, and transmission electron microscopy , confirming highly textured structures with (00n) orientation and the presence of characteristic Raman-active vibrational modes. Electrical characterization revealed that pristine WS_2 exhibited n-type behavior with a mobility of approximately 0.1 $cm^2/V{\cdot}s$ and an on/off current ratio of 8. Nb-doped WS_2 demonstrated very weak p-type conduction under higher voltage stresses, though incomplete conversion of tungsten layers hindered device performance.

4.5.1 Number of Devices and repeatability

The table 4.9 shows the substrates used to characterize pristine and Nb doped WS_2 films. Variations are calculated based on the minimum and maximum values of the electrical characterization results, more specifically mobility difference, for the pristine WS_2 transistor.

Table 4.9: Number of devices and variations for pristine and 1.76 at.% Nb-doped WS_2 samples. The numbers in parentheses next to the substrate in the table indicate the number of devices.

Sample	**XRR**	**XRD**	**Raman**	**TEM**	**Transistor**	**Variations**
WS_2	R cut(1)	R cut(1)	R cut(1)	R cut(1)	SiO_2(3)	Up to 60.56%
Nb-WS_2	R cut(1)	R cut(1)	R cut(1)	Glass(1)	SiO_2(3)	

4.6 Future Work

The table 4.9 reveals the number of samples used in this chapter. It underscores the need for further optimization of the metal film thickness for WS_2 films. In the MoS_2 chapter, all films exhibited full conversion, with segregated Rhenium attributed to excessive doping beyond the solubility limit of the Mo matrix. However, in this

chapter, complete conversion of tungsten (W) to WS_2 was not achieved, likely due to sulfur diffusion limitations in the thicker tungsten films. The presence of unconverted W residues, even in pristine samples, suggests that the sulfurization process requires further refinement. Therefore, optimizing the film thickness and systematically investigating structural and electrical properties are essential.

Future research should address several critical areas to optimize the synthesis process and fully exploit the potential of pristine WS_2 and Nb-doped WS_2. One significant challenge lies in the incomplete conversion of tungsten layers to WS_2, particularly in Nb-doped samples. This incomplete sulfurization compromises the uniformity and performance of the films. To overcome this, alternative sulfurization techniques, such as plasma-enhanced or high-pressure sulfurization, should be explored to improve the quality of WS_2 films by reducing voids and enhancing layer adhesion to the substrate.

Another critical area is achieving enhanced control of Nb doping to ensure uniform distribution and minimize clustering or metallic behavior in the doped films. Advanced deposition techniques, such as atomic layer deposition or molecular beam epitaxy, could offer the precision required for more consistent incorporation of Nb atoms into the WS_2 lattice. Systematic investigations of higher Nb doping concentrations could help enhance p-type behavior while addressing the issue of unconverted W layers. This would require detailed studies on the solubility limits of Nb and its impact on crystallinity.

Further, advanced characterization techniques, such as in situ Raman spectroscopy or X-ray diffraction during the sulfurization process, should be employed to monitor phase evolution and doping effects in real-time. High-resolution transmission electron microscopy, combined with elemental mapping techniques such as energy-dispersive X-ray spectroscopy or electron energy loss spectroscopy, could provide deeper insights into the spatial distribution of Nb and its impact on the film structure.

By addressing these areas, future research can overcome current limitations and unlock the full potential of Nb-doped WS_2 for applications in next-generation electronics, including complementary metal-oxide-semiconductor technologies and flexible devices. These advancements will contribute to bridging the performance gap between n-type and p-type TMDs, enabling more efficient and versatile electronic systems.

References

(1) Z. Hu, Z. Wu, C. Han, J. He, Z. Ni and W. Chen, *Chemical Society Reviews*, 2018, **47**, 3100–3128.

(2) M. Das, D. Sen, N. U. Sakib, H. Ravichandran, Y. Sun, Z. Zhang, S. Ghosh, P. Venkatram, S. Subbulakshmi Radhakrishnan, A. Sredenschek et al., *Nature Electronics*, 2024, 1–12.

(3) J. L. Lyons, A. Janotti and C. G. Van de Walle, *Applied Physics Letters*, 2009, **95**, 252105.

(4) H. C. Movva, A. Rai, S. Kang, S. Kim, L. Tan, S. Larentis, B. Fallahazad and E. Tutuc, *Nature*, 2022, **610**, 273–278.

(5) Y. Xiong, D. Xu, Y. Feng, G. Zhang, P. Lin and X. Chen, *Advanced Materials*, 2023, **35**, 2206939.

(6) L. Tang, R. Xu, J. Tan, Y. Luo, J. Zou, Z. Zhang, R. Zhang, Y. Zhao, J. Lin, X. Zou, B. Liu and H.-M. Cheng, *Advanced Functional Materials*, 2021, **31**, 2006941.

(7) S. M. Sze, Y. Li and K. K. Ng, *Physics of semiconductor devices*, John wiley & sons, 2021.

(8) Z. Qin, L. Loh, J. Wang, X. Xu, Q. Zhang, B. Haas, C. Alvarez, H. Okuno, J. Z. Yong, T. Schultz et al., *ACS nano*, 2019, **13**, 10768–10775.

(9) K. Dolui, I. Rungger, C. Das Pemmaraju and S. Sanvito, *Physical Review B—Condensed Matter and Materials Physics*, 2013, **88**, 075420.

(10) M. Shafer et al., *Physical Review Letters*, 1972, **28**, 808.

(11) W. Zheng, J. Lin, W. Feng, K. Xiao, Y. Qiu, X. Chen, G. Liu, W. Cao, S. T. Pantelides, W. Zhou et al., *Advanced Functional Materials*, 2016, **26**, 6371–6379.

(12) H. Zhou, C. Wang, J. C. Shaw, R. Cheng, Y. Chen, X. Huang, Y. Liu, N. O. Weiss, Z. Lin, Y. Huang et al., *Nano letters*, 2015, **15**, 709–713.

(13) M. R. Laskar, D. N. Nath, L. Ma, E. W. Lee, C. H. Lee, T. Kent, Z. Yang, R. Mishra, M. A. Roldan, J.-C. Idrobo et al., *Applied Physics Letters*, 2014, **104**.

(14) J. Suh, T.-E. Park, D.-Y. Lin, D. Fu, J. Park, H. J. Jung, Y. Chen, C. Ko, C. Jang, Y. Sun et al., *Nano letters*, 2014, **14**, 6976–6982.

(15) M. Björck and G. Andersson, *Journal of Applied Crystallography*, 2007, **40**, 1174–1178.

(16) A. Glavic and M. Björck, *Journal of applied crystallography*, 2022, **55**, 1063–1071.

(17) G. D. Wilk, R. M. Wallace and J. Anthony, *Journal of applied physics*, 2001, **89**, 5243–5275.

(18) D. Keane, Ph.D. Thesis, Trinity College Dublin, 2020.

(19) R. Roberge, *J. Less-Common Met.;(Switzerland)*, 1975, **40**.

(20) S. Lin, Y. Liu, Z. Hu, W. Lu, C. H. Mak, L. Zeng, J. Zhao, Y. Li, F. Yan, Y. H. Tsang et al., *Nano Energy*, 2017, **42**, 26–33.

(21) J. Huang, N. Dong, N. McEvoy, L. Wang, C. O. Coileain, H. Wang, C. P. Cullen, C. Chen, S. Zhang, L. Zhang et al., *ACS nano*, 2019, **13**, 13390–13402.

(22) C. P. Cullen, Ph.D. Thesis, Trinity College Dublin, School of Chemistry, 2020.

(23) F. Wang, I. A. Kinloch, D. Wolverson, R. Tenne, A. Zak, E. O'Connell, U. Bangert and R. J. Young, *2D Materials*, 2016, **4**, 015007.

(24) R. I. Romanov, M. G. Kozodaev, A. G. Chernikova, I. V. Zabrosaev, A. A. Chouprik, S. S. Zarubin, S. M. Novikov, V. S. Volkov and A. M. Markeev, *ACS omega*, 2021, **6**, 34429–34437.

(25) A. Barbosa, N. Figueroa, M. Giarola, G. Mariotto and F. Freire Jr, *Materials Chemistry and Physics*, 2020, **243**, 122599.

(26) M. R. Molas, K. Nogajewski, M. Potemski and A. Babiński, *Scientific reports*, 2017, **7**, 5036.

(27) A. Berkdemir, H. R. Gutiérrez, A. R. Botello-Méndez, N. Perea-López, A. L. Elías, C.-I. Chia, B. Wang, V. H. Crespi, F. López-Urías, J.-C. Charlier et al., *Scientific reports*, 2013, **3**, 1755.

(28) M. Kim, J. Seo, J. Kim, J. S. Moon, J. Lee, J.-H. Kim, J. Kang and H. Park, *ACS nano*, 2021, **15**, 3038–3046.

(29) C. Ballif, M. Regula, P. Schmid, M. Remškar, R. Sanjines and F. Lévy, *Applied Physics A*, 1996, **62**, 543–546.

(30) F. Bozheyev, K. Harbauer, C. Zahn, D. Friedrich and K. Ellmer, *Scientific reports*, 2017, **7**, 16003.

(31) I. Hotovy, L. Spiess, M. Mikolasek, I. Kostic and H. Romanus, *Vacuum*, 2020, **179**, 109570.

(32) A. Jäger-Waldau, M. C. Lux-Steiner, G. Jäger-Waldau and E. Bucher, *Applied surface science*, 1993, **70**, 731–736.

(33) M. M. S. Villamayor, A. Lindblad, F. O. Johansson, T. Tran, N. H. Pham, D. Primetzhofer, N. L. Sorgenfrei, E. Giangrisotomi, A. Föhlisch, P. Lourenço et al., *Vacuum*, 2021, **188**, 110205.

(34) K. Ellmer, *Physica status solidi (b)*, 2008, **245**, 1745–1760.

(35) Y. Zhang, L. Yin, J. Chu, T. A. Shifa, J. Xia, F. Wang, Y. Wen, X. Zhan, Z. Wang and J. He, *Advanced Materials*, 2018, **30**, 1803665.

(36) H. R. Gutiérrez, N. Perea-López, A. L. Elías, A. Berkdemir, B. Wang, R. Lv, F. López-Urías, V. H. Crespi, H. Terrones and M. Terrones, *Nano letters*, 2013, **13**, 3447–3454.

(37) H. Li, H. Wu, S. Yuan and H. Qian, *Scientific reports*, 2016, **6**, 21171.

(38) P. Gultom, J.-Y. Chiang, T.-T. Huang, J.-C. Lee, S.-H. Su and J.-C. A. Huang, *Nanomaterials*, 2023, **13**, 1276.

(39) Z. Zhang, Y. Zhao, J. Lin, X. Zou, B. Liu and H.-M. Cheng, *Advanced Electronic Materials*, 2023, **9**, 2300735.

(40) M.-H. Yang, K. B. Teo, L. Gangloff, W. I. Milne, D. G. Hasko, Y. Robert and P. Legagneux, *Applied Physics Letters*, 2006, **88**.

(41) C. Hu, in *Modern Semiconductor Devices for Integrated Circuits*, Accessed from https://www.chu.berkeley.edu/wp-content/uploads/2020/01/Chenming-Hu$_c$h5 − 1.*pdf*, Prentice Hall, 2010, pp. 145–160.

(42) H. F. Haneef, A. M. Zeidell and O. D. Jurchescu, *Journal of Materials Chemistry C*, 2020, **8**, 759–787.

(43) M. Shaji, K. Saji and M. Jayaraj, 2020 5th IEEE International Conference on Emerging Electronics (ICEE), 2020, pp. 1–3.

(44) A. Mondal, C. Biswas, S. Park, W. Cha, S.-H. Kang, M. Yoon, S. H. Choi, K. K. Kim and Y. H. Lee, *Nature Nanotechnology*, 2024, **19**, 34–43.

(45) R. Misra, M. McCarthy and A. F. Hebard, *Applied Physics Letters*, 2007, **90**.

(46) T. Hallam, S. Monaghan, F. Gity, L. Ansari, M. Schmidt, C. Downing, C. P. Cullen, V. Nicolosi, P. K. Hurley and G. S. Duesberg, *Applied Physics Letters*, 2017, **111**.

(47) M. Sojková, K. Vegso, N. Mrkyvkova, J. Hagara, P. Hutár, A. Rosová, M. Čaplovičová, U. Ludacka, V. Skákalová, E. Majková et al., *RSC advances*, 2019, **9**, 29645–29651.

(48) Y. H. Lee, X. Zhang, W. Zhang, M.-T. Chang, C.-T. Lin, K. Chang, Y.-C. Yu, J.-K. Wang, C.-S. Chang, L.-J. Li et al., *Advanced Materials*, 2012, **24**, 2320–2325.

(49) L. Bencze, G. Hasemann, D. Sergeev, V. Motalov, M. Müller and M. Krüger, *Journal of Alloys and Compounds*, 2024, **976**, 173279.

5 | Solution Processed Negative Gauge Factor $PtSe_2$ Sensors

5.1 Background and Motivation

Piezoresistance is the property of certain materials to change their electrical resistance in response to applied mechanical stress. This effect is widely harnessed in strain sensors, where piezoresistive materials respond electrically to mechanical deformation. In piezoresistive sensors, sensor sensitivity is quantified by the gauge factor G, defined as $\Delta R/R_0 = G\epsilon$ under low strain conditions, where the resistance response $\Delta R/R_0$ is directly proportional to the applied strain ϵ [1]. This gauge factor is crucial and widely studied in piezoresistor research [2].

Traditional piezoresistive sensors include metallic strain gauges, which typically exhibit gauge factors between 1 and 5 and are effective for strains below 0.01% [3], as well as silicon-based sensors, which offer a higher gauge factor (50–200) [4] allowing for the detection of small strains (1%) [4]. However, silicon sensors are brittle and lack conformality, limiting their effectiveness in applications requiring flexibility. For applications involving non-flat, adaptable surfaces—such as wearables or biomedical devices—strain sensors need to be flexible and conformal to adapt to dynamic functionality. Flexible electronic applications necessitate that materials be processed at low temperatures to accommodate the flexibility of substrates such as polyimide, polyethylene terephthalate (PET), foil, paper, and starch-based materials

[5]. Several strategies have been suggested to broaden the range of compatible substrates, including the introduction of new materials. For instance, two-dimensional (2D) materials play a crucial role in nanostructured piezoresistive sensors, serving as a conductive additive in nanocomposites and forming the basis of polymer-free films and networks [6].

Using the piezoresistive qualities of 2D materials, strain sensors exhibiting gauge factors ranging between 0.55 for graphene [7] to 350 [8] have been developed. The wide range of gauge factors is due to different growth conditions for materials synthesized at high temperatures ($> 120°C$) as well as varying percolation and cracking behaviors in materials, which influence the continuity of conductive pathways and the mechanical stability under strain [9].

Among 2D materials, $PtSe_2$, a typical member of the group-10 TMDs, exhibits properties that could be useful in sensor applications due to its tunable electronic band structure [10]. The most common method for producing few-layer $PtSe_2$ (<1 mg) involves using furnaces, where the transformation of TMD materials incurs significant thermal-budget costs estimated at 0.75 kWh for an hour growth at 400 °C with the assumption of 3 kW power rating and 80% furnace efficiency. Furthermore, this processing method is not compatible with flexible substrates due to the high-temperature requirements [11–14]. Other low-temperature methods are available, but they often require acidic chemical treatments [15, 16], further limiting compatibility. Consequently, fabricating piezoresistive materials on soft and transparent substrates without thermal or electrochemical treatments remains a challenge.

One technique that shows promise in addressing the challenges is electrochemical exfoliation (EE), which offers a low-energy pathway for producing materials without harsh chemical treatments or high temperatures. EE leverages ions' intercalation to induce layered materials' exfoliation [17], resulting in the formation of nanosheets with thicknesses below 10 nm [18]. By controlling the electrochemical parameters, such as voltage and electrolyte composition, the lateral size, thickness, and mor-

phology of the exfoliated flakes can be tailored, offering greater control over the final network properties [19]. Another critical aspect of fabricating flexible electronic devices is the deposition method used to assemble $PtSe_2$ flakes into functional networks. The alignment and packing of flakes play a crucial role in determining the overall performance of the devices. Several deposition techniques have been explored to align $PtSe_2$ flakes, including spin-coating [20] and dip-coating [21]. However, these techniques often suffer from limitations such as poor coverage, non-uniformity, and limited scalability, thereby hindering their widespread adoption in flexible electronic applications.

Langmuir-Schaefer (LS) deposition offers a promising solution to overcome the limitations of conventional deposition techniques [22]. LS deposition involves the self-assembly of $PtSe_2$ flakes at the liquid-liquid interface [23], followed by the transfer of the assembled network onto a substrate. LS deposition enables precise control over the packing density and orientation of flakes, resulting in a highly aligned and conformal network with minimal mesoporosity [19].

Furthermore, LS deposition can be performed at room temperature, eliminating the need for high-temperature processing steps that are incompatible with flexible substrates [24]. This study leverages the LS deposition technique to explore networks of EE-processed $PtSe_2$, aiming to demonstrate its potential for enhancing the performance and scalability of nanosheet-based sensors on flexible substrates.

5.2 Methodology

5.2.1 Electrochemical Exfoliation of $PtSe_2$ Crystal

The electrochemical exfoliation process started intercalating the $PtSe_2$ bought from HQ Graphene crystals. To incorporate $PtSe_2$ (HQ Graphene) crystals, a two-electrode electrochemical setup is employed. The cathode comprises a small amount of crystal piece, measuring 5 mm, while a platinum foil sourced from Alfa Aesar acts as the an-

ode. Copper crocodile clips are used to secure the electrodes in the solution securely. The electrolyte solution consists of 5 mg/ml tetrapropylammonium (TPA) bromide obtained from Sigma-Aldrich mixed with 50 ml of propylene carbonate. Applying a voltage of -8V across the electrodes for 30 mins facilitates the intercalation of the 2D crystal with TPA+ cations. The observed expansion of the 2D crystal to over twice its original volume corroborates successful intercalation. Later, the expanded $PtSe_2$ crystal went through a bath sonication process utilizing the Fisherbrand 1122xx series bath sonicator using 1mg/ml poly(vinylpyrrolidone) (PVD) and (DMF) for 5 minutes, the details in the next section.

5.2.2 Ink Formulation with $PtSe_2$ Crystal

The $PtSe_2$ crystal undergoes a series of treatments: it is first bath-sonicated in a solution containing 1 mg/mL polyvinylpyrrolidone (PVP) in dimethylformamide (DMF) for 5 minutes. Then, centrifugation at 500 rpm (24g) for 20 minutes removes any unexfoliated crystals. The resulting dispersion is further size-selected by centrifuging the supernatant (top 90%) at 1000 rpm (97g) for 1 hour and collecting the sediment. To eliminate the PVP, the sediment is diluted with 2 mL of DMF and centrifuged at 10k rpm (9744g) for 1 hour, repeating this process twice and collecting the sediment each time. A third washing step, using isopropano (IPA), removes residual DMF: the sediment is diluted in 0.5 mL of IPA and centrifuged at 10k rpm (9744g), with the sediment collected afterward. The sediment is then redispersed in IPA (approximately 0.5 mL, concentration around 2.5 mg/mL) to create the 97g dispersion used for $PtSe_2$ in the study. IPA is chosen for its low boiling point (approximately 82.5°C), allowing for rapid evaporation after LS deposition.

5.2.3 $PtSe_2$ Network Formation by Langmuir-Schaefer

The LS assembly involves positioning a Si/SiO_2 and PET chips (2 × 2 cm) on top of a Teflon stand (10 cm long), placed within a beaker containing approximately 100 mL of deionized water. A layer of distilled hexane (around 20 mL) is then deposited

onto the water's surface to create a water/hexane interface, under which the chip is submerged. Next, inks of $PtSe_2$ are drop-cast (approximately 140 μL) onto the hexane surface until complete coverage is achieved. The Teflon stand and Si/SiO_2 chip are carefully lowered through the 2D crystal layer to coat the substrate surface with the TMD network. The resulting TMD networks are then allowed to dry in ambient air within a fume hood for approximately 6 hours.

5.2.4 Atomic Force Microscopy

AFM measurements were carried out with a Bruker Multimode 8 microscope to assess flake thickness and size. After diluting in IPA (1:100), $PtSe_2$ inks were applied to Si/SiO_2 surfaces and then annealed at 120°C) for 15 minutes. Employing OLTESPA R3 cantilevers in ScanAsyst mode allowed us to scan and statistically analyze x flakes, calculating their lateral size as the square root of length times width.

5.2.5 Raman Spectroscopy

The $PtSe_2$ inks drop casted on Si/SiO_2 substrates. Raman analysis was carried out using Witec Alpha 300R confocal Raman microscope with a laser wavelength of 532 nm at a power of < 300 μW and a spectral grating with 1800 lines/mm. The spectra shown for the sample were obtained by averaging 20 discrete point spectra.

5.2.6 Optical Absorption Spectroscopy

The transmission spectra of he single LS deposited network was acquired using a Cary50 UV-Vis spectrometer.

5.2.7 X-Ray Diffraction

XRD spectra were captured using a Panalytical X'Pert Pro diffractometer with a Cu tube emitting Kα radiation (1.5406). The spectra were acquired in the 2θ range from 10° to 80° on the films prepared via LS technique using the Si/SiO_2 (100) orientated

wafers that have 300 nm oxide.

5.2.8 Electromechanical Testing

Mechanical testing was performed using a Zwick Z0.5 ProLine Tensile Tester fitted with a 100 N load cell. We attached silver wires to the $PtSe_2$ network, which was deposited on PET through the LS method, using silver paint to form electrical connections. The dimensions of the samples were approximately 5 mm by 25 mm, and they featured a PET layer thickness of 130 μm. Before testing, the sensors were subjected to a conditioning regimen that included cyclic stretching using a sawtooth strain profile, a critical step to prevent inaccurate electrical readings during the initial stretch/release cycle due to the network's original non-equilibrium condition. Resistance measurements were conducted with a Keithley KE2601 Source-Meter, controlled through a 2-probe LabView configuration. The electromechanical testing was limited to a maximum strain of 0.5 % to avoid permanent damage such as cracking or electrode delamination.

5.3 Results and Discussion

5.3.1 $PtSe_2$ Ink Production and Characterization

Electrochemical exfoliation is utilized to intercalate and expand bulk $PtSe_2$ crystals. A photograph of a $PtSe_2$ crystal is shown in Figure 5.1 (a). Figure 5.1 (b) illustrates the schematic of the setup used in the electrochemical exfoliation (EE) process, where a single $PtSe_2$ crystal is connected to the anode via crocodile clips, while a Pt foil serves as the cathode. A bias of -8V is applied between the electrodes for 30 minutes to insert TPA^+ cations into the $PtSe_2$ crystal. Tian *et al.* demonstrated the effectiveness of this bias for other TMD films such as MoS_2 and WS_2, which justifies using the same voltage for $PtSe_2$ [19]. This applied bias causes the crystal to expand to more than twice its original volume [19], indicating successful cation insertion under the applied negative bias. The resulting exfoliated $PtSe_2$ ink is shown in a

bottle in Figure 5.1 (c).

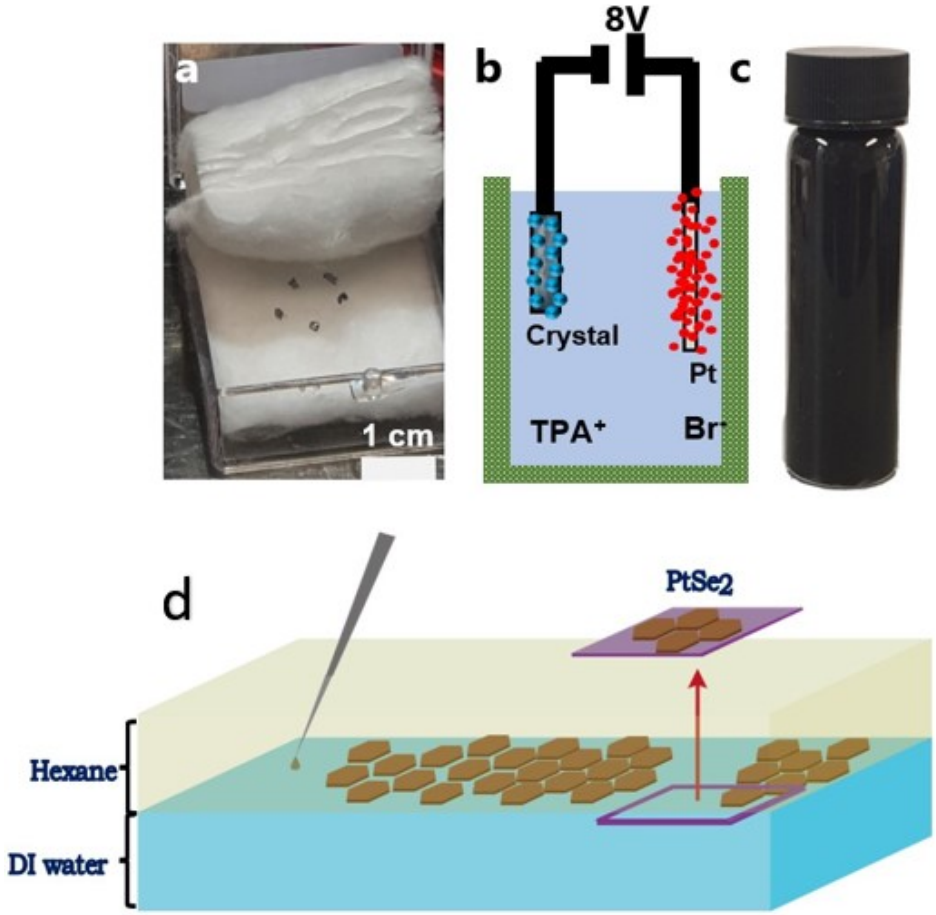

Figure 5.1: (a) Photograph of a bulk $PtSe_2$ crystal before exfoliation, showing its compact structure. (b) Schematic of the electrochemical exfoliation (EE) setup: a $PtSe_2$ crystal is connected to the anode via crocodile clips, and a Pt foil serves as the cathode. A bias of -8V is applied between the electrodes to intercalate TPA^+ cations into the crystal. (c) Image of the exfoliated $PtSe_2$ ink in a bottle, demonstrating its dispersion in solution. (d) The schematic of the Langmuir Scaheffer deposition. [TALK]The scale bar in (a) is 5 mm.

To verify the presence and assess the quality of the $PtSe_2$ flakes after electrochemical exfoliation, Raman spectroscopy is employed as the initial analytical technique, as shown in Figure 5.2 (a) and (b). Initially, $PtSe_2$ flakes are deposited on a polyimide substrate to perform strain measurements. However, polyimide exhibits strong fluorescence under laser excitation [25], resulting in significant background noise that obscures the vibrational modes of $PtSe_2$, as shown in Figure 5.2 (a). To overcome this issue, the flakes are instead deposited on a Si/SiO_2 substrate. Using this approach, the characteristic vibrational modes of the $PtSe_2$ flakes are resolved, while carefully controlling the laser power to remain below 300 μW to avoid heating the

$PtSe_2$ network on the Si/SiO_2 substrate.

This technique reveals two prominent Raman peaks at 178 cm^{-1} and 206 cm^{-1}, corresponding to the E_g in-plane vibrational mode and the A_{1g} out-of-plane vibrational mode, respectively. Additionally, a subtle peak near 232 cm^{-1} is observed, attributed to the longitudinal optical (LO) mode. The E_g mode reflects in-plane atomic vibrations, describing lateral properties of the layers. The A_{1g} mode corresponds to out-of-plane vibrations, highlighting interlayer interactions. The LO mode, a mixed vibrational and electronic mode, is linked to longitudinal phonons and electron-phonon coupling. The Raman results align with findings reported in the literature [26–29].

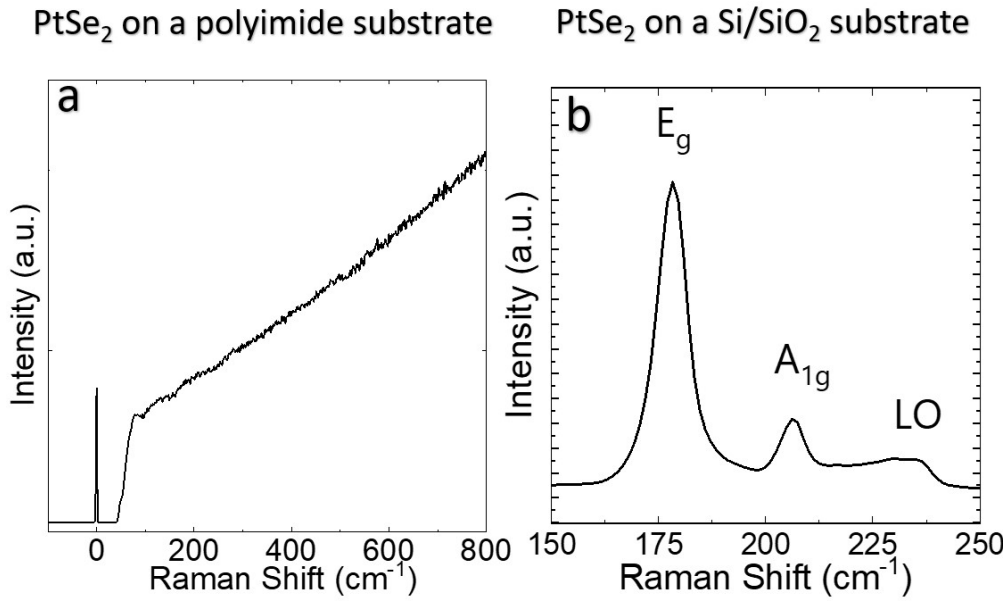

Figure 5.2: Raman spectroscopy of $PtSe_2$ flakes on different substrates. (a) Raman spectrum of $PtSe_2$ deposited on a polyimide substrate, showing high fluorescence and background interference. (b) Raman spectrum of $PtSe_2$ on a Si/SiO_2 substrate, revealing distinct vibrational peaks at 178 cm^{-1} (E_g mode), 206 cm^{-1} (A_{1g} mode), and a subtle LO mode near 232 cm^{-1}.

Subsequently, atomic force microscopy (AFM) is applied to analyze the structural properties of deposited $PtSe_2$ flakes, as illustrated in Figure 5.3(a). Since polyimide is a flexible substrate, a Si/SiO_2 substrate is used for depositing the flakes prior to AFM characterisation. The AFM image provides a detailed micrograph of a flake with a thickness of 4 nm and its corresponding cross-sectional profile. Furthermore,

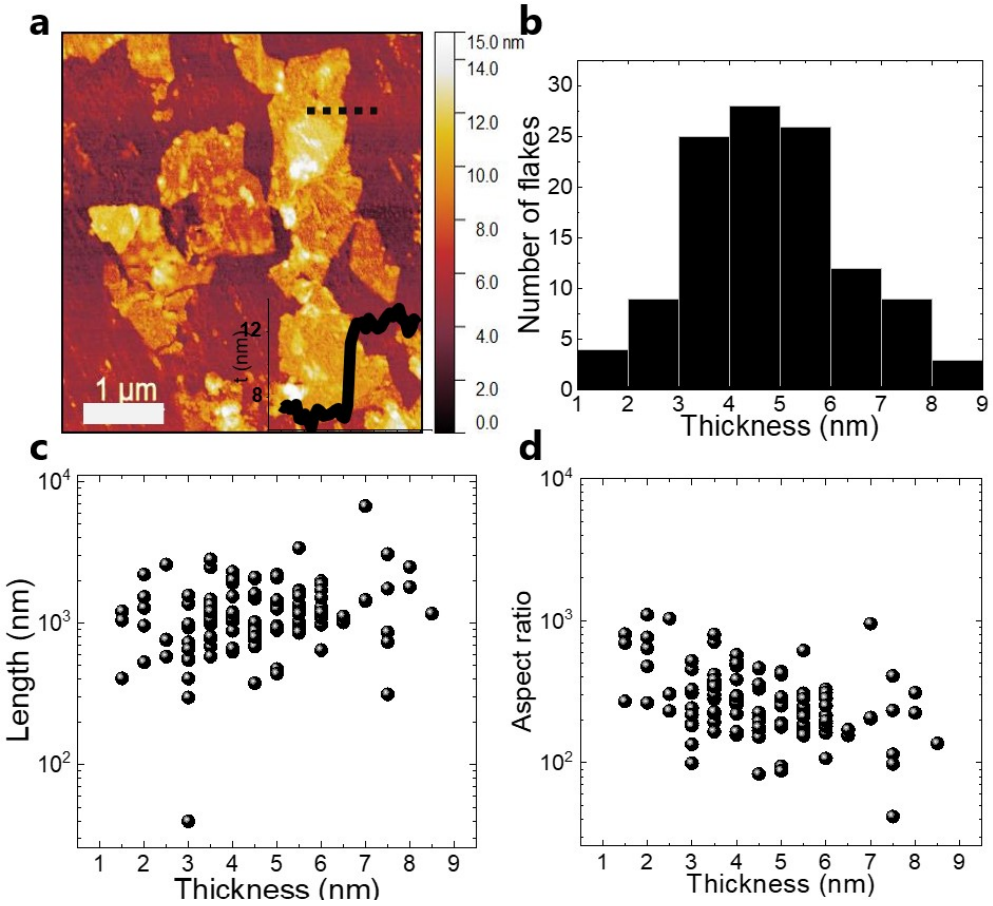

Figure 5.3: AFM analysis of the $PtSe_2$ network. (a) AFM micrograph of $PtSe_2$ flakes showing a flake with a thickness of approximately 4 nm, as indicated by the cross-sectional profile. (b) Histogram of flake thickness distribution, with an average thickness of 4.5 nm and a standard deviation of $\pm$1.57 nm. (c) Thickness vs. length scatter plot, showing the length distribution of flakes, with an average length of 1.3 μm and a standard deviation of $\pm$0.8 μm. (d) Aspect ratio vs. thickness scatter plot, revealing a broad range of aspect ratios with an average exceeding 300, emphasizing the significant anisotropy in the flakes' dimensional properties.

the distribution of flake thicknesses and lengths is statistically analyzed, with histograms presented in Figures 5.3(b), 5.3(c), and 5.3(d), respectively. The average flake thickness is recorded as 4.5 nm with a standard deviation of $\pm$1.57 nm, as seen in Figure 5.3(b). This measurement suggests the presence of fewer than 10 layers, considering an interlayer distance of 0.5 nm [30]. The average flake length is measured as 1.3 µm with a standard deviation of $\pm$0.8 µm, as shown in Figure 5.3(c). Additionally, the aspect ratio distribution of the flakes, depicted in Figure 5.3(d), shows a broad range, with an average aspect ratio exceeding 300. This high aspect ratio underscores the significant anisotropy in the dimensional properties of

the flakes. This high aspect ratio underscores the significant anisotropy in the dimensional properties of the flakes, highlighting their elongated geometry with a much greater length compared to their thickness. Such anisotropy is characteristic of exfoliated 2D materials, where the atomic layers are strongly bonded within the plane but weakly bonded between the layers, resulting in unique structural and mechanical properties. This feature is crucial for applications requiring directional conductivity or flexibility [31].

Transmission spectra of the $PtSe_2$ network on a polyimide substrate were measured using an integrating sphere to separate the influence of the substrate from that of the $PtSe_2$, as shown in Figure 5.4(a). The transmission behavior of $PtSe_2$ was determined to be approximately 60% at a wavelength of 1000 nm after subtracting the substrate influence. The inset in Figure 5.4(a) shows an optical micrograph of the $PtSe_2$ network on the polyimide substrate, revealing uniform deposition over a large area.

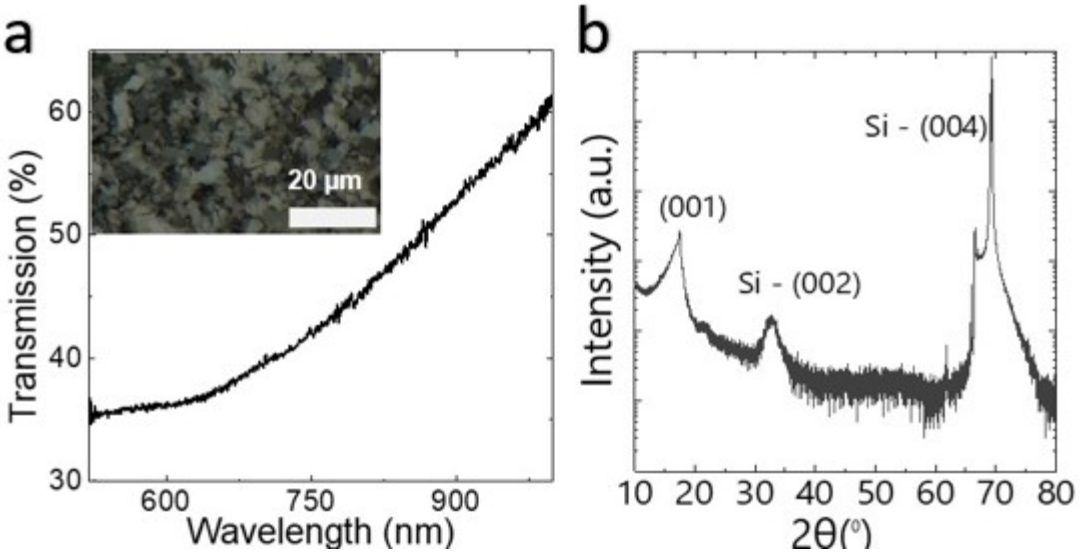

Figure 5.4: (a) Transmission spectrum of the $PtSe_2$ network on a polyimide substrate, showing approximately 60% transmission at 1000 nm. The inset displays an optical micrograph of the $PtSe_2$ network, demonstrating uniform flake distribution with a scale bar of 20 µm. (b) XRD pattern of the $PtSe_2$ network on a Si/SiO_2 substrate, with a prominent peak at 17.4° corresponding to the (001) orientation and an interlayer spacing of 0.5 nm. Peaks associated with the Si substrate, such as Si-(002) and Si-(004), are also identified.

Verification of the orientation of the $PtSe_2$ flakes on the Si/SiO_2 substrate was con-

ducted using X-ray diffraction (XRD) analysis, as illustrated in Figure 5.4(b). XRD was employed to assess the crystalline plane orientations of the $PtSe_2$ network. A prominent peak at 17.4°, corresponding to an inter-layer spacing of 0.5 nm [32], confirms the (001) orientation of the flakes [33, 34]. Additional peaks, such as Si-(002) and Si-(004), arise from the substrate, and their intensities validate the proper alignment of the $PtSe_2$ flakes on the substrate.

The key point of electromechanical properties of $PtSe_2$, was previously, was found based on the stacking order of the assemblies [35, 36] and alignment of the crystals[37]. Following EE and LS deposition processes, the $PtSe_2$ networks demonstrated a unique 001 diffraction peak. This observation suggests that the flakes within the network are primarily aligned along the basal plane, without the presence of additional peaks indicative of varied orientations.

5.3.2 Sensor Measurements of $PtSe_2$ Networks

The piezoresistance of a material is closely linked to its electrical properties. For this reason, the electrical resistivity of the $PtSe_2$ networks was first measured, yielding $\rho_{\mathrm{Net}} = 0.83 \pm 0.05\,\Omega\mathrm{m}$ [38]. It has been shown that, for low-porosity networks composed of high-carrier-density nanosheets [39], the resistivity can be expressed as:

$$\rho_{\mathrm{Net}} = t_{\mathrm{NS}}(R_{\mathrm{NS}} + R_{\mathrm{J}}) \tag{1}$$

Here, t_{NS} represents the nanosheet thickness, while R_{NS} and R_{J} denote the resistances of the nanosheets and the inter-nanosheet junctions, respectively. This relationship reflects the fact that charge carriers traversing the network must cross an inter-nanosheet junction each time they pass through a nanosheet. When the junction resistance is significantly larger than the nanosheet resistance, the network resistivity becomes much higher than that of its individual nanosheets [39]. Previous studies on $PtSe_2$ networks have indicated that $R_{\mathrm{NS}} \ll R_{\mathrm{J}}$ [38], suggesting that

these networks are dominated by junction resistance. This allows Equation (1) to be simplified to $\rho_{\mathrm{Net}} \approx t_{\mathrm{NS}} R_{\mathrm{J}}$. Using the measured value of $t_{\mathrm{NS}} = 4.5 \pm 1.6\,\mathrm{nm}$, the junction resistance was estimated to be $R_{\mathrm{J}} \approx 90\,\mathrm{M\Omega}$, which is significantly larger than the few MΩ values previously reported for MoS_2 networks [38].

To evaluate the suitability of the $PtSe_2$ networks fabricated via electrochemical exfoliation and Langmuir-Schaefer deposition for piezoresistive sensor applications, electrical measurements under tensile strain were conducted. The strain sensor had a gauge length of 2 cm, as shown in Figure 5.5 (a) (inset). The network was kept taut at the start of the measurement. A reduction in electrical resistance was observed as tensile strain was applied, as illustrated in Figure 5.5 (a), indicating a negative gauge factor of -5.0.

The linear response of the $PtSe_2$ strain gauge up to 0.5% tensile strain demonstrates its potential for strain-sensing applications, particularly in low-strain conditions. Furthermore, the sensitivity of the strain gauge, represented by the slope of $\Delta R/R_0$ versus ϵ, was higher than that of conventional metal foil strain gauges [40]. This negative piezoresistive effect, where resistance decreases under tensile strain, is characteristic of semiconductor strain gauges, differing from the behavior of metal foil strain gauges [41]. A similar negative gauge factor of -12 has been reported for nickel metal [1]. Long-term stability of the devices was assessed through cyclic tests, as shown in Figure 5.5 (b). The upper graph in Figure 3b shows the strain profile during cyclic electromechanical testing, with a triangular sawtooth pattern ranging from 0 to 0.5% strain and a strain rate of 1%/s. The lower graph illustrates corresponding resistance changes over time, showing periodic resistance variations aligned with the applied strain, 5.5 (b). This confirms the strain gauge's responsiveness. Figure 5.5 (c) presents a histogram of the calculated gauge factors from repeated measurements, with values normally distributed around -5.45 ± 0.33. These results align with findings by Boland et al., who reported a negative gauge factor of up to -12 in $PtSe_2$ layers converted from a platinum coating on polymer substrates through high-temperature processing [42]. Wagner et al. observed an even

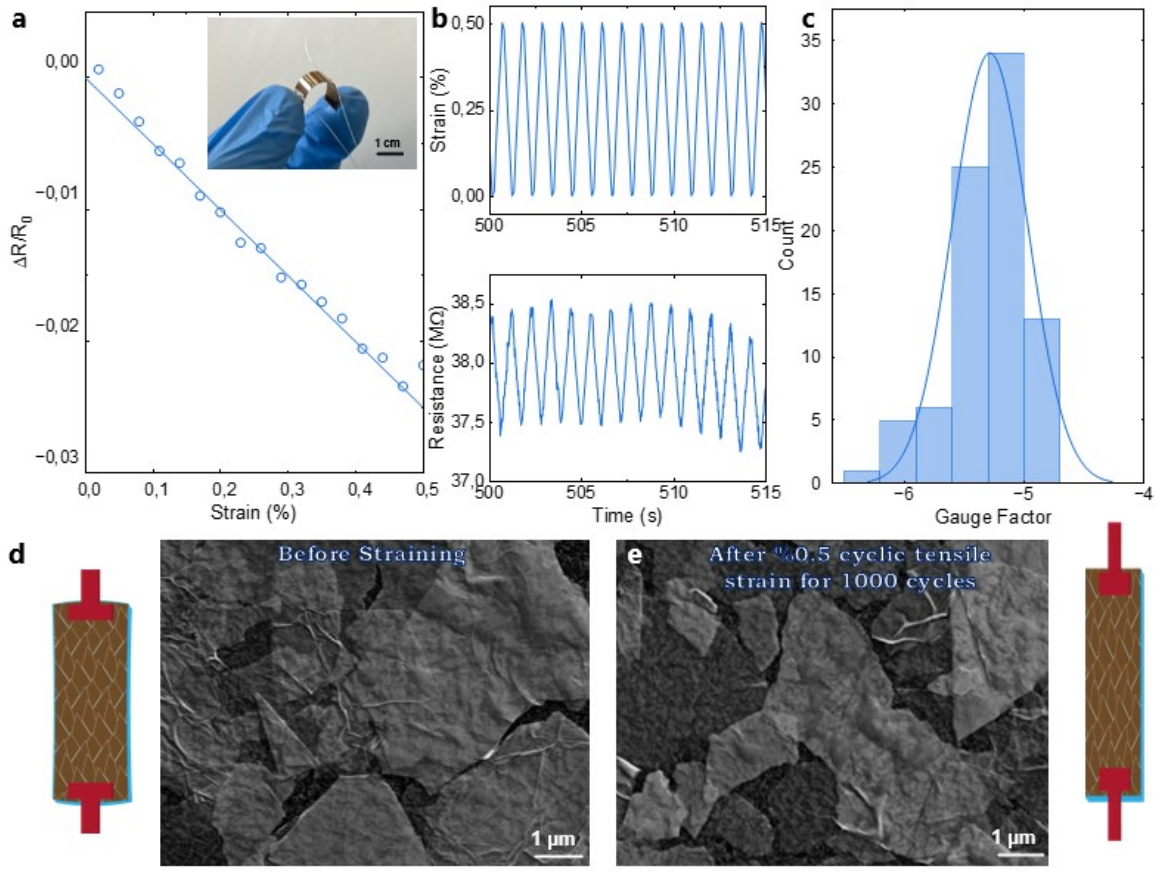

Figure 5.5: Electromechanical characterization of the $PtSe_2$ network. (a) Relative resistance change ($\Delta R/R_0$) as a function of applied tensile strain up to 0.5%, showing a negative gauge factor of -5.0. The inset illustrates the strain gauge with a gauge length of 2 cm. (b) Cyclic strain testing with a triangular sawtooth strain profile (top) and corresponding resistance response (bottom), demonstrating the stability of the strain gauge over 1000 cycles. (c) Histogram of gauge factor measurements, showing a normal distribution centered around -5.45 ± 0.33. (d, e) SEM images of the $PtSe_2$ network before and after 1000 cycles of 0.5% tensile strain, showing the network's structural integrity with continuous percolation paths and long junction overlaps.

higher negative gauge factor of -84.8 in TAC-grown $PtSe_2$ films transferred onto polyimide, attributed to an increase in the density of states under strain [43]. The observation of a negative gauge factor in $PtSe_2$ networks represents a significant distinction from the positive gauge factors seen in metallic strain gauges. This behavior highlights the semiconductor-like properties of $PtSe_2$, with resistance decreasing under tensile strain. The LS deposition technique enhances this behavior by creating highly aligned and densely packed flakes, improving the network's mechanical stability. SEM imaging was conducted before and after 1000 cycles of 0.5% cyclic

tensile strain (Figures 5.5 (d) and 5.5 (e)). The $PtSe_2$ flakes maintained a continuous percolating network, with junctions characterized by long overlaps and edge-to-edge contacts.

It is noted that the gauge factor measured in the solution deposited networks (-5.45) is significantly lower than the value reported by Wagner [43] (-85). To understand the nature of this discrepancy, a simple model is developed to describe passive resistance in the networks. Details of this model are provided in the Appendix A3. For any isotropic piezoresistive material, the gauge factor is expressed as [1]:

$$G = (1 + 2\nu) + \frac{1}{\rho_0}\frac{d\rho}{d\epsilon} \tag{2}$$

where ν and ρ represent the Poisson ratio and resistivity of the piezoresistive material, and ρ_0 denotes its zero-strain resistivity. The first term accounts for the effect of strain on sample dimensions (and resistance), while the second term describes the effect of strain on the intrinsic material properties. This general equation is combined with Equation 1, which describes the resistivity of a nanosheet network, to obtain the network gauge factor:

$$G_{\text{Net}} = (1 + \nu_y + \nu_z) + \frac{\frac{dR_{\text{NS}}}{d\epsilon} + \frac{dR_J}{d\epsilon}}{R_{\text{NS},0} + R_{J,0}} \tag{3}$$

Here, the subscript "0" denotes the values of the nanosheet and junction resistances at $\epsilon = 0$. Additionally, the first term is modified to account for the fact that nanosheet networks are anisotropic and are expected to exhibit different Poisson ratios in the in-plane (y) and out-of-plane (z) directions (since the strain is applied in the x direction).

Equation 3 is presented as a general expression for the gauge factor of a low-porosity network of highly aligned nanosheets. This equation is applicable to various specific scenarios by considering the nature of the parameters $\frac{dR_{\text{NS}}}{d\epsilon}$ and $\frac{dR_J}{d\epsilon}$. The simplest situation is that where straining the network results in the nanosheets sliding

past each other without themselves becoming strained. Within this scenario, $\frac{dR_{\mathrm{NS}}}{d\epsilon}$ = 0, because the nanosheets themselves remained undeformed. This situation has been observed previously in aligned networks of electrochemically exfoliated MoS_2 nanosheets [44]. However, as it is shown in Appendix A3, such a scenario cannot describe a negative gauge factor within the network.

The second simplest situation is one where all the strain applied to the substrate is transferred to the nanosheets. As described in the Appendix A3, the parameters $\frac{dR_{\mathrm{NS}}}{d\epsilon}$ and $\frac{dR_J}{d\epsilon}$ were calculated under circumstances of full strain transfer. Under these conditions, Equation 3 is derived as:

$$G_{\mathrm{Net}} = (2\nu_y + \nu_z) + \frac{\rho_{\mathrm{NS},0}}{\rho_{\mathrm{Net},0}} \left[G_{\mathrm{NS}} - (\nu_y - 1) \right] \tag{4}$$

Here, G_{NS} denotes the intrinsic gauge factor of the nanosheets, while $\rho_{\mathrm{NS},0}$ and $\rho_{\mathrm{Net},0}$ represent the zero-strain resistivities of the individual nanosheets and the network, respectively. The Poisson ratios $\nu_y = 0.5$ (associated with the polymer substrate) and $\nu_z = 0$ (consistent with networks) are approximated [45, 46].

By further simplifying the relationship, Equation 4 can be approximated as:

$$G_{\mathrm{Net}} \sim G_{\mathrm{NS}} \frac{\rho_{\mathrm{NS},0}}{\rho_{\mathrm{Net},0}} \tag{5}$$

This equation 5 demonstrates in a straightforward manner that, for nanosheet networks that are severely junction limited ($\rho_{NS,0} \ll \rho_{Net,0}$), the gauge factor of the network is significantly reduced compared to that of the nanosheets themselves. Such junction limitations are observed in most nanosheet networks [39]. Indeed, Carey [38] showed that, for networks of electrochemically exfoliated $PtSe_2$ nanosheets, the intrinsic mobility of the nanosheets was $\mu_{NS} = 20\,\mathrm{cm}^2/\mathrm{Vs}$, while the mobility of the overall network was $\mu_{Net} = 1\,\mathrm{cm}^2/\mathrm{Vs}$. This discrepancy is attributed to the fact that $R_{NS} \ll R_J$ in these networks.

By assuming that the carrier density remains the same in both nanosheets and the network, it is possible to write:

$$\frac{\rho_{NS,0}}{\rho_{Net,0}} = \frac{\mu_{Net}}{\mu_{NS}} \sim 0.05$$

for networks of electrochemically exfoliated $PtSe_2$ nanosheets. By combining this value with the measured value for $G_{Net} = 5.45$, equation (4b) can be used to estimate $G_{NS} = 109$. This value is reasonably close to the value of $G_{NS} = 85$, which was measured by Wagner for thermally grown $PtSe_2$ films [43].

This agreement indicates that the model is consistent with the experimental data. It is suggested that the strain applied to the substrate is fully transferred to the $PtSe_2$ nanosheets within the network. However, this raises the question as to why Caffrey [8] observed no strain transfer from the substrate to electrochemically exfoliated MoS_2 nanosheets, despite the network being fabricated in a manner very similar to that used here.

5.4 Conclusion

Our research presents advancements in $PtSe_2$ strain sensor technology using both electrochemical intercalation and LS deposition, which speeds up the production process from days to hours and removes the need for strict thermal and environmental controls. The LS deposition results in $PtSe_2$ flakes with high degree alignment without cracking even after 1000 cycles under low $< 1\%$ strain. The study identifies a gauge factor of $-5.45\,\mathrm{nm} \pm 0.33$. The high gauge factors are crucial for applications demanding high precision, and lower gauge factors are more suitable for environments with high stress, such as in harsh industrial settings. These findings also have implications for health monitoring and electronic skin applications, where the durability of low gauge factors allows for effective strain monitoring of minor joint movements, ultimately improving the comfort of monitoring devices in everyday use.

5.5 Future Plan

The next steps in this research aim to build upon the demonstrated potential of $PtSe_2$ as a high-performance material for strain sensing applications, focusing on material properties, device integration, and process optimization to broaden its applicability in flexible electronics and beyond.

Exploration of Material Properties

To fully understand the origin of the negative gauge factor observed in $PtSe_2$, detailed studies on the strain-dependent electronic band structure will be conducted using density functional theory (DFT) simulations. This approach will provide deeper insights into how strain modulates the material's electronic properties, enabling more precise control over its piezoresistive behavior. Additionally, the role of interlayer interactions in multilayer flakes will be investigated to optimize their piezoresistive performance. This includes studying how the stacking order, flake thickness, and interlayer coupling influence the material's response under mechanical deformation.

Electrochemical exfoliation (EE), which has already proven to be an energy-efficient method for producing $PtSe_2$ nanosheets, will be extended to other semiconducting materials. Systematic experiments will explore the influence of key material properties, such as bandgap, carrier density, and ductility, on the exfoliation process. This effort aims to broaden the range of materials that can be effectively exfoliated, enabling new applications in piezoresistive sensors and other flexible electronic devices.

Device Integration and Performance Enhancement

Future work will focus on integrating $PtSe_2$ sensors into advanced device architectures. Flexible electronics, such as wearable biomedical monitors and robotic skins,

will be developed to demonstrate the potential of $PtSe_2$ in real-world applications. Transparent electronics will also be explored, leveraging the semi-transparent nature of $PtSe_2$ networks to create multifunctional devices that combine strain sensing with optoelectronic functionalities. To achieve this, prototypes will be tested under practical conditions, such as dynamic strain and complex surface geometries.

The modulation of the gauge factor and sensing range will also be explored by altering the composition and structure of the 2D materials used. Building on recent findings, future studies will systematically vary the proportions of 2D materials and modify the mechanical properties of the substrates. This will enable the development of sensors tailored to specific applications, with optimized performance characteristics such as sensitivity, stretchability, and durability.

Process Optimization and Scalability

While Langmuir-Schaefer (LS) deposition has shown promise for creating well-aligned networks of $PtSe_2$ nanosheets, its limitations in controlling the overlap and connectivity between nanosheets remain a challenge. Future efforts will refine the LS deposition process by systematically studying the effects of surface tension, ink concentration, and deposition parameters. Advanced characterization techniques, including optical microscopy, atomic force microscopy, and scanning electron microscopy, will be employed to optimize the overlap and alignment of nanosheets, enhancing the mechanical and electrical performance of the resulting networks.

To further improve scalability, the LS deposition technique will be adapted for larger substrates and combined with complementary methods, such as inkjet printing or spray coating. This hybrid approach aims to balance the precision of nanosheet alignment with the demands of large-scale manufacturing, ensuring that the sensors remain viable for industrial applications.

Long-Term Stability and Environmental Testing

Ensuring the reliability of $PtSe_2$-based sensors under varied operational conditions is critical for their widespread adoption. The long-term stability of the sensors will be evaluated through extended cyclic testing, surpassing the current 1000-cycle benchmark, and under different strain levels. Environmental testing will examine the effects of temperature, humidity, and mechanical wear, providing essential insights into the durability of these sensors in real-world scenarios.

By addressing these challenges and leveraging the unique properties of $PtSe_2$ and other exfoliated 2D materials, this future work aims to advance the field of flexible electronics. The ultimate goal is to develop scalable, high-performance piezoresistive sensors capable of meeting the demands of emerging applications in healthcare, robotics, and beyond.

References

(1) A. Fiorillo, C. Critello and S. Pullano, *Sensors and Actuators A: Physical*, 2018, **281**, 156–175.

(2) E. Little and J. Finlay, in *Strain measurement in biomechanics*, Springer, 1992, pp. 1–13.

(3) Y.-C. Lu, C.-Y. Chiang, Y.-C. Chen, Y.-C. Lin, T. Ono and Y.-C. Tsai, *Japanese journal of applied physics*, 2020, **59**, SIIG10.

(4) W. Yan, H.-R. Fuh, Y. Lv, K.-Q. Chen, T.-Y. Tsai, Y.-R. Wu, T.-H. Shieh, K.-M. Hung, J. Li, D. Zhang et al., *Nature communications*, 2021, **12**, 2018.

(5) R. Bez, P. Pavan, G. Meneghesso et al., PROCEEDINGS OF THE EUROPEAN SOLID STATE DEVICE RESEARCH CONFERENCE, 2014, pp. i–viii.

(6) C. S. Boland, U. Khan, G. Ryan, S. Barwich, R. Charifou, A. Harvey, C. Backes, Z. Li, M. S. Ferreira, M. E. Möbius et al., *Science*, 2016, **354**, 1257–1260.

(7) Y. Lee, S. Bae, H. Jang, S. Jang, S.-E. Zhu, S. H. Sim, Y. I. Song, B. H. Hong and J.-H. Ahn, *Nano letters*, 2010, **10**, 490–493.

(8) E. Caffrey, J. R. Garcia, D. O'Suilleabhain, C. Gabbett, T. Carey and J. N. Coleman, *ACS Applied Materials & Interfaces*, 2022, **14**, 7141–7151.

(9) M. Hempel, D. Nezich, J. Kong and M. Hofmann, *Nano letters*, 2012, **12**, 5714–5718.

(10) Y. Zhao, J. Qiao, Z. Yu, P. Yu, K. Xu, S. P. Lau, W. Zhou, Z. Liu, X. Wang, W. Ji et al., *Advanced Materials*, 2017, **29**, 1604230.

(11) Y. Wang, L. Li, W. Yao, S. Song, J. Sun, J. Pan, X. Ren, C. Li, E. Okunishi, Y.-Q. Wang et al., *Nano letters*, 2015, **15**, 4013–4018.

(12) F. Bonaccorso, L. Colombo, G. Yu, M. Stoller, V. Tozzini, A. C. Ferrari, R. S. Ruoff and V. Pellegrini, *Science*, 2015, **347**, 1246501.

(13) C. P. Cullen, O. Hartwig, C. Ó. Coileáin, J. B. McManus, L. Peters, C. Ilhan, G. S. Duesberg and N. McEvoy, *arXiv preprint arXiv:2106.07366*, 2021.

(14) T.-Y. Su, H. Medina, Y.-Z. Chen, S.-W. Wang, S.-S. Lee, Y.-C. Shih, C.-W. Chen, H.-C. Kuo, F.-C. Chuang and Y.-L. Chueh, *Small*, 2018, **14**, 1800032.

(15) J. Kim, M. Jung, D. U. Lim, D. Rhee, S. H. Jung, H. K. Cho, H.-K. Kim, J. H. Cho and J. Kang, *Nano letters*, 2021, **22**, 570–577.

(16) J. Kim, D. Rhee, O. Song, M. Kim, Y. H. Kwon, D. U. Lim, I. S. Kim, V. Mazánek, L. Valdman, Z. Sofer et al., *Advanced Materials*, 2022, **34**, 2106110.

(17) M. Zhao, C. Casiraghi and K. Parvez, *Chemical Society Reviews*, 2024.

(18) S. Wang, J. Xue, D. Xu, J. He, Y. Dai, T. Xia, Y. Huang, Q. He, X. Duan and Z. Lin, *Nature Protocols*, 2023, **18**, 2814–2837.

(19) T. Carey, O. Cassidy, K. Synnatschke, E. Caffrey, J. Garcia, S. Liu, H. Kaur, A. G. Kelly, J. Munuera, C. Gabbett et al., *ACS nano*, 2023, **17**, 2912–2922.

(20) Z. Lin, Y. Liu, U. Halim, M. Ding, Y. Liu, Y. Wang, C. Jia, P. Chen, X. Duan, C. Wang et al., *Nature*, 2018, **562**, 254–258.

(21) J. Shen, Y. Pei, P. Dong, J. Ji, Z. Cui, J. Yuan, R. Baines, P. M. Ajayan and M. Ye, *Nanoscale*, 2016, **8**, 9641–9647.

(22) A. Kalosi, M. Demydenko, M. Bodik, J. Hagara, M. Kotlar, D. Kostiuk, Y. Halahovets, K. Vegso, A. Marin Roldan, G. S. Maurya et al., *Langmuir*, 2019, **35**, 9802–9808.

(23) K. Ariga, Y. Yamauchi, T. Mori and J. P. Hill, *Advanced Materials*, 2013, **25**, 6477–6512.

(24) J. Neilson, M. P. Avery and B. Derby, *ACS applied materials & interfaces*, 2020, **12**, 25125–25134.

(25) M. Lian, L. Tian, G. Huang, S. Liang, Y. Zhang, N. Yi, L. Fan, Q. Wu, F. Gan and Y. Wu, *Molecules*, 2024, **29**, 4072.

(26) K. Zhang, M. Wang, X. Zhou, Y. Wang, S. Shen, K. Deng, H. Peng, J. Li, X. Lai, L. Zhang et al., *Nano Research*, 2021, **14**, 1663–1667.

(27) M. Tharrault, E. Desgué, D. Carisetti, B. Plaçais, C. Voisin, P. Legagneux and E. Baudin, *2D Materials*, 2024, **11**, 025011.

(28) M. Yan, E. Wang, X. Zhou, G. Zhang, H. Zhang, K. Zhang, W. Yao, N. Lu, S. Yang, S. Wu et al., *2D Materials*, 2017, **4**, 045015.

(29) B. M. Szydłowska, O. Hartwig, B. Tywoniuk, T. Hartman, T. Stimpel-Lindner, Z. Sofer, N. McEvoy, G. S. Duesberg and C. Backes, *2D Materials*, 2020, **7**, 045027.

(30) A. Kjekshus and F. Gronvold, *Acta Chem. Scand*, 1959, **13**, 1767–1774.

(31) J. N. Coleman, M. Lotya, A. O'Neill, S. D. Bergin, P. J. King, U. Khan, K. Young, A. Gaucher, S. De, R. J. Smith et al., *Science*, 2011, **331**, 568–571.

(32) R. A. B. Villaos, C. P. Crisostomo, Z.-Q. Huang, S.-M. Huang, A. A. B. Padama, M. A. Albao, H. Lin and F.-C. Chuang, *npj 2D Materials and Applications*, 2019, **3**, 2.

(33) S. Zeng, M. Zhao, F. Li, Z. Yang, H. Wu, C. Tan, Q. Sun, L. Yang, L. Lei and Z. Wang, *Advanced Functional Materials*, 2024, **34**, 2308681.

(34) C. An, X. Chen, Y. Zhou, Y. Zhou, B. Zhang, C. Chen, Y. Yuan, R. Zhang, L. Zhang, X. Zhu et al., *Journal of Physics: Condensed Matter*, 2019, **31**, 415402.

(35) X. Lin, J. Lu, Y. Shao, Y. Zhang, X. Wu, J. Pan, L. Gao, S. Zhu, K. Qian, Y. Zhang et al., *Nature materials*, 2017, **16**, 717–721.

(36) R. Kempt, S. Lukas, O. Hartwig, M. Prechtl, A. Kuc, T. Brumme, S. Li, D. Neumaier, M. C. Lemme, G. S. Duesberg et al., *Advanced Science*, 2022, **9**, 2201272.

(37) S. S. Han, J. H. Kim, C. Noh, J. H. Kim, E. Ji, J. Kwon, S. M. Yu, T.-J. Ko, E. Okogbue, K. H. Oh et al., *ACS applied materials & interfaces*, 2019, **11**, 13598–13607.

(38) T. Carey, K. Synnatschke, G. Ghosh, L. Anzi, E. Caffrey, E. Coleman, C. Lin, A. Dawson, S. Liu, R. Wells, M. McCrystall, J. Plutnar, I. Plutnarova, J. Neilson, N. Marzari, L. D. Siebbeles, R. Sordan, Z. Sofer and J. N. Coleman, *Research Square Preprint*, 2024, DOI: 10.21203/rs.3.rs-5319871/v1.

(39) C. Gabbett, A. G. Kelly, E. Coleman, L. Doolan, T. Carey, K. Synnatschke, S. Liu, A. Dawson, D. O'Suilleabhain, J. Munuera et al., *Nature Communications*, 2024, **15**, 4517.

(40) S. Lukas, N. Rademacher, S. Cruces, M. Gross, E. Desgué, S. Heiserer, N. Dominik, M. Prechtl, O. Hartwig, C. Ó. Coileáin et al., *arXiv preprint arXiv:2409.03053*, 2024.

(41) A. L. Window and G. S. Holister, *Strain Gauge Technology*, Elsevier Applied Science, London, UK, 1982.

(42) C. S. Boland, *ACS nano*, 2019, **13**, 13627–13636.

(43) S. Wagner, C. Yim, N. McEvoy, S. Kataria, V. Yokaribas, A. Kuc, S. Pindl, C.-P. Fritzen, T. Heine, G. S. Duesberg et al., *Nano letters*, 2018, **18**, 3738–3745.

(44) E. Caffrey, T. Carey, L. Doolan, A. Dawson, E. Coleman, Z. Sofer, O. Cassidy, C. Gabbett and J. N. Coleman, *arXiv preprint arXiv:2410.19911*, 2024.

(45) K. H. Kim, Y. Oh and M. F. Islam, *Advanced Functional Materials*, 2013, **23**, 377–383.

(46) S. Rawson, R. Menzel, G. Johnson, P. Withers, L. Cartwright, A. Bodey, P. Lee, E. Mooney and N. Grobert, *ACS Nano*, 2022, **16**, 1896–1908.

Published Articles

Tungsten

Title: Synthesis of Tungsten Ditelluride Thin Films and Highly Crystalline Nanobelts from Pre-Deposited Reactants

2020-06-15 | Journal Article

DOI: 10.1007/s42864-020-00056-4

Contributors: J.B. McManus, **Cansu Ilhan**, B. Balsamo, C. Downing, C.P. Cullen, T.S. Lindner, G. Cunningham, L. Peters, L. Jones, D. Mullarkey, I.V. Shvets, G.S. Duesberg, N. McEvoy

arXiv

Title: Synthesis and Thermal Stability of TMD Thin Films: A Comprehensive XPS and Raman Study

2021-06-14 | Preprint

DOI: arXiv:2106.07366

Contributors: Conor P. Cullen, Oliver Hartwig, Cormac Ó Coileáin, John B. McManus, Lisanne Peters, **Cansu Ilhan**, Georg S. Duesberg, Niall McEvoy

ACS Applied Nano Materials

Title: Epitaxial Grown VO_2 with Suppressed Hysteresis and Low Room Temperature Resistivity for High-Performance Thermal Sensor Applications

2023-05-15 | Journal Article

DOI: 10.1021/acsanm.2c05297

Contributors: Ardak Ainabayev, Brian Walls, Daniel Casey, David Caffrey, Daragh Mullarkey, Amy McGlinchey, Amit Khare, Alexander Tikhonov, **Cansu Ilhan**, Darragh Brennan, Sean McCormack, Igor Shvets

The Journal of Physical Chemistry C

Title: Tailoring Epitaxial VO_2 Thin Films with Tunable Properties via Spray Pyrolysis for Enhanced Multifunctionality

2023-12-21 | Journal Article

DOI: 10.1021/acs.jpcc.3c06057

Contributors: Ardak Ainabayev, Brian Walls, Daniel Casey, David Caffrey, Daragh Mullarkey, Amy McGlinchey, Amit Khare, Alexander Tikhonov, **Cansu Ilhan**, Darragh Brennan, Sean McCormack, Igor Shvets

Small Methods

Title: Knot Architecture for Biocompatible Semiconducting Two-Dimensional Electronic Fibre Transistors

2024-01-10 | Journal Article

DOI: 10.1002/smtd.202301654

Contributors: Tom Carey, James Maughan, Liam Doolan, Eoghan Caffrey, Juan Garcia, Shuyang Liu, Harjinder Kaur, **Cansu Ilhan**, S. Seyedin, Jonathan N. Coleman

Submissions

Materials Today Energy

Title: Flexible Thermoelectric Generators from Spray-Printed PEDOT:PSS/$Bi_{0.5}Sb_{1.5}Te_3$ Composites

2024 | Submitted

Contributors: S. Masoumi, R. Xiong, E. Caffrey, R. Gatensby, **Cansu Ilhan**, Jonathan N. Coleman, A. Pakdel

In Preparation

Title: Solution Processed Negative Gauge Factor $PtSe_2$ Sensors

2024 | In Preparation

Contributors: Cansu Ilhan, E. Caffrey, S. Liu, J. Garcia, T. Carey, J.N. Coleman, M. Morris

A1 | Appendix 1

The appendix provides an overview of supplementary materials and detailed calculations that support the main findings discussed in this thesis. The first section presents detailed calculations and characterization data for rhenium-doped molybdenum disulfide (MoS_2), including XRR fitting results, atomic percent calculations for various doping concentrations, and activation energy analyses derived from Arrhenius plots. Following this, the thickness and roughness profiles of MoS_2 films at different doping levels are discussed using advanced techniques such as TEM and AFM. Subsequent sections explore similar analyses for WS_2) films doped with niobium, highlighting the structural and compositional modifications induced by doping. Finally, the appendix includes a theoretical model for gauge factor in piezoresistive networks of nanosheets, using $PtSe_2$ as a case study to elucidate strain transfer mechanisms and their effects on network resistivity. The modeling studies for $PtSe_2$) network is completed by Prof. Jonathan Coleman. These materials aim to provide the necessary context and detail to support the experimental and theoretical conclusions drawn in the main chapters.

A1.1 Rhenium doped Molybdenum XRR Results

The XRR fitting results are shown in Figure A1.1. The table that includes the XRR fitting results, as well as the values after conversion, is shown in Table A1.1. In the section on Re-doped MoS_2, three different compositions are presented. These are: pristine MoS_2, meaning there is no Re contribution; 0.2 nm Re in a nominal thickness of a 20 nm stack, corresponding to 2.63 at.% Re; and 2 nm Re, corresponding to 10.48 at.% Re-doped MoS_2. Atomic weight calculations are provided following section.

A1.1.1 Thickness of MoS_2 Before and After Conversion

Initial transition metal thicknesses were determined using XRR, with the related fit shown in Figure A1.1. After conversion, the pristine and 10.48 at.% Re-doped MoS_2 films were sent for imaging, while the 2.63 at.% Re-doped MoS_2 film was examined using AFM. The examination of the samples using TEM for pristine and 10.48 at.% Re-doped films, or AFM for the 2.63 at.% Re-doped film, aimed to understand the resultant thickness after the furnace process and to investigate the structural properties.

Table A1.1: Comparison of thickness values before and after conversion for pristine and rhenium-doped MoS_2 samples with varying concentrations of Re. The techniques used for measuring thickness are listed for each sample, highlighting the combined use of TEM and AFM for structural and topographical characterization.

Concentration (at.%)	**Thickness/Before**	**Thickness/After**	**Technique**
Pristine	18.1 nm	49 nm	TEM
2.63 at.% Re	19.6 nm	50 nm	AFM
10.48 at.% Re	19.9 nm	41 nm	TEM

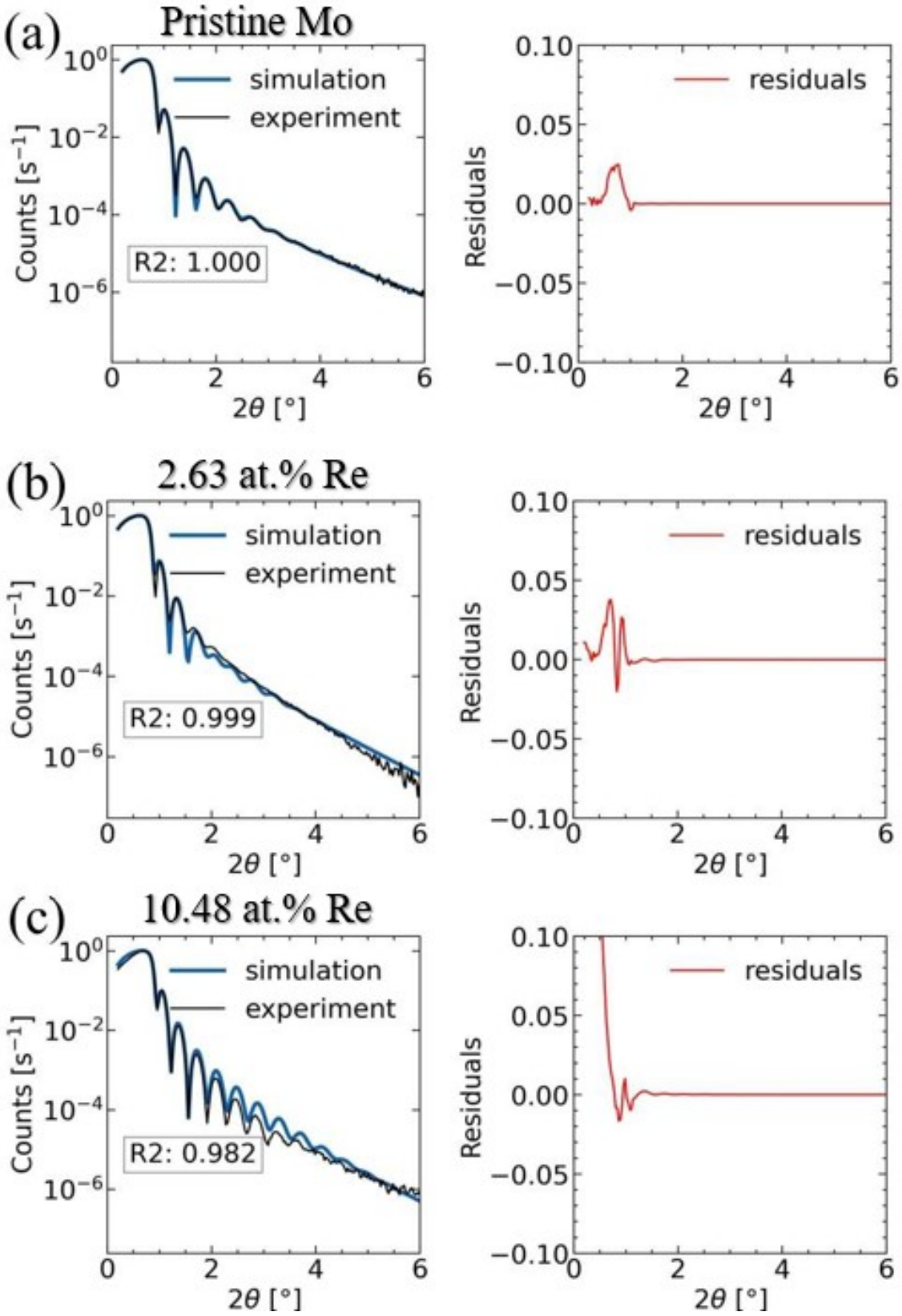

Figure A1.1: XRR fit of three samples using GenX, showing R_2 fit and residual distribution. The residual represents the difference between the experimental and simulated values. The R^2 values demonstrate that the fits are reliable.

A1.2 Calculation of Atomic Percent of Rhenium [Re: 0.2 nm]

Step 1: Parameters. Substrate area: $A = 1\,\text{cm}^2$. Atomic weights: $M_{\text{Mo}} = 95.95\,\text{g/mol}$, $M_{\text{Re}} = 186.21\,\text{g/mol}$. Densities: $\rho_{\text{Mo}} = 10.28\,\text{g/cm}^3$, $\rho_{\text{Re}} = 21.02\,\text{g/cm}^3$. Thicknesses:

$$t_{\text{Mo}} = 19.5\,\text{nm} = 19.5 \times 10^{-7}\,\text{cm}, \quad t_{\text{Re}} = 0.5\,\text{nm} = 0.5 \times 10^{-7}\,\text{cm}.$$

Avogadro's number: $N_A = 6.022 \times 10^{23}\,\text{atoms/mol}$.

Step 2: Calculate Volumes. The volume of each layer: $V = t \cdot A$:

$$V_{\text{Mo}} = t_{\text{Mo}} \cdot A = (19.5 \times 10^{-7}) \cdot 1 = 19.5 \times 10^{-7}\,\text{cm}^3,$$

$$V_{\text{Re}} = t_{\text{Re}} \cdot A = (0.5 \times 10^{-7}) \cdot 1 = 0.5 \times 10^{-7}\,\text{cm}^3.$$

Step 3: Calculate Masses. The mass of each layer is given by $m = V \cdot \rho$:

$$m_{\text{Mo}} = V_{\text{Mo}} \cdot \rho_{\text{Mo}} = (19.5 \times 10^{-7}) \cdot 10.28 = 2.003 \times 10^{-5}\,\text{g},$$

$$m_{\text{Re}} = V_{\text{Re}} \cdot \rho_{\text{Re}} = (0.5 \times 10^{-7}) \cdot 21.02 = 1.051 \times 10^{-6}\,\text{g}.$$

Step 4: Calculate Number of Atoms. The number of atoms in each layer is:

$$N_{\text{Mo}} = \frac{m_{\text{Mo}}}{M_{\text{Mo}}} \cdot N_A = \frac{2.003 \times 10^{-5}}{95.95} \cdot 6.022 \times 10^{23} = 1.26 \times 10^{17}\,\text{atoms},$$

$$N_{\text{Re}} = \frac{m_{\text{Re}}}{M_{\text{Re}}} \cdot N_A = \frac{1.051 \times 10^{-6}}{186.21} \cdot 6.022 \times 10^{23} = 3.40 \times 10^{15}\,\text{atoms}.$$

Step 5: Calculate Atomic Percent. The atomic percent of Re (x_{Re}) is calculated:

$$x_{\mathrm{Re}} = \frac{N_{\mathrm{Re}}}{N_{\mathrm{Re}} + N_{\mathrm{Mo}}} \times 100 = \frac{3.40 \times 10^{15}}{3.40 \times 10^{15} + 1.26 \times 10^{17}} \times 100 = 2.63\,\mathrm{at.\%}.$$

A1.3 Calculation of Atomic Percent of Rhenium [Re : 2 nm]

Step 1: Parameters. Substrate area: $A = 1\,\text{cm}^2$. Atomic weights: $M_{\text{Mo}} = 95.95\,\text{g/mol}$, $M_{\text{Re}} = 186.21\,\text{g/mol}$. Densities: $\rho_{\text{Mo}} = 10.28\,\text{g/cm}^3$, $\rho_{\text{Re}} = 21.02\,\text{g/cm}^3$. Thicknesses:

$$t_{\text{Mo}} = 18.0\,\text{nm} = 18.0 \times 10^{-7}\,\text{cm}, \quad t_{\text{Re}} = 2.0\,\text{nm} = 2.0 \times 10^{-7}\,\text{cm}.$$

Avogadro's number: $N_A = 6.022 \times 10^{23}\,\text{atoms/mol}$.

Step 2: Calculate Volumes. The volume of each layer: $V = t \cdot A$:

$$V_{\text{Mo}} = t_{\text{Mo}} \cdot A = (18.0 \times 10^{-7}) \cdot 1 = 18.0 \times 10^{-7}\,\text{cm}^3,$$

$$V_{\text{Re}} = t_{\text{Re}} \cdot A = (2.0 \times 10^{-7}) \cdot 1 = 2.0 \times 10^{-7}\,\text{cm}^3.$$

Step 3: Calculate Masses. The mass of each layer is given by $m = V \cdot \rho$:

$$m_{\text{Mo}} = V_{\text{Mo}} \cdot \rho_{\text{Mo}} = (18.0 \times 10^{-7}) \cdot 10.28 = 1.850 \times 10^{-5}\,\text{g},$$

$$m_{\text{Re}} = V_{\text{Re}} \cdot \rho_{\text{Re}} = (2.0 \times 10^{-7}) \cdot 21.02 = 4.204 \times 10^{-6}\,\text{g}.$$

Step 4: Calculate Number of Atoms. The number of atoms in each layer is:

$$N_{\text{Mo}} = \frac{m_{\text{Mo}}}{M_{\text{Mo}}} \cdot N_A = \frac{1.850 \times 10^{-5}}{95.95} \cdot 6.022 \times 10^{23} = 1.16 \times 10^{17}\,\text{atoms},$$

$$N_{\text{Re}} = \frac{m_{\text{Re}}}{M_{\text{Re}}} \cdot N_A = \frac{4.204 \times 10^{-6}}{186.21} \cdot 6.022 \times 10^{23} = 1.36 \times 10^{16}\,\text{atoms}.$$

Step 5: Calculate Atomic Percent. The atomic percent of Re (x_{Re}) is calculated:

$$x_{\mathrm{Re}} = \frac{N_{\mathrm{Re}}}{N_{\mathrm{Re}} + N_{\mathrm{Mo}}} \times 100 \frac{1.36 \times 10^{16}}{1.36 \times 10^{16} + 1.16 \times 10^{17}} \times 100 = 10.48\,\mathrm{at.\%}.$$

A1.4 Activation Energy Calculations

The activation energy (E_a) for charge carriers was determined using the Arrhenius equation:

$$\ln(R) = \ln(R_0) + \frac{E_a}{k_B T}$$

The slope obtained from the $\ln(R)$ vs. $1/T$ plot corresponds to:

$$\text{slope} = \frac{E_a}{k_B}$$

where E_a is the activation energy and k_B is the Boltzmann constant ($8.617 \times 10^{-5}\,\text{eV/K}$).

Pristine MoS_2:

The slope of the linear fit for pristine MoS_2 is 1.28. Using the relation:

$$E_a = \text{slope} \cdot k_B$$

we calculate:

$$E_a = 1.28 \cdot 8.617 \times 10^{-5} = 1.1018 \times 10^{-3}\,\text{eV} = 110.2\,\text{meV}$$

2.63 at.% Rhenium-Doped MoS_2:

The slope of the linear fit for 2.63 at.% Rhenium-doped MoS_2 is 0.81. Using the same relation:

$$E_a = \text{slope} \cdot k_B$$

Then,

$$E_a = 0.81 \cdot 8.617 \times 10^{-5} = 6.980 \times 10^{-4}\,\text{eV} = 69.8\,\text{meV}$$

These calculations confirm that the activation energy decreases with Rhenium doping, consistent with donor levels being introduced near the conduction band.

A1.5 Pristine MoS_2 Thickness Profile (TEM)

The thickness of pristine MoS_2 was analyzed using High-Angle Annular Dark Field (HAADF) imaging in a TEM setup, which provides high contrast based on the atomic number (Z) for thin film characterization. The extracted intensity profile was used to determine the full-width at half-maximum (FWHM) of the intensity peak, yielding a film thickness of 49 nm. Figure A1.2 shows the HAADF image and corresponding intensity profile, highlighting the electron scattering behavior of MoS_2 and its substrate.

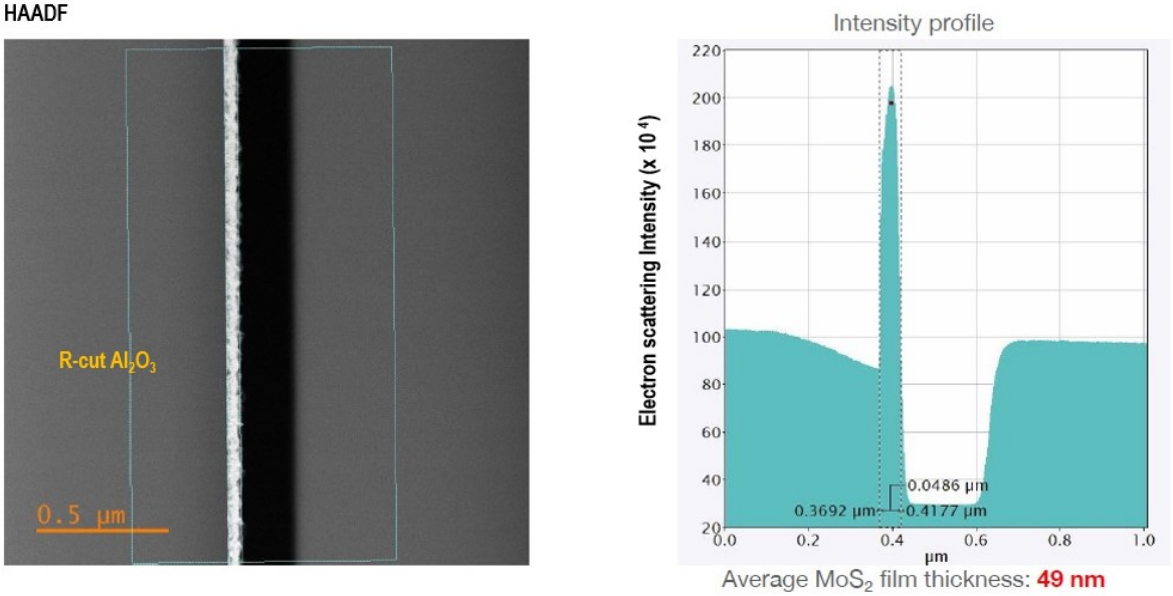

Figure A1.2: The thickness of the pristine MoS_2 film that grown on R-cut Al_2O_3 substrate, was measured using HAADF imaging in a STEM setup. The intensity profile extracted from the cross-sectional image was analyzed, and the FWHM of the intensity peak was determined to be 49 nm, corresponding to the film thickness. The y-axis represents the electron scattering intensity ($\times 10^4$), quantifying the HAADF signal across the pristine MoS_2 film and substrate. HAADF detectors collect electrons scattered at high angles, which are sensitive to the atomic number (Z) of the material (proportional to Z^2). Materials with higher atomic numbers scatter more electrons, resulting in higher intensity peaks on the y-axis. The peaks in the profile indicate the presence of the MoS_2 film, while the lower intensity regions correspond to the substrate and vacuum.

A1.6 2.63 at.% Re doped MoS_2 Thickness Profile (AFM)

Thickness in the Range of 2.5 µm to 3.5 µm (Excluding Peaks):

- **Line 1 (Black):**

  Ignoring the peak, the thickness fluctuates around 45–55 nm in this region. This range represents a more realistic film thickness.

- **Line 2 (Red):**

  Excluding the peak, the thickness lies in the range of 50–60 nm. This is consistent with the overall average thickness of the film.

- **Line 3 (Blue):**

  The thickness fluctuates between 40–50 nm in this range. This is slightly below the average but still realistic for the film.

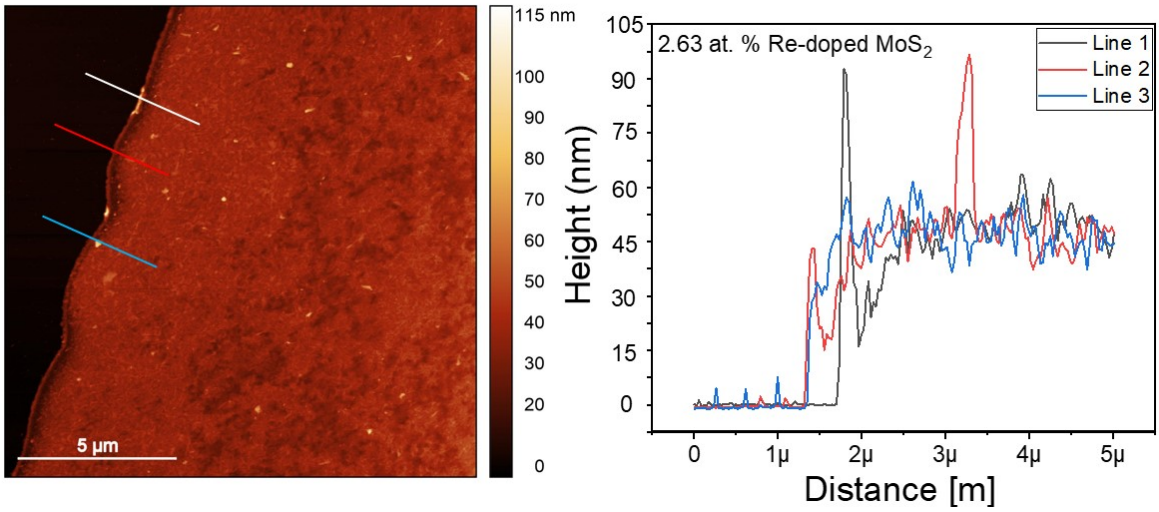

Figure A1.3: The image shows the AFM micrograph of 2.63 at.% Re-doped MoS_2 film grown on R-cut Al_2O_3 substrate and the corresponding line profiles of height across three selected areas (labeled as Line 1, Line 2, and Line 3). The left panel represents the surface topography, with the height variation color-coded from 0 to 115 nm. The right panel illustrates the height profiles along the three marked lines in the AFM image. For AFM image analysis, an open source software Gwyddion is used [1]. The detail about it is given in the Section 2.9.

A1.7 10.48 at.% Re doped MoS_2 Thickness Profile (TEM)

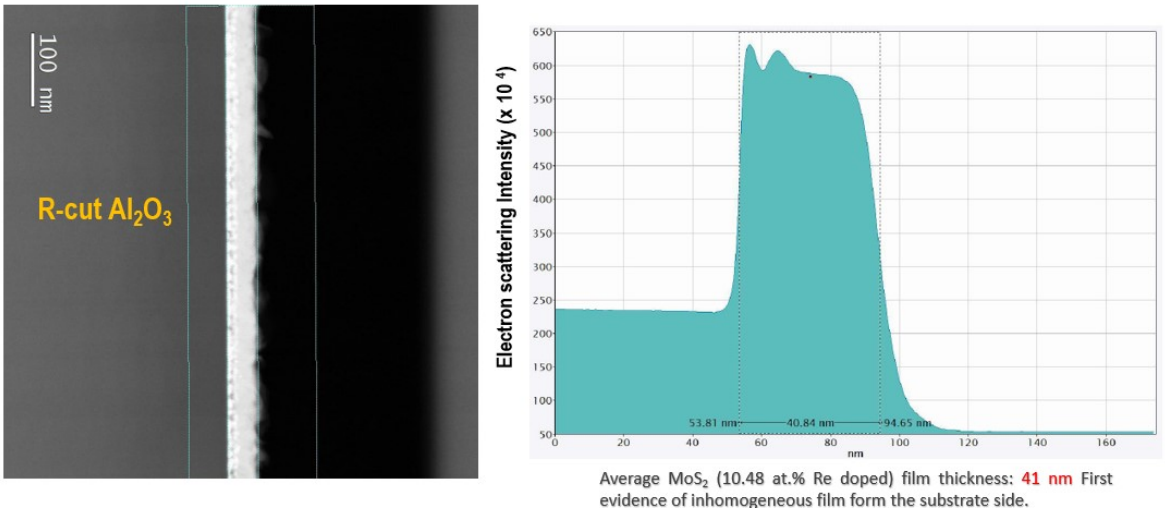

Figure A1.4: HAADF imaging and intensity profile analysis of 10.48 at.% Re-doped MoS_2 film grown on R-cut Al_2O_3 substrate. The left panel shows the cross-sectional HAADF image, while the right panel displays the corresponding intensity profile. The film thickness was determined to be 41 nm based on the full-width at half-maximum of the intensity peak. The intensity profile highlights the electron scattering behavior, with higher intensity peaks corresponding to the MoS_2 film and lower intensity regions indicating the substrate. Evidence of inhomogeneity in the film is observed near the substrate side.

A1.8 Pristine MoS_2 Roughness analysis (AFM)

The figure A1.5 shows the AFM topographic image of a selected area on pristine MoS_2 that grown on R-cut Al_2O_3 substrate, highlighting its surface morphology. The analysis reveals a surface roughness of over 6 nm along the red line. XRR fitting for this sample was not feasible (as discussed in the Methods section 2.8) due to insufficient diffuse X-ray scattering, which limits the signal detected by the X-ray detector. When surface roughness exceeds a certain threshold, as observed here, XRR becomes unreliable for characterizing thickness and roughness. In such cases, alternative techniques such as AFM or cross-sectional TEM are more suitable for accurate thickness determination and surface characterization.

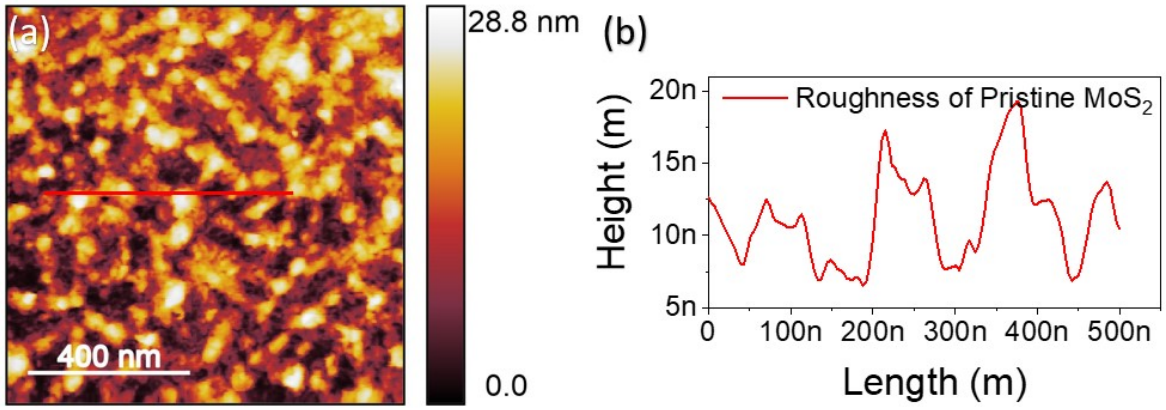

Figure A1.5: (a) AFM topographic image of pristine MoS_2 showing the surface morphology over a chosen area where scale bar is 400 nm. (b) Line profile analysis along the red arrow in (a) reveals the surface roughness with a height variation more than 5 nm.

A2 | Appendix 2

A2.1 Calculation of Atomic Percent (W:Nb)

Step 1: Parameters. Substrate area: $A = 1\,\text{cm}^2$. Atomic weights: $M_W = 183.84\,\text{g/mol}$, $M_{Nb} = 92.91\,\text{g/mol}$. Densities: $\rho_W = 19.25\,\text{g/cm}^3$, $\rho_{Nb} = 8.57\,\text{g/cm}^3$. Thicknesses: $t_W = 9.8\,\text{nm} = 9.8 \times 10^{-7}\,\text{cm}$, $t_{Nb} = 0.2\,\text{nm} = 0.2 \times 10^{-7}\,\text{cm}$. Avogadro's number: $N_A = 6.022 \times 10^{23}\,\text{atoms/mol}$.

Step 2: Calculate Volumes. The volume of each layer: $V = t \cdot A$:

$$V_W = t_W \cdot A = 9.8 \times 10^{-7} \cdot 1 = 9.8 \times 10^{-7}\,\text{cm}^3, \quad V_{Nb} = t_{Nb} \cdot A = 0.2 \times 10^{-7} \cdot 1 = 0.2 \times 10^{-7}\,\text{cm}$$

Step 3: Calculate Masses. The mass of each layer is given by $m = V \cdot \rho$:

$$m_W = V_W \cdot \rho_W = (9.8 \times 10^{-7}) \cdot 19.25 = 1.887 \times 10^{-5}\,\text{g},$$

$$m_{Nb} = V_{Nb} \cdot \rho_{Nb} = (0.2 \times 10^{-7}) \cdot 8.57 = 1.714 \times 10^{-7}\,\text{g}.$$

Step 4: Calculate Number of Atoms. The number of atoms in each layer is: $N = \frac{m}{M} \cdot N_A$:

$$N_W = \frac{m_W}{M_W} \cdot N_A = \frac{1.887 \times 10^{-5}}{183.84} \cdot 6.022 \times 10^{23} = 6.18 \times 10^{16}\,\text{atoms},$$

$$N_{Nb} = \frac{m_{Nb}}{M_{Nb}} \cdot N_A = \frac{1.714 \times 10^{-7}}{92.91} \cdot 6.022 \times 10^{23} = 1.11 \times 10^{15}\,\text{atoms}.$$

Step 5: Calculate Atomic Percent. The atomic percent of Nb (x_{Nb}) is calculated:

$$x_{\mathrm{Nb}} = \frac{N_{Nb}}{N_{Nb} + N_W} \times 100,$$

$$x_{\mathrm{Nb}} = \frac{1.11 \times 10^{15}}{1.11 \times 10^{15} + 6.18 \times 10^{16}} \times 100 = \approx 1.76\,\mathrm{at.\%}.$$

A2.2 Pristine WS_2 Thickness Profile (TEM)

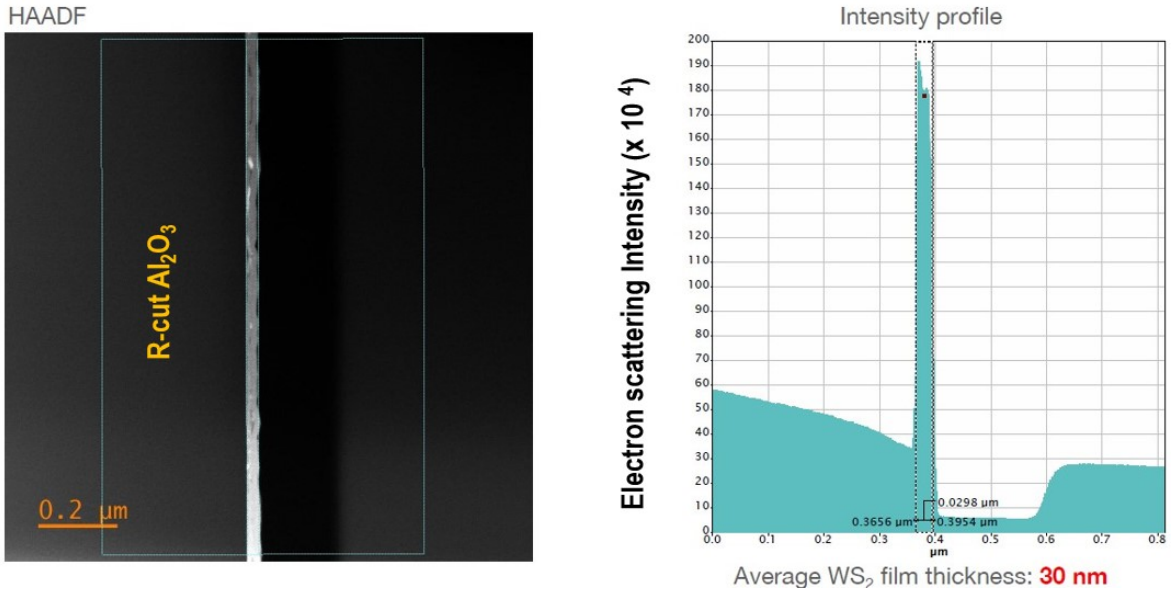

Figure A2.1: The thickness of the pristine WS_2 film was measured using HAADF imaging in a STEM setup. The intensity profile extracted from the cross-sectional image was analyzed, and the FWHM of the intensity peak was determined to be 30 nm, corresponding to the film thickness. The y-axis represents the electron scattering intensity ($\times 10^4$), quantifying the HAADF signal across the pristine WS_2 film and substrate. HAADF detectors collect electrons scattered at high angles, which are sensitive to the atomic number (Z) of the material (proportional to Z^2). Materials with higher atomic numbers scatter more electrons, resulting in higher intensity peaks on the y-axis. The peaks in the profile indicate the presence of the WS_2 film, while the lower intensity regions correspond to the substrate and vacuum.

A2.3 Nb doped WS_2 Thickness Profile (TEM)

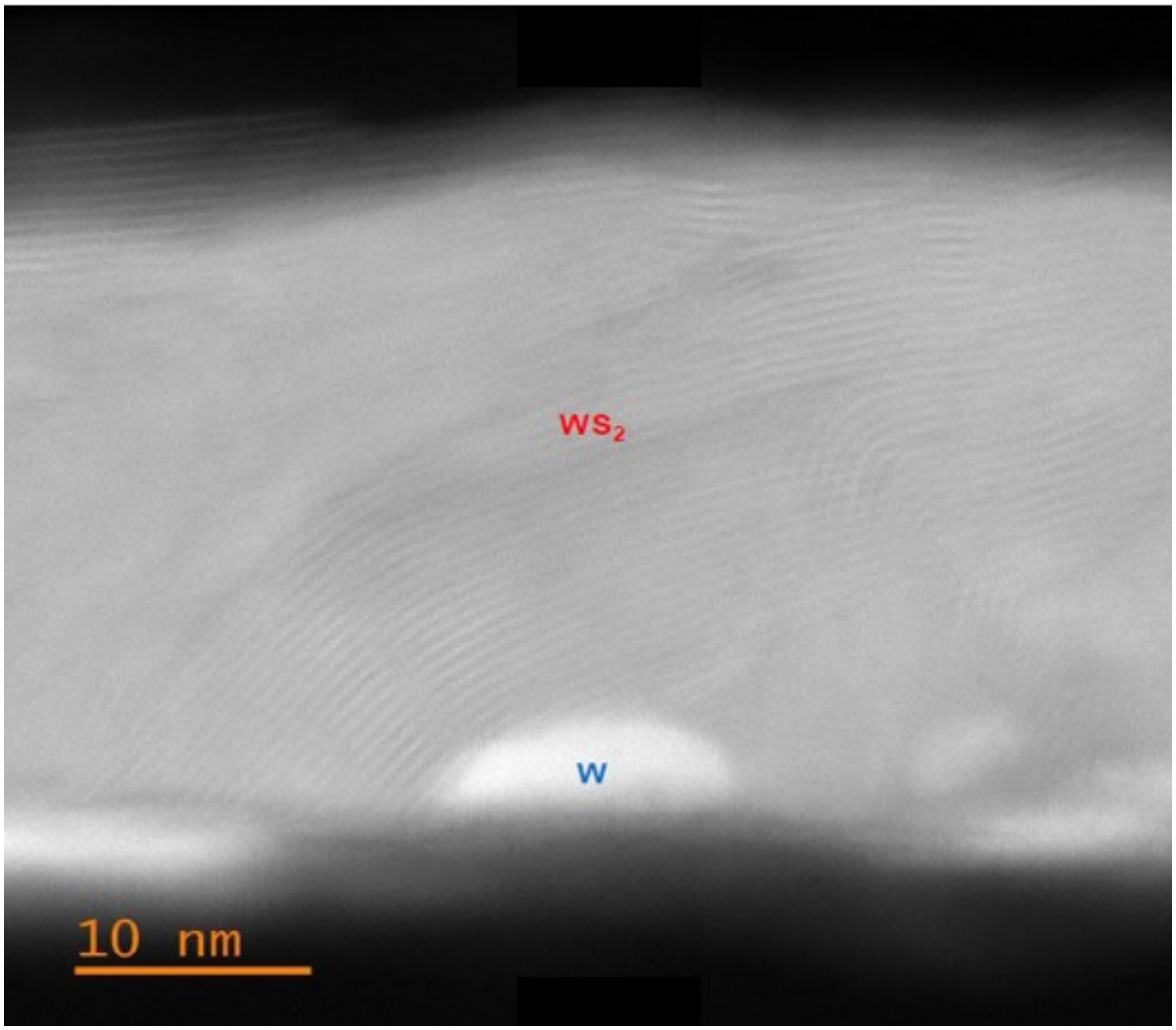

Figure A2.2: The thickness of the Nb-doped WS_2 film was measured using HAADF imaging in a STEM setup. The thickness of the film is similar to pristine WS_2 film. However, unconverted metal blocks are obvious with Nb doped WS_2 film. The substrate is here Glass (Amorph SiO_2).

A3 | Appendix 3

A3.1 Generating a Model for Gauge Factor in $PtSe_2$ Networks

The parameter that quantifies the magnitude of the piezoresistive effect is the gauge factor, G, defined as the fractional resistance change $\Delta R/R_0$ per unit strain ϵ in the linear, low-strain regime [1, 2]

$$G = \frac{\Delta R/R_0}{\epsilon}. \tag{1}$$

Here, R_0 denotes the resistance in the unstrained state. Usually, the gauge factor is measured at low strain, and in that limit, it can be shown that for an isotropic material:

$$G = (1 + 2\nu) + \frac{1}{\rho_0}\frac{d\rho}{d\epsilon} \tag{2}$$

where ν and ρ are the Poisson ratio and resistivity of the piezoresistive material, and ρ_0 is its zero-strain resistivity. The first term describes the effect of strain on sample dimensions (and resistance), while the second term describes the effect of strain on the intrinsic material properties.

To properly analyze our data, it is necessary to understand the factors controlling conduction in networks of highly aligned, electrochemically exfoliated nanosheets such as those under study here. Recently, Gabbett et al. proposed a model that well-describes conduction in nanosheet networks [3]. This paper provides an equation for network resistivity which, in the case of very low-porosity networks of high-

carrier-density nanosheets [3], can be written as:

$$\rho_{\text{network}} \approx t_{NS}[R_{NS} + R_J], \tag{3}$$

where t_{NS} is the mean nanosheet thickness and R_{NS} and R_J are the mean resistances of individual nanosheets and junctions within the network, respectively. Combining equation (2) and equation (3) allows us to generate an equation for the gauge factor of our networks. In addition to calculating the second term in equation (2), we modify the first term to account for the anisotropic nature of nanosheet networks, which are expected to have different Poisson ratios in the in-plane (y) and out-of-plane (z) directions (here the strain is applied in the x-direction):

$$G_{\text{Network}} = (1 + \nu_y + \nu_z) + \frac{dR_{\text{NS}}/d\epsilon + dR_J/d\epsilon}{R_{\text{NS0}} + R_{J0}}, \tag{4}$$

where the subscript "0" denotes the value at $\epsilon = 0$. The first term describes the contribution to the piezoresistance from dimensional changes under deformation ($G_{\text{Dimensional}}$), while the second term describes the intrinsic piezoresistance of the material ($G_{\text{Intrinsic}}$).

Case 1: No Strain Transfer from Substrate to Nanosheets

This scenario is relevant if applying strain causes the nanosheets to slide past each other without themselves deforming. Because the nanosheets do not change size:

$$\frac{dR_{\text{NS}}}{d\epsilon} = 0. \tag{5}$$

Then the problem reduces to calculating $dR_J/d\epsilon$. To do this, we note that for a junction resistance:

$$R_J = \frac{\rho_J}{A_J}, \tag{6}$$

where A_J is the junction area that must depend on strain, while ρ_J is a constant associated with transport across the junction. In Figure S1, we model a junction in

the simplest possible way.

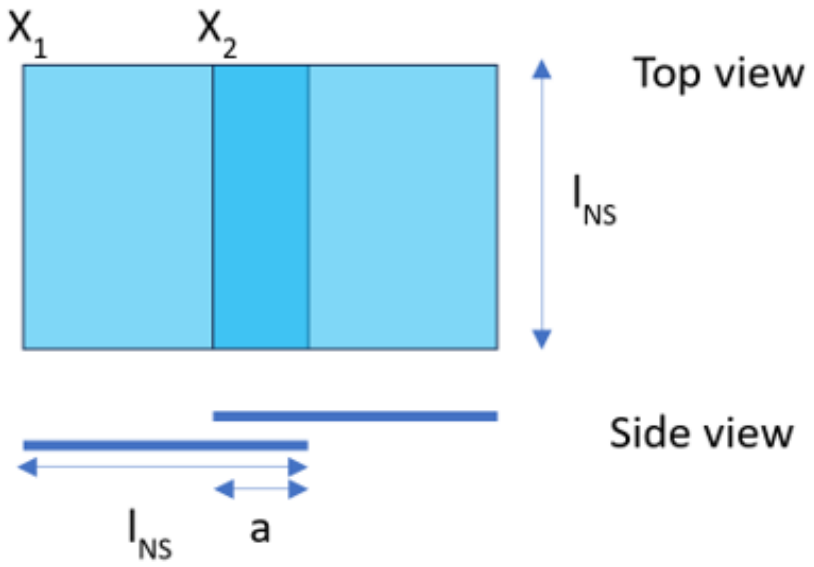

Figure A3.1: Nanosheet overlap schematic, showing top view and side view of two square overlapping nanosheets. Here, the x-direction is the direction of strain (horizontal in the figure), while y is the perpendicular in-plane direction (vertical in the figure).

Consider two square nanosheets (length l_{NS}) partially overlapping, as shown in the schematic. The overlapping area is the junction. The junction area is:

$$A_J = a l_{NS}, \tag{7}$$

where a is the length of the partial overlap. The left-hand edge of the nanosheets is at positions X_1 and X_2. Then the distance between edges is:

$$\Delta X = (X_2 - X_1) = l_{NS} - a. \tag{8}$$

When strain is applied to the system, the left-hand edges of the nanosheets will become further apart:

$$\Delta X = (\epsilon + 1)\Delta X_0, \tag{9}$$

where the subscript "0" denotes the unstrained case.

Assume that when strain is applied, the nanosheets slide across each other, and the

nanosheet length does not change. Then:

$$\Delta X = l_{NS} - a, \tag{10}$$

and in the absence of strain:

$$\Delta X_0 = l_{NS} - a_0, \tag{11}$$

where a_0 is the unstrained value of a.

Rearranging:

$$A_J = A_{J0}\left[1 - \frac{(1 - f_{J0})}{f_{J0}}\epsilon\right]. \tag{12}$$

Thus:

$$R_J \approx \frac{\left(\frac{\rho_J}{A_{J0}}\right)}{(1 - (1 - f_{J0})/f_{J0})\,\epsilon}. \tag{13}$$

At small strain:

$$\frac{dR_J}{d\epsilon} = R_{J0}\,(1 - f_{J0})\,/f_{J0}. \tag{14}$$

This is a positive value. Combining this result with equations (2) and (3), we find that:

$$G_{\text{Network}} = (1 + \nu_y + \nu_z) + \frac{2\rho_{NS0}}{\rho_{J0}}\,(1 - f_{J0})\,/f_{J0}. \tag{15}$$

Here, the gauge factor must be positive. This is NOT consistent with our experimental data, ruling out Case 1. However, we note that Case 1 has been observed previously for networks of MoS_2 nanosheets, which have slightly lower aspect ratios than those here [4].

Case 2: Maximum strain is transferred from the substrate to the nanosheets such that the nanosheet strain is the same as the applied strain

Here we assume that enough stress is transferred between the substrate and nanosheets, and between nanosheets, such that all nanosheets feel the same strain as the applied strain.

In this scenario, all dimensions in the x-direction will be stretched by a factor of $(1+\epsilon)$, while dimensions in the y-direction will be changed (i.e., reduced) by a factor of $(1-\nu_y\epsilon)$, where ν_y is the Poisson ratio in the y-direction, which, for simplicity, is assumed to be the same for the substrate and nanosheets.

Then the junction area is:

$$A_J = al_{NS}(1+\epsilon)(1-\nu_y\epsilon), \tag{16}$$

where a is increased by the strain and l_{NS} (representing the nanosheet length in the y-direction) is reduced by strain.

Simplifying:

$$A_J \approx A_{J0}(1+\epsilon-\nu_y\epsilon), \tag{17}$$

valid at small strain, where ϵ^2 is neglected. Then:

$$R_J = \frac{\rho_J}{A_J} = \frac{\rho_J}{A_{J0}(1+\epsilon-\nu_y\epsilon)}. \tag{18}$$

At small strain, this becomes:

$$\Delta R_J \approx \frac{\rho_J}{A_{J0}}(-\nu_y)\epsilon. \tag{19}$$

Noting that:

$$\left.\frac{R_J}{A_J}\right|_0 = \frac{\rho_J}{A_{J0}}, \quad \text{(from equation S4)}, \tag{20}$$

we have:

$$\frac{dR_J}{d\epsilon} = \frac{-\nu_y R_J}{\epsilon}. \tag{21}$$

This is true at small strain. N.B. Assuming $\nu_y < 1$, this value is negative.

We can find ΔR_{NS} by modifying the definition of the gauge factor ($\Delta R/R_0 = G\epsilon$):

$$\Delta R_{\mathrm{NS}}/R_J = G_R. \tag{22}$$

For $PtSe_2$, $G_{\mathrm{NS}} < 0$, so this value is negative. Using equation (S3):

$$G_{\mathrm{Network}} = (1 + \nu_y + \nu_z) + G_R \frac{\rho_{NS0}}{\rho_{J0}} \left(G_{\mathrm{NS}} - (\nu_y - 1)\right). \tag{23}$$

Interestingly, symmetry implies that we can consider $G_R = (\nu_y - 1)$. This implies that, in this scenario of efficient strain transfer from the substrate to nanosheets, the junction gauge factor is negative. This is because the junction area increases with strain in this scenario.

We can now apply the network conductivity model, equation (2), (written for zero strain), and the equivalent equation for individual nanosheets, and use these to eliminate the resistances from the equation above. This yields:

$$G_{\mathrm{Network}} = (1 + \nu_y + \nu_z) + G_R \frac{\rho_{NS0}}{\rho_{J0}} + \frac{\rho_{NS0}}{\rho_{J0}} \left(G_{\mathrm{NS}} - (\nu_y - 1)\right). \tag{24}$$

Which simplifies to:

$$G_{\mathrm{Network}} = (2\nu_y + \nu_z) + G_R \frac{\rho_{NS0}}{\rho_{J0}} \left[G_{\mathrm{NS}} - (\nu_y - 1)\right]. \tag{25}$$

We can approximate $\nu_y = 0.5$ (that of the polymer) and $\nu_z = 0$ (consistent with

networks) [5–11], meaning:

$$2\nu_y + \nu_z = 1 \quad \text{and} \quad (\nu_y - 1) = -0.5. \tag{26}$$

This equation means that a 2D material like $PtSe_2$, with a large negative intrinsic gauge factor ($G_{\text{NS}} = -85$) [**ref13**], can form networks that display a small negative gauge factor, as long as $2\nu_y + \nu_z$ is small enough.

We can test the agreement between this model and our experiment using known values of various parameters. Taking the published value of $G_{\text{NS}} = -85$[12] and our value of $G_{\text{Network}} = -5.45$, combined with:

$$\frac{\rho_{NS0}}{\rho_{J0}} = 0.076, \tag{27}$$

this data implies:

$$\mu_{NS0}/\mu_{\text{Network}} = 13. \tag{28}$$

This value is reasonably close to the ratio of 20 recently reported for similar $PtSe_2$ networks [13], and shows that case 2 is consistent with experimental data.

This strongly supports scenario 2 and implies that enough stress is transferred to the nanosheets for them to reach close to the full applied strain.

References

(1) A. Window, *Strain Gauge Technology*, Springer, 1992.

(2) A. Fiorillo, C. Critello and S. Pullano, *Sensors and Actuators A: Physical*, 2018, **281**, 156–175.

(3) C. Gabbett, A. G. Kelly, E. Coleman, L. Doolan, T. Carey, K. Synnatschke, S. Liu, A. Dawson, D. O'Suilleabhain, J. Munuera et al., *Nature Communications*, 2024, **15**, 4517.

(4) E. Caffrey, T. Carey, L. Doolan, A. Dawson, E. Coleman, Z. Sofer, O. Cassidy, C. Gabbett and J. N. Coleman, *arXiv preprint arXiv:2410.19911*, 2024.

(5) K. H. Kim, Y. Oh and M. F. Islam, *Advanced Functional Materials*, 2013, **23**, 377–383.

(6) M. Mecklenburg, A. Schuchardt, Y. Mishra, S. Kaps, R. Adelung, A. Lotnyk, L. Kienle and K. Schulte, *Advanced Materials*, 2012, **24**, 3486–3490.

(7) Y. Wu, N. Yi, L. Huang, T. Zhang, S. Fang, H. Chang, N. Li, J. Oh, J. Lee, M. Kozlov et al., *Nature Communications*, 2015, **6**, 6141.

(8) S. Woo, H. Park and Y.-W. Son, *Physical Review B*, 2016, **93**, 075420.

(9) H. Zhan, D. Guo and G. Xie, *Nanoscale*, 2019, **11**, 13181–13212.

(10) Y. Fan, Y. Xiang and H.-S. Shen, *Research*, 2020, **2020**.

(11) S. Rawson, R. Menzel, G. Johnson, P. Withers, L. Cartwright, A. Bodey, P. Lee, E. Mooney and N. Grobert, *ACS Nano*, 2022, **16**, 1896–1908.

(12) S. Wagner, C. Yim, N. McEvoy, S. Kataria, V. Yokaribas, A. Kuc, S. Pindl, C.-P. Fritzen, T. Heine, G. S. Duesberg et al., *Nano letters*, 2018, **18**, 3738–3745.

(13) T. Carey, K. Synnatschke, G. Ghosh, L. Anzi, E. Caffrey, E. Coleman, C. Lin, A. Dawson, S. Liu, R. Wells, M. McCrystall, J. Plutnar, I. Plutnarova, J. Neilson, N. Marzari, L. D. Siebbeles, R. Sordan, Z. Sofer and J. N. Coleman, *Research Square Preprint*, 2024, DOI: `10.21203/rs.3.rs-5319871/v1`.